Exploration of Higher-Order Quantum Interference Landscapes

by

Sascha Agne

A thesis
presented to the University of Waterloo
in fulfillment of the
thesis requirement for the degree of
Doctor of Philosohy
in
Physics (Quantum Information)

Waterloo, Ontario, Canada, 2017

Examining Committee Membership

The following served on the Examining Committee for this thesis. The decision of the Examining Committee is by majority vote.

Supervisor: Dr. Thomas Jennewein, Associate Professor
Internal Member: Dr. Kyung Soo Choi, Assistant Professor
Internal Member: Dr. Michele Mosca, Professor
Internal-external Member: Dr. Michal Bajcsy, Assistant Professor
External Examiner: Dr. Todd Pittman, Associate Professor

Author's Declaration

This thesis consists of material all of which I authored or co-authored: see Statement of Contributions included in the thesis. This is a true copy of the thesis, including any final revisions, as accepted by my examiners.

I understand that my thesis may be made electronically available to the public.

Statement of Contributions

This thesis contains work done in collaboration with others but to which I made major contributions. The contributions are listed below.

Chapter 1:
Sascha Agne wrote the introductory chapter.

Chapter 2:
Sascha Agne, Thomas Kauten and Jeongwan Jin carried out the experiment with help from Jeff Z. Salvail and Evan Meyer-Scott. All authors discussed the results and Sascha Agne, Deny R. Hamel, Thomas Kauten and Thomas Jennewein analyzed the data. Thomas Jennewein conceived the experimental idea and Thomas Jennewein, Gregor Weihs, Kevin J. Resch, Deny R. Hamel, Thomas Kauten, Evan Meyer-Scott and Sascha Agne developed the experimental setup. Thomas Kauten build the interferometer and Sascha Agne wrote the manuscript with contributions from all authors. In addition, Sascha Agne performed the detailed theoretical derivation shown in this thesis.
Sascha Agne fabricated the glass plate holders using a 3D printer in Michal Bajcsy's laboratory with help from Rubayet Al Maruf. Kyung Soo Choi lent us power splitters used to share 842 nm photon counts between three time taggers. Aaron Miller provided much help in updating and optimizing our superconducting nanowire single photon detectors.

Chapter 3:
Sascha Agne is sole author of idea and results presented in this chapter. He benefited from discussions with Gregor Weihs, Robert Koenig, Aharon Brodutch, Vincent Russo, Matt Brown, Markus Mueller, Piotr Kolenderski, Thomas Jennewein, Joshua Combes, and Joseph Emerson.

Chapter 4:
Sascha Agne built the experimental setup and carried out the experiments with help from all authors. Thomas Jennewein conceived the experimental idea. Data analysis was carried out by Sascha Agne with help from Jean-Philippe Bourgoin and Thomas Jennewein. All

authors discussed the theoretical idea and experimental results. Jean-Philippe Bourgoin built the polarization modulator. Sascha Agne did the theoretical derivation in this thesis. Matteo Mariantoni lent us the high-speed arbitrary waveform generator used in square HOM interference experiments.

Chapter 5:
Thomas Jennewein conceived the experimental idea. Jeongwan Jin and Sascha Agne built the experimental setup and carried out the experiments with help from Jean-Philippe Bourgoin and Thomas Jennewein. Data analysis was carried out by Jeongwan Jin and Sascha Agne with contributions from all authors. Yanbao Zhang and Norbert Luetkenhaus worked on the theory support, which is included in the preprint, but not covered in this thesis.
Jacob Koenig contributed to the initial modeling of correcting optics in unbalanced interferometers. Rolf Horn, Evan Meyer-Scott, Patrick Coles, and Jacob Koenig helped us with fruitful discussions. Martin Laforest lent us the Hamamatsu EM-CCD camera used to take images of spatial modes of single photons.

Chapter 6:
Sascha Agne wrote the concluding chapter.

Abstract

Earth, Moon and Sun unite when they star together in the *three-body problem*, whose intricate plot still baffles us today. For some reason, the factorization of the two-body problem into two one-body problems does not, in general, cross the $N = 2$ border. Is computational irreducibility responsible for this emergence of complexity, as Stephen Wolfram likes to think? We don't know. The introduction to this thesis in Chapter 1, however, makes it clear that the history of science is marked by intermittent encounters of sudden complexities when the number 2 is left behind. In Chapter 2, I present an experiment that is quite similar in spirit, for my colleagues and I observe three-photon interference without two-photon and single-photon interference. We had to overcome significant experimental challenges that are typical for most quantum interference experiments involving more than two photons. Next in line is the three-slit interference experiment. Again a deceptively simple extension of the famous double-slit experiment, we are faced with questions that are difficult to access experimentally: the existence of genuine three-slit interference was first denied and then affirmed, though no experiment has decided yet. My contribution to the study of this problem is outlined in Chapter 3, where I use symmetry of measurement settings in such interference experiments to theoretically derive higher-order interference terms. In Chapter 4, I take a step back in one sense, for we study a two-photon phenomenon, but we also leap forward and discover entirely new interference landscapes. Theoretically and experimentally, I demonstrate how to use a polarization-modulated lasers to go beyond the standard Hong-Ou-Mandel (HOM) dip, and generate both triangular and square wave HOM interference patterns. Two-photon interference is also subject of Chapter 5, but with an interesting twist. While laser HOM interference relies on two independent photons, here we endow the pair with the strongest known correlations, namely entanglement. More specifically, we entangle a polarization and a time-bin qubit and use this hybrid to assess the viability of a rather special interferometer for quantum communication purposes.

Acknowledgements

I think it is pretty hard to find a doctoral advisor who is juggling fundamental and applied questions in one laboratory. Some talk or write about it but only a few actually practice daily to see both worlds converge. Hence, Thomas Jennewein offered me both. I was able to pursue basic science for my thesis and accompany the other part of the group on their field trips to experiments on airfields and radiation facilities. Thank you, Thomas, for sharing with me your enthusiasm in the lab and giving me the freedom to work on my own questions and from time to time nudging me towards a more focused approach to projects.

I was also lucky in that with Kyung Soo Choi and Michal Bajcsy I had two advisory committee members who just started their academic career. As they set up their very first lab I was able to learn a great deal about the *dos and don'ts*. Kyung and Michal, I sincerely enjoyed inspiring late night and weekend discussions —and excursions! I also had the guidance of Michele Mosca. Mike, I will keep the bigger picture in the back of my mind! Thank you, Todd Pittman, for serving as my external thesis examiner!

Special greetings to Thomas Kauten in Innsbruck, who visited our group for the three-photon interference experiment. Thomas, I will never forget those three weeks when every day we would start at 6:30 am in the lab, had breakfast at 7.30 am, returned to the lab at 8 am, where we stayed until 7 pm (and beyond)! My constant lab partner for the time-bin qubit experiments was Jeongwan Jin. I would like thank you for sharing your knowledge with me and in particular that you kept the experiments running over Christmas while I was on holidays! Thank you also to Deny Hamel without whom I would have had no clue were to start looking for photon triplets.

Lab life can be really frustrating. Luckily, with Aimee Gunther, Evan Meyer-Scott, Rolf Horn, Chris Pugh, Katanya Kuntz, Nigar Sultana, Jean-Philippe Bourgoin, Brendon Higgins, Ramy Tannous, John Matthew Donohue, Mike Mazurek, Matt Brown, Hammam Qassim, Hemant Katiyar, Zak Webb, and Audrey Dot I had plenty of room for joy. With David Luong and Michael Epping I also had office mates who I could rely on in any kind of situation. Special thanks are directed to Vincent Russo, Patrick Coles, Marian Berek, Christopher Chamberland, Robert Jonsson, Shihan Sajeed, John Rinehart, and Jean-Luc

Orgiazzi with truly open minds for any sort of discussion. And finally, what would I have done without "my" septet consisting of Hyeran Kong, Chang Liu, Anqi Huang, Stefanie Beale, Julia Amoros Binefa, Annie Jihyun Park, and Nayeli Azucena Rodriguez Briones? Late night or weekend, it didn't matter, for at least a few of you have always been around at IQC, persistently ready for science and a good portion of fun. Thank you! Gomawo! Xièxiè! Gracias!

From the bottom of my heart, a big thanks to my family and dearest friends.
In spirit you constitute the fellowship on my long academic journey.

Dedication

To all those in need of perseverance in their pursuit to solve big problems.

Table of Contents

List of Figures

List of Tables

Chapter 1

Introduction

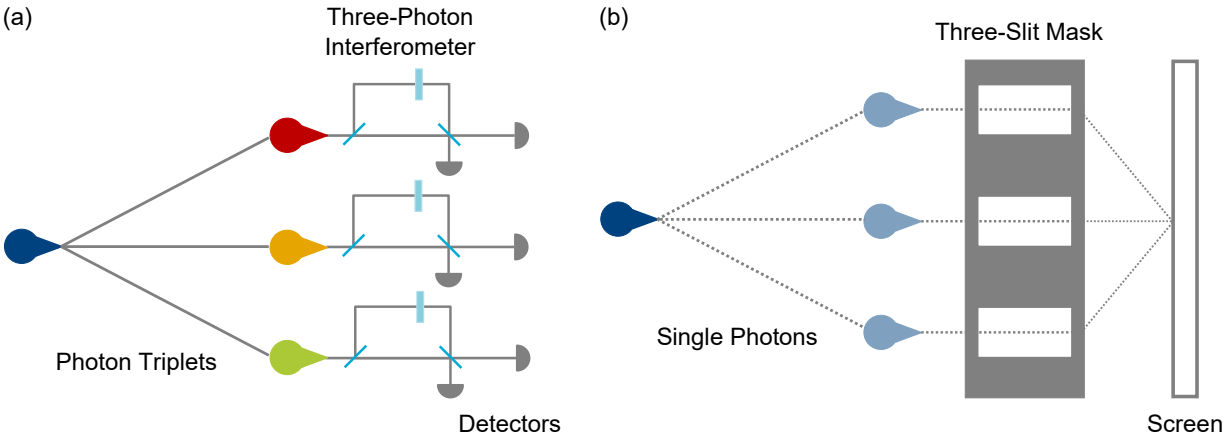

Figure 1.1: **Three-Photon and Three-Slit Interference Experiments.** Two quantum interference phenomena shape this thesis' heart. Its beating is driven by two questions. First, is it possible to observe three-photon interference without two-photon and without single-photon interference? Second, is a three-slit interference pattern always determined by double-slit and single-slit patterns? **(a)** Three entangled photons propagate through three optical interferometers and are detected by single-photon detectors. **(b)** A single photon has three alternative paths for a detection on a screen behind a three-slit mask.

What is the difference between classical and quantum interference? There is no simple answer to this question, although, asking quantum opticians, one often hears "Hong-Ou-Mandel (HOM) interference with 100 % visibility is only possible using single photons". Classical fields can also interfere at a beam splitter to form an anticorrelation dip, however, the visibility is limited to 50 % (and even this number is model-dependent: (i) two phase-randomized coherent input states and (ii) bucket detectors). Still, this quantitative

difference seems a bit unsatisfactory, for we do not gain, to use Ian Hacking's terminology, a *Cartesian* cognizance of interference. The *Leibnizian* understanding we have instead does grant us access to the mathematical machinery of both theories, but we can rarely step beyond a simple comparison of results, the strength of interference fringes in particular. To a certain extent, this betrays the complexity inherent in recently discovered interference phenomena and partially explains the difficulties encountered in applying advanced interference concepts to biological systems, where work at the classical-quantum boundary is paramount. This border is as intangible as ever and we lost a little bit the motivation to go through the trouble and calculate, for example, classical visibility bounds. Firmly established numbers can be attached to only a few interference phenomena, notably fourth-order interference, of which HOM interference is an example. Finding classical models in closest correspondence to multiparticle quantum interference phenomena is a daunting task. Why should we bother anyway? For we *know* that, ultimately, light is quantized, which guarantees the existence of a quantum-theoretical model for every interference phenomena (though we do not know yet whether gravity can be quantized, which means interference of gravitational waves are interesting). Still, we should pin down the difference between classical and quantum interference. I do not suggest that we will find an interference phenomena with a classical but no quantum model. However, the conclusion that, because the quantum nature of light is so thoroughly established, we can safely abandon classical theories altogether at the frontier of interference phenomena, cannot be upheld for several reasons.

First, there is the question whether a newly discovered interference phenomena has a classical model. The past ten years or so have witnessed a series of claims, falsely proclaiming genuine quantum effects where, in fact, classical interference has taken place. Examples are "ghost" imaging, anticorrelation dips and superresolution interferometry, as discussed later. Not only a resource question (see next point) for metrology, applications in quantum information critically rely on true non-classicality for both computational speed-up and ultimate communication security. Those advantages disappear as soon as we can fake, or simulate, quantum correlations with, potentially quite complex, statistically correlated, classical systems. Hence the importance of identifying with utmost confidence the closest available classical model for a newly discovered interference phenomena.

Second, classical interference is "cheaper". The generation of non-classical field states, be they independent, indistinguishable single photons, or multiphoton states with tailored entanglement, is, and for the foreseeable future will remain so, experimentally challenging. However, it is often possible to replace quantum with classical sources and use a qualitatively identical interference pattern —at a calculable visibility cost. One can go further

and safely treat the whole system classically as long as the detector is based on quantum effects, in which case quantum interference is deferred to the end of the experiment (the principle of deferred measurement is also a powerful concept in quantum circuits). This is not only a cost-saving strategy but sometimes the only viable route for realizations of ideas with great potential. Practical quantum key distribution, for instance, makes extensive and efficient use of weak coherent states as an approximation to single photon Fock states. In fact, the essential ingredient for the security of quantum communication systems is not "single photons" but "non-orthogonality", illustrating the importance of knowing what resources are actually needed [1].

Third, classical models are indispensable for a complete categorization of interference phenomena. Wading through the newly discovered interference landscapes inhabited by more than two photons, we are in need of the map and compass afforded by such a classification. In particular, we want to have knowledge on the whereabouts of classical-quantum borders; to know what concepts reign supreme in each part, and what concepts bind fast the two contending territories. The strongest tie is the superposition principle: it is applied to electromagnetic fields and quantum states in classical and quantum theories, respectively, though superposition is only half the story. Whereas quantum systems possess intrinsic interference capabilities, namely entanglement and exchange symmetry, classical systems typically rely on another, statistical layer on top of Maxwell's equations. The result is *coherence theory* and fully accounts for fluctuating fields and how these translate into beautiful and intricate interference patterns. More generally, statistical optics tells us a great deal about light where there is simply no need for quantum theory. Just to name one example, a classic result of coherence theory is that fields emitted from independent sources, upon propagation, become correlated and their spectral decomposition in the far field can be altered —without any matter interaction! Quantum optics adopted the most important concepts such as correlation functions, mainly through the work of Glauber, Sudarshan, and others in the 1960s. A new wave of ideas from group theory and combinatorics recently backed the analysis of interferometers, linear optical networks in particular. I expect that group and representation theory will carry the bulk of the burden of a full classification of interference phenomena. Once we possess the mathematical tools and experimental methods that inevitably come with structured knowledge, we can incorporate principles from quantum information and biology to full effect and study interference phenomena in truly complex systems.

How complexity arises in simple systems ranks among the perennial questions in sciences. From Newton's three-body problem, through symmetric polyhedra in solid ge-

ometry, all the way to cellular automata in modern times, intermittent encounters with surprising complexities define, shape and extend scientific thinking and concepts. Venturing beyond two-photon interference, we may witness another such occurrence. Already three-photon interference, discussed and demonstrated in this thesis, shows novel interference phenomena and, looking closely enough, we may see vestiges of a similar happening around 320 years ago. Hon and Goldstein [2] traced back our modern concept of *symmetry* to a definition of Adrien-Marie Legendre in 1794. The usages of symmetry in mathematics, natural sciences, and the arts prior to that year have little in common with our modern notion. As every student of Euclid's *Elements* will remember, in *two* dimensions, polygons such as squares, triangles and so on are completely categorized by their number of edges. Any two similar polygons can be scaled, moved and rotated to *superpose* them; and if two polygons are mirror images, we can make use of the third dimension as a temporary resource and flip over one polygon to superpose them. Thus, in (two-dimensional) Euclidean geometry, the notion of congruence is a triviality because of superposeability. However, things change dramatically when moving up a dimension. In three dimensions, polyhedra exist that are equal (congruent faces, same volume) but *cannot* be superposed. Think of your two hands: no matter how much you rotate, twist and move them, you will never be able to superpose them. Moreover, we cannot make use of a fourth dimension to flip them over. Thus, in solid geometry we have to deal with objects that are equal, but which cannot be superposed. In 1794, Adrien-Marie Legendre recognized this in his *Éléments de géométrie* and defined a new form of equality, namely *equality by symmetry*:

> Thus two equal solid angles which are formed (by the same plane angles) but in the inverse order will be called *angles equal by symmetry*, or simply *symmetric angles*.[1]

Wielding this novel concept, Legendre answered Euler's call to study solid geometry, and delivered a complete proof of Euler's polyhedra formula $V + F = E + 2$, as he was now able to properly use spherical angles.

The development in geometry spurned by the third dimension is paralleled by a similar progress in algebra (the following examples are taken from [3]). In the 16th century, algebra was little more than solving polynomial equations. Formulas for calculating roots of those equations formed the theoretical backbone. Problematic was only that those formulas yielded solutions containing terms of the form $\sqrt[n]{a}$, where a is any real number, i.e. also

[1] Ainsi les deux angles solides dont il s'agit, qui sont formés par trois angles plans égaux chacun à chacun, mais disposés dans un order inverse, s'appelleront *angles égaux par symmétrie*, ou simplement *angles symmétriques*.

negative ones. For example, the equation

$$x^2 + 3 = 2x \tag{1.1}$$

has the formal solution

$$x_2 = 1 \pm \sqrt{-2}\,, \tag{1.2}$$

but since only numbers on the real line were accepted, mathematicians would have said that this equation possesses no solution. For quadratic equations, it is true that "nonsensical" terms like $\sqrt{-2}$ only appear if the equation has no real solution but are absent otherwise. This provided comfort, for the "artifact" $\sqrt{-2}$ is synonymous with lack of a solution. For cubic equations such as

$$x^3 = 15x + 4\,, \tag{1.3}$$

turning a blind eye on roots of negative numbers is no longer an option. Why? Well, the solution

$$x_3 = \sqrt[3]{2 + \sqrt{-121}} + \sqrt[3]{2 - \sqrt{-121}} \tag{1.4}$$

is in fact equal to $x_3 = 4$! Mathematicians knew, now that they arrive at *real* solutions through those negative-square-root terms, their formal structure merit a stringent study. Thus, the emergence of complex numbers, with their formal perfection by Hamilton in the first half of the 19th century, was initiated by a phenomenon that only appears in the third dimension. This little digression conveys how two great ideas, namely the concept of symmetry and complex numbers, came into being through study of essentially the same problem, but with an additional dimension. As demonstrated in this thesis, three photons display behavior that goes beyond a simple extension of two-photon interference.

I commenced my graduate studies with the goal to answer the introductory question and was hoping to find a thorough and exhausting answer by the time I write my *Doktorarbeit*. I did not quite achieve this lofty goal but finished work on four main projects, the results of which I report here. The first two chapters form the core of this thesis and deal with two diametrically opposite interference phenomena, which are sketched in Figure 1.1. In Chapter 2, I report the *Observation of Genuine Three-Photon Interference*. In this experiment, we realized a Greenberger-Horne-Zeilinger interferometer, which has been studied theoretically since 1990. Using energy-time entangled photon triplets we were able to isolate pure three-photon interference. This is the interferometric way to demonstrate that the photon triplet, despite separation of its constituents (single photons), still acts as a whole. Then, in Chapter 3, I turn my attention to the *Origin of Interference Terms*. Remember that interference between two paths in a double-slit experiment means they are indistinguishable. When a third path, via another slit, is added, however, a degree of

distinguishability is introduced, despite the fact that full interference is still observed. How can we understand this? After initial experimental evidence that the three-slit interference term is zero, we now believe there is genuine three-slit interference. I studied the problem theoretically using an algebraic (group and representation theory) approach and was able to derive the three-slit interference term (in fact, any N-slit interference term). This is quite surprising, for I did not make use of concepts such as waves or quantum interference. In Chapter 4 we discover new interference landscapes, as we study the HOM effect with lasers in three different degrees of freedom. Chapter 5 summarizes the development of a multimode time-bin qubit analyzer and we demonstrate its usability for experiments with hybrid-entangled photon pairs.

Nomenclature. Correlation or coherence functions can be used to roughly classify interference phenomena. Traditionally, there have been two schools. The Harvard school centered around Roy J. Glauber defines interference order according to the number of intensities in the expectation value, whereas the definition according to Rochester's Institute of Optics, centered around Leonard Mandel and Emil Wolf, the number of E-fields is the more accurate and general one. I follow the latter in this thesis, i.e. what the former calls "first-order" and "second-order" interference, is "second-order" and "fourth-order" interference in the latter.

Chapter 2

Observation of Genuine Three-Photon Interference

2.1 Notes

The results presented in this chapter have been partially published as [4]

> Sascha Agne, Thomas Kauten, Jeongwan Jin, Evan Meyer-Scott, Jeff Z. Salvail, Deny R. Hamel, Kevin J. Resch, Gregor Weihs, and Thomas Jennewein, "Observation of Genuine Three-Photon Interference", *Physical Review Letters*, **118**, 153602 (2017)

and be presented under the same title at

> Conference on Lasers and Electro-Optics (CLEO) 2017, San Jose, California, Postdeadline Papers Session II (JTh5B).

2.2 Introduction

> Maximal knowledge of a total system does not necessarily include total knowledge of all its parts, not even when these are fully separated from each other and at the moment are not influencing each other at all.[1]
>
> —Erwin Schrödinger (1935)

When Schrödinger coined the term *Verschränkung* in 1935, he had in mind the simplest system comprising just two particles. In the same year, Einstein, Podolsky and Rosen directed attention to the consequences of the strong correlations graced by entanglement [5], but it took another 55 years before the next logical step was taken by Greenberger, Horne and Zeilinger (GHZ) in 1989 [6]. As they put more than two particles on the dissecting table, they discovered even stronger correlations than those that exists for two particles. Ramifications for the foundations of quantum mechanics were profound [7, 8] but those correlations are hard to create. Hence, it took another 20 years to directly generate photon triplets [9] and another half decade to make the source viable for interferometery. The observation of genuine three-photon interference, which I describe in detail in this chapter, testifies to the ongoing efforts to access (pure) higher-order correlations for fundamental questions and applications.

2.3 A Three-Photon Coincidence

Multiparticle quantum interference lies at the heart of quantum information processing and fundamental tests of quantum mechanics [10]. However, interference phenomena involving more than two photons are largely unexplored. As we dive deeper into mathematical structures and empirical methods, the challenges are both theoretical and experimental. Here we study the simplest, non-trivial interference effect of more than two photons, namely *genuine three-photon interference*. What the adjective "genuine" attempts to communicate is three-photon interference without two-photon and single photon interference —a pure three-photon effect. Its isolation has recently been achieved by us [4] and Menssen *et al.* [11] using entangled and independent photons, respectively. In our setup, the strong correlations of energy-time entangled photon triplets are converted into the desired interference

[1] Maximale Kenntnis von einem Gesamtsystem schließt nicht notwendig maximale Kenntnis aller seiner Teile ein, auch dann nicht, wenn dieselben völlig voneinander abgetrennt sind und einander zur Zeit gar nicht beeinflussen.

pattern using a so-called Greenberger-Horne-Zeilinger (GHZ) interferometer. Introduced in 1990 by Greenberger *et al.* [12], this approach has been studied theoretically [10, 13–23] but the experimental challenges were not overcome until now. The biggest problem is posed by the source: how can we directly generate genuinely tripartite entangled photons? In their original proposal [12], Greenberger *et al.* included the possibility to cascade two parametric downconversion processes, each of which can produce two entangled photons. When such a source was finally realized in our labs in 2010 [9], the triplet generation rate would not allow the compilation of robust measurement statistics needed for interferometry. Only with an improved source design, substantially more efficient single photon detectors, a stable three-photon interferometer, and clever detection and analysis techniques, were we able to observe genuine three-photon interference.

The hurdle in Menssen *et al.*'s experiment is a theoretical one, for there is no obvious phase in their interferometer. Experimental setups to interfere three independent photons at a three-port beam splitter, or tritter, are in use for a couple of years now [24, 25]. However, because of the photon's mutual independence, the tritter cannot convert optical phase differences into photon number fluctuations (which are measurable). This phase-independence is already known from the Hong-Ou-Mandel interferometer, of which the tritter setup is the three-photon generalization. So where do we find the missing phase? A couple of years ago, around 2010, the boson sampling problem was discovered [26], which reinvigorated group theoretical and combinatorial considerations of interferometers. These mathematical structures allow us to extract a three-photon, or triad, phase [27]. In contrast to our *interferometric* three-photon phase, which is the sum of three optical phases, the phase in Menssen *et al.*'s experiment refers to the argument of the complex scalar product of states of two photons. While no optical phase dependence exists for any number of independent photons, the *distinguishability* phase only shows up for more than two photons. This is the equivalent for three-photon correlation without two-photon correlations and the mechanism that allows Menssen *et al.* to observe phase-dependent count rates as well. The conceptual puzzle, how three photons, strongly correlated in one hand, and statistically independent in the other, give rise to the same same interference phenomena, is thereby partially explained. A full understanding will only be formed in the future, with differences emerging in setups with four or more photons and common traits explored in the interference of entangled, identical photons.

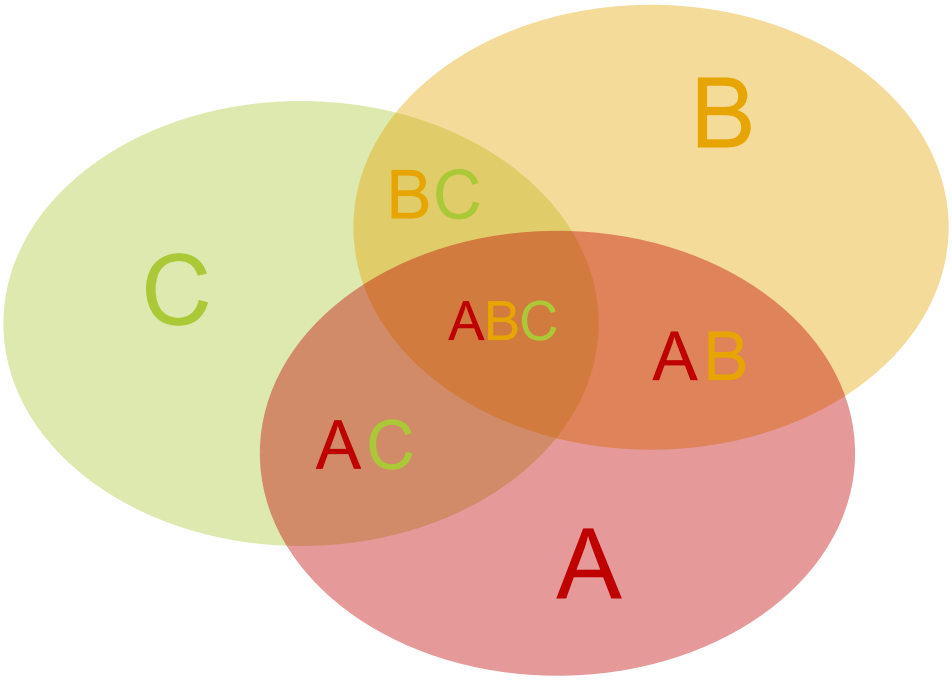

Figure 2.1: **Venn Diagram for Three Correlated Variables.** Illustrating the nature of genuine tripartite correlations using Venn diagrams. Shown here is the union of three sets, which can be expressed using the inclusion-exclusion expansion as $|A \cup B \cup C| = |A| + |B| + |C| - |A \cap B| - |A \cap C| - |B \cap C| + |A \cap B \cap C|$. We see in the center the overlap of all three sets together, $|A \cap B \cap C|$, but we also see this automatically implies in this region $|A \cap B| \neq \emptyset$, $|A \cap C| \neq \emptyset$, and $|B \cap C| \neq \emptyset$. However, for the phenomena we study, these three intersections need to be empty—but how is this possible?

2.4 What are Genuine Correlations?

Think of two correlated *things* A and B. Standing on George Boole's shoulders, the laws of thought nudge us towards an association of correlation with synchronization and causality. This fallacy is met with immense academic force ever since the introduction of the statistical concept of correlation by Francis Galton in the 19th century, yet prevails to this day. Our failure to imbibe a correct notion of correlation is symptomatic for the progress of both natural and social sciences. Only rarely do the systems we study demand a venture (far) beyond the most trivial correlations or statistical moments, namely averages and variance. The empirical information we throw away by neglecting higher orders is, admittedly, of little value in the overwhelming number of cases. However, all this means, really, is that we restrict our studies to systems that permit explanations of complex phenomena in terms of simple observations. This possibility of reduction is usually encoded in a powerful theorem,

for instance the Gaussian moment-factoring theorem. In Gaussian random systems, all the first and second order moments completely determine all higher-order moments. It is likely, however, that truly complex systems, such as life, require pure higher-order phenomena. Most likely, traditional methods will either be supplemented or even replaced by new methods, as for example suggested by Stephen Wolfram [28].

The complexity is already evident when we consider three correlated things A, B, and C. If there is some correlation in the system, we would instinctively say that either $A\,\&\,B$, $A\,\&\,C$, or $B\,\&\,C$ must be correlated. Kant's pure intuition aside, this thinking takes root in the observation that synchronized behavior of, say, three persons implies an act in tandem for any pair. However, tripartite without bipartite correlations exist and are not confined to quantum-mechanical systems. A typical classical situation bearing this correlation signature is the following. We wish three persons to have access to a secret or trigger an action —but only all three together: a single person is without power and no collusion with any other person should be possible. This example outlines an important class of security protocols [29] comprising secret sharing, N-man rule, separation of duties, and so on (think of the procedure to launch a nuclear missile), and is perhaps the most general way to illustrate what we mean with genuine three-photon correlations, or genuine three-photon interference.

Mathematically, correlations are put on firm foundations within probability theory. Think of two random variables X and Y with probability distributions $P_X(x)$ and $P_Y(y)$. These do not necessarily tell us anything about the joint probability distribution $P_{XY}(x,y)$. Even in case $P_{XY}(x,y) = P_X(x)P_Y(y)$ do we need to *postulate* the independence of X and Y. This is a piece of information not contained in either X or Y but exclusively in the joint consideration of both. Similarly, for three random variables X, Y, and Z with given probability distributions, we have substantial freedom to construct $P_{XY}(x,y)$, $P_{XZ}(x,z)$, $P_{YZ}(y,z)$ and $P_{XYZ}(x,y,z)$. The rich diversity is exemplified by the existence of probability models with pairwise independent events that are not independent [30]: in a fair drawing of four balls 1,2,3,4 from an urn, the events $X = \{1,2\}$, $Y = \{1,3\}$ and $Z = \{1,4\}$ all have probability $1/2$ and the three joint probabilities are $1/4$, which means the events are pair-wise independent, i.e. $P(XY) = P(X)P(Y)$, $P(XZ) = P(X)P(Z)$, and $P(YZ) = P(Y)P(Z)$. However, the events are not totally independent because the intersection of X, Y, and Z is $\{1\}$; thus, $P(XYZ) = 1/4 \neq P(X)P(Y)P(Z)$. The simplicity of this example should not blind us from the fact that identification of naturally occurring (higher-order) random processes with desired properties is difficult in general (as well as engineering a corresponding system). Simple models nevertheless have the benefit to start the mathematical engine and in the next section we construct an elementary statis-

tical prototype for three-photon interference, before proceeding to systems with quantum correlations.

2.5 Classical Genuine Third-Order Interference

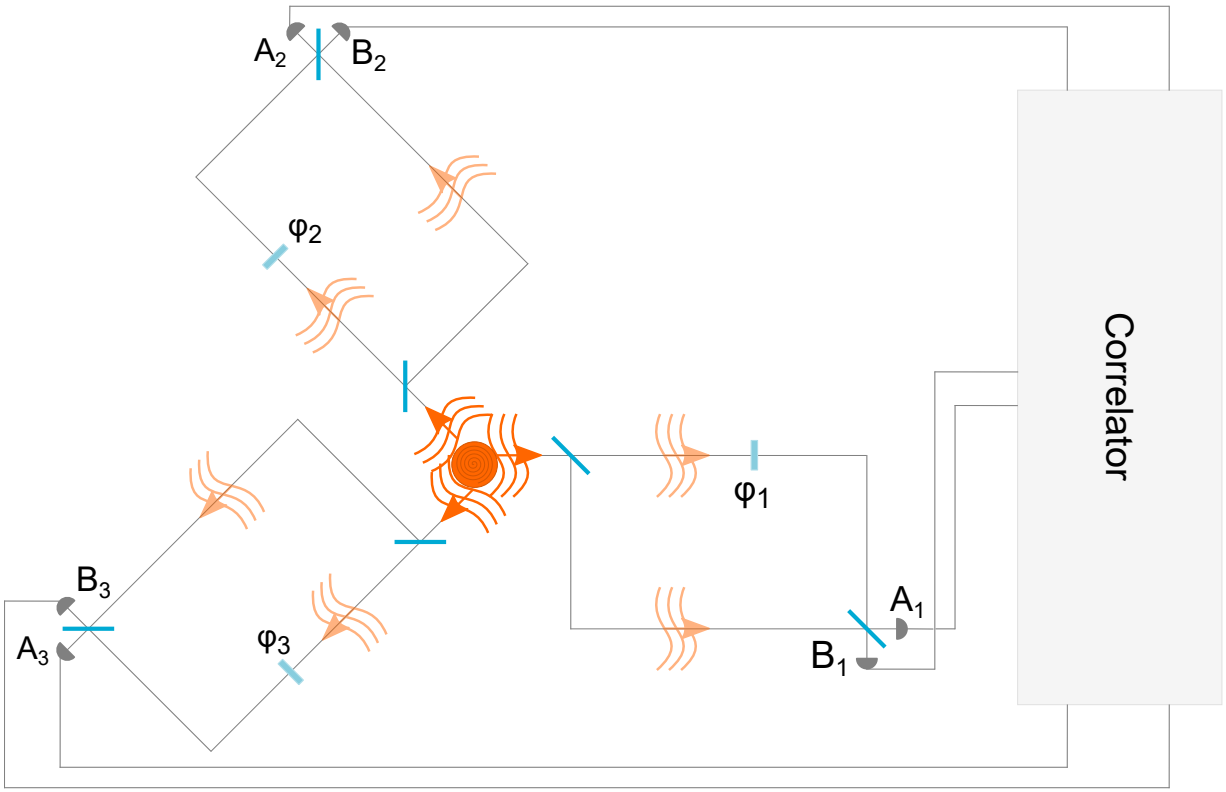

Figure 2.2: **Classical Third-Order Interference.** Setup for classical third-order interference. Three fields are emitted into three Mach-Zehnder interferometers with phases $\varphi_k \equiv \varphi_k(t_k)$, $k \in \{1,2,3\}$, that are subject to a random process. The detectors A_k, B_k measure field intensities, and their current outputs are fed into a correlator.

Higher-order interference or correlation phenomena are actually quite common through statistical, or accidental correlations coming from lower orders. Their elimination defines hard problems and is at the heart of genuine three-photon interference. Consider three fields, each transmitted through an interferometer with phase $\varphi_k \equiv \varphi_k(t_k)$, $k \in \{1,2,3\}$, and harmonic intensities,

$$I_k(\varphi_k) = \frac{I_0}{2}\Big(1 + \cos\left(\varphi_k\right)\Big)\,. \tag{2.1}$$

Simply multiplying the signals we get

$$\begin{aligned} I^{(3)}(\varphi_1,\varphi_2,\varphi_3) &= I_1(\varphi_1)I_2(\varphi_2)I_3(\varphi_3) \\ &= \frac{I_0^3}{8}\Bigg(1+\cos\left(\varphi_1\right)+\cos\left(\varphi_2\right)+\cos\left(\varphi_3\right) \\ &\qquad +\cos\left(\varphi_1\right)\cos\left(\varphi_2\right)+\cos\left(\varphi_1\right)\cos\left(\varphi_3\right)+\cos\left(\varphi_2\right)\cos\left(\varphi_3\right) \\ &\qquad +\frac{1}{4}\cos\left(\varphi_1-\varphi_2+\varphi_3\right)+\frac{1}{4}\cos\left(\varphi_1+\varphi_2-\varphi_3\right) \\ &\qquad +\frac{1}{4}\cos\left(\varphi_1-\varphi_2+\varphi_3\right)+\frac{1}{4}\cos\left(\varphi_1+\varphi_2+\varphi_3\right)\Bigg), \end{aligned} \tag{2.2}$$

where we used trigonometric identities to break up $\cos\left(\varphi_1\right)\cos\left(\varphi_2\right)\cos\left(\varphi_3\right)$. Obviously, the third-order intensity is phase-dependent, though in a highly convoluted way. We are absolutely not interested in the constant term, the single-phase cosine terms, and the product-cosine terms, for we can obtain these through zeroth-, first-, and second-order measurements, respectively. The interesting terms, however, namely the linear combinations of *all three* phases, contribute only a small and hardly discernible part to the overall signal. This is what we mean when we say the lower orders swamp the higher-order signals. So what can we do to isolate, say the term carrying the $\varphi_1+\varphi_2+\varphi_3$ information? We could use a tailored random process and try to impose the desired correlations as follows. Consider the correlation functions

$$\begin{aligned} G^{(2)}_{mn}(\varphi_m,\varphi_n) &= \Big\langle I_m(\varphi_m)I_n(\varphi_n)\Big\rangle \\ &= \frac{I_0^2}{4}\left(1+\Big\langle\cos\left(\varphi_1\right)\Big\rangle+\Big\langle\cos\left(\varphi_2\right)\Big\rangle+\Big\langle\cos\left(\varphi_1\right)\cos\left(\varphi_2\right)\Big\rangle\right) \end{aligned} \tag{2.3}$$

for all $mn\in\{12,13,23\}$, and the triple intensity correlation function

$$G^{(3)}(\varphi_1,\varphi_2,\varphi_3)=\Big\langle I^{(3)}(\varphi_1,\varphi_2,\varphi_3)\Big\rangle. \tag{2.4}$$

For genuine third-order interference, we would like to have

$$\bar{I}_k(\varphi_k)=\Big\langle I_k(\varphi_k)\Big\rangle=\frac{I_0}{2}\left(1+\Big\langle\cos\left(\varphi_k\right)\Big\rangle\right)\stackrel{!}{=}\frac{I_0}{2}\qquad\forall\,k\in\{1,2,3\}, \tag{2.5}$$

and

$$G^{(2)}_{mn}(\varphi_m,\varphi_n)\stackrel{!}{=}\frac{I_0^2}{4}\qquad\forall\,mn\in\{12,13,23\}, \tag{2.6}$$

while

$$G^{(3)}(\varphi_1,\varphi_2,\varphi_3)\stackrel{!}{=}G^{(3)}(\varphi_1+\varphi_2+\varphi_3). \tag{2.7}$$

The random process to realize this interference phenomena is characterized by the probability distributions

$$\begin{aligned} P_k(\varphi_k) &= \frac{1}{2\pi} \quad \forall\, k \in \{1,2,3\} \\ P_{kl}(\varphi_k,\varphi_l) &= P_k(\varphi_k)P_l(\varphi_l) \quad \forall\, k,l \in \{1,2,3\} \end{aligned} \tag{2.8}$$

with the single constraint

$$\varphi_1 + \varphi_2 + \varphi_3 = \varphi_c\,, \tag{2.9}$$

where φ_c is an arbitrary constant. We immediately calculate

$$\left\langle \cos\left(\varphi_k\right) \right\rangle = \frac{1}{2\pi}\int_0^{2\pi} \cos\left(\varphi_k\right) d\varphi_k = 0\,, \tag{2.10}$$

and, using elementary trigonometric identities, we find that all expectation values of cosine products vanish as well. For the remaining terms we find, for example,

$$\left\langle \cos\left(\varphi_1 - \varphi_2 + \varphi_3\right) \right\rangle = \left\langle \cos\left(\varphi_c - 2\varphi_2\right) \right\rangle = 0\,, \tag{2.11}$$

and the only term left is, by construction of the random process, the one involving the sum of all phases. We obtain constant intensities, Equation (2.5), constant second-order correlations, Equation (2.6), and a third-order correlation function dependent on the sum of the phases,

$$G^{(3)}(\varphi_c) = \frac{I_0^3}{8}\left(1 + \frac{1}{4}\cos\left(\varphi_c\right)\right). \tag{2.12}$$

However, we incur a visibility cost of 75 %, because

$$\mathcal{V}_3 = \frac{G^{(3)}_{\max} - G^{(3)}_{\min}}{G^{(3)}_{\max} + G^{(3)}_{\min}} = 25\,\%\,, \tag{2.13}$$

which is incompatible with the more than 90 % we observe in our experiment. Admittedly, our toy model was simple, yet even more sophisticated classical models cannot do better than 50 % [31–33]. Thus, there is always a visibility penalty if we "cheat", i.e. if we want to remove contamination by lower-order interference. Evidently, a more sophisticated model is needed to explain a complete elimination of single-photon and two-photon interference while retaining, ideally, perfect three-photon visibility. What we need are three photons in a GHZ state.

2.6 Greenberger-Horne-Zeilinger Correlations

Greenberger, Horne and Zeilinger (GHZ) [6, 12] discovered the strong correlations of three entangled particle while noticing a gap in Bell's test of EPR's *local realism* —the idea that

"If, without in any way disturbing a system, we can predict with certainty the value of a physical quantity, then there exists an element of physical reality corresponding to this quantity" [5]. To this day, the elements of reality are cross-examined in Bell tests and are consistently found to be at odds with the concepts ordained by nature [34–36]. However, "Bell's results say nothing in the special case covered directly by the EPR argument, namely the case where a measurement on one particle allows one to predict what happens to the other particle with 100 % certainty" [6]. What was missing is a situation where local realism and quantum mechanics make diametrically opposed predictions without a layer of statistical arguments obscuring judgment. As we observed in the introduction to this thesis, history abounds of situations where the step from two to three is accompanied by radically new concepts. In the case at hand, not only are the elements of really attacked from a different angle, but, as Mermin puts it [7], their "demolition is spectacularly more efficient". To understand Mermin, and those strong three-particle correlations, we follow Mermin's succinct exposition, and consider three spin-1/2 particles living in an eight-dimensional Hilbert space $\mathcal{H}_2 \otimes \mathcal{H}_2 \otimes \mathcal{H}_2$, spanned by the product basis

$$\mathcal{B} = \Big\{ |\uparrow\uparrow\uparrow\rangle, |\uparrow\uparrow\downarrow\rangle, |\uparrow\downarrow\uparrow\rangle, |\uparrow\downarrow\downarrow\rangle, |\downarrow\uparrow\uparrow\rangle, |\downarrow\uparrow\downarrow\rangle, |\downarrow\downarrow\uparrow\rangle, |\downarrow\downarrow\downarrow\rangle \Big\}, \tag{2.14}$$

where the isomorphism to the canonical Hilbert space associates

$$|\uparrow\rangle \equiv \begin{pmatrix} 1 \\ 0 \end{pmatrix} \qquad \text{and} \qquad |\downarrow\rangle \equiv \begin{pmatrix} 0 \\ 1 \end{pmatrix}. \tag{2.15}$$

The following single-particle observables (Pauli operators),

$$\hat{\sigma}_x \equiv \frac{\hbar}{2} \begin{pmatrix} 0 & 1 \\ 1 & 0 \end{pmatrix} \qquad \text{and} \qquad \hat{\sigma}_y \equiv \frac{\hbar}{2} \begin{pmatrix} 0 & -i \\ i & 0 \end{pmatrix}, \tag{2.16}$$

anticommute, $\{\sigma_x, \sigma_y\} = 0$, but do not commute, $[\sigma_x, \sigma_y] = 2i\sigma_z$. For an experiment where two spins are measured in the y-direction and one in the x-direction, consider the three-particle observables

$$\begin{aligned} \hat{\Sigma}_1 &= \hat{\sigma}_x^1 \hat{\sigma}_y^2 \hat{\sigma}_y^3 \\ \hat{\Sigma}_2 &= \hat{\sigma}_y^1 \hat{\sigma}_x^2 \hat{\sigma}_y^3 \\ \hat{\Sigma}_3 &= \hat{\sigma}_y^1 \hat{\sigma}_y^2 \hat{\sigma}_x^3 . \end{aligned} \tag{2.17}$$

They commute,

$$\left[\hat{\Sigma}_k, \hat{\Sigma}_l\right] = 0 \quad \forall\, k, l \in \{1, 2, 3\}, \tag{2.18}$$

and have unit-square,

$$\hat{\Sigma}_k^2 = \mathbb{1}, \tag{2.19}$$

implying common eigenvectors and eigenvalues of ± 1. Among the eight possible eigenstates, labeled by a triple of signs of eigenvalues

$$(\lambda_1\lambda_2\lambda_3) \in \Big\{ +++, ++-, +-+, +--, -++, -+-, --+, --- \Big\}, \tag{2.20}$$

we consider

$$|+++\rangle = \frac{1}{\sqrt{2}}\Big(|\uparrow\uparrow\uparrow\rangle - |\downarrow\downarrow\downarrow\rangle\Big)\,. \tag{2.21}$$

A measurement of any two spins immediately tells us, with certainty, the outcome of a measurement on the third spin—without disturbing it.

The EPR reality criterion is thus fulfilled and we can assign elements of reality

$$m_o^s \in \{+1,-1\}, \qquad s \in \{1,2,3\},\, o \in \{x,y\}\,, \tag{2.22}$$

to measurements. Consistent with the measurement outcome (eigenvalue of $|+++\rangle$ for all three operators is 1), we must have

$$\begin{aligned} m_1 &= m_x^1 m_y^2 m_y^3 = 1 \\ m_2 &= m_y^1 m_x^2 m_y^3 = 1 \\ m_3 &= m_y^1 m_y^2 m_x^3 = 1\,, \end{aligned} \tag{2.23}$$

which implies the prediction that a measurement of all three spins in the x-direction yields a product of unity,

$$m_1 m_2 m_3 = m_1 = m_x^1 m_x^2 m_x^3 = 1\,. \tag{2.24}$$

Quantum mechanics, on the other hand, predicts the opposite result,

$$\hat\sigma_x^1\hat\sigma_x^2\hat\sigma_x^3|+++\rangle = -1|+++\rangle\,, \tag{2.25}$$

and therefore, neglecting unavoidable experimental imperfections, a single experiment can give the verdict. Using polarization [37, 38], Mermin's *three-spin gadget* [8] became experimentally feasible around 1999, and the results clearly favor quantum mechanics [39]. The GHZ interferometer we use here to study GHZ correlations in continuous variables, was put to a deep slumber, while skillful extensions of the original polarization-GHZ setup allowed the experimental study of up to ten-photon correlations [40]. Before we proceed, I would like to point out that it is perfectly possible to obtain GHZ correlations classically [41]. However, this only works in an orchestra of single particle degrees of freedom. Breaking it up, as we do when we split a pump photon into three photons, immediately destroys the correlations in the same step, and classical optics loses its grip.

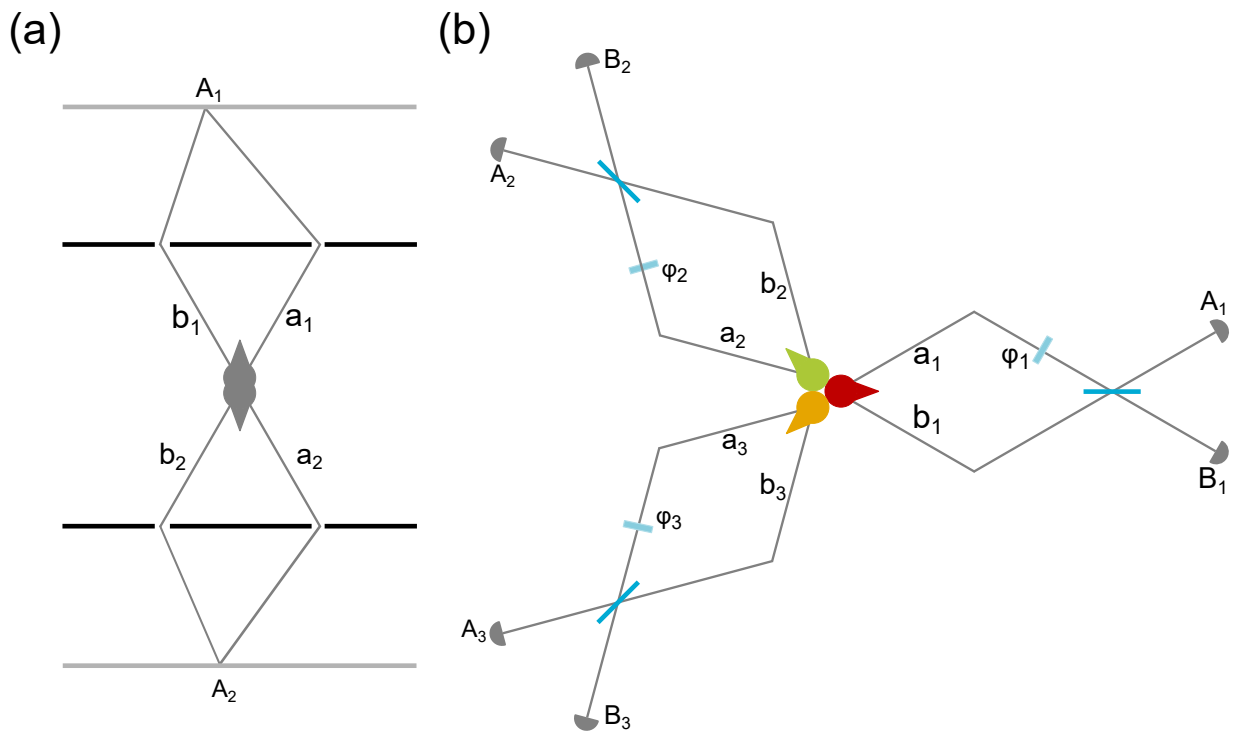

Figure 2.3: **From Two-Particle Interferometry to GHZ Interferometer. (a)** Example of a two-photon interferometer. Each photon of a (continuously) momentum-entangled pair is transmitted through a Young double-slit. The slit mask defines two paths, or beams, and thus discretizes the continuous state, as explained in the main text. In contrast to the historic experiment with classical fields or single photons, no interference pattern shows up on either screen. The correlation of the two photons has the effect to transfer the pattern into the coincidences (registered by detectors A_1 and A_2). **(b)** The GHZ interferometer generalizes this idea of pre-selection of a continuously entangled state to three photons, and has been extensively studied theoretically since its conception in 1990 [12].

2.7 From Two to Three Photon Interferometry

The generic GHZ state

$$|\mathrm{GHZ}\rangle = \frac{1}{\sqrt{2}}\Big(|000\rangle + |111\rangle\Big) \tag{2.26}$$

describes strong correlations of three entangled *particles*, though we could also probe the *wave* nature of such a *triphoton* [23]. If we do this, qualitatively new effects appear. For example, we can force a pair of the triphoton into a product or entangled state, depending on whether we chose to probe the particle or wave properties of the third photon, respectively [13, 42]. In our endeavors, what kind of interferometer is needed to probe the triphoton wave?

A single interferometer allows us to observe interference in single-photon detection events. Having two interferometers at our disposal, we can "wire" them and, in addition, observe interference in the two-photon coincidences. Already we face quite interesting problems. For example, we can ask whether single-photon and two-photon interference are independent phenomena? We quickly come up with setups where one is observed without the other, which in terms of visibility means that $(\mathcal{V}_1, \mathcal{V}_2) = (1, 0)$ or $(\mathcal{V}_1, \mathcal{V}_2) = (0, 1)$. However, given any $\mathcal{V}_1 \in [0, 1]$, $\mathcal{V}_2$ can not take on arbitrary values in $[0, 1]$, for the duality relation

$$\mathcal{V}_1^2 + \mathcal{V}_2^2 \leq 1 \tag{2.27}$$

imposes a surprising restriction [43]. Obviously, fourth-order (two-photon) interference is much richer than second-order (single-photon) interference, though only the photon picture allows a seamless integration of information-theoretic principles, through which duality relations are easily derived. Famously, Einstein refused to believe in the simplest such relation, namely wave-particle duality [44], which essentially amalgamates continuous and discrete natural structures. Imbibed with classical ideals, it is thus not surprising that Einstein, together with co-workers Podolsky and Rosen (EPR), assaulted the consequences of *continuous*-variable entanglement, namely position and momentum [5]. Attention shifted to discrete variables only with the work of Bohm [45] and Bell [46]. Thence, research efforts were channeled into spin or polarization entanglement until a series of experiments, initiated by results of Freedman and Clauser [47], and later Aspect *et al.* [48], sufficiently supported quantum mechanics. Around 1985, Horne and Zeilinger returned to continuous variables, studying a setup more akin to the original EPR scenario [49, 50], which was finally realized experimentally in 2004 [51]. Their work paved the way for two-particle interferometry [52], as it was recognized that interferometers work as a sort-of analogue-to-digital converter. For instance, two particles from a source that emits them in a superposition of all directions (but always opposite and with the same absolute value of linear momentum $k = |\vec{k}|$), will be continuously entangled,

$$|\Psi\rangle = \int d^3\vec{k}\, \delta(k) \left|\vec{k}\right\rangle_1 \left|-\vec{k}\right\rangle_2 . \tag{2.28}$$

By a suitable post-selection procedure, for example using a slit mask around the source, we can easily discretize this state, yielding

$$|\Psi\rangle = \frac{1}{\sqrt{2}} \left(\left|\vec{k}\right\rangle_1 \left|-\vec{k}\right\rangle_2 + \left|\vec{k}'\right\rangle_1 \left|-\vec{k}'\right\rangle_2 \right) . \tag{2.29}$$

Since the k's label a certain direction, and thereby a path, states of the type (2.29) became known to the literature as *beam entanglement* [15]. Having *two* beams at our disposal, we

can propagate a photon within each beam through a standard Mach-Zehnder interferometer with two internal paths and phases ϕ_1 and ϕ_2. Each photon is guided to either of the two, complementary, output ports. Detectors there define two-valued (labels "+" and "-") *which port* [53] observables. The output state

$$|\Psi\rangle = \frac{1}{\sqrt{2}}\Big[\sin(\Delta\phi)\Big(|-\rangle_1|+\rangle_2 - |+\rangle_1|-\rangle_2\Big) - \cos(\Delta\phi)\Big(|-\rangle_1|-\rangle_2 + |+\rangle_1|+\rangle_2\Big)\Big], \quad (2.30)$$

where $\Delta\phi = (\phi_1 - \phi_2)/2$, gives constant detection probabilities for each detector, but phase-dependent joint detection probabilities

$$\begin{aligned} P(+_1,+_2) = P(-_1,-_2) &= \frac{1}{2}\Big(1+\cos(2\Delta\phi)\Big) \\ P(+_1,-_2) = P(-_1,+_2) &= \frac{1}{2}\Big(1-\cos(2\Delta\phi)\Big). \end{aligned} \quad (2.31)$$

The first demonstration of non-classical interference without polarization modulation (a defining feature of two-particle interferometry [15]) was given by Gosh and Mandel [54]. In their double-slit-like setup, the interpretation of two-photon interference without single-photon interference is lucid enough to merit quotation: "Despite the fact that any one photon can be detected at any position x, we see that if the photon is detected at x_1, there are certain positions x_2 where the other photon can never be found". This understanding is naturally formed when calculating conditional instead of joint probabilities and is template for all interferometers employing entangled photon pairs. Though in Gosh and Mandel's setup photon-pairs overlapped in the interferometer, later implementations such as [55] showed that (local) optical mixing prior detection is not necessary and in fact may even be detrimental. So, entangled photons can be separated spatially but still form a logical whole. If one insists on assigning a name to this single entity, the preferred choice is biphoton [56]. Using entangled photons, we can eliminate the detrimental effects of lower-order interference. This is the case for any number of particles in a state of the GHZ type—thus the name GHZ interferometry [16]. As we saw above for three photons, a classical analogue always incurs a visibility loss, which can be significant. This quantum advantage showed itself in a couple of two-photon interferometers towards the end of the 1980s, most prominently in setups of Hong, Ou and Mandel [59], Shih and Alley [60], and Franson [61]. The GHZ interferometer is related to so-called NOON- or de Broglie-interferometers [22]. There, as shown in Figure 2.4, N photons are collectively presented with two alternative paths and are not broken up, as is the case in GHZ-interferometry. Both interferometry paradigms share the common goal to eliminate lower-order interference, though the erasure in NOON-interferometry is usually partial [10, 22, 62, 63]. In principle, GHZ-interferometers can be converted into NOON-interferometers simply by keeping the three

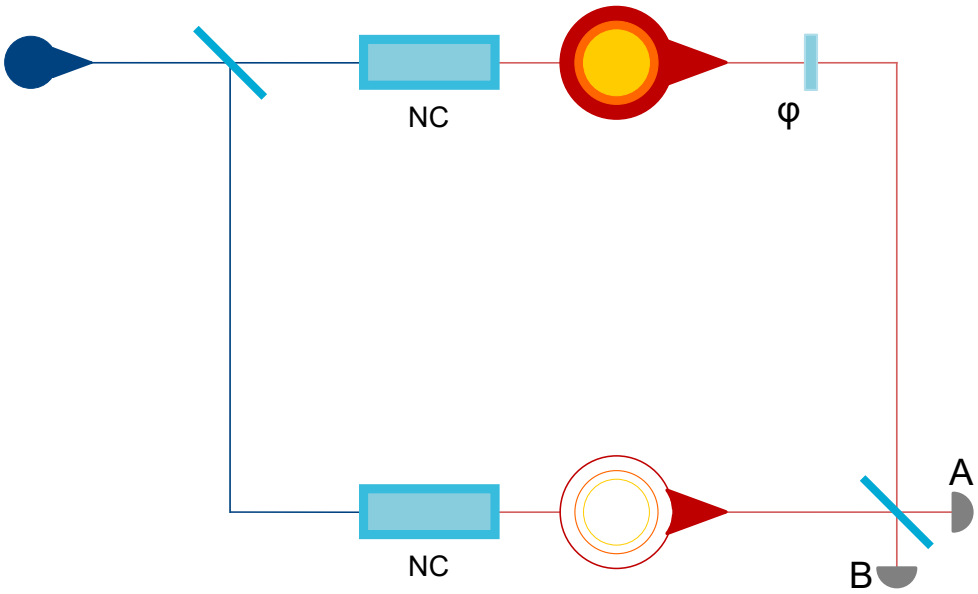

Figure 2.4: **Sketch of a NOON or de Broglie Interferometer.** Three photons are emitted together in either of two alternative paths with phase-difference φ. The triphoton is more sensitive, however, and picks up a phase 3φ. The way the three photons are drawn reminds us of a "super-photon", which appears in photonic Bose-Einstein condensates [57]. When N is the number of photons in the condensate, we may assign a wavelength λ/N [58], with λ the individual photon wavelength, to this super-photon, yielding a complementary picture: a photon with wavelength $\lambda/3$ is three times more sensitive to phase changes.

photons together. This might be experimentally challenging because the triplet source may produce non-identical photons. For instance, our source, as we see shortly, produces three photons with wavelength differences of more than 700 nm. When combined with the ability to break up triphotons, the versatility of the GHZ interferometer may be of use in novel imaging techniques that would like to probe non-local correlations of molecules differing in their optical traits, for example neuroscience. Similar to GHZ-interferometry, NOON-interferometry aims to suppress lower-order signals for extraction of higher-order phase terms [22]. We have a brief look at the defining problem, as I deem its resolution beneficial to the general understanding of how interferometers work. Consider the unitary describing a phase-shift,

$$\hat{U} = \exp\left(-i\phi\hat{n}\right) = \exp\left(-i\phi\hat{a}^\dagger\hat{a}\right) , \tag{2.32}$$

where $\hat{n}$ is the photon number operator, and apply it to an input state,

$$|\Psi(\phi)\rangle = \hat{U}|\Psi\rangle = \sum_{n=0}^{\infty} c_n \exp\left(-in\phi\right)|n\rangle . \tag{2.33}$$

We see that the phase shift is proportional to the number n of photons. However, in standard interferometry, the whole superposition (2.33) contributes to the signal, in which case the photon number information is lost. If we could isolate a term with a particularly high n, then we were able to detect phase-differences with n-times better resolution. Quantum states that can pick up this phase in an interferometer, like the one shown in Figure 2.4, are called NOON-states,

$$|\text{NOON}\rangle = \frac{1}{\sqrt{2}}\Big(|N0\rangle + |0N\rangle\Big)\,. \tag{2.34}$$

Though phase superresolution has been demonstrated experimentally [63][64], classical interference models can achieve the same improvement, and it really is phase supersensitivity [65] that confers a quantum-advantage.

2.8 Photon Triplet Sources

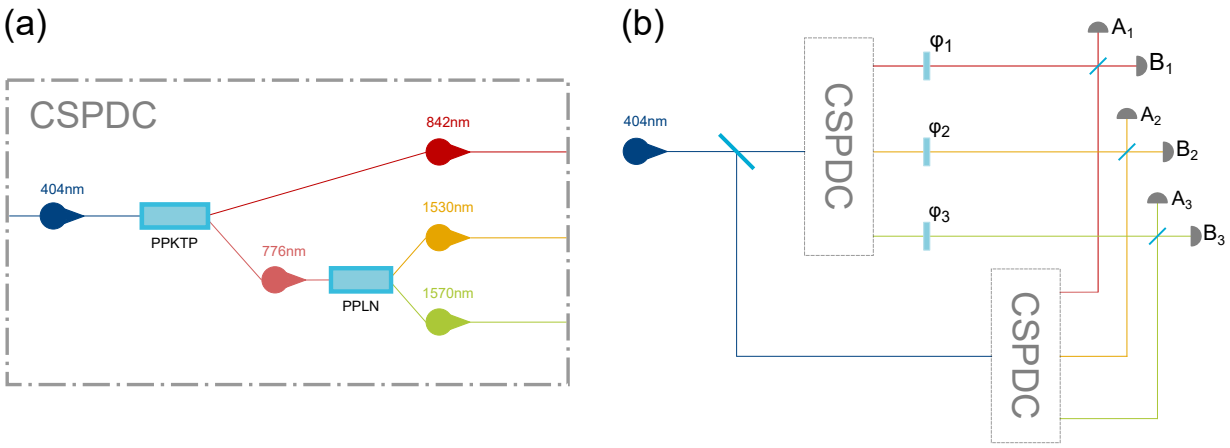

Figure 2.5: **Cascaded Spontaneous Parametric Downconversion.** **(a)** Cascaded spontaneous parametric downconversion (CSPDC) employing a periodically poled potassium titanyl phosphate (PPKTP) and a periodically poled lithium niobate (PPLN) for the first and second stage of the conversion, respectively. **(b)** Realization of the GHZ interferometer employing two CSPDC sources. Photon triplets are generated in either of the two paths of an interferometer and are optically mixed at beam splitters. If there is no source information attached to photon triplets, interference in three-photon coincidences is observed.

From mixing independent biphotons to cascaded spontaneous parametric downconversion, quite a few proposals to generate three entangled photons have been proposed. Few

have been realized, however. The idea for the first viable three-photon source originated from a similar consideration for two-photon sources. Yurke and Stole were the first to note that entangled particles can be obtained from two *independent* pair-sources. The idea is to mix photons from each source on a symmetric beam splitter in such a way that we cannot tell from which source a detected photon was emitted [66, 67]. This erasure of source information is necessary for the scheme to work, as highlighted by Zukowski *et al.* [68]. The effect is similar to randomization of path bits in conventional second-order interferometry such as in Young's double slit [69], and underlines yet again the fundamental role played by the beam splitter [70]. At the same time, Zukowski *et al.* introduced entanglement swapping, which developed into viable tools in quantum communication, namely quantum cryptography [71] and quantum repeaters [72]. Extension of the idea to the production of three entangled photons did not take long [73] and a viable proposal came in 1997 [19, 20, 74], with experimental realization in 1999 [39]. Note that the nature of the source does not matter too much as long as we work in the single-photon counting regime and experimental setups, detectors in particular, can work with the source statistics. Thus, one can work with non-maximally entangled states [75] and even replace one of the SPDC sources in the scheme of Zeilinger *et al.* with a weak coherent state source [76].

For some experiments, we would actually like to have three simultaneously *existing* photons in a genuinely tripartite entangled state and not merely their strong correlations in detection (though these are sufficient for some experiments, including GHZ tests of local realism). Photon triplets can be directly generated using various nonlinear processes. One way is to first produce photon pairs in spontaneous parametric downconversion (SPDC) and then take a single photon from each pair for sum-frequency generation (SFG) [77]. Another proposal makes use of $\chi^{(3)}$-interaction in a single nonlinear medium, for example in fiber [78] and in crystals [79]. So far, however, third-order spontaneous parametric downconversion has not been shown to be a viable source for photon triplets. Lastly, cascaded spontaneous parametric downconversion (CSPDC), as shown in Figure 2.5 (a), was developed by my predecessors in a collaboration between the groups of Thomas Jennewein and Kevin Resch [9]. There, pump photons at 404 nm are converted into two daughter photons at 842 nm and 776 nm. The latter give birth to two granddaughter photons at 1530 nm and 1570 nm and so we have three photons that are genuinely tripartite entangled in energy and time [80]. As a proof of versatility, the CSPDC source has been embedded in a polarization-interferometer setup to directly generate a polarization GHZ state [81]. As shown in Figure 2.5 (b), CSPDC sources can be used to realize the GHZ interferometer from Figure 2.3 (b). The drawback of this design is that it requires two CSPDC sources. The three-photon Franson interferometer, however, requires only one triplet source.

2.9 The Franson Interferometer

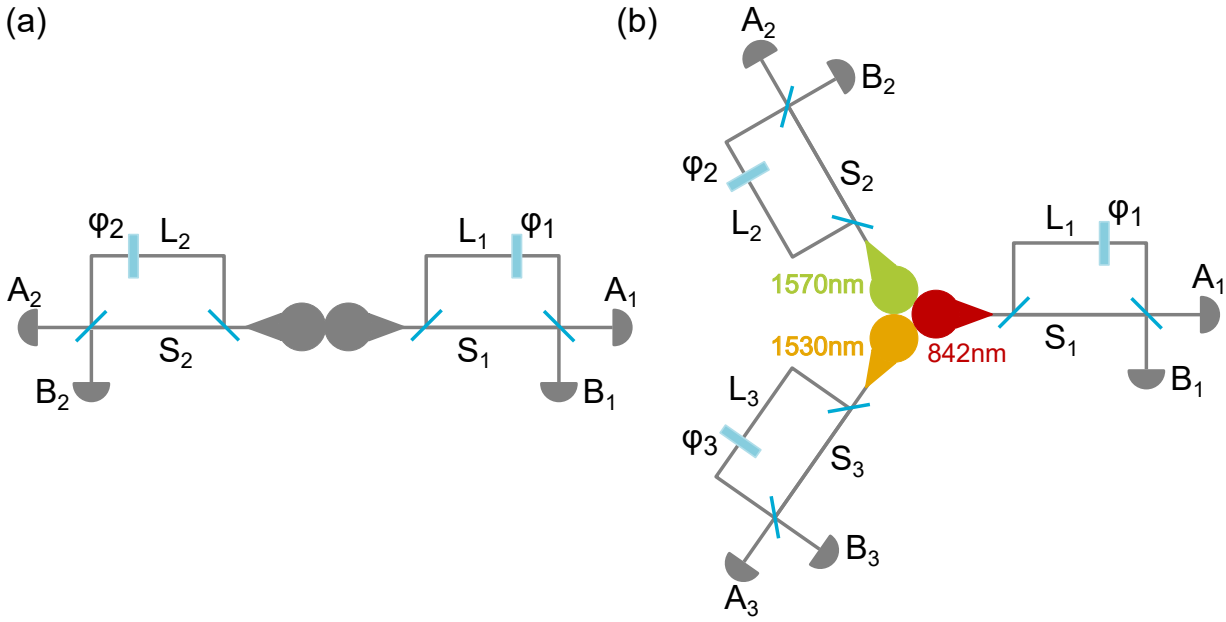

Figure 2.6: **Franson Interferometers.** **(a)** Sketch of the original two-photon Franson interferometer [61]. **(b)** Photons triplets are emitted into a three-photon Franson interferometer with identical short ($S_1 = S_2 = S_3$) and long ($L_1 = L_2 = L_3$) paths, optical phases $\varphi_1, \varphi_2, \varphi_3$ that are set by glass plates, and pairs of complementary detectors A_k, B_k, $k \in \{1, 2, 3\}$. The three-photon Franson interferometer is a special case of a GHZ interferometer where energy-time entanglement is converted into post-selected beam-entangled states.

The original motivation behind development of the CSPDC source was to generalize the two-photon Franson interferometer shown in 2.6 (a). It turns out that the three-photon pendant is in fact a probabilistic, or post-selected, version of the GHZ interferometer [18], which is sketched in 2.6 (b). Similar to Horne and Zeilinger's momentum interferometer [49], Franson [61] considered a source of energy-time entangled photon pairs. The understanding of energy-time entanglement relies on generalizations of the standard energy-time uncertainty relation,

$$\Delta E \Delta t \geq \frac{\hbar}{2}. \tag{2.35}$$

Classically we may think of time-frequency inequalities imposed by the theory of Fourier (and more general) transforms. Franson's source emits two photons simultaneously (within a very small time window), though when the emission happens is quite uncertain. One photon is send to Alice, the other to Bob. Alice has a huge uncertainty in the prediction

when her photon is arrives (Bob as well). However, given that the other photon has been detected by Bob, with high precision she can pin-point the arrival of her photon because they are emitted simultaneously (for sake of illustration, we here neglect the necessary communication between the two parties). So far, there is nothing "quantum" about this source. With interferometers between source and detectors, however, things start to get interesting. The interferometers provide two alternatives for each photon, namely a short (S) and long (L) path. With this additional degree of freedom we can ask a new question given that we have coincident clicks, say of detectors A_1 and A_2: we know that both photons must have taken the same path, but which alternative has been realized? S-S or L-L? It turns out, the interferometer erased the bit containing the S/L information for the following simple reason: there is no origin of time, no zero with respect to which we can reverse-calculate the time it took for the pair to travel from source to detectors. As a result, we do have interference, which is revealed by changing either of the two phases φ_1 or φ_2. Similar to the coincidence probability in the Horne-Zeilinger interferometer, Equation (2.31), the two-photon detection rate

$$R_{2-\text{Franson}} \propto 1 \pm \cos\left(\varphi_1 + \varphi_2\right) . \tag{2.36}$$

Single-photon detection rates are not phase-sensitive, however, because if we just look at one photon, the path information is carried by the other photon, whether we chose to look at it or not. The optical explanation for this interference pattern (fourth-order without second-order interference) is readily available as well. Individually, fields have a coherence length much short than the S/L path difference. Correlations between the two-fields, however, translates into a joint-field coherence length much longer than the path difference. This interference phenomenon has been observed in a variety of experiments [53, 82, 83], and later served to introduce time-bins [84], which is subject of another experiment presented later.

2.10 Theory of the Experiment

2.10.1 Input Triplet State

The general wavefunction describing photon triplets is given by

$$|\Psi\rangle = \int d\omega_1 \int d\omega_2 \int d\omega_3 \, \psi(\omega_1, \omega_2, \omega_3) \hat{a}_1^\dagger(\omega_1) \hat{a}_2^\dagger(\omega_2) \hat{a}_3^\dagger(\omega_3) |0\rangle \, , \tag{2.37}$$

where the joint-spectral function $\psi(\omega_1, \omega_2, \omega_3)$ describes coherence properties of photon triplets and $|0\rangle \equiv |0\rangle_1 |0\rangle_2 |0\rangle_3$ is the vacuum state. In CSPDC, fields for the three photons

are generated in a two-step process. First, a pump photon at central frequency ω_p gives birth to a photon pair with frequencies such that $\omega_0+\omega_1=\omega_p$ and a joint-spectral function $\psi_1(\omega_1,\omega_p-\omega_1)$ determined by phase-matching conditions. Next, the photon at frequency ω_0 pumps a second nonlinear crystal, where two photons are created such that $\omega_2+\omega_3=\omega_0$ and joint-spectral function $\psi_2(\omega_2,\omega_p-\omega_1-\omega_2)$. Even though the cascade of downconversion processes leads to a factorization

$$\psi(\omega_1,\omega_2,\omega_3)=\psi_1(\omega_1,\omega_p-\omega_1)\psi_2(\omega_2,\omega_p-\omega_1-\omega_2) \tag{2.38}$$

of the three-photon spectrum [80], the photon triplets are strongly frequency correlated. This is evident from the arguments of the two joint-spectral functions and is a result from the constraint that in a parametric process, frequencies of downconverted fields sum up to the pump frequency, reflecting energy conservation. If we furthermore assume that the pump coherence length approaches infinity and coherence lengths of the three photon fields approach zero, the joint-spectral function takes on an analytically convenient form

$$\psi(\omega_1,\omega_2,\omega_3)=\delta(\omega_p-\omega_1-\omega_2-\omega_3)\,. \tag{2.39}$$

Strictly speaking, this is not a true field state, though it works fine as an approximation to bring out the desired effect [22]. Inserting into (2.37) yields

$$|\Psi\rangle=\int d\omega_1\int d\omega_2\int d\omega_3\,\delta(\omega_p-\omega_1-\omega_2-\omega_3)\,\hat{a}_1^\dagger(\omega_1)\hat{a}_2^\dagger(\omega_2)\hat{a}_3^\dagger(\omega_3)|0\rangle\,. \tag{2.40}$$

where integration is from $-\infty$ to $+\infty$. Now, it turns out that photon triplets are not only strongly correlated in energy, but also in time. One can show this experimentally by measuring the arrival time distribution of photon triplets. One then finds that the histogram peak width, i.e. time uncertainty, is much smaller than is expected from a classical perspective coming from energy-time uncertainty relations (we will meet the inequalities later). Strong time-correlations are evident in the time-domain, to which we switch now using a Fourier transform of the creation operators [85],

$$\hat{a}_k^\dagger(\omega_k)=\frac{1}{\sqrt{2\pi}}\int dt\,\hat{a}_k^\dagger(t)\exp(i\omega_k t)\qquad k\in\{1,2,3\}\,. \tag{2.41}$$

Inserting into (2.40), and re-arranging integrals, we obtain

$$\begin{aligned}|\Psi\rangle=\frac{1}{(2\pi)^{3/2}}&\int dt_1\int dt_2\int dt_3\,\hat{a}_1^\dagger(t_1)\hat{a}_2^\dagger(t_2)\hat{a}_3^\dagger(t_3)\\&\times\int d\omega_1\int d\omega_2\int d\omega_3\,\delta(\omega_p-\omega_1-\omega_2-\omega_3)e^{i(\omega_1t_1+\omega_2t_2+\omega_3t_3)}|0\rangle\,.\end{aligned} \tag{2.42}$$

We can now use two well-known identities from Fourier theory of generalized functions to evaluate

$$\int d\omega_1\, \delta(\omega_p - \omega_1 - \omega_2 - \omega_3) \exp(i\omega_1 t_1) = \exp\left(i[\omega_p - \omega_2 - \omega_3]t_1\right), \tag{2.43}$$

and then

$$\frac{1}{\sqrt{2\pi}} \int d\omega_2\, \exp\left(i\omega_2[t_2 - t_1]\right) = \delta(t_2 - t_1)\,, \tag{2.44}$$

and

$$\frac{1}{\sqrt{2\pi}} \int d\omega_3\, \exp\left(i\omega_3[t_3 - t_1]\right) = \delta(t_3 - t_1)\,, \tag{2.45}$$

and thus

$$\begin{aligned} |\Psi\rangle &= \int dt_1 \int dt_2 \int dt_3\, \hat{a}_1^\dagger(t_1)\hat{a}_2^\dagger(t_2)\hat{a}_3^\dagger(t_3)\delta(t_2 - t_1)\delta(t_3 - t_1)e^{i\omega_p t_1}|0\rangle \\ &= \int dt\, \hat{a}_1^\dagger(t)\hat{a}_2^\dagger(t)\hat{a}_3^\dagger(t)e^{i\omega_p t}|0\rangle\,, \end{aligned} \tag{2.46}$$

where we changed the variable notation from t_1 to t.[2] We now send each photon individually through a two-path interferometer.

2.10.2 Propagation Through Three-Photon Interferometer

The three interferometers are independent, allowing us to perform the mode transformations separately. Consider an unbalanced interferometer with short and long propagation times τ_S and τ_L, respectively, and phase φ. The first beam splitter transforms the annihilation operators according to

$$\begin{aligned} \hat{a}_S(\omega) &= \mathcal{T}\hat{a}_1(\omega) + \mathcal{R}\hat{a}_2(\omega) \\ \hat{a}_L(\omega) &= \mathcal{R}\hat{a}_1(\omega) + \mathcal{T}\hat{a}_2(\omega)\,, \end{aligned} \tag{2.47}$$

where we assumed frequency-independence of both transmission $\mathcal{T}$ and reflection $\mathcal{R}$ coefficients within the frequency-band of interest. Propagation along short and long interferometer paths is described, respectively, by transforms

$$\begin{aligned} t \to t + \tau_S \qquad &\text{and} \qquad \hat{a}_S(\omega) \to \hat{a}_S(\omega)\exp(i\omega\tau_S) \\ t \to t + \tau_L \qquad &\text{and} \qquad \hat{a}_L(\omega) \to \hat{a}_L(\omega)\exp(i\omega\tau_L)\exp(i\varphi)\,, \end{aligned} \tag{2.48}$$

[2] The state used in the brief analysis by Barnett *et al.* [22], which we cite in [4], misses the pump phase factor $\exp(i\omega_p t)$, which, depending on the concrete experiment, may be of relevance.

and the final beam splitter gives us the *detection modes*

$$\begin{aligned}\hat{A}(t) &= \frac{1}{\sqrt{2\pi}}\int d\omega\, \hat{A}(\omega)e^{-i\omega t} \\ &= \frac{\mathcal{R}^2 e^{i\varphi}}{\sqrt{2\pi}}\int d\omega\, \hat{a}(\omega)e^{-i\omega(t-\tau_L)} + \frac{\mathcal{T}^2}{\sqrt{2\pi}}\int d\omega\, \hat{a}(\omega)e^{-i\omega(t-\tau_S)} \\ &+ \frac{\mathcal{R}\mathcal{T} e^{i\varphi}}{\sqrt{2\pi}}\int d\omega\, \hat{b}(\omega)e^{-i\omega(t-\tau_L)} + \frac{\mathcal{R}\mathcal{T}}{\sqrt{2\pi}}\int d\omega\, \hat{b}(\omega)e^{-i\omega(t-\tau_S)} \\ &= \mathcal{R}^2 e^{i\varphi}\hat{a}(t-\tau_L) + \mathcal{T}^2\hat{a}(t-\tau_S) + \mathcal{R}\mathcal{T}e^{i\varphi}\hat{b}(t-\tau_L) + \mathcal{R}\mathcal{T}\hat{b}(t-\tau_S)\,,\end{aligned} \tag{2.49}$$

and

$$\begin{aligned}\hat{B}(t) &= \frac{1}{\sqrt{2\pi}}\int d\omega\, \hat{B}(\omega)e^{-i\omega t} \\ &= \frac{\mathcal{R}\mathcal{T} e^{i\varphi}}{\sqrt{2\pi}}\int d\omega\, \hat{a}(\omega)e^{-i\omega(t-\tau_L)} + \frac{\mathcal{R}\mathcal{T}}{\sqrt{2\pi}}\int d\omega\, \hat{a}(\omega)e^{-i\omega(t-\tau_S)} \\ &+ \frac{\mathcal{T}^2 e^{i\varphi}}{\sqrt{2\pi}}\int d\omega\, \hat{b}(\omega)e^{-i\omega(t-\tau_L)} + \frac{\mathcal{R}^2}{\sqrt{2\pi}}\int d\omega\, \hat{b}(\omega)e^{-i\omega(t-\tau_S)} \\ &= \mathcal{R}^2\hat{b}(t-\tau_S) + \mathcal{T}^2 e^{i\varphi}\hat{b}(t-\tau_L) + \mathcal{R}\mathcal{T}e^{i\varphi}\hat{a}(t-\tau_L) + \mathcal{R}\mathcal{T}\hat{a}(t-\tau_S)\,.\end{aligned} \tag{2.50}$$

A symmetric beam splitter is characterized by

$$\mathcal{T} = \frac{1}{\sqrt{2}} \quad \text{and} \quad \mathcal{R} = \frac{e^{i\pi/2}}{\sqrt{2}} = \frac{i}{\sqrt{2}}\,, \tag{2.51}$$

which gives us, for $k \in \{1,2,3\}$, interferometer transformations

$$\begin{aligned}\hat{A}_k(t) &= \frac{e^{i\varphi_k}}{2}\Big(\hat{a}_k(t-\tau_L) + i\hat{b}_k(t-\tau_L)\Big) - \frac{1}{2}\Big(\hat{a}_k(t-\tau_S) - i\hat{b}_k(t-\tau_S)\Big) \\ \hat{B}_k(t) &= \frac{ie^{i\varphi_k}}{2}\Big(\hat{a}_k(t-\tau_L) + i\hat{b}_k(t-\tau_L)\Big) + \frac{i}{2}\Big(\hat{a}_k(t-\tau_S) - i\hat{b}_k(t-\tau_S)\Big)\end{aligned} \tag{2.52}$$

with inverse relations

$$\begin{aligned}\hat{a}_k(t) &= -\frac{1}{2}\Big(\hat{A}_k(t+\tau_S) + i\hat{B}_k(t+\tau_S)\Big) + \frac{e^{-i\varphi_k}}{2}\Big(\hat{A}_k(t+\tau_L) - i\hat{B}_k(t+\tau_L)\Big) \\ \hat{b}_k(t) &= -\frac{i}{2}\Big(\hat{A}_k(t+\tau_S) + i\hat{B}_k(t+\tau_S)\Big) - \frac{ie^{-i\varphi_k}}{2}\Big(\hat{A}_k(t+\tau_L) + i\hat{B}_k(t+\tau_L)\Big)\,.\end{aligned} \tag{2.53}$$

Finally, Hermitian conjugation gives us creation operators[3]

$$\begin{aligned}\hat{a}_k^\dagger(t) &= -\frac{1}{2}\Big(\hat{A}_k^\dagger(t+\tau_S) - i\hat{B}_k^\dagger(t+\tau_S)\Big) + \frac{e^{i\varphi_k}}{2}\Big(\hat{A}_k^\dagger(t+\tau_L) + i\hat{B}_k^\dagger(t+\tau_L)\Big) \\ \hat{b}_k^\dagger(t) &= \frac{i}{2}\Big(\hat{A}_k^\dagger(t+\tau_S) - i\hat{B}_k^\dagger(t+\tau_S)\Big) + \frac{ie^{i\varphi_k}}{2}\Big(\hat{A}_k^\dagger(t+\tau_L) - i\hat{B}_k^\dagger(t+\tau_L)\Big)\,.\end{aligned} \tag{2.54}$$

[3]The transformations used in the brief analysis by Barnett *et al.* [22], namely their Equation (38), which we use in [4], misses the minus sign between the terms in parenthesis.

Note that we can factor out a minus sign and replace integration variables from $t \to t+\tau_S$, whence, with propagation time difference $\tau \coloneqq \tau_L - \tau_S$, we obtain the triplet state in terms of the detection modes as

$$
\begin{aligned}
|\Psi\rangle = &\int dt\, \frac{e^{i\omega_p t}}{8} \prod_{k=1}^{3} \left\{ \left(\hat{A}_k^\dagger(t) - i\hat{B}_k^\dagger(t) \right) - e^{i\varphi_k} \left(\hat{A}_k^\dagger(t+\tau) + i\hat{B}_k^\dagger(t+\tau) \right) \right\} |0\rangle \\
&= \frac{1}{8} \int dt\, e^{i\omega_p t} \prod_{k=1}^{3} \left\{ \hat{A}_k^\dagger(t) - i\hat{B}_k^\dagger(t) \right\} |0\rangle \\
&- \frac{e^{i\varphi_1}}{8} \int dt\, e^{i\omega_p t} \left(\hat{A}_1^\dagger(t+\tau) + i\hat{B}_1^\dagger(t+\tau) \right) \prod_{k=2,3} \left\{ \hat{A}_k^\dagger(t) - i\hat{B}_k^\dagger(t) \right\} |0\rangle \\
&- \frac{e^{i\varphi_2}}{8} \int dt\, e^{i\omega_p t} \left(\hat{A}_2^\dagger(t+\tau) + i\hat{B}_2^\dagger(t+\tau) \right) \prod_{k=1,3} \left\{ \hat{A}_k^\dagger(t) - i\hat{B}_k^\dagger(t) \right\} |0\rangle \\
&- \frac{e^{i\varphi_3}}{8} \int dt\, e^{i\omega_p t} \left(\hat{A}_3^\dagger(t+\tau) + i\hat{B}_3^\dagger(t+\tau) \right) \prod_{k=1,2} \left\{ \hat{A}_k^\dagger(t) - i\hat{B}_k^\dagger(t) \right\} |0\rangle \\
&+ \frac{e^{i(\varphi_1+\varphi_2)}}{8} \int dt\, e^{i\omega_p t} \left(\hat{A}_3^\dagger(t) - i\hat{B}_3^\dagger(t) \right) \prod_{k=1,2} \left\{ \hat{A}_k^\dagger(t+\tau) + i\hat{B}_k^\dagger(t+\tau) \right\} |0\rangle \\
&+ \frac{e^{i(\varphi_1+\varphi_3)}}{8} \int dt\, e^{i\omega_p t} \left(\hat{A}_2^\dagger(t) - i\hat{B}_2^\dagger(t) \right) \prod_{k=1,3} \left\{ \hat{A}_k^\dagger(t+\tau) + i\hat{B}_k^\dagger(t+\tau) \right\} |0\rangle \\
&+ \frac{e^{i(\varphi_2+\varphi_3)}}{8} \int dt\, e^{i\omega_p t} \left(\hat{A}_1^\dagger(t) - i\hat{B}_1^\dagger(t) \right) \prod_{k=2,3} \left\{ \hat{A}_k^\dagger(t+\tau) + i\hat{B}_k^\dagger(t+\tau) \right\} |0\rangle \\
&- \frac{e^{i(\varphi_1+\varphi_2+\varphi_3)}}{8} \int dt\, e^{i\omega_p t} \prod_{k=1}^{3} \left\{ \hat{A}_k^\dagger(t+\tau) + i\hat{B}_k^\dagger(t+\tau) \right\} |0\rangle \,.
\end{aligned}
\tag{2.55}
$$

Each term corresponds to a possible path combination and we can write

$$
|\Psi\rangle = |\mathrm{SSS}\rangle + |\mathrm{LSS}\rangle + |\mathrm{SLS}\rangle + |\mathrm{SSL}\rangle + |\mathrm{LLS}\rangle + |\mathrm{LSL}\rangle + |\mathrm{SLL}\rangle + |\mathrm{LLL}\rangle \,. \tag{2.56}
$$

2.10.3 Calculation of Coincidence Detection Rates

In our experiment we can look at all detection events in a time-resolved manner, in which case we can *post-select* on those terms that are of interest. Genuine three-photon interference is only observed in triple coincidence events, which correspond to path combination short-short-short (SSS) or long-long-long (LLL). Hence, we are interested in the first and

last term,

$$
\begin{aligned}
|\mathrm{cGHZ}\rangle \coloneqq\ & |\mathrm{SSS}\rangle + |\mathrm{LLL}\rangle \\
& \frac{1}{8}\int dt\, e^{i\omega_p t} \prod_{k=1}^{3} \left\{ \hat{A}_k^\dagger(t) - i\hat{B}_k^\dagger(t) \right\} |0\rangle \\
& - \frac{e^{i(\varphi_1+\varphi_2+\varphi_3)}}{8} \int dt\, e^{i\omega_p t} \prod_{k=1}^{3} \left\{ \hat{A}_k^\dagger(t+\tau) + i\hat{B}_k^\dagger(t+\tau) \right\} |0\rangle \,,
\end{aligned}
\tag{2.57}
$$

which is a continuous version of the GHZ state (cGHZ). Now, since we pump CSPDC with a continuous-wave laser having a coherence time much longer than the interferometer path difference τ, we actually have no special triplet generation time. Similar to a stationary random process, we can shift the time origin without changing the integral. Thus, in the second integral we can change the variable of integration to $t' = t + \tau$, and after pulling out the constant pump-phase term, we obtain

$$
\begin{aligned}
|\mathrm{cGHZ}\rangle = & \frac{1}{8}\int dt\, e^{i\omega_p t} \prod_{k=1}^{3} \left\{ \hat{A}_k^\dagger(t) - i\hat{B}_k^\dagger(t) \right\} |0\rangle \\
& - \frac{e^{i(\varphi_1+\varphi_2+\varphi_3+\omega_p\tau)}}{8} \int dt'\, e^{i\omega_p t'} \prod_{k=1}^{3} \left\{ \hat{A}_k^\dagger(t') + i\hat{B}_k^\dagger(t') \right\} |0\rangle \,.
\end{aligned}
\tag{2.58}
$$

Multiplying out brackets, the first and second term indeed yield identical integrals (we can relabel $t' \to t$),

$$
\begin{aligned}
|\mathrm{cGHZ}\rangle = & \frac{\xi_-}{8}\int dt\, e^{i\omega_p t} \hat{A}_1^\dagger(t)\hat{A}_2^\dagger(t)\hat{A}_3^\dagger(t)|0\rangle - \frac{i\xi_+}{8}\int dt\, e^{i\omega_p t} \hat{A}_1^\dagger(t)\hat{A}_2^\dagger(t)\hat{B}_3^\dagger(t)|0\rangle \\
& - \frac{i\xi_+}{8}\int dt\, e^{i\omega_p t} \hat{A}_1^\dagger(t)\hat{B}_2^\dagger(t)\hat{A}_3^\dagger(t)|0\rangle - \frac{\xi_-}{8}\int dt\, e^{i\omega_p t} \hat{A}_1^\dagger(t)\hat{B}_2^\dagger(t)\hat{B}_3^\dagger(t)|0\rangle \\
& - \frac{i\xi_+}{8}\int dt\, e^{i\omega_p t} \hat{B}_1^\dagger(t)\hat{A}_2^\dagger(t)\hat{A}_3^\dagger(t)|0\rangle - \frac{\xi_-}{8}\int dt\, e^{i\omega_p t} \hat{B}_1^\dagger(t)\hat{A}_2^\dagger(t)\hat{B}_3^\dagger(t)|0\rangle \\
& - \frac{\xi_-}{8}\int dt\, e^{i\omega_p t} \hat{B}_1^\dagger(t)\hat{B}_2^\dagger(t)\hat{A}_3^\dagger(t)|0\rangle + \frac{i\xi_+}{8}\int dt\, e^{i\omega_p t} \hat{B}_1^\dagger(t)\hat{B}_2^\dagger(t)\hat{B}_3^\dagger(t)|0\rangle \,,
\end{aligned}
\tag{2.59}
$$

with $\xi_\pm \coloneqq 1 \pm \xi$, where $\xi \coloneqq \exp\big(i[\varphi_1 + \varphi_2 + \varphi_3 + \omega_p\tau]\big)$. Each term corresponds to one detector combination,

$$
\begin{aligned}
|\mathrm{cGHZ}\rangle = & |A_1A_2A_3\rangle + |A_1A_2B_3\rangle + |A_1B_2A_3\rangle + |A_1B_2B_3\rangle \\
& + |B_1A_2A_3\rangle + |B_1A_2B_3\rangle + |B_1B_2A_3\rangle + |B_1B_2B_3\rangle \,,
\end{aligned}
\tag{2.60}
$$

which are all orthogonal to each other because at least one detector pair is always unmatched, e.g.

$$
\begin{aligned}
\langle A_1A_2A_3|A_1A_2B_3\rangle &\propto \int dt \int dt'\, e^{i\omega_p(t'-t)} \langle 0|\hat{A}_1(t)\hat{A}_2(t)\hat{A}_3(t)\hat{A}_1^\dagger(t')\hat{A}_2^\dagger(t')\hat{B}_3^\dagger(t')|0\rangle \\
&= 0 \,,
\end{aligned}
\tag{2.61}
$$

because

$$\langle 0|\hat{A}_3(t)|0\rangle = \langle 0|\hat{B}_3^\dagger(t)|0\rangle = 0 \tag{2.62}$$

for all times t. The scalar product of a detector state with itself, however, is in general non-zero. For instance,

$$\langle A_1A_2A_3|A_1A_2A_3\rangle = \frac{|\xi_-|^2}{64}\int dt \int dt'\, e^{i\omega_p(t'-t)}\alpha_1(t,t')\alpha_2(t,t')\alpha_3(t,t') \tag{2.63}$$

with

$$\alpha_k(t,t') = \langle 0|\hat{A}_k(t)\hat{A}_k^\dagger(t')|0\rangle = \delta(t-t')\,. \tag{2.64}$$

The delta function collapses integrals and we get

$$\langle A_1A_2A_3|A_1A_2A_3\rangle = \frac{1}{8}\Big(1-\cos(\varphi_1+\varphi_2+\varphi_3+\omega_p\tau)\Big)\,. \tag{2.65}$$

This result indicates a non-trivial triple coincidence rate, which is given by

$$R_{A_1A_2A_3}(t_0,t_{12},t_{13}) = \eta\int_{t_0}^{t_0+\Delta T} dt_1 \int_{t_0+t_{12}}^{t_0+t_{12}+\Delta T} dt_2 \int_{t_0+t_{13}}^{t_o+t_{13}+\Delta T} dt_3\, G^{(3)}_{A_1A_2A_3}(t_1,t_2,t_3)\,, \tag{2.66}$$

with t_{12} and t_{13} the detection time differences, $\eta = \eta_1\eta_2\eta_3$ the product of detector efficiencies, and where the third-order correlation function is defined as

$$G^{(3)}_{A_1A_2A_3}(t_1,t_2,t_3) \coloneqq \langle A_1A_2A_3|\hat{A}_1^\dagger(t_1)\hat{A}_2^\dagger(t_2)\hat{A}_3^\dagger(t_3)\hat{A}_3(t_3)\hat{A}_2(t_2)\hat{A}_1(t_1)|A_1A_2A_3\rangle\,. \tag{2.67}$$

If the correlation time is much longer than our detector time-resolution ΔT, then we can analyze the correlation function in a time-resolved manner, in which case

$$R_{A_1A_2A_3}(t_0,t_{12},t_{13}) \approx \eta\Delta T^3 G^{(3)}_{A_1A_2A_3}(t_0,t_0+t_{12},t_0+t_{13})\,. \tag{2.68}$$

Furthermore, when the absolute detection time is of no relevance, we can simply integrate over all detection events during measurement time T_M, i.e.

$$R_{A_1A_2A_3}(t_{12},t_{13}) = \int_{-T_M/2}^{T_M/2} dt_0\, P_{A_1A_2A_3}(t_0,t_{12},t_{13})\,. \tag{2.69}$$

Now, let us calculate

$$\begin{aligned}
\hat{A}_3(t_3)\hat{A}_2(t_2)\hat{A}_1(t_1)|A_1A_2A_3\rangle &= \frac{\xi_-}{8}\int dt\, e^{i\omega_p t}\hat{A}_3(t_3)\hat{A}_2(t_2)\hat{A}_1(t_1)\hat{A}_1^\dagger(t)\hat{A}_2^\dagger(t)\hat{A}_3^\dagger(t)|0\rangle \\
&= \frac{\xi_-}{8}\int dt\, e^{i\omega_p t}\delta(t-t_1)\delta(t-t_2)\delta(t-t_3)|0\rangle \\
&= \frac{\xi_-}{8}\,,
\end{aligned} \tag{2.70}$$

and likewise

$$\begin{aligned}\langle A_1A_2A_3|\hat{A}_1^\dagger(t_3)\hat{A}_2^\dagger(t_2)\hat{A}_3^\dagger(t_1) &= \Big(\hat{A}_3(t_3)\hat{A}_2(t_2)\hat{A}_1(t_1)|A_1A_2A_3\rangle\Big)^\dagger \\ &= \frac{\xi_-^*}{8}\,,\end{aligned} \tag{2.71}$$

so that

$$G^{(3)}_{A_1A_2A_3}(t_0, t_0+t_{12}, t_0+t_{13}) = \frac{|\xi_-|^2}{64} \tag{2.72}$$

and

$$R_{A_1A_2A_3}(t_{12}, t_{13}) = \frac{\eta\Delta T^3 T_M}{8}\Big(1-\cos(\varphi_1+\varphi_2+\varphi_3+\omega_p\tau)\Big)\,. \tag{2.73}$$

The proportionality constant shows how crucial high detection efficiencies are and the reduction by factor 8 is due to the probabilistic nature of the Franson interferometer, splitting transmitted triplets into eight possible detector combinations. We could of course increase the measurement time T_M indefinitely, but the choice is ultimately constrained by practical considerations such as phase stability of the interferometer, as well as alignment of the setup, in particular mechanical relaxation of setup components. Furthermore, the detector time resolution ΔT has to be kept small enough to pick out the $|\mathrm{cGHZ}\rangle$ term from the triplet state (2.56), and cannot be increased arbitrarily. The detection rates of all other detector combinations are obtained in a likewise manner,

$$\begin{aligned}
R_{A_1A_2B_3} &= \frac{\eta\Delta T^3 T_M}{8}\Big(1+\cos(\varphi_1+\varphi_2+\varphi_3+\omega_p\tau)\Big)\\
R_{A_1B_2A_3} &= \frac{\eta\Delta T^3 T_M}{8}\Big(1+\cos(\varphi_1+\varphi_2+\varphi_3+\omega_p\tau)\Big)\\
R_{A_1B_2B_3} &= \frac{\eta\Delta T^3 T_M}{8}\Big(1-\cos(\varphi_1+\varphi_2+\varphi_3+\omega_p\tau)\Big)\\
R_{B_1A_2A_3} &= \frac{\eta\Delta T^3 T_M}{8}\Big(1+\cos(\varphi_1+\varphi_2+\varphi_3+\omega_p\tau)\Big)\\
R_{B_1A_2B_3} &= \frac{\eta\Delta T^3 T_M}{8}\Big(1-\cos(\varphi_1+\varphi_2+\varphi_3+\omega_p\tau)\Big)\\
R_{B_1B_2A_3} &= \frac{\eta\Delta T^3 T_M}{8}\Big(1-\cos(\varphi_1+\varphi_2+\varphi_3+\omega_p\tau)\Big)\\
R_{B_1B_2B_3} &= \frac{\eta\Delta T^3 T_M}{8}\Big(1+\cos(\varphi_1+\varphi_2+\varphi_3+\omega_p\tau)\Big)\,.
\end{aligned} \tag{2.74}$$

The rates actually observed in the experiment also depend on source efficiency, intrinsic triplet generation rate in particular, and losses throughout the experimental setup. We see that detection events split up into two sets of *complementary* detector combinations,

$$\begin{aligned}
AAA &= \{A_1A_2A_3,\ A_1B_2B_3,\ B_1A_2B_3,\ B_1B_2A_3\}\\
BBB &= \{B_1B_2B_3,\ B_1A_2A_3,\ A_1B_2A_3,\ A_1A_2B_3\}\,.
\end{aligned} \tag{2.75}$$

These sets are easily found if we remember (see Section 2.7) that each interferometer defines a two-valued variable with $A \equiv +1$ and $B \equiv -1$. Multiplication of detector combinations in the set AAA and BBB yields $+1$ and -1, respectively, which is why we can call them even and odd parity detectors. Summing up all detection events in AAA and BBB, we get a triple coincidence detection rate

$$R_3 \propto 1 \pm \cos(\varphi_1 + \varphi_2 + \varphi_3 + \varphi_p)\,, \tag{2.76}$$

where the minus and plus sign are for AAA and BBB detection events, respectively. The pump phase $\varphi_p := \omega_p \tau$ is constant to a very good approximation over the duration of the experiment and can be ignored in later analysis of the data (though one could use the pump phase to control triplet coincidences as well).

Each of the other states in (2.56) is unmatched in the sense that the corresponding triple photon detection events are distinguishable in time. This is visible in the histogram of detection events in Figure 2.15 and implies that these events are not phase-sensitive.

We also see that the two-photon coincidences are constant, e.g.

$$R_{A_1A_2} = R_{A_1A_2A_3} + R_{A_1A_2B_3} = \frac{\eta \Delta T^3 T_M}{4}\,, \tag{2.77}$$

and so are the single detection rates, e.g.

$$R_{A_1} = R_{A_1A_2A_3} + R_{A_1A_2B_3} + R_{A_1B_2A_3} + + R_{A_1B_2B_3} = \frac{\eta \Delta T^3 T_M}{2}\,. \tag{2.78}$$

2.11 Experimental Setup

2.11.1 Overview

The experimental setup consists of three parts: a CSPDC source producing three energy-time entangled photons, a compact and phase-stable three-photon Franson interferometer, and a detection setup that allows to both efficiently register single photons and assign time-stamps with high time-resolution. An overview photo of the experimental setup is shown in Figure 2.7 and a schematic can be found in Figure 2.8. Table 2.1 shows a count rate estimation calculation we did just before commencing the experiment. Following the formula

$$R_T = \frac{R_0 \eta_1 \eta_2 \eta_3 \gamma_1 \gamma_2 \gamma_3}{4}\,, \tag{2.79}$$

we find more than 10 triplets per hour usable for interferometry. This means that, given the interferometer and source are stable enough for a few days, each phase can be set for a

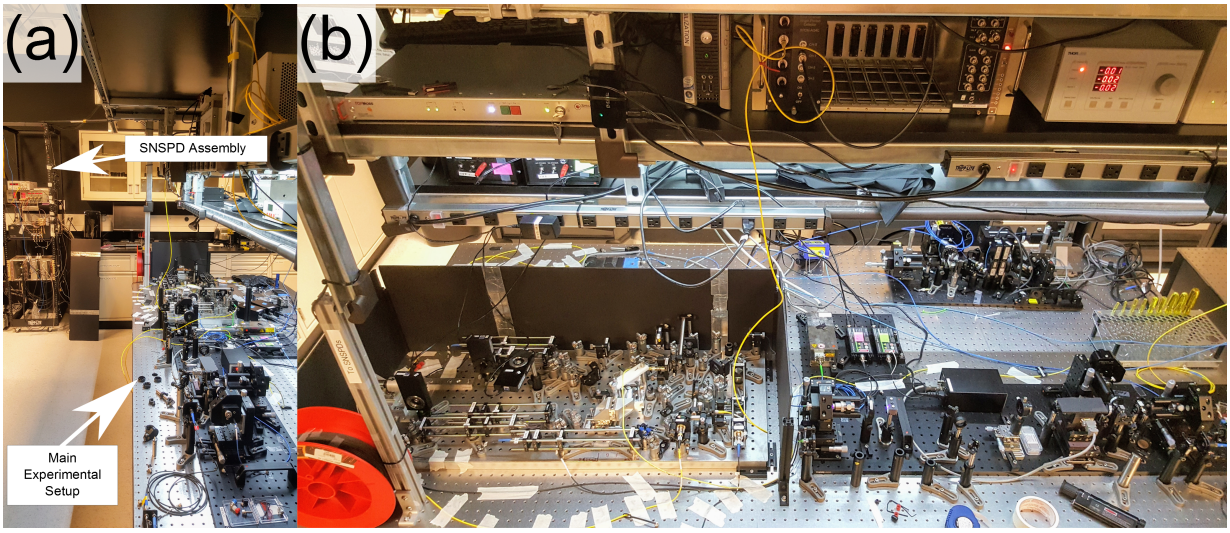

Figure 2.7: **Overview of the Three-Photon Interference Experiment.** The triplet source, three-photon Franson interferometer and silicon avalanche photo diodes were on an optical table. The superconducting nanowire single photon detectors and the time taggers were installed in a separate rack, which is connected to a helium compressor in a small room next to the main lab.

couple of hours. This should give us a few tens of photons per phase angle, in which case $\sqrt{N}$ counting errors should not be detrimental for a clear maximum-minimum separation.

Directly generated photon triplets per hour	R_0	2000
Si-APD Detection Efficiency (for 842nm photons)	η_1	0.4
SNSPD Detection Efficiency (for 1530nm photons)	η_2	0.8
SNSPD Detection Efficiency (for 1570nm photons)	η_3	0.8
Detected photon triplets per hour		512
Interferometer throughput at 842nm	γ_1	0.4
Interferometer throughput at 1530nm	γ_2	0.5
Interferometer throughput at 1570nm	γ_3	0.5
Detected photon triplets per hour through interferometer	R_I	51.2
Interfering photon triplets per hour (divide by 4)	R_T	12.8

Table 2.1: **Photon Triplet Count Rate Estimation.** Si-APD: silicon avalanche photo diodes. SNSPD: superconducting nanowire single photon detectors.

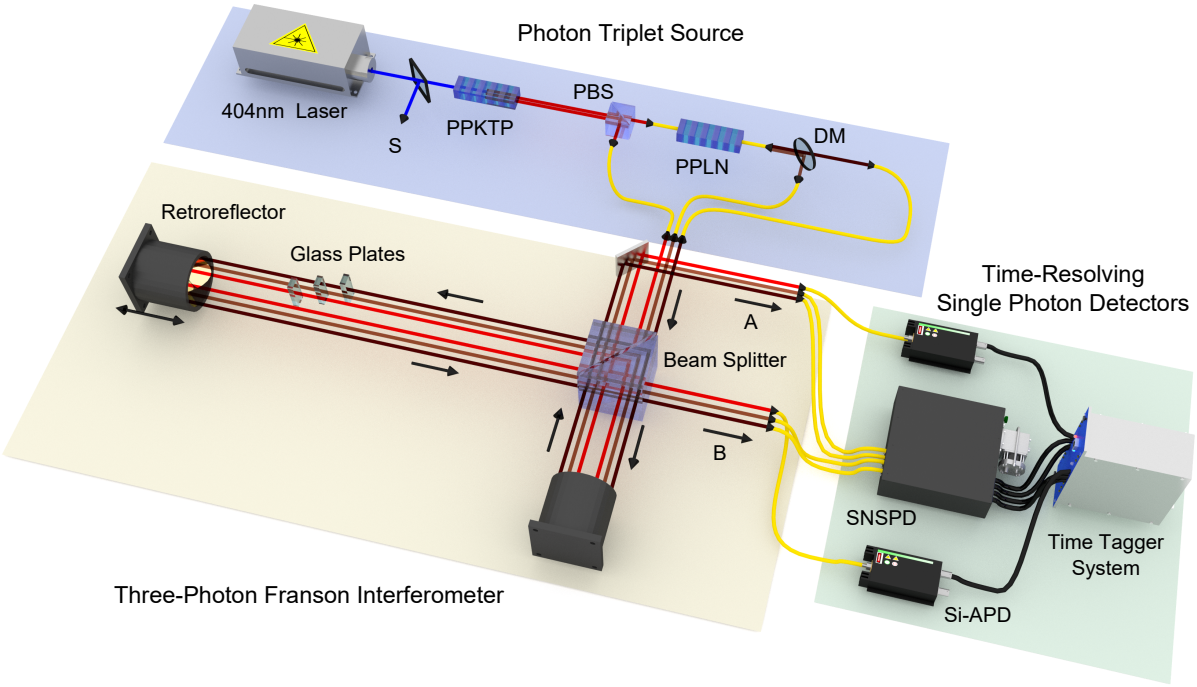

Figure 2.8: **Experimental Setup for the Observation of Genuine Three-Photon Interference.** (from Agne *et al.* [4]) A continuous-wave grating-stabilized laser diode (404 nm, 43 mW, >25 m coherence length) pumps a 25 mm periodically-poled potassium titanyl phosphate (PPKTP) crystal to generate pairs of 842/776 nm photons in type-II down-conversion, which are split at a polarizing beam splitter (PBS). The 776 nm photons pump a periodically-poled lithium niobate (PPLN) waveguide to generate 1530/1570 nm photon pairs in type-0 down-conversion. These infrared photons are split in free-space by a dichroic mirror (DM) before entering the three-photon Franson interferometer, which is realized as three spatial modes of a single interferometer with a path difference $\tau = 3.7$ ns. Photon phase control is achieved with motorized glass plates. At the two output ports A and B, the 842 nm and 1530/1570 nm photons are detected with free-running silicon avalanche photodiodes (Si-APD) and superconducting nanowire single photon detectors (SNSPD), respectively, and their arrival time is registered with a time tagger system. All fibers (yellow) are single-mode fibers at respective wavelengths. A few pump photons are picked off and sent through another interferometer path (S — not drawn) for interferometer stabilization.

2.11.2 Triplet Source

In the theoretical derivation of the count rate we already alluded to the fact that in higher-order interference experiments the losses scale exponentially with the number of interferometers. Schemes relying on post-selection, like ours, suffer from additional photon depletion, as non-interfering paths are equally populated. Moreover, current methods to tailor multiphoton states of the kinds we need are very inefficient. For instance, with the original CSPDC source in our lab [9], my colleagues were barely able to detect 6 (coincident) triplets *per hour*. One has to be absolutely convinced, both in the working principle of idea and ensuing benefits, in order to attempt such an experimental demonstration! A three-photon interferometer experiment was unthinkable back then, not only because of all additional losses due to the interferometer, but also triplets have to be distributed over a couple of phase settings to compile a meaningful interference fringe. Now, with an an improved triplet source and more efficient detectors, we detect around 46000 triplets in 24 hours, i.e. approximately 2000 triplets *per hour*, which is a factor ~ 400 improvement. This is mainly due to a brighter first-stage (PPKTP) pair source: we detect 6.5 million singles per second and 1.9 million 776/842 nm pairs per second within a 3.125 ns coincidence window in either early or late time slot. The rates used in the experiment are around 10 % below the maximum previously achieved with this PPKTP and are probably very close to the optimum before multiphoton emissions, which supply non-interfering background photons, degrade entanglement quality. At the moment, the coincidences-to-accidentals ratio (CAR), solely due to multi-pair emissions in the PPKTP, is

$$CAR = \frac{C_{12}}{S_1 S_2 \delta t} \approx 14\,, \tag{2.80}$$

with single count rates $S_1 = 7$ and $S_2 = 6$, and a coincidence rate of $C_{12} = 1.85$ in a $\delta t = 3.125\,\text{ns}$ window (all rates in million per second). Note that these are half the detected rates because photons, upon propagation through the interferometer with short and long arm, distribute across two time bins. Furthermore, the corresponding dark counts rate of ~ 200 per second are low enough that we need not subtract these from the single count rates. This CAR value yields an upper bound of

$$\mathcal{V} = \frac{CAR}{CAR + 1} \approx 93\,\% \tag{2.81}$$

for both two-photon and three-photon fringe visibilities. Consequently, multi-pair emissions cannot explain the lack of two-photon interference in our experiment, but agrees well with our maximum triplet interference visibilities. At this point, only an increase in the intrinsic conversion efficiency of the PPKTP seems to be the way forward to increase the

usable pair-rate from the first source. The typical internal conversion probabilities for bulk and waveguide crystals are on the order of 10^{-9} (PPKTP) and 10^{-6} (PPLN), respectively, indicating that an improvement of two or three orders may be feasible with a waveguide PPKTP. Photos and more experimental information of both the first-stage and second-stage source can be found in Figures 2.9 and 2.10, respectively. The crystal cascade results in an exponential drop in number of generated photon pairs in the second crystal. The asymmetry in count rates between the three channels (842 nm, 1530 nm and 1570 nm) is visible in Figure 2.16. More concretely, the detected number of 842 nm photons is between 1.6 and 2.2 million per second. The 1530/157 nm detectors, on the other hand, see only 150-400 photons per second, which is the dark count level of our superconducting nanowire single photon detectors. Fortunately, the asymmetry does not translate into problems for the observed effect. What it means is that we have to measure longer, because not every 842 nm photon has matching 1530/1570 nm partner. Also, we cannot resolve modulation of telecom single detection events. Three-photon interference is unaffected, however, since we post-select on triple coincidences.

2.11.3 Three-Photon interferometer

A photo of the three-photon Franson interferometer used in the experiment is shown in Figure 2.11. We integrate all three interferometers into one big interferometer, using common retroreflectors and beam splitter. We have four well-separated paths for 842 nm, 1530 nm, 1570 nm and 404 nm photons. This monolithic design avoids cross-stabilization of three spatially separated interferometers. Phase stabilization in this interferometer is achieved as follows. Pump photons at 404 nm, having a coherence length much larger than the interferometer path difference, are obtained from the first-stage source setup (see Figure 2.9) and are sent through the interferometer (we have a fourth path through the interferometer) and detected with a silicon avalanche photo diode. Scanning the interferometer phase with a piezo electric actuator attached to the long path retroreflector, we observe second-order interference fringes. Employing a simple PID feedback loop with set point equal to half-fringe counts ($\sim$ 600000 counts per second), we can stabilize the interferometer for at least 96 hours without re-alignment. The interferometer throughput is roughly 44% for all paths, including all fiber coupling losses. Individual phase control for 842 nm, 1530 nm and 1570 nm photons is achieved with 3 mm thick BK7 windows (anti-reflection coated at the respective wavelength) mounted on motorized glass phase plates (see Figure 2.12). We characterize the zero-position of the glass phase plates with lasers and verify the nonlinear relationship between glass phase plate angle and induced optical phase. Based on these measurements, we pre-tilt the glass phase plate by a few degrees to observe at

least one fringe over two degrees and define the pre-tilt angle as the zero-position for our measurements.

2.11.4 Detection Setup

For each photon channel (1530, 1570 and 842 nm), the interferometer has two outputs A and B. Therefore, we need six single photon detectors. For 842 nm photons we employ standard silicon avalanche photodiodes (Si-APD) and for the 1530/1570 nm photons we employ newly developed superconducting nanowire single photon detectors (see Figure 2.13), operated at system efficiencies (measured) of 80, 48, 60 and 85 % with 150-400 dark counts per second. We use three time taggers to simultaneously record 842A-telecom, 842B-telecom coincidences and single detection events. Here, "telecom" refers to all events in the 1530/1570 nm detectors. The resolution with which the time taggers assign time stamps to detection events are 78 ps for coincidence recording and 156 ps for singles recording (higher resolution not needed here). The time taggers assign time stamps to *all* detection events so that later analysis can extract single photon detections, as well as two-photon and three-photon coincidences. All time taggers receive the same 10 MHz signal from an arbitrary waveform generator (Agilent 33250A) as an external timing reference and to increase long-term stability. Figure 2.14 shows both the time tagger setup and a schematic of the information flow, from photon detection to registration by a computer. In total we used four computers in the experiment: one for singles collection, one for 842A-telecom coincidences and glass plate control, one for 842B-telecom coincidences, pump laser control and temperature logging, and one for interferometer stabilization. The reason we use three time taggers and three corresponding computers is that in the beginning we worried about the coincidences-time-tag file size (estimate ∼GBs over a few minutes). The reason for this are the high 842 nm singles (up to 4 million per second) which results in lots of accidental coincidences. The lab computers running the experiment control program (LabVIEW) might struggle and post-processing and analysis with Matlab would require more resources. We therefore used two time taggers for coincidences, one for each 842 nm channel. However, after a 42 hour experiment, we only had file sizes of about $\sim$ 1.8 GB for each time tagger, which can be easily stored and processed: Matlab running on my office computer (12GB, Quad-Core i7-4770 at 3.4GHz) can easily analyze these files within a few minutes. Later measurements generated 13 GB files due to higher dark counts in the SNSPDs, which I analyzed with a 32GB 16-Core computer. For these measurements, the split-up of time tags paid off.

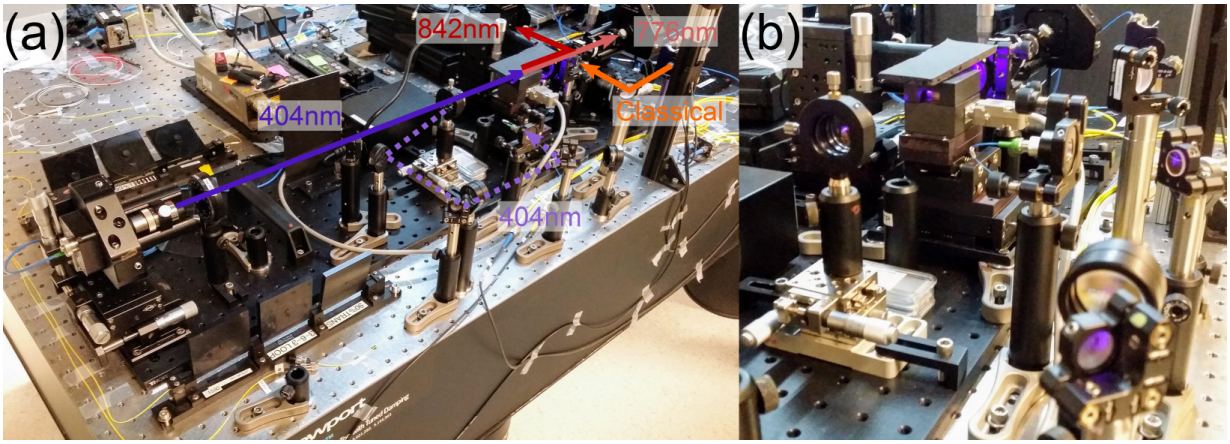

Figure 2.9: **The First-Stage (PPKTP) Source. (a)** Shown is the new and brighter first-stage source for cascaded spontaneous parametric downconversion. It was built in Kevin Resch's group and for the experiment we added two modifications. First, we pick off some 404 nm pump photons (path indicated by solid purple line) and send them into the interferometer for active phase stabilization. Photons are reflected off the focusing lens (which is slightly tilted) and directed into a single mode fiber (path indicated by dashed light purple line). Second, we have a classical light coupling path for interferometer alignment and measurement of its path difference. Light is sent into the second input port of the polarizing beam splitter (PBS), which splits 776/842 nm photon based on their polarization. The amount of light coupled into 776 nm and 842 nm fibers is controlled with both half-wave plate and neutral density filters before the PBS. **(b)** Close-up photo of the crystal mount. The periodically poled potassium titanyl phosphate (PPKTP) crystal is stabilized at a temperature of $T_{\mathrm{PPKTP}} = 41.7°\mathrm{C}$ (the original temperature, 42.1°C, was not optimal for second-stage crystal with 776 nm photons). At its peak, 14 million 776 nm and 842 nm photons were produced per second, of which 4 million were coincident (within a ~ 3 ns coincidence window). The tilt stage of the crystal mount was the primary reason for gradual misalignment of the source. Counts rates consistently dropped by about 20 % over two days, but could be brought back to normal with a few turns of four tilt screws.

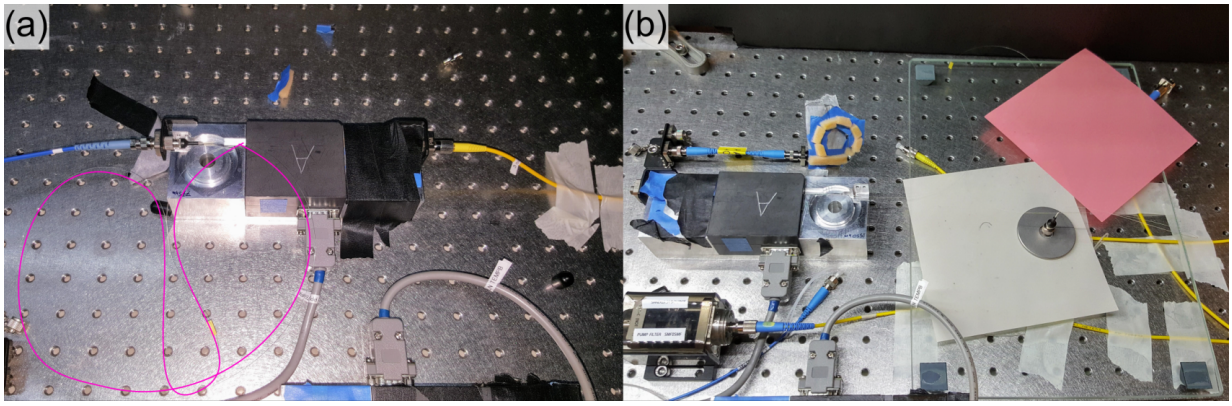

Figure 2.10: **The Second Stage (PPLN) Source. (a)** Shown is the periodically-poled lithium niobate (PPLN) waveguide with exposed bare input fiber (highlighted in pink, for otherwise it would hardly be visible). During the experiment we found that we lose a few percent of coupling efficiency into the PPLN itself when the fiber is curled up in the silver round tray. This is probably due to some polarization rotation through the fiber (input has to be H-polarized). The PPLN was held at a temperature $T = 51.3°\mathrm{C}$ for duration of the experiment. **(b)** Polishing of the PPLN output fiber. We regularly switched between two connecting fibers (one to the interferometer, the other directly to detectors), in which case we are almost guaranteed to contaminate the PPLN output. Thus, regular fiber cleaning and polishing to maintain a high coupling efficiency of 1530/1570 nm photon was crucial for the experiment's success.

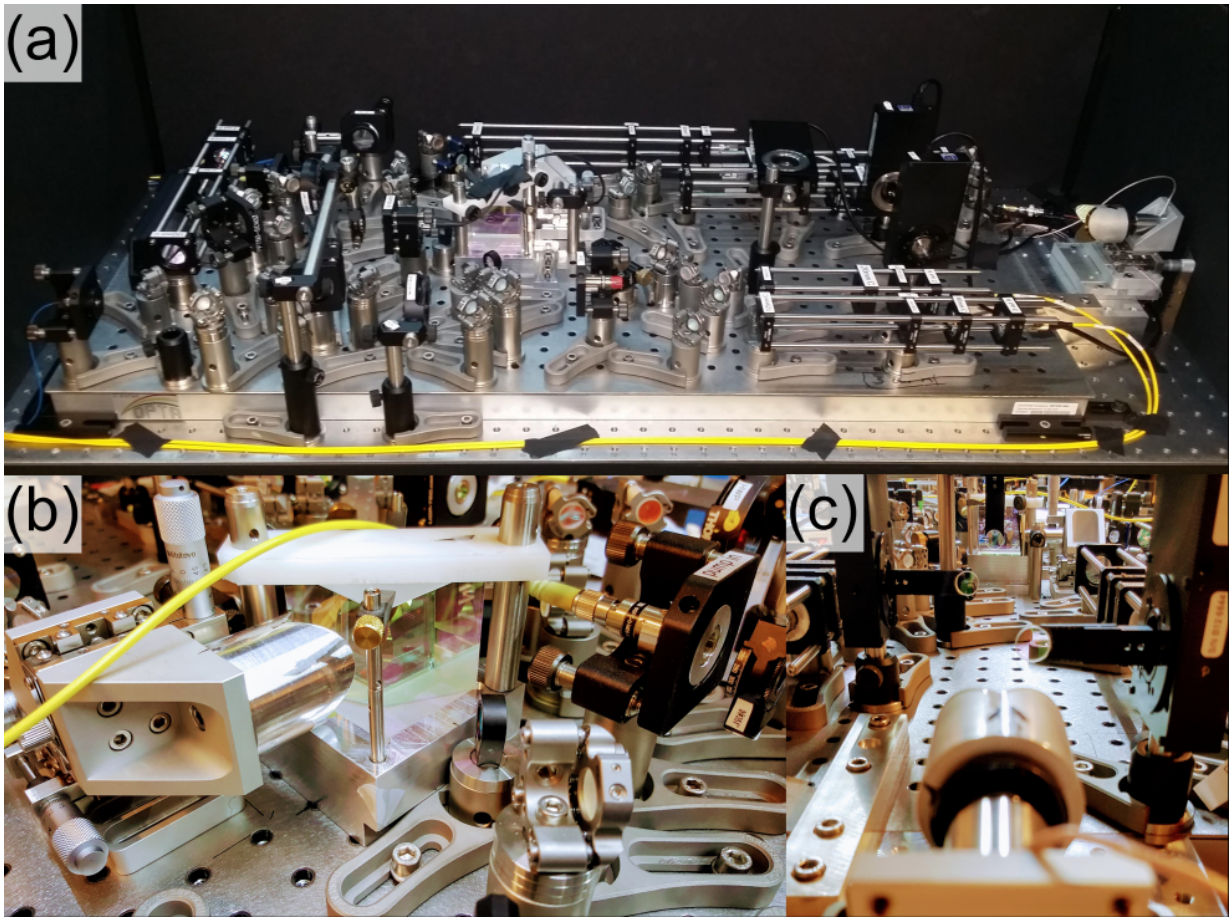

Figure 2.11: **The Three-Photon Franson Interferometer. (a)** The three-photon Franson interferometer, as used in the experiment. The interferometer was built by Thomas Kauten in Innsbruck and modified in Waterloo for the experiment: (1) Addition of half-wave plates after the input coupler for each photon to mitigate polarization effects. (2) Addition of a 1530/1570 nm dichroic mirror to split in free-space photons coming from the PPLN. (3) Addition of a long-pass filter after the 1530/1570 nm input coupler to subtract residual 776 nm photons. (4) Replacement of optical fibers with ones that have anti-reflection coating to reduce back-reflection losses. (5) Replacement (and addition for the 842 nm path) of motorized glass plates with a new set (use motors compatible with our data acquisition system). (6) Installation of a piezoelectric actuator attached to the long path retroreflector for use with our PID feedback system (phase stabilization). (7) Increase of the interferometer long path by 10 cm to get a path difference sufficiently larger than the detector timing jitter of up to 2 ns. **(b)** The beam splitter is optimized for 1530/1570 nm photons (reduced splitting efficiency for 842 nm photons, but we have orders of magnitudes more 842 nm photons so that losses are acceptable). **(c)** View down the long path of the interferometer. Visible are the three glass plates that we installed for the second round of high-visibility measurements (see also Figure 2.12).

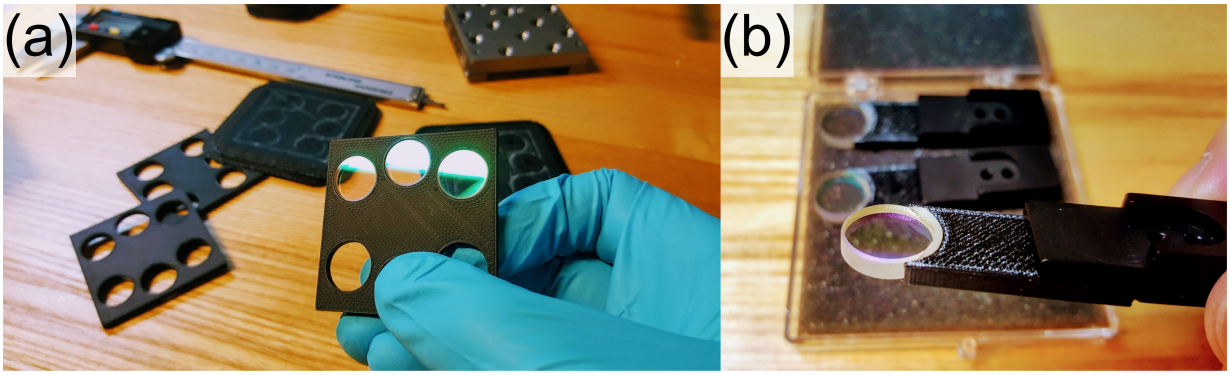

Figure 2.12: **Three-Photon Franson Interferometer Glass Plates.** Compensation **(a)** and phase-scan **(b)** glass plates for the short and long arm of the interferometer, respectively (all glass holders 3D-printed). In the first round of measurements (some results are shown in Figure 2.18) we used 2 mm and 1 mm thick BK7 glass plates for 1530/1570 nm and 842 nm photons, respectively, and did not have compensation glass plates in the short path. For the second round of measurements, and thus the main results shown in Figures 2.16 and 2.17, we switched to 3 mm glass plates (with anti-reflection coating at the respective wavelength) for both short and long path.

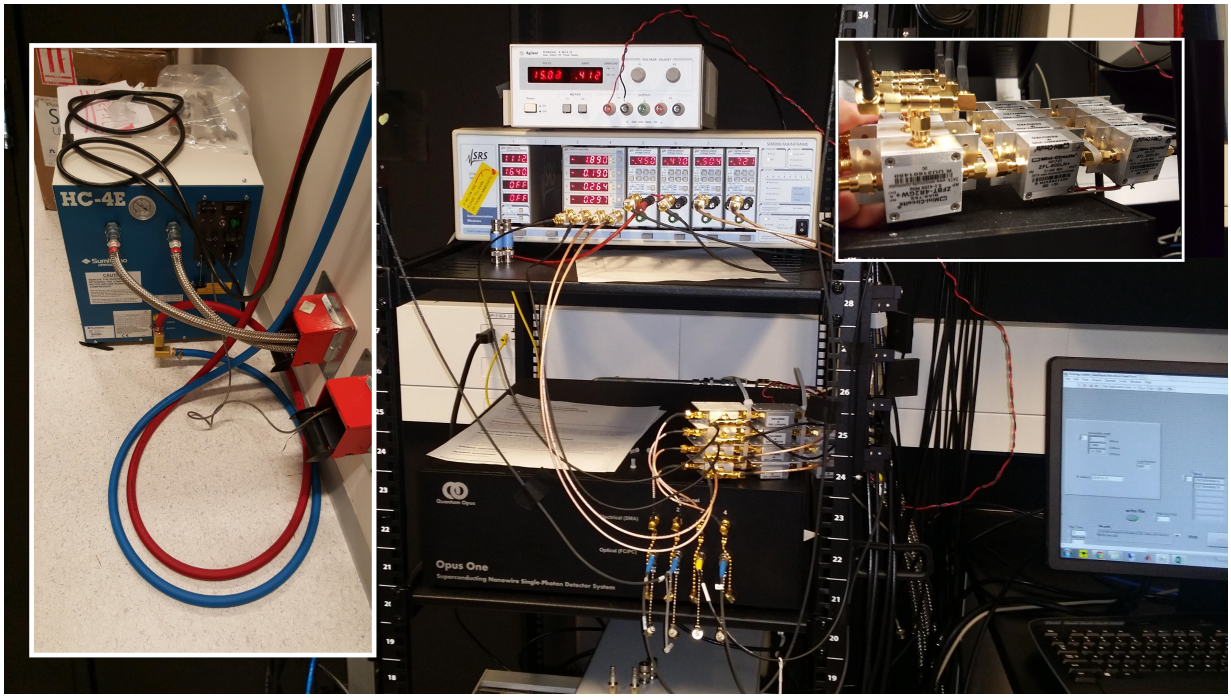

Figure 2.13: **Superconducting Nanowire Single Photon Detectors.** Photo of the rack housing our Quantum Opus One superconducting nanowire single photon detector (SNSPD) system with four channels. For the first round of measurement, the maximum measured efficiencies were 44 %, 81 %, 72 % and 74 %, respectively. However, these values came at a cost of high dark counts. Consequently, we set the bias voltage such that we had around 300-1000 dark counts, reducing the efficiency a bit. For the second round of measurements, we received a detector upgrade from Aaron Miller (Quantum Opus), resulting in measured system efficiencies up to 85 % (see main text). The SNSPDs are cooled to $\sim 2.2-2.3$ K with a 4 K two-stage cryocooler Sumitomo Model SRDK-101D, part of the Sumitomo Model RDK-101D cold head system, which is supplied with helium by a Sumitomo HC-4E2 water cooled compressor (shown in the left inset). The end temperature below 4 K depends on how good the initial vacuum is. The temperature is monitored by Stanford Research System SIM 922, whose silicon diodes can detect as low as 1.4 K. The nanowire voltages are monitored by a SIM 970 quad digital voltmeter with good long-term stability. Nanowire bias voltages are delivered by four SIM 928 isolated voltage sources, which deliver "ultra-clean DC voltages" with mV resolution. All SIM modules are mounted in a SIM 900 mainframe. A stack of Mini-Circuit components connects the nanowires with SIM electronics and time taggers. For each of the four channels this stack consists of a ZFBT-4R2GW+ bias-tee and two ZFL-500LN+ amplifiers in series. The nanowire electrical signal is fed into the RF+DC input port of the bias-tee and the bias voltage is fed into the DC port, to which the SIM 970 channels are hooked up as well. The RF output is connected to the two-stage amplifier, whose output is sent to the time tagger system.

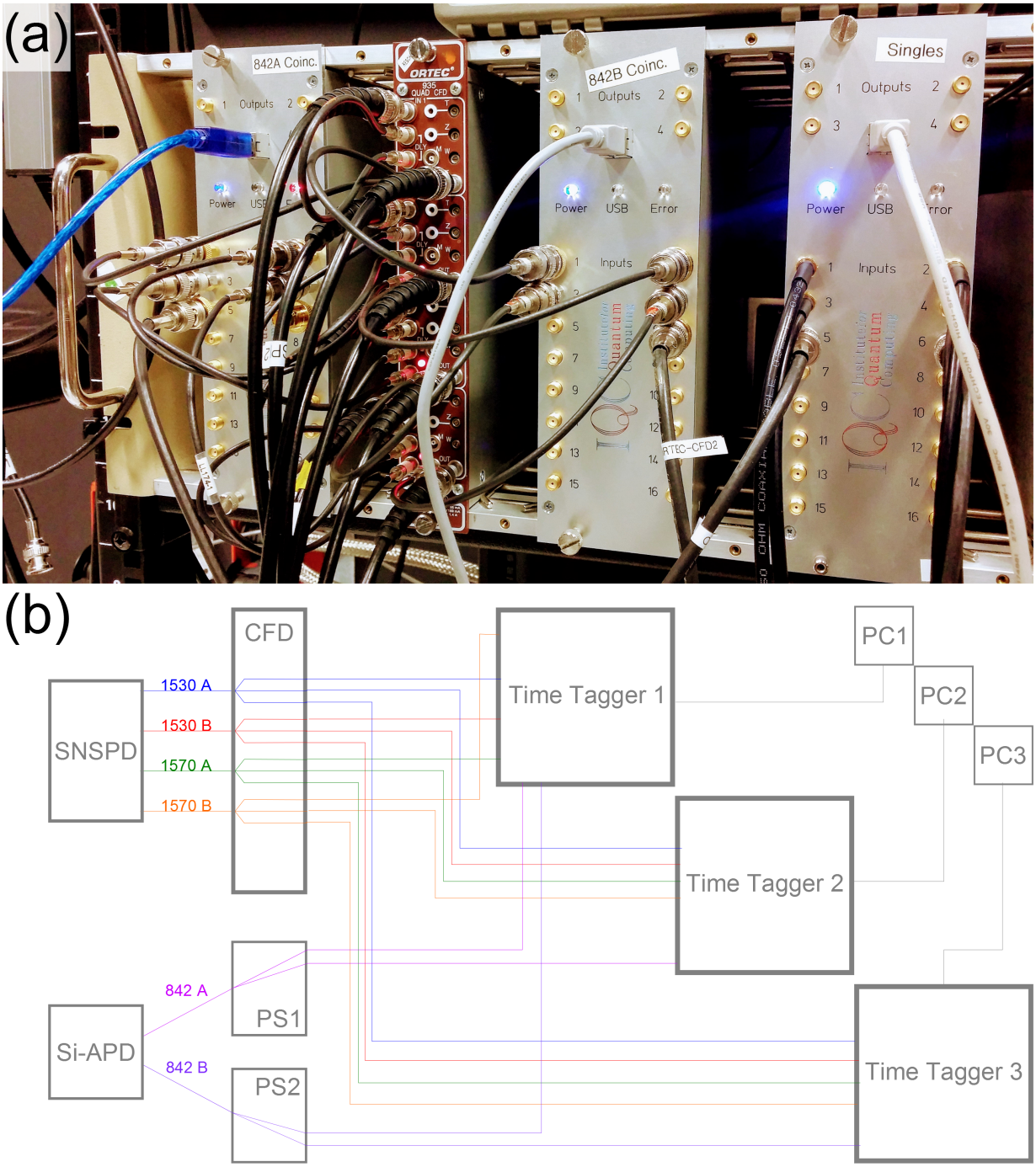

Figure 2.14: **Time Taggers and Detection Schematic.** **(a)** Photo of the three Universal Quantum Devices time taggers (silver boxes) and the Ortec 935 constant-fraction discriminator (CFD, brown box) used in the experiment. The CFD is employed to both clean up the (electronic) detection signal from SNSPDs and split up signals. **(b)** Schematic showing the information flow from single photon detection (SNSPD and Si-APD), to power splitting (PS and CFD), assignment of time stamps (Time Taggers) and digital processing (PC's).

2.12 Experimental Results

We first record photon events for 12 phase settings of 1570 nm photons by changing angles of the glass phase plate in the 1570 nm long arm. Measuring for 2 hours per angle, over 24 hours we detect 4648 triplets within a coarse 20 ns coincidence window. The histogram in Figure 2.15 shows the distribution of arrival times with seven peaks that reflect the eight possible path combinations. With a bin size of 0.78 ns in both dimensions, we have 309 triplets in the central bin and an average of 137 triplets in each of the six highest side bins. The triplets in the central bin are shown as a function of the 1570 nm phase in Figure 2.16 (a). We now want to fit Equation (2.76) to the triple coincidences and obtain the fringe visibility. The first step in estimating the fringe visibility is to calculate the phase that results from tilting the glass plate in the interferometer of, for example, 1570 nm photons. The phase difference due to optical path difference is a function of photon wavelength λ, refractive indices of surrounding medium (air, $n_1 = 1$) and glass (BK7, $n_2 \approx 1.5$), glass thickness ($t = 3\,\text{mm}$) and of course tilt angle α, which determines the optical path length. Using geometric optics and the laws of refraction, one can derive the relationship

$$\varphi = kt\left(n_1 - n_2 + \frac{n_2 - n_1\cos(\alpha-\beta)}{\cos(\beta)}\right), \tag{2.82}$$

with $k = 2\pi/\lambda$ and

$$\beta = \arcsin\left(\frac{n_1\sin(\alpha)}{n_2}\right). \tag{2.83}$$

Using this formula, we convert all angles α to phase φ and then estimate the fringe visibility with a fit

$$f(\varphi) = a_1\Big(1 + V_1\sin(b_1\cdot\varphi + c_1)\Big) \tag{2.84}$$

to BBB data and then use b_1 and c_1 for fitting

$$g(\varphi) = a_2\Big(1 + V_2\sin(b_1\cdot\varphi + c_1)\Big) \tag{2.85}$$

to AAA data. Here, $a_1, a_2, b_1, c_1, V_1, V_2$ are fit parameters (the latter ones being estimated visibilities). With that we get visibilities

$$\begin{aligned} V_{\text{AAA}} &= (92.8 \pm 6.6)\,\% \\ V_{\text{BBB}} &= (92.7 \pm 6.4)\,\%, \end{aligned} \tag{2.86}$$

and the corresponding fits are shown in Figure 2.16 (a). The average visibility is thus

$$V_{\text{Average}} = (92.7 \pm 4.6)\,\% \tag{2.87}$$

without background subtraction, which is above the classical visibility bound of 50 % for genuine three-photon interference [31–33]. Note that we performed a phase-locked fit procedure since the AAA and BBB curves should be complementary and thus have the same phase. Independent fits to the AAA and BBB data yield slightly higher visibilities (e.g. 94.6 % for the 1570 nm phase scan in Figure 2.16), which are, however, well within the visibility uncertainty. The visibility errors are determined as follows. From the original data set, ten new data sets are generated from a Poisson distribution with mean equal to measured data points (Monte Carlo method). Following the same fitting procedure as above, visibilities were obtained for each sample. The standard deviation of those visibilities form the reported visibility error bars.

As shown in Figure 2.16 (b) and (c), two-photon coincidences and single count rates from the same data set display only small drifts in count rates over the course of the experiment but no systematic, complementary modulation. We observe no two-photon Franson interference of 1530/1570 nm photons because the coherence length of 776 nm photons as a pump for the second SPDC process is much smaller than the interferometer path difference (spectra are shown in Figures 2.19 and 2.20). Variations in two-photon coincidences can be due to fluctuations in the mean SNSPD dark count rate, which affects observed three-fold coincidences. For example, comparing Figures 2.16 (a) and (b) at the fifth ($\approx \pi/2$) and ninth ($\approx 3\pi/2$) data point we see that the higher three-fold coincidences agree with an isolated increase in two-fold coincidences. Note that whereas the infrared singles are dominated by dark counts, the ratio of signal to dark counts per second in the Si-APDs is $\sim 10^5$ and therefore any modulation present in the 842 nm single counts would be clearly visible.

In a second measurement, we scan the phase of 1530 nm photons. Figure 2.17 (a) shows the result of a scan in which the 1530 nm glass phase plate is pre-tilted so that two fringes are observed over 2.2 degrees. The three-photon interference visibilities are

$$\begin{aligned} V_{\mathrm{AAA}} &= (77.9 \pm 7.9)\,\% \\ V_{\mathrm{BBB}} &= (91.4 \pm 9.9)\,\%\,, \end{aligned} \tag{2.88}$$

giving us an average visibility of

$$V_{\mathrm{Average}} = (84.6 \pm 6.3)\,\% \tag{2.89}$$

without background subtraction. The visibility difference between AAA and BBB curves is consistent with statistical errors that we observe when generating Monte Carlo data sets for visibility error estimation.

The phase of 842 nm photons is scanned in a third measurement. Given that the wavelength is about half the other photon's wavelengths and the glass plates have identical thicknesses, we expect a full three-photon interference fringe over half the 1570 nm scan range. Indeed, as Figure 2.17 (b) shows, we observe fringe visibilities of

$$\begin{aligned} V_{\mathrm{AAA}} &= (82.9 \pm 6.4)\,\% \\ V_{\mathrm{BBB}} &= (86.3 \pm 5.2)\,\%\,, \end{aligned} \tag{2.90}$$

giving us an average visibility of

$$V_{\mathrm{Average}} = (84.6 \pm 4.1)\,\% \tag{2.91}$$

without background subtraction. As for the 1570 nm phase scan, two-photon coincidences and single detection rates show no modulation for both the 1530 nm and 842 nm phase scans.

In a last series of measurements, we block individual or all interferometer paths and record photon events. As expected, three-photon coincidences are no longer phase-sensitive. If modulation of three-photon coincidences is due to interference of indistinguishable paths, then the modulation should vanish when individual paths are blocked. Figure 2.18 (b)-(d) show the results of several blocked-paths experiments, which are compared with the case where all paths are open in (a). Using the phase-locked fitting procedure described above, we estimate average visibilities of $(63.6 \pm 7.5)\,\%$, $(33.1 \pm 15.1)\,\%$, $(10.0 \pm 13.9)\,\%$ and $(24.1 \pm 16.6)\,\%$ for (a)-(d), respectively. Note that the visibilities for (b)-(d) are only so high because the large error bars admit a reasonable sinusoidal fit to the first data set. Crucially, however, a phase-locked fit to the complementary data set fails. For example, in (c) we obtain a reasonable fit to BBB data but not AAA data. If instead we first perform a sinusoidal fit to AAA data and then a phase-locked fit to BBB data, we obtain nearly zero visibility for the AAA data. In contrast, the order, in which the fits are performed in (a), only change the visibilities for both AAA and BBB by $\sim$1 %. Note that for blocked-path measurements, the count rates are much lower (measurement time is 6 hours), only eight phase settings were used and the three-photon interference visibility is reduced. The reason is that those measurements were carried out in the beginning where we used SNSPDs with lower efficiencies and higher dark counts.

Further evidence that three-photon interference is not due to lower-order interference is found in the spectra of photons produced in CSPDC. As shown in Figure 2.19 and 2.20, the approximate coherence lengths $l_c = c/(\pi\Delta\nu)$ for near-infrared and infrared photons are $\approx 260\,\mu$m and $\approx 15\,\mu$m, respectively, and thus much shorter than the interferometer path difference of ≈ 1.11 m. The slight spectral asymmetry is mainly due to the SPDC process

itself and spectral filters before our spectrometer. The results are not affected, however, as fringe visibilities are mainly determined by photon bandwidths.

We now show that the photon triplets we produce violate energy-time inequalities (these results have not been reported in [4]). The correlations observed in energy-time entanglement can be interpreted in terms of uncertainties in time and frequency, wherein the three-photon wavepacket is localized both in time and frequency, summarized by a violation of the following set of inequalities [80],

$$\begin{aligned} Q_1 &= (\Delta t_{21} + \Delta t_{31})\Delta\omega_{123} \geq 1 && (2.92)\\ Q_2 &= (\Delta t_{21} + \Delta t_{32})\Delta\omega_{123} \geq 1 && (2.93)\\ Q_3 &= (\Delta t_{32} + \Delta t_{31})\Delta\omega_{123} \geq 1 && (2.94)\\ Q_4 &= (\Delta t_{21} + \Delta t_{31} + \Delta t_{32})\Delta\omega_{123} \geq 2\,, && (2.95) \end{aligned}$$

where $\Delta t_{ij} = \Delta(t_i - t_j)$ and $\Delta\omega_{123} = \Delta(\omega_1 + \omega_2 + \omega_3)$ are uncertainties in arrival time of two photons and sum-frequency of the three-photon wavepacket, respectively. Following the method in [80], time uncertainties are obtained from Gaussian fits to the central peak in the arrival time histogram shown in Figure 2.15 as

$$\begin{aligned} \Delta t_{21} &= (1.07 \pm 0.18)\,\text{ns}\\ \Delta t_{32} &= (1.06 \pm 0.01)\,\text{ns}\\ \Delta t_{31} &= (0.70 \pm 0.07)\,\text{ns}\,. \end{aligned} \qquad (2.96)$$

The interferometer path difference τ upper bounds $\Delta\omega_{123}/2\pi \leq 1/\tau$ if the pump spectrum is single-peaked, which we verify with a spectrum analyzer (2 GHz resolution). From peak separations in the arrival time histogram we calculate $\tau = (3.72 \pm 0.02)\,\text{ns}$. Using $\Delta\omega_{123} = 2\pi/\tau$, we obtain

$$\begin{aligned} Q_1 &= 0.477 \pm 0.055\\ Q_2 &= 0.572 \pm 0.05\\ Q_3 &= 0.474 \pm 0.022\\ Q_4 &= 0.761 \pm 0.055\,, \end{aligned} \qquad (2.97)$$

representing in all cases a clear violation. A stronger violation was reported by Shalm *et al.* [80], but there only time correlations were directly measured and $\Delta\omega_{123}$ had to be approximated from $\Delta\omega_{\text{pump}}/2\pi = (6 \pm 2)\,\text{MHz}$ under the assumption of energy conservation in CSPDC [80]. In our setup, the unbalanced interferometers automatically ensure tight frequency correlations when three-photon interference is observed without two-photon and single-photon interference. By increasing the interferometer path difference τ we can, in principle, approach $\Delta\omega_{123} \approx \Delta\omega_{\text{pump}}$.

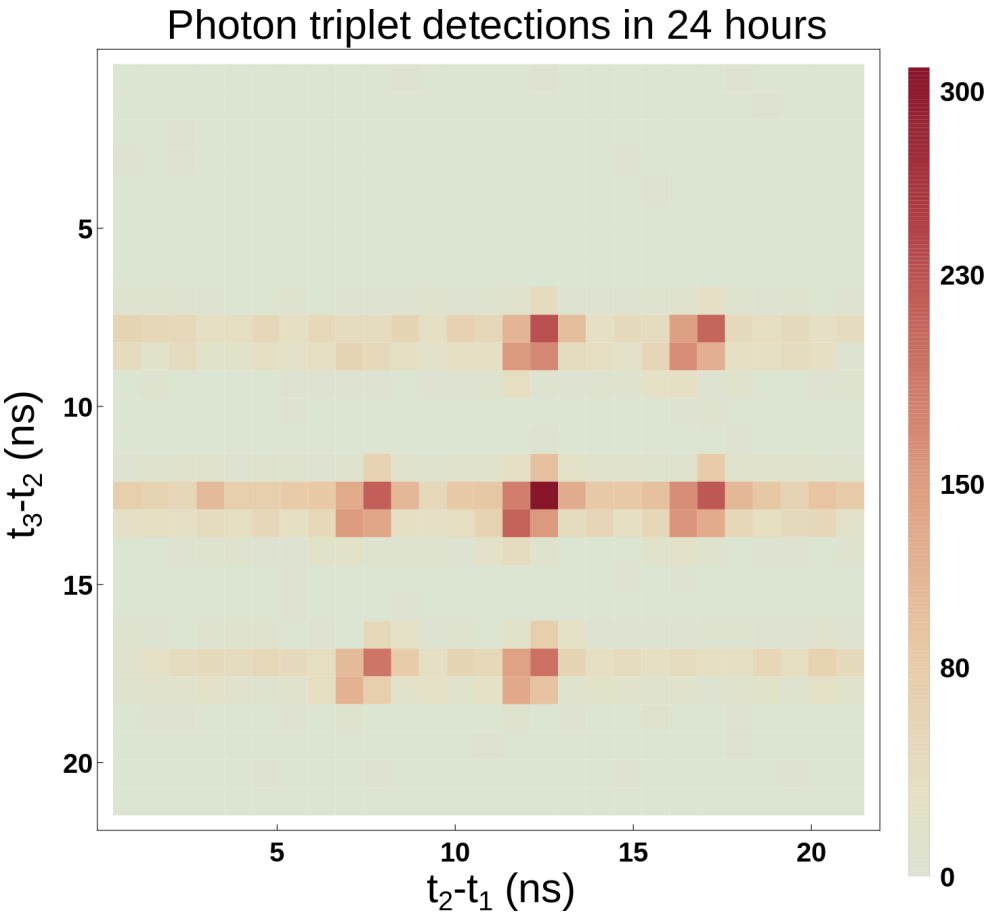

Figure 2.15: **Three-Photon Time-of-Arrival-Histogram.** (from Agne *et al.* [4]) The measured arrival time difference histogram with a bin size of 0.78 ns and peak separation of $\tau = 3.7$ ns displays seven narrow peaks corresponding to the eight possible path combinations $S_1S_2S_3$, $L_1S_2S_3$, $S_1L_2S_3$, $S_1S_2L_3$, $L_1L_2S_3$, $L_1S_2L_3$, $S_1L_2L_3$, and $L_1L_2L_3$. When all three photons take either the short or the long path the relative arrival time is the same, so the $S_1S_2S_3$ and $L_1L_2L_3$ events overlap, forming the central peak. This overlap is a coherent superposition, leading to a three-photon coincidence rate that depends on phases φ_n $(n = 1, 2, 3)$.

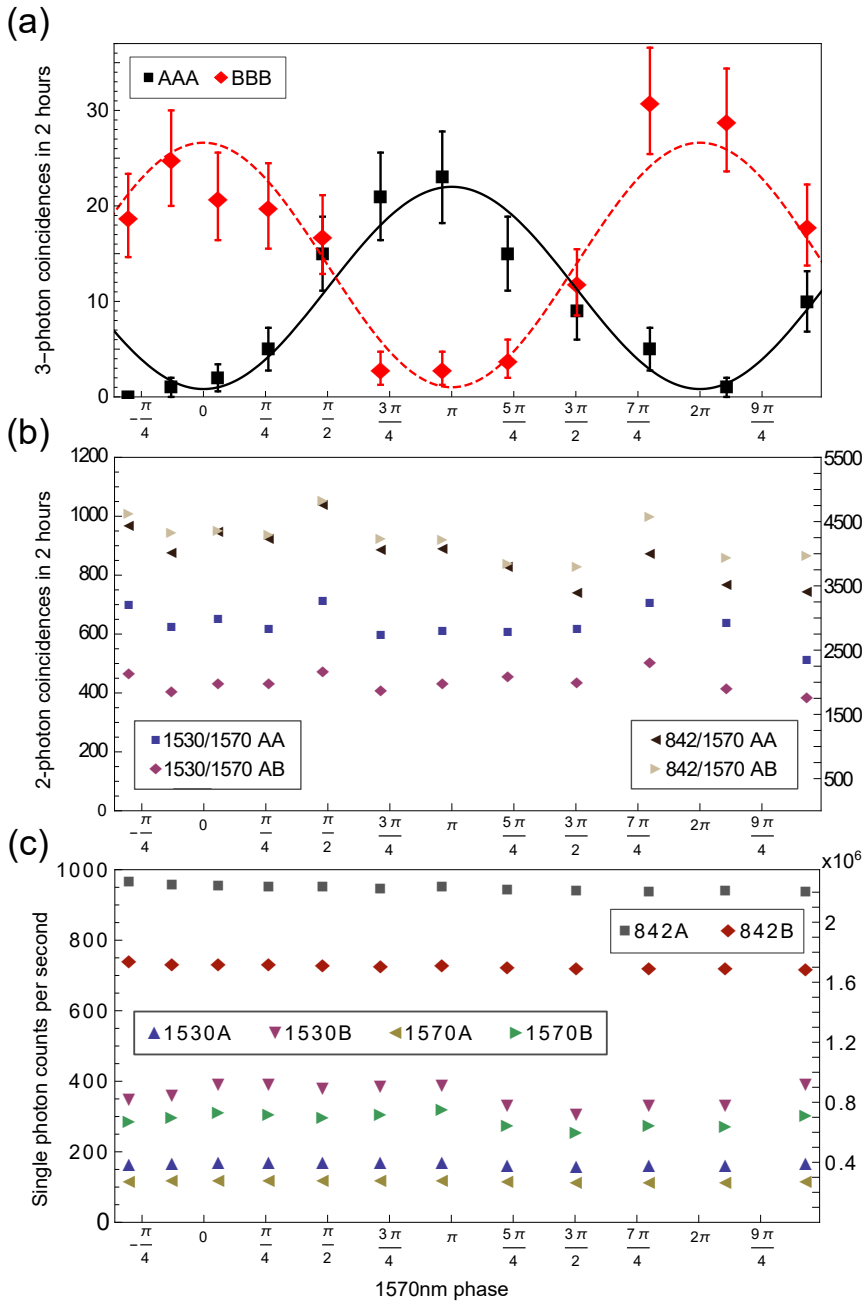

Figure 2.16: **Genuine Three-Photon Interference for 1570 nm Phase Scan.** (from Agne *et al.* [4]) **(a)** Three-photon coincidences show interference with an average visibility of $(92.7 \pm 4.6)\,\%$ without background subtraction (error bars are Poissonian count errors). Plots **(b)** and **(c)** show no systematic modulation of two-photon coincidences and single detection events, respectively. The letters in the legend of the two-fold coincidences indicate the set of detector combinations. For example 1530/1570 AA is is the sum of 1530/1570 coincidences in detector combinations A_2A_3 and B_2B_3. The shown single detection rates for the 1530/1570 nm photons are dominated by dark counts of the SNSPDs, while the 842 nm dark counts (Si-APDs, ∼2400 per second) are negligible.

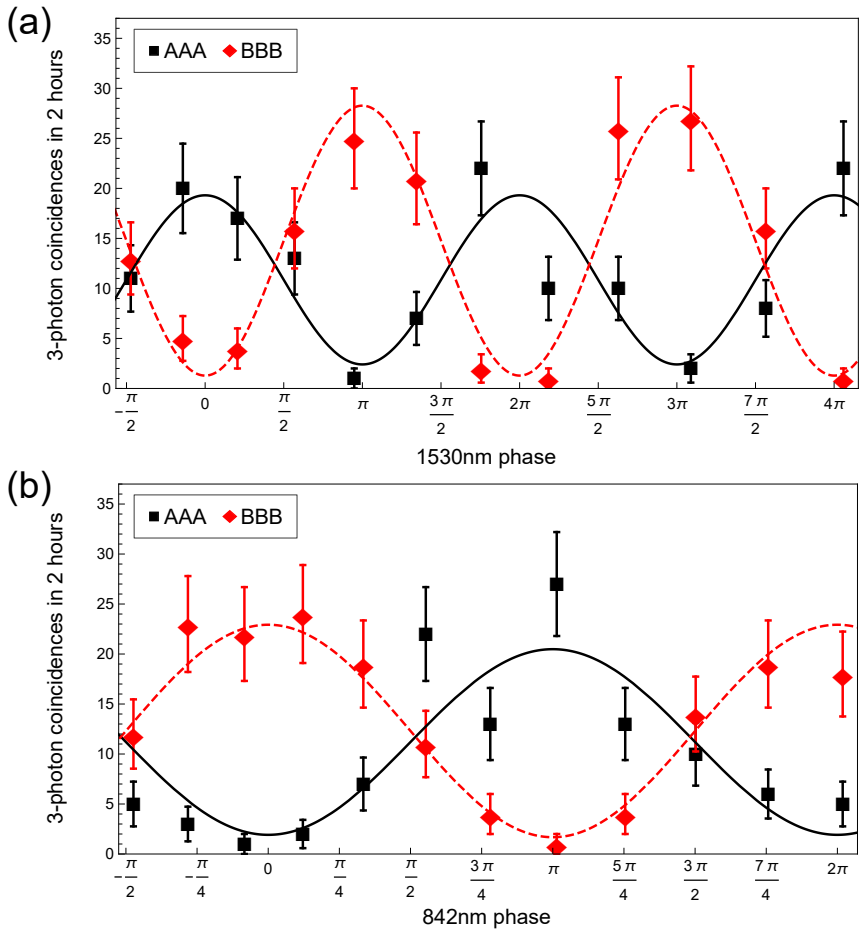

Figure 2.17: **Genuine Three-Photon Interference for 1530 nm and 842 nm Phase Scans.** (from Agne *et al.* [4]) The phase scan for 1530 nm **(a)** and 842 nm **(b)** photons of photon triplets provide further evidence for genuine three-photon interference, yielding average interference visibilities of $(84.6 \pm 6.3)\,\%$ and $(84.6 \pm 4.1)\,\%$, respectively.

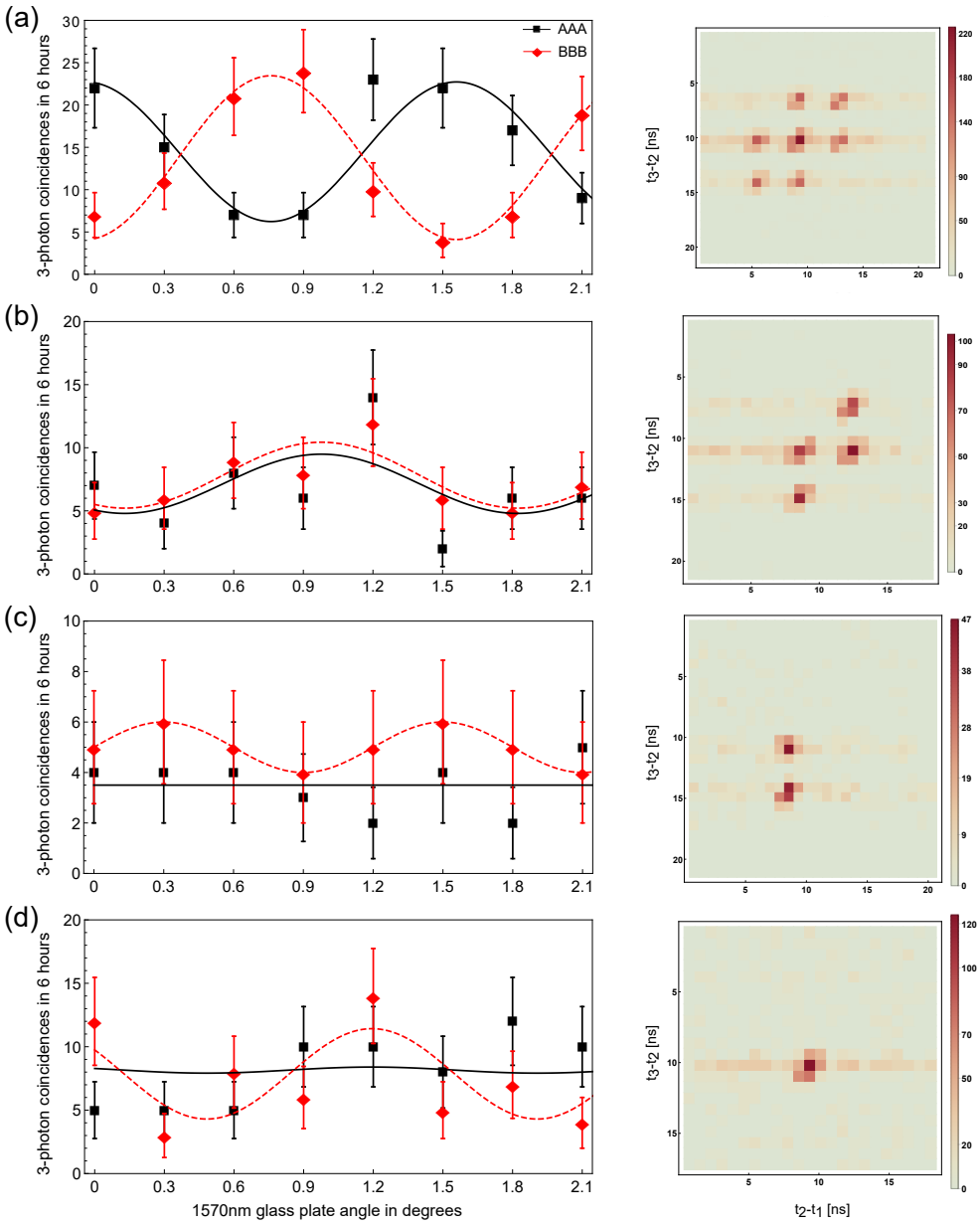

Figure 2.18: **Three-Photon Interference with Blocked Paths.** (from Agne *et al.* [4])These measurements compare cases when all paths are open **(a)**, 842 nm long path is blocked **(b)**, 842 nm and 1530 nm long paths are blocked **(c)** and all short paths are blocked **(d)**, and demonstrate vanishing complementarity. The histograms reflect the restriction to path combinations ($S_1S_2S_3$, $S_1S_2L_3$, $S_1L_2S_3$, $S_1L_2S_3$), ($S_1S_2S_3$, $S_1S_2L_3$) and $L_1L_2L_3$, respectively. See text for a discussion of visibilities.

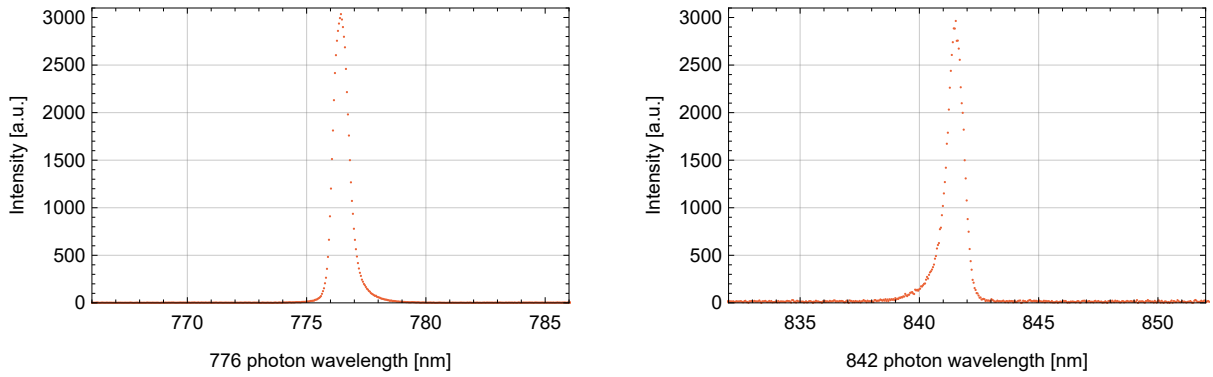

Figure 2.19: **Spectra of Near-Infrared Photons from our CSPDC Source.** (from Agne *et al.* [4]) We fit Gaussian functions $I(x) = I_0 \exp(-(\lambda - \lambda_0)/2\sigma^2)$ to peaks and calculate the full width at half maximum FWHM$= 2\sqrt{2\ln(2)}\sigma$: $\mathrm{FWHM}_{776} = 0.75\,\mathrm{nm}$ and $\mathrm{FWHM}_{842} = 0.86\,\mathrm{nm}$. The center wavelengths are $\lambda_{0,776} = 776.45\,\mathrm{nm}$ and $\lambda_{0,842} = 841.50\,\mathrm{nm}$. The finite width introduces a phase error $\Delta\varphi = \Delta\lambda/\lambda \approx 0.1\,\%$.

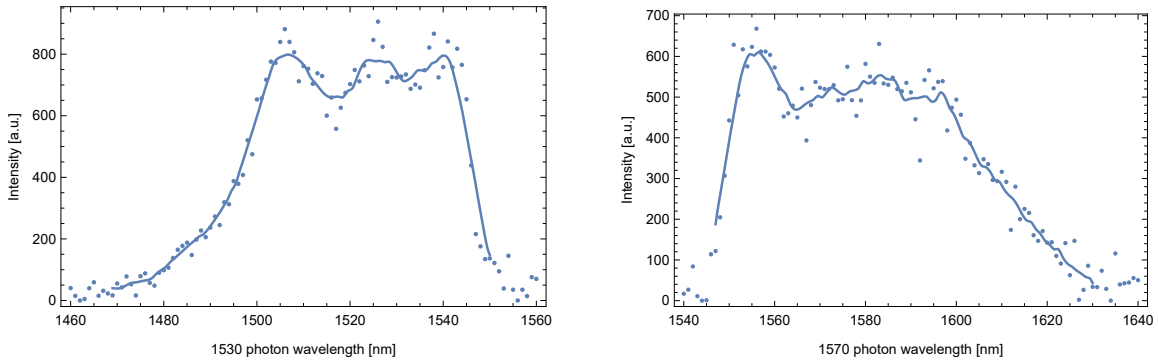

Figure 2.20: **Spectra of Infrared Photons from our CSPDC Source.** (from Agne *et al.* [4]) We measured these by pumping the PPLN waveguide with 776 nm light from a mode-locked Ti:sapphire laser (Coherent MIRA 900) whose spectrum approximates that of the 776 nm photons from the PPKTP, and scanning a diffractive spectrometer coupled to a single-photon detector. Here the pump bandwidth is of the same order as the acceptance band of our PPLN waveguides, leading to non-Gaussian output spectra by summing over many down-conversion spectral modes. We estimate the spectral width by the full width at half maximum (FWHM) of a moving average fit (solid line). We obtain $\mathrm{FWHM}_{1530} = (51 \pm 1)\,\mathrm{nm}$ and $\mathrm{FWHM}_{1570} = (60 \pm 1)\,\mathrm{nm}$, respectively. The finite width introduces phase errors $\Delta\varphi = \Delta\lambda/\lambda$, which is about 3% for both photons.

2.13 Conclusion and Outlook

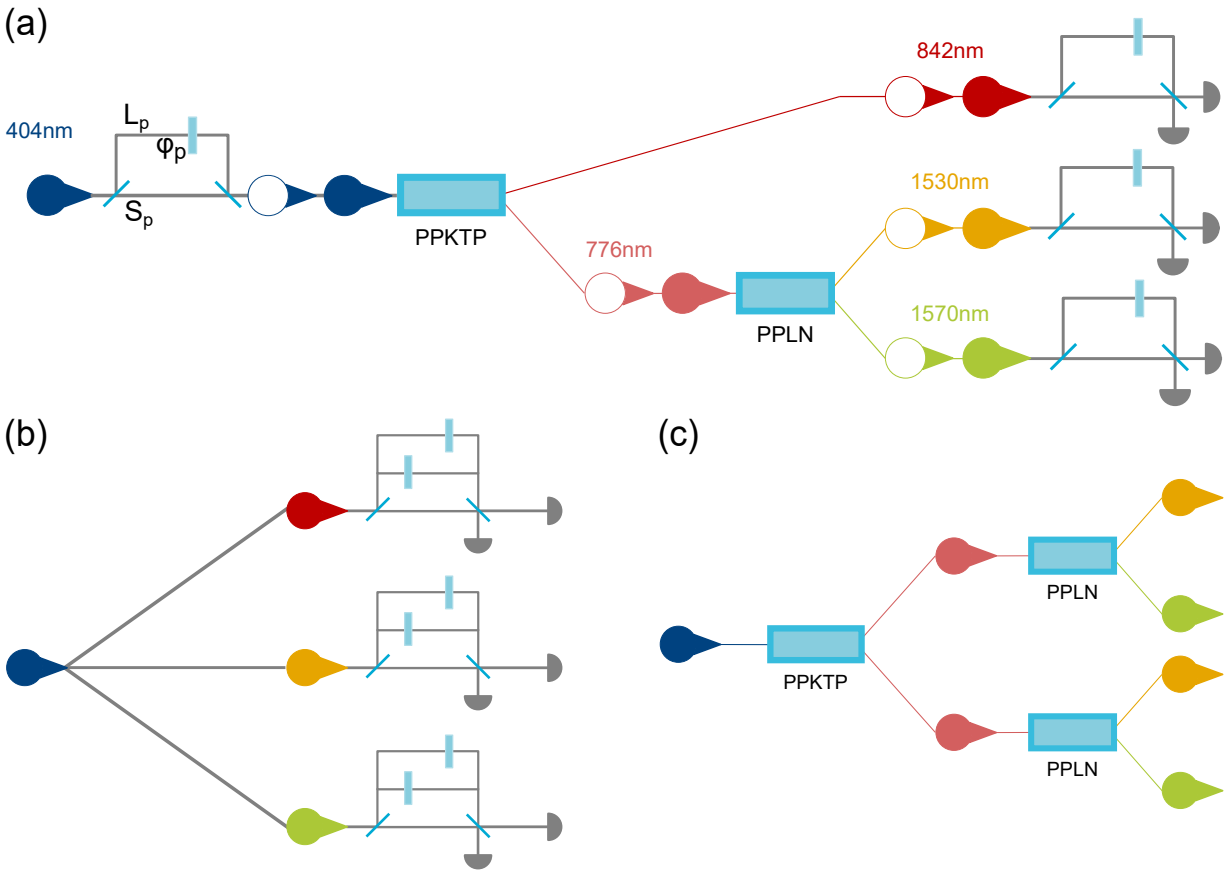

Figure 2.21: **Future Directions for Photon Triplets.** **(a)** Using a pulsed laser one can pump CSPDC in two discrete time-slots using an unbalanced interferometer (with the continuous-wave lasers we currently use, the full continuum over the long coherence length of the laser defines possible triplet generation times). The three-photon analyzer need not change. **(b)** One can increase the dimension of the system by providing more alternative paths through the interferometer. **(c)** With the current triplet rate and the prospect of a more efficient PPKTP, the direct generation of four entangled photons seems feasible.

We have experimentally demonstrated that genuine three-photon interference is accessible with energy-time entangled photon triplets. Such states, and new quantum interference phenomena they exhibit, suggest several interesting directions for future research. Using a pulsed pump, our experimental apparatus should be able to generate and analyze three-photon time-bin states [84], Figure 2.21 (a), for direct implementations of quantum communication protocols [86]. Our setup could be converted to perform NOON-style interferometry with applications in phase superresolution and supersensitivity [22]. Further-

more, this system could be used for fundamental questions of non-locality [87] in tests of both Mermin [88] and Svetlichny inequalities [89], more detailed study on the three-photon joint-spectral function [80], and enable the realization and study of genuine tripartite hyperentanglement [90] and entanglement in higher dimensions, Figure 2.21 (b). Another step upward in higher-order interference phenomena would be possible with a source that directly produces four entangled photons [91], Figure 2.21 (c).

Chapter 3

On the Origin of Interference Terms

3.1 Notes

The results have not been published yet but were partially presented at a conference and a summer school,

- Sascha Agne, "Mathematical Structure of a Three-Slit Experiment", *Quantum Communication, Measurement and Computing* (QCMC) 2014, Hefei, Anhui, China, Poster Presentation A24
- Sascha Agne, "Origin of Interference Terms", *Canadian Summer School on Quantum Information* (CSSQI) 2015, Toronto, Ontario, Canada, Poster Presentation.

3.2 Introduction

In 2010, Sinha *et al.* experimentally realized the three-slit experiment [92], which generalizes Young's double slit experiment that has been so crucial in establishing the wave nature of light. Living up to the the legacy of Young's experiment, Sinha *et al.* interrogated Born's rule. Ranking among the essential ideas of elementary quantum mechanics, Born's rule states, in simplest terms, the following. If $\Psi(x)$ is the wavefunction (in position representation) of a particle, then the probability that a particle is found at x is $P(x) = |\Psi(x)|^2$. Nothing exciting thus far. However, particles share with humans an insatiable desire for *alternatives*, and, if the set is big enough, they display extraordinary *interference* phenomena. Though progressively more important in modern quantum mechanics (think of

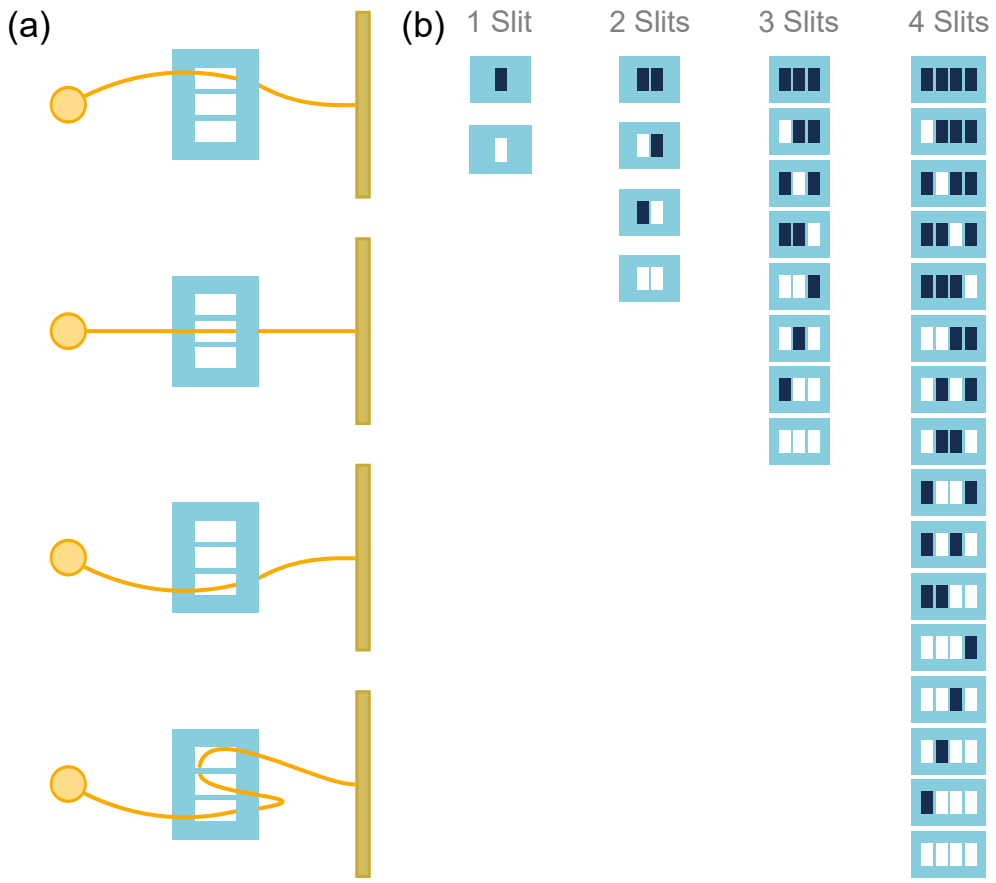

Figure 3.1: **Slit Interference Experiments and Measurement Settings.** **(a)** Illustration of possible *alternative* paths through a three-slit mask. The "straight" paths through just one slit are obvious. The looped path is rather exotic and definitely non-classical, but considering "alternatives" or "paths" abstractly, one can find it. The important observation is that one has to take into account all possibilities. **(b)** Defining paths with a slit mask, there are 2^N measurements, or measurement settings, for a slit interference experiment. The combinatorial aspects to count these alternatives is further enriched with an algebraic structure that can handle the notion of indistinguishability or symmetry, namely group theory.

computational paths in quantum information), only rarely can we agree on what we actually mean with "alternatives". The N-slit experiment is one of those few systems where we can easily abstract from the concrete setup and think of the N slits *defining* N paths from a source to a detector, as illustrated in Figure 3.1 (a). In other words, we say each path can be excited by a particle and so each path defines a possible state and together

they span an N-dimensional Hilbert space, embodied by the completeness relation

$$\mathbb{1} = \sum_{k=1}^{N} |k\rangle\langle k| \,. \tag{3.1}$$

Following Duarte [93], for a particle traveling from source s to a detector x, we assign the probability amplitude

$$\langle x|s\rangle = \langle x|\mathbb{1}|s\rangle = \sum_{k=1}^{N} \langle x|k\rangle\langle k|s\rangle \,. \tag{3.2}$$

This mathematical decomposition follows Feynman's physical insight that in order to travel from source to detector, the particle travels from source to slit k with amplitude

$$\langle k|s\rangle = \Psi(x_{k,s}) \exp(-i\Theta_k) \,, \tag{3.3}$$

and then from slit k to detector x with amplitude

$$\langle x|k\rangle = \Psi(x_{x,k}) \exp(-i\phi_k) \,. \tag{3.4}$$

The wave functions Ψ can describe optical fields, in which case the phases Θ and ϕ are optical phases, but we don't need this specificity here and simply treat the amplitudes as complex scalar products. Note that, as long as we have no means to distinguish between the N alternatives, we have to sum over all possibilities. To come back to Born's rule, and the notation used in Sinha *et al.*'s paper, we write (3.2) as

$$\Psi(x) = \sum_{k=1}^{N} \Psi_k(x) \,, \tag{3.5}$$

with $\Psi(x) \equiv \langle x|s\rangle$, and $\Psi_k(x) \equiv \Psi(x_{k,s})\Psi(x_{x,k}) \exp\big(-i[\phi_k + \Theta_k]\big)$. The detection probability then is

$$\begin{aligned} P(x) &= \Big(\Psi_1(x)\Psi_2(x)\cdots\Psi_N(x)\Big)\Big(\Psi_1^*(x)\Psi_2^*(x)\cdots\Psi_N^*(x)\Big) \\ &= \sum_{k=1}^{N} |\Psi_k(x)|^2 + \sum_{k=1,l\neq k}^{N} \Psi_k(x)\Psi_l^*(x) \,, \end{aligned} \tag{3.6}$$

from which we may infer that only quadratic terms contribute to the probability. This is a direct consequence of *squaring* the wave function and what seems suggested here is that only *pair-wise* "interactions" ever contribute to the probability but not *higher-order* terms such as $\Psi_k\Psi_l\Psi_m$. For instance, for two slits we get

$$\begin{aligned} P_{12}(x) &= |\Psi_1(x)|^2 + |\Psi_2(x)|^2 + 2\mathfrak{Re}\Big\{\Psi_1(x)\Psi_2^*(x)\Big\} \\ &= P_1(x) + P_2(x) + \mathcal{I}_{12} \,, \end{aligned} \tag{3.7}$$

and for three slits

$$\begin{aligned} P_{123}(x) &= |\Psi_1(x)|^2 + |\Psi_2(x)|^2 + |\Psi_3(x)|^2 \\ &\quad + 2\mathfrak{Re}\Big\{\Psi_1(x)\Psi_2^*(x)\Big\} + 2\mathfrak{Re}\Big\{\Psi_1(x)\Psi_3^*(x)\Big\} + 2\mathfrak{Re}\Big\{\Psi_2(x)\Psi_3^*(x)\Big\} \\ &= P_1(x) + P_2(x) + P_3(x) + \mathcal{I}_{12} + \mathcal{I}_{13} + \mathcal{I}_{23}\,, \end{aligned} \tag{3.8}$$

which we can express in a different way using (3.7) as

$$P_{123}(x) = P_{12}(x) + P_{13}(x) + P_{23}(x) - P_1(x) - P_2(x) - P_3(x)\,. \tag{3.9}$$

This equation says there is no third-order interference term $\mathcal{I}_{123}$ and consequently, the three-slit interference pattern is explained entirely by diffraction at the three single slits and the three implicit double-slit interference patterns. This is in fact the conclusion of Sinha *et al.*: "we are able to bound the magnitude of the third-order interference term to less than 10^{-2} of the regular expected second-order interference, at several detector positions". In a surprising turn of events, Sawant *et al.* actually found a three-slit interference term [94], which, moreover, does not violate Born's rule, i.e. is not of the form $\Psi_k\Psi_l\Psi_m$ indicated above. The problem is that we failed to specify the complete set of alternative paths in the beginning, i.e. we said that there are N paths from source to detector because there are N slits that define them. This intuition finds its mathematical expression in the completeness relation (3.1). But did we really capture the whole set of alternative paths? The answer is a resounding "no" and even in hindsight, the curvy path shown in Figure 3.1 (a) is not obvious from a physical point of view. And we are quite right, for the amplitude associated with this path is very small indeed ($\sim 10^{-6}$) and explains why we were not able to detect its presence so far. Theoretically, however, an abstract point of view we promulgated when writing down (3.1) and (3.2), it must be clear that such a path does add another dimension to our Hilbert space simply because it is a possible alternative path (again, theoretically; the physical relevance is a completely different matter), which highlights yet again how difficult it is to actually construct a complete set of alternatives —hence our difficulty in fully classifying interference phenomena (which also means more surprises lie still ahead of us). Thus, just to add this one path to our Hilbert space, we would write, for three slits,

$$\begin{aligned} \mathbb{1} &= \sum_{k=1}^{3+m} |k\rangle\langle k| \\ &= \underbrace{|1\rangle\langle 1| + |2\rangle\langle 2| + |3\rangle\langle 3|}_{\text{direct paths}} + \underbrace{\sum_{k=4}^{m} |k\rangle\langle k|}_{\text{looped path}}\,, \end{aligned} \tag{3.10}$$

where the last sum is over of non-classical paths we take into consideration. The theoretical derivation leading to (3.10) will not be discussed here but the crux of the matter is that the superposition of wave functions for the three slit setup does not consists of three terms, but of more terms. Taking into account only the lower-order looped paths, we find [95]

$$\begin{aligned}\Psi(x) &= \Psi_1(x) + \Psi_2(x) + \Psi_2(x) + \Psi_{NC}(x) \\ &= \Psi_1(x) + \Psi_2(x) + \Psi_3(x) \\ &+ \Psi_{12}(x) + \Psi_{21}(x) + \Psi_{13}(x) + \Psi_{31}(x) + \Psi_{23}(x) + \Psi_{32}(x)\,.\end{aligned} \tag{3.11}$$

Taking the absolute-square of this wave function to calculate, following Born's rule, the probability for a detection at position x on the screen, we obtain terms in addition to those in (3.8), namely

$$\mathcal{I}_{123} \approx 2\mathfrak{Re}\Big\{\Psi_1^*\big(\Psi_{23}+\Psi_{32}\big) + \Psi_2^*\big(\Psi_{13}+\Psi_{31}\big) + \Psi_3^*\big(\Psi_{12}+\Psi_{21}\big)\Big\}\,, \tag{3.12}$$

which we may justly call *genuine* three-slit interference terms. As the theory of the triple slit experiment was refined, Kauten *et al.* pushed the experimental accuracy further and now bound genuine three-slit interference terms to 3×10^{-5} [96], thus approaching the regime where terms like (3.12) play a role.

3.3 Interference Terms

The subject matter are interference terms, *defined* for two and three slits as

$$\mathcal{I}_{12} \coloneqq P_{12}(x) - P_1(x) - P_2(x)\,, \tag{3.13}$$

and

$$\mathcal{I}_{123} \coloneqq P_{123}(x) - P_{12}(x) - P_{13}(x) - P_{23}(x) + P_1(x) + P_2(x) + P_3(x)\,. \tag{3.14}$$

Later we will see that these linear combinations of probabilities are obtained via natural transformations on our data from slit experiments. But already, we may ask why *these* linear combinations in particular? Sorkin [97] wrote in 1994: "superimpose the eight patterns, using a plus sign when an odd number (3 or 1) of the slits were open, and a minus sign when an even number (2 or 0) were open". There is a piece missing here, for what *really* determines the plus and minus sign in front of the terms? What is the origin of those term? How elaborate does the theory need to be? Elementary probability theory

provides us with structurally identical terms, namely via the inclusion-exclusion formula [30],

$$P\left(\bigcup_{i=1}^{N} E_i\right) = \sum_i P(E_i) - \sum_{i<j} P(E_i E_j) + \sum_{i<j<k} P(E_i E_j E_k) - \sum_{i<j<k<l} P(E_i E_j E_k E_l) + \cdots + (-1)^{n+1} P(E_1 E_2 \cdots E_N)\,, \tag{3.15}$$

where E_k denotes events to which we attach probabilities $P(E_k)$ and products such as $E_k E_l$ denote intersections. For example, for two events

$$P(E_1 \cup E_2) = P(E_1) + P(E_2) - P(E_1 E_2)\,, \tag{3.16}$$

and for three events

$$P(E_1 \cup E_2 \cup E_3) = P(E_1 E_2 E_3) - P(E_1 E_2) - P(E_1 E_3) - P(E_2 E_3) + P(E_1) + P(E_2) + P(E_3)\,. \tag{3.17}$$

We see that interference terms correspond to the union of events and particular linear combinations are simply a way to break up probabilities—a process which is illustrated in Figure 3.2. We may associate $P(E_k)$ with $P_k(x)$, $P(E_k E_l)$ with $P_{kl}(x)$ and so on, in which case two and three slit interference terms correspond to intersection of two and three slits, respectively. If we then compare (3.16) and (3.17) with (3.13) and (3.14), respectively, we find, however, that we would have to multiply the former by -1 to get the latter. This sign difference is interesting and is something we will encounter later again, namely when we have the results from group and representation theory.

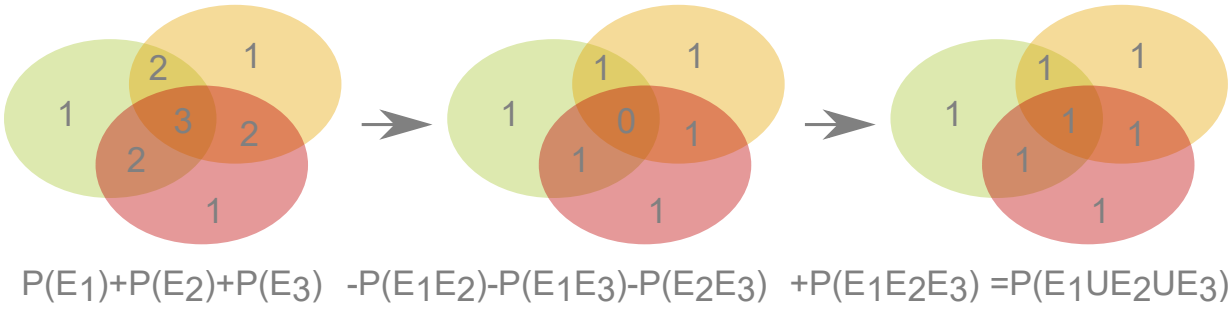

Figure 3.2: **Venn Diagrams for Inclusion-Exclusion Formula.** A two-step process illustrates the structure of the inclusion-exclusion formula in probability theory [98]. Our goal is to calculate the probability for the union of three events. We first add probabilities for all events individually. In doing so we overcount: there are points in sample space that are common to pairs of events (whose probability we count twice) and common to all three events (whose probability we count thrice). This is why we subtract the probabilities corresponding to the pair-wise intersection of events. Because there are three pairs, no contribution to the probability from the intersection of all three is left. Thus, in the last step we have to add it. Now, each portion of the union is counted exactly once.

3.4 The Cyclic Group

What does group theory has to do with slit interference experiments? First of all, it is *the* mathematical structure embodying the concept of symmetry like no other formal system [99]. The idea is actually quite simple. As with any other algebraic structure, a group G is a set together with a composition $\circ$, which fulfills certain axioms. In the case of a group, apart from the obvious closure requirement (composition of two elements in G yields another element in G), the axioms are

1. Associativity: For any $a, b, c \in G$, $a \circ (b \circ c) = (a \circ b) \circ c$.
2. Identity element: There exists an $e \in G$ such that $a \circ e = e \circ a = a$ for all $a \in G$.
3. Inverse: For each $a \in G$ there exists an $a^{-1} \in G$ such that $a \circ a^{-1} = a^{-1} \circ a = e$.

The first axiom ensures that the (binary!) composition of more than two group elements is well-defined, i.e. the result does not depend on the order in which group elements are composed. The second axiom immediately tells us the difference between an ordinary set and a group: while the "smallest" set is the empty set $\emptyset$, a group must contain at least one element, namely the identity e. The third axiom, namely the insistence of inverses, is the heart of the matter. We feel its consequences already when we look at the set of

all matrices $M_n(\mathbb{R})$, which form a vector space. When restricting ourselves to all those matrices that possess an inverse, we obtain the (very important) group $GL_n(\mathbb{R})$. But these elements do *not* form a vector space anymore. The reason is that matrix addition cannot be defined. For example, though

$$\begin{pmatrix} 1 & 0 \\ 0 & 1 \end{pmatrix} \qquad \text{and} \qquad \begin{pmatrix} -1 & 0 \\ 0 & -1 \end{pmatrix} \tag{3.18}$$

both have inverses, their sum, being the zero-matrix, is not invertible. This, in a nutshell, is the definition of a group.

The general group we are interested in here are direct product groups

$$\mathbb{Z}_2^{\otimes N} = \underbrace{\mathbb{Z}_2 \otimes ... \otimes \mathbb{Z}_2}_{N \text{ times}} \tag{3.19}$$

of the cyclic group

$$\mathbb{Z}_2 \coloneqq \left(\{0, 1\}, +_{\text{mod2}} \right), \tag{3.20}$$

where addition modulo 2 is defined as

$$\begin{aligned} 0 +_{\text{mod2}} 0 &= 0 \\ 0 +_{\text{mod2}} 1 &= 1 \\ 1 +_{\text{mod2}} 0 &= 1 \\ 1 +_{\text{mod2}} 1 &= 0\,. \end{aligned} \tag{3.21}$$

Shortly, we will associate these elements with measurement settings and measurement results constitute a function over a group. This means we have to consider all formal sums

$$P_0 \cdot 0 + P_1 \cdot 1\,, \tag{3.22}$$

where $P_0, P_1 \in \mathbb{R}$. These can be regarded as data vectors $(P_0, P_1)^T$ in the associated vector space $\mathbb{R}^2$ with canonical basis $\mathcal{B} = \{e_0, e_1\}$. Cyclic groups are Abelian and therefore all irreducible representations are one-dimensional. What this means in terms of vector spaces is that we can decompose it into two one-dimensional subspaces. The two irreducible representations of $\mathbb{Z}_2$ are $(\mathbb{R}, T)$ and $(\mathbb{R}, S)$, which are called trivial and sign representation, respectively. Without going too much into representation theory, let it suffice to say that representations associate with abstract group elements concrete elements of vector spaces. In our case we consider $\mathbb{R}$ and the homomorphisms are given by

$$\begin{aligned} T &\coloneqq \begin{cases} 0 & \mapsto & 1 \\ 1 & \mapsto & 1 \end{cases} \\ S &\coloneqq \begin{cases} 0 & \mapsto & 1 \\ 1 & \mapsto & -1 \end{cases} . \end{aligned} \tag{3.23}$$

One easily verifies that, indeed, the group structure is preserved (with ordinary multiplication $\cdot$ in $\mathbb{R}$),

$$\begin{aligned} 1 = T(0) = T(0 +_{\text{mod}2} 0) = T(0) \cdot T(0) = 1 \cdot 1 = 1 \\ 1 = T(1) = T(0 +_{\text{mod}2} 1) = T(0) \cdot T(1) = 1 \cdot 1 = 1 \\ 1 = T(1) = T(1 +_{\text{mod}2} 0) = T(1) \cdot T(0) = 1 \cdot 1 = 1 \\ 1 = T(0) = T(1 +_{\text{mod}2} 1) = T(1) \cdot T(1) = 1 \cdot 1 = 1\,, \end{aligned} \tag{3.24}$$

and

$$\begin{aligned} 1 = S(0) = S(0 +_{\text{mod}2} 0) = S(0) \cdot S(0) = 1 \cdot 1 = 1 \\ -1 = S(1) = S(0 +_{\text{mod}2} 1) = S(0) \cdot S(1) = 1 \cdot (-1) = -1 \\ -1 = S(1) = S(1 +_{\text{mod}2} 0) = S(1) \cdot S(0) = (-1) \cdot 1 = -1 \\ 1 = S(0) = S(1 +_{\text{mod}2} 1) = S(1) \cdot S(1) = (-1) \cdot (-1) = 1\,. \end{aligned} \tag{3.25}$$

Irreducible representations can be identified with group-invariant subspaces of our (data) vector space. The projection of $(P_0, P_1)^T$ onto these subspaces is realized by the generalized Fourier transform $\mathcal{F}$ at T and S, which is to say

$$\begin{pmatrix} \mathcal{F}(T) \\ \mathcal{F}(S) \end{pmatrix} = \begin{pmatrix} 1 & 1 \\ 1 & -1 \end{pmatrix} \begin{pmatrix} P_0 \\ P_1 \end{pmatrix} = \begin{pmatrix} P_0 + P_1 \\ P_0 - P_1 \end{pmatrix}. \tag{3.26}$$

One may also recognize this as a Hadamard matrix (also compare the entries with (3.23)). The interpretation of these data transforms are simple: we obtain information about the average and difference of the observation.

3.5 Cyclic Groups and Measurement Settings

We will now connect the abstract group concept with interference experiments. The probabilities appearing on the right-hand side of (3.13) and (3.14) are measured using certain *measurement settings*, which are composed of open and closed slit combinations and which I denote by □ and ■, respectively. The possible combinations are shown in Figure 3.1 (b). Thus, we make the following association for two-slit experiments

$$\begin{aligned} &\blacksquare\blacksquare \to P_{00} \\ &\square\blacksquare \to P_1 \\ &\blacksquare\square \to P_2 \\ &\square\square \to P_{12} \end{aligned}\,, \tag{3.27}$$

and likewise for three-slit experiments,

$$\begin{aligned}
\blacksquare\blacksquare\blacksquare &\to P_{000} \\
\square\blacksquare\blacksquare &\to P_1 \\
\blacksquare\square\blacksquare &\to P_2 \\
\blacksquare\blacksquare\square &\to P_3 \\
\square\square\blacksquare &\to P_{12} \\
\square\blacksquare\square &\to P_{13} \\
\blacksquare\square\square &\to P_{23} \\
\square\square\square &\to P_{123}
\end{aligned} \quad . \tag{3.28}$$

Note that in both cases, one more measurement is included, namely the case when all slits are closed. The corresponding probabilities P_{00} and P_{000} are usually not found in theoretical expressions like (3.13) and (3.14), though in experiments we always perform a "background measurement", to which the all-slits-closed measurement setting corresponds to (roughly, see discussion later). After all measurements are done, we are left with data vectors

$$D_2 = \begin{pmatrix} P_{00} \equiv P_{\blacksquare\blacksquare} \\ P_1 \equiv P_{\square\blacksquare} \\ P_2 \equiv P_{\blacksquare\square} \\ P_{12} \equiv P_{\square\square} \end{pmatrix} , \tag{3.29}$$

and

$$D_3 = \begin{pmatrix} P_{000} \equiv P_{\blacksquare\blacksquare\blacksquare} \\ P_1 \equiv P_{\square\blacksquare\blacksquare} \\ P_2 \equiv P_{\blacksquare\square\blacksquare} \\ P_3 \equiv P_{\blacksquare\blacksquare\square} \\ P_{12} \equiv P_{\square\square\blacksquare} \\ P_{13} \equiv P_{\square\blacksquare\square} \\ P_{23} \equiv P_{\blacksquare\square\square} \\ P_{123} \equiv P_{\square\square\square} \end{pmatrix} . \tag{3.30}$$

Data analysis now consists of finding *linear combinations* of interest—and interference terms are particular linear combinations. But what makes them special? To answer this question, we now associate measurement settings with group elements, namely a closed slit with 0 and an open slit with 1. The group thus defined is, by construction, isomorphic to the cyclic group,

$$\mathbb{M}_1 = \Big(\{\blacksquare, \square\}, \bowtie \Big) \cong \Big(\{0,1\}, +_{\text{mod}2} \Big) = \mathbb{Z}_2 \,, \tag{3.31}$$

where $\bowtie$ is the formal equivalent of $+_{\text{mod}2}$. Then the possible data transformation is given by Eq. (3.26) from which we can calculate, for example, a visibility

$$\mathcal{V} = \frac{\mathcal{F}_1(S)}{\mathcal{F}_1(T)} = \frac{P_{\blacksquare} - P_{\square}}{P_{\blacksquare} + P_{\square}} \,. \tag{3.32}$$

3.6 Interference Terms from Representation Theory

We now have the basics to proceed to the more interesting cases of $N = 2$ and more slits. With two-slits we can use four measurement settings

$$M_2 = \big\{ \blacksquare\blacksquare, \square\blacksquare, \blacksquare\square, \square\square \big\} \,, \tag{3.33}$$

for which it will be recognized that

$$\mathbb{M}_2 = \mathbb{M}_1 \otimes \mathbb{M}_1 \cong \mathbb{Z}_2 \otimes \mathbb{Z}_2 \,. \tag{3.34}$$

This group, being Abelian, has four one-dimensional irreducible representations $(\mathbb{R}, \sigma_1)$, $(\mathbb{R}, \sigma_2)$, $(\mathbb{R}, \sigma_3)$, and $(\mathbb{R}, \sigma_4)$. From the direct product structure, the homomorphisms are easily determined,

$$\begin{aligned}
\sigma_1 &\coloneqq T_1 \times T_2 \quad \text{(average over both slits)} \\
\sigma_2 &\coloneqq S_1 \times T_2 \quad \text{(average over second slit)} \\
\sigma_3 &\coloneqq T_1 \times S_2 \quad \text{(average over first slit)} \\
\sigma_4 &\coloneqq S_1 \times S_2 \quad \text{(average over no slit)} \,.
\end{aligned} \tag{3.35}$$

In words, these are products of the single slit irreducible representation. For instance, σ_2 means to apply the sign representation to slit one and the trivial representation to slit two. More concretely, for σ_4 we have

$$\begin{aligned}
\sigma_4\big(\blacksquare\blacksquare\big) &= S_1\big(\blacksquare\big) \cdot S_2\big(\blacksquare\big) = 1 \cdot 1 = 1 \\
\sigma_4\big(\square\blacksquare\big) &= S_1\big(\square\big) \cdot S_2\big(\blacksquare\big) = (-1) \cdot 1 = -1 \\
\sigma_4\big(\blacksquare\square\big) &= S_1\big(\blacksquare\big) \cdot S_2\big(\square\big) = 1 \cdot (-1) = -1 \\
\sigma_4\big(\square\square\big) &= S_1\big(\square\big) \cdot S_2\big(\square\big) = (-1) \cdot (-1) = 1 \,.
\end{aligned} \tag{3.36}$$

These numbers will be recognized in the last row of the Fourier transform

$$\mathcal{F}_2(\sigma) = \begin{pmatrix} 1 & 1 & 1 & 1 \\ 1 & -1 & 1 & -1 \\ 1 & 1 & -1 & -1 \\ 1 & -1 & -1 & 1 \end{pmatrix} \,. \tag{3.37}$$

Applying this transform to our data vector (3.29), i.e. evaluating the (generalized) Fourier transform at σ_4, yields the standard interference term

$$\mathcal{F}_2(\sigma_4) \quad = \quad P_{\blacksquare\blacksquare} - P_{\square\blacksquare} - P_{\blacksquare\square} + P_{\square\square}\,. \tag{3.38}$$

Or nearly. What is this odd term $P_{\blacksquare\blacksquare}$ doing there? Of course, it corresponds to a background measurement. But then why add instead of subtracting it? The thing is that the theory does not *interpret* ■■ as corresponding to "measurement of unwanted signal" (in fact, the information obtained from this measurement can be quite valuable). What we request from group and representation theory is structural information intrinsic to the measurement! What do I mean with that? Well, we invoke group theory because measurement settings are not picked randomly but for reasons of comparison. We can do this without having any idea about the inner workings of the underlying system, which is why the exact same formalism is applicable remote fields such as agriculture (see later). To make this more precise, what we do when we assign 0 to ■, and 1 to □, is to take the first step towards gaining knowledge about how these two measurement settings influence *something* individually and combined. For that we need to make sense of differences, or inverses, which is the hallmark of the concept of symmetry, or group theory. Representations map the structural difference (the difference between two measurement settings *is* abstract) to 1 and -1, respectively, to make them amenable to ordinary calculation in $\mathbb{R}$. If we were used to calculate and interpret results in $\mathbb{Z}_2$, then we could stay there (it is of course a fun fact that our computers do exactly that so that the translation to and from $\mathbb{R}$ really is only for us humans). To wrap this up, we could replace the measurement setting ■ with ■, i.e. half-transparent slit. The formalism would still be correct, and group theory duly reports average and difference for a single slit, plus non-trivial linear combinations containing interference terms for two and more slits. In this case, we would not interpret ■ as corresponding to a background measurement setting, and we would be glad that our theory does not simply drop the term. For an intuition as to why this term is added instead of subtracted, it helps to look at (3.16) and Figure 3.2 in conjunction with (3.38): the ■■ term compensates for the subtraction of the individual closed slit contributions.

Let us for now continue with the addition of further slits, and hence measurement settings. For the triple slit we have to look at the group

$$\mathbb{M}_3 = \mathbb{M}_1 \otimes \mathbb{M}_1 \otimes \mathbb{M}_1 \cong \mathbb{Z}_2 \otimes \mathbb{Z}_2 \otimes \mathbb{Z}_2\,. \tag{3.39}$$

The measurement settings, homomorphisms of irreducible representations $(\mathbb{R}, \rho_i)$, i =

$1, ..., 8$, and Fourier transform are summarized succinctly by the *character table*,

	■ ■ ■	□ ■ ■	■ □ ■	■ ■ □	□ □ ■	□ ■ □	■ □ □	□ □ □
$\rho_1 \coloneqq T_1 \times T_2 \times T_3$	1	1	1	1	1	1	1	1
$\rho_2 \coloneqq S_1 \times T_2 \times T_3$	1	−1	1	1	−1	−1	1	−1
$\rho_3 \coloneqq T_1 \times S_2 \times T_3$	1	1	−1	1	−1	1	−1	−1
$\rho_4 \coloneqq T_1 \times T_2 \times S_3$	1	1	1	−1	1	−1	−1	−1
$\rho_5 \coloneqq S_1 \times S_2 \times T_3$	1	−1	−1	1	1	−1	−1	1
$\rho_6 \coloneqq S_1 \times T_2 \times S_3$	1	−1	1	−1	−1	1	−1	1
$\rho_7 \coloneqq T_1 \times S_2 \times S_3$	1	1	−1	−1	−1	−1	1	1
$\rho_8 \coloneqq S_1 \times S_2 \times S_3$	1	−1	−1	−1	1	1	1	−1 .

(3.40)

Evaluating the Fourier transform at ρ_8, i.e. applying the matrix in (3.40) to data vector (3.30) gives us the three-slit interference term,

$$\mathcal{F}_3(\rho_8) = P_{\blacksquare\blacksquare\blacksquare} - P_{\square\blacksquare\blacksquare} - P_{\blacksquare\square\blacksquare} - P_{\blacksquare\blacksquare\square} + P_{\square\square\blacksquare} + P_{\square\blacksquare\square} + P_{\blacksquare\square\square} - P_{\square\square\square}\,, \tag{3.41}$$

which is in fact -1 times the standard expression (3.14).

The general idea may now become apparent. The N-slit interference experiment is described by the group

$$\mathbb{Z}_2^{\otimes N} = \underbrace{\mathbb{Z}_2 \otimes \cdots \otimes \mathbb{Z}_2}_{N \text{ times}}\,, \tag{3.42}$$

and its direct product representations. The irreducible representation we are particularly interested in is what we now call *interference representation*, namely

$$S_{\text{int}}^N \coloneqq S_1 \times \cdots \times S_N\,, \tag{3.43}$$

which gives rise to the N^{th} order interference term $\mathcal{F}_N\left(S_{\text{int}}^N\right)$. We benefit greatly from the fact that representation theory of finite Abelian groups is well-understood, and character tables such as (3.40) are, more or less, readily available or easily constructible. Thus, one easily computes the four-slit interference term as

$$\begin{aligned}\mathcal{F}_4(S_{\text{int}}^4) = {} & P_{\blacksquare\blacksquare\blacksquare\blacksquare} - P_{\square\blacksquare\blacksquare\blacksquare} - P_{\blacksquare\square\blacksquare\blacksquare} - P_{\blacksquare\blacksquare\square\blacksquare} - P_{\blacksquare\blacksquare\blacksquare\square} + P_{\square\square\blacksquare\blacksquare} + P_{\square\blacksquare\square\blacksquare} + P_{\square\blacksquare\blacksquare\square} \\ & + P_{\blacksquare\square\square\blacksquare} + P_{\blacksquare\square\blacksquare\square} + P_{\blacksquare\blacksquare\square\square} - P_{\square\square\square\blacksquare} - P_{\square\square\blacksquare\square} - P_{\square\blacksquare\square\square} - P_{\blacksquare\square\square\square} + P_{\square\square\square\square}\,.\end{aligned} \tag{3.44}$$

The theory gives us even more than that, because the Fourier transform can be evaluated at N irreducible representations (the transformed data vector has N entries). What are those N quantities? To answer this question, let us finish the analysis of the triple slit experiment. First of all we have

$$\mathcal{F}_3(\rho_1) = P_{\blacksquare\blacksquare\blacksquare} + P_{\square\blacksquare\blacksquare} + P_{\blacksquare\square\blacksquare} + P_{\blacksquare\blacksquare\square} + P_{\square\square\blacksquare} + P_{\square\blacksquare\square} + P_{\blacksquare\square\square} + P_{\square\square\square}\,, \tag{3.45}$$

which gives is the total sum or average. This term is trivial and present for any N. Next, we extract information about the single-slit contributions, for which we average out slit 2 and 3,

$$\begin{aligned}\mathcal{F}_3(\rho_2) &= P_{\blacksquare\blacksquare\blacksquare} - P_{\square\blacksquare\blacksquare} + P_{\blacksquare\square\blacksquare} + P_{\blacksquare\blacksquare\square} - P_{\square\square\blacksquare} - P_{\square\blacksquare\square} + P_{\blacksquare\square\square} - P_{\square\square\square} \\ &= \underbrace{\left(P_{\blacksquare\blacksquare\blacksquare} + P_{\blacksquare\square\blacksquare} + P_{\blacksquare\blacksquare\square} + P_{\blacksquare\square\square}\right)}_{\text{First slit closed}} - \underbrace{\left(P_{\square\blacksquare\blacksquare} + P_{\square\square\blacksquare} + P_{\square\blacksquare\square} + P_{\square\square\square}\right)}_{\text{First slit open}}\,,\end{aligned} \tag{3.46}$$

or slit 1 and 3,

$$\begin{aligned}\mathcal{F}_3(\rho_3) &= P_{\blacksquare\blacksquare\blacksquare} + P_{\square\blacksquare\blacksquare} - P_{\blacksquare\square\blacksquare} + P_{\blacksquare\blacksquare\square} - P_{\square\square\blacksquare} + P_{\square\blacksquare\square} - P_{\blacksquare\square\square} - P_{\square\square\square} \\ &= \underbrace{\left(P_{\square\blacksquare\blacksquare} + P_{\blacksquare\blacksquare\blacksquare} + P_{\blacksquare\blacksquare\square} + P_{\square\blacksquare\square}\right)}_{\text{Second slit closed}} - \underbrace{\left(P_{\blacksquare\square\blacksquare} + P_{\square\square\blacksquare} + P_{\blacksquare\square\square} + P_{\square\square\square}\right)}_{\text{Second slit open}}\,,\end{aligned} \tag{3.47}$$

or slit 1 and 2,

$$\begin{aligned}\mathcal{F}_3(\rho_4) &= P_{\blacksquare\blacksquare\blacksquare} + P_{\square\blacksquare\blacksquare} + P_{\blacksquare\square\blacksquare} - P_{\blacksquare\blacksquare\square} + P_{\square\square\blacksquare} - P_{\square\blacksquare\square} - P_{\blacksquare\square\square} - P_{\square\square\square} \\ &= \underbrace{\left(P_{\blacksquare\square\blacksquare} + P_{\square\square\blacksquare}P_{\square\blacksquare\blacksquare} + P_{\blacksquare\blacksquare\blacksquare}\right)}_{\text{Third slit closed}} - \underbrace{\left(P_{\blacksquare\square\square} + P_{\square\square\square} + P_{\blacksquare\blacksquare\square} + P_{\square\blacksquare\square}\right)}_{\text{Third slit open}}\,.\end{aligned} \tag{3.48}$$

More interestingly, we also have the three two-slit interference terms, namely contributions from the double slit formed by slits 1 and 2,

$$\begin{aligned}\mathcal{F}_3(\rho_5) &= P_{\blacksquare\blacksquare\blacksquare} - P_{\square\blacksquare\blacksquare} - P_{\blacksquare\square\blacksquare} + P_{\blacksquare\blacksquare\square} + P_{\square\square\blacksquare} - P_{\square\blacksquare\square} - P_{\blacksquare\square\square} + P_{\square\square\square} \\ &= \underbrace{\left(P_{\blacksquare\blacksquare\blacksquare} + P_{\blacksquare\blacksquare\square}\right)}_{\equiv P_{\blacksquare\blacksquare\times}} - \underbrace{\left(P_{\square\blacksquare\blacksquare} + P_{\square\blacksquare\square}\right)}_{\equiv P_{\square\blacksquare\times}} - \underbrace{\left(P_{\blacksquare\square\blacksquare} + P_{\blacksquare\square\square}\right)}_{\equiv P_{\blacksquare\square\times}} + \underbrace{\left(P_{\square\square\blacksquare} + P_{\square\square\square}\right)}_{\equiv P_{\square\square\times}}\,,\end{aligned} \tag{3.49}$$

the double slit formed by slits 1 and 3,

$$\begin{aligned}\mathcal{F}_3(\rho_6) &= P_{\blacksquare\blacksquare\blacksquare} - P_{\square\blacksquare\blacksquare} + P_{\blacksquare\square\blacksquare} - P_{\blacksquare\blacksquare\square} - P_{\square\square\blacksquare} + P_{\square\blacksquare\square} - P_{\blacksquare\square\square} + P_{\square\square\square} \\ &= \underbrace{\left(P_{\blacksquare\blacksquare\blacksquare} + P_{\blacksquare\square\blacksquare}\right)}_{\equiv P_{\blacksquare\times\blacksquare}} - \underbrace{\left(P_{\square\blacksquare\blacksquare} + P_{\square\square\blacksquare}\right)}_{\equiv P_{\square\times\blacksquare}} - \underbrace{\left(P_{\blacksquare\blacksquare\square} + P_{\blacksquare\square\square}\right)}_{\equiv P_{\blacksquare\times\square}} + \underbrace{\left(P_{\square\blacksquare\square} + P_{\square\square\square}\right)}_{\equiv P_{\square\times\square}}\,,\end{aligned} \tag{3.50}$$

and lastly, the double slit formed by slits 2 and 3,

$$\begin{aligned}\mathcal{F}_3(\rho_7) &= P_{\blacksquare\blacksquare\blacksquare} + P_{\square\blacksquare\blacksquare} - P_{\blacksquare\square\blacksquare} - P_{\blacksquare\blacksquare\square} - P_{\square\square\blacksquare} - P_{\square\blacksquare\square} + P_{\blacksquare\square\square} + P_{\square\square\square} \\ &= \underbrace{\left(P_{\blacksquare\blacksquare\blacksquare} + P_{\square\blacksquare\blacksquare}\right)}_{\equiv P_{\times\blacksquare\blacksquare}} - \underbrace{\left(P_{\blacksquare\square\blacksquare} + P_{\square\square\blacksquare}\right)}_{\equiv P_{\times\square\blacksquare}} - \underbrace{\left(P_{\blacksquare\blacksquare\square} + P_{\square\blacksquare\square}\right)}_{\equiv P_{\times\blacksquare\square}} + \underbrace{\left(P_{\blacksquare\square\square} + P_{\square\square\square}\right)}_{\equiv P_{\times\square\square}} .\end{aligned} \tag{3.51}$$

Two-slit interference terms (3.38) emerge here through marginal distributions, which reflects the obvious fact that the double-slit is intrinsic to the triple-slit experiment. To conclude the formal part, note how the irreducible representations in (3.40) point out those slits that are compared (sign representation S), and those that are averaged out (trivial representation T).

3.7 Conclusion and Outlook

What we have found is a mathematical structure describing simple slit interference experiments, and we were able to derive all classical interference terms. It is a bit surprising that we did not invoke wave theory, quantum mechanics or probability theory at all. Though at some points I used the language of these theories to illustrate or interpret certain aspects, the derivation itself is free of any such baggage. The success relies critically on abstracting everything except for measurement settings. We are left with the simplest of all analytical tools, namely plain old data comparison. For that we need a notion of differences or inverses, and the simplest algebraic structure imbibed with this concept is the group. Representation theory then was necessary to translate relationships between the measurement settings into real space (because that's where our data lives). The Fourier transform then decomposes the data into its natural constituents, and in our case gives us interference terms.

I would like to conclude this investigation with an example taken from agriculture. Statisticians there perform experiments operationally similar to slit experiments, which are called factorial design experiments. These kinds of statistical experiments were introduced by Yates and Hotelling [100, 101] into agriculture in the years around 1940. Their aim was to increase the yield of crops given certain *factors* that presumably influence the crop yield. Usually, controlled quantities of these factors can be applied, which is why they are also called *treatments*. It is obvious that factors in isolation do not wholly determine the yield. Rather, we need to understand their *interaction*. This is easier said than done, however, as we are dealing with a complex biological process. Yates and Hotelling realized,

however, that we can make *statistical experiments* and to a desired degree of accuracy answer very specific *questions*. Rockmore [102] gives a very illuminating example for this. Suppose we grow wheat and we want to know how a high / low amount of sunlight, weed killer, and fertilizer influence the growth. Hence, we measure the height of plants for each of the eight possible factor combinations, whereby for each treatment we can answer the corresponding question "what is the plant height"? However, looking at the eight measurements together, we may isolate what is known as the *effects*: "what is the effect of sunlight or weed killer or fertilizer alone", "what is the effect of sunlight and weed killer or sunlight and fertilizer or weed killer and fertilizer combined", and finally "what is the effect of all three factors combined"? Intuitively, these are sensible questions to ask since the eight treatments are not picked randomly but a link is imparted: each factor appears in each measurement, either as "low" or "high". Answers therefore only make use of these intrinsic connections, without further assumptions. In complete analogy, in slit experiments we ask, for example, "what is the influence (on the detection probability) of two slits"? The irreducible representations of the underlying symmetry group answer precisely these kinds of questions, whose answers can be read off the Fourier transform, summarized for one, two, and three slits by the following equations.

$$\begin{pmatrix} 1 & 1 \\ 1 & -1 \end{pmatrix} \begin{pmatrix} P_0 \\ P_1 \end{pmatrix} = \begin{pmatrix} \text{Average} \\ \text{Difference} \end{pmatrix} \tag{3.52}$$

$$\begin{pmatrix} 1 & 1 & 1 & 1 \\ 1 & -1 & 1 & -1 \\ 1 & 1 & -1 & -1 \\ 1 & -1 & -1 & 1 \end{pmatrix} \begin{pmatrix} P_{00} \\ P_{10} \\ P_{01} \\ P_{11} \end{pmatrix} = \begin{pmatrix} \text{Average} \\ \text{Slit 1 Amplitude} \\ \text{Slit 2 Amplitude} \\ \text{Slit 3 Amplitude} \\ \text{Slit 12 Interference} \end{pmatrix} \tag{3.53}$$

$$\begin{pmatrix} 1 & 1 & 1 & 1 & 1 & 1 & 1 & 1 \\ 1 & -1 & 1 & 1 & -1 & -1 & 1 & -1 \\ 1 & 1 & -1 & 1 & -1 & 1 & -1 & -1 \\ 1 & 1 & 1 & -1 & 1 & -1 & -1 & -1 \\ 1 & -1 & -1 & 1 & 1 & -1 & -1 & 1 \\ 1 & -1 & 1 & -1 & -1 & 1 & -1 & 1 \\ 1 & 1 & -1 & -1 & -1 & -1 & 1 & 1 \\ 1 & -1 & -1 & -1 & 1 & 1 & 1 & -1 \end{pmatrix} \begin{pmatrix} P_{000} \\ P_{100} \\ P_{010} \\ P_{001} \\ P_{110} \\ P_{101} \\ P_{011} \\ P_{111} \end{pmatrix} = \begin{pmatrix} \text{Average} \\ \text{Slit 1 Amplitude} \\ \text{Slit 2 Amplitude} \\ \text{Slit 3 Amplitude} \\ \text{Slit 12 Interference} \\ \text{Slit 13 Interference} \\ \text{Slit 23 Interference} \\ \text{Slit 123 Interference} \end{pmatrix} \tag{3.54}$$

I believe this rather high-level way of thinking about interference experiments is what will lead us to a full classification of interference phenomena simply because we abstract of

everything except for *alternatives*, distinguishable or not, which are the conceptual basis for (quantum) interference.

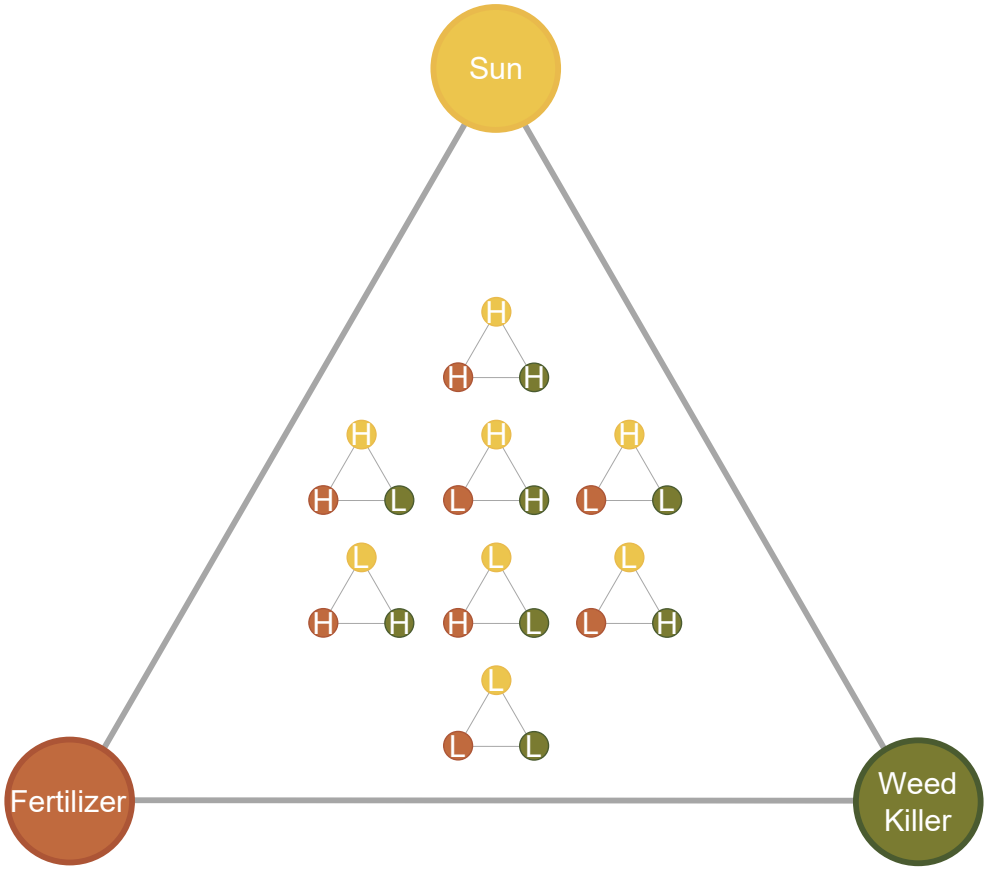

Figure 3.3: **Factorial Design Experiment in Agriculture.** Illustration of the use of group theory in agriculture, which is operationally similar to three-slit interference experiments. We have eight plots (small triangles) where we grow a plant under different, but related conditions (colored balls): there are three factors that influence the growth (sun light, fertilizer, and weed killer) and we chose to apply two dosages, namely high (H) and low (L). Note that we do not need to specify "high" and "low" because the questions the experiment will answer are not sensitive to factor *quantities*. However, the qualitative differences between the eight setups translate into eight quantities based on, say, the measured height of the plant under the eight conditions. The mathematical structure enabling us to achieve this feat is group theory, leading, via representation theory, to Fourier transform of data vectors.

Chapter 4

Hong-Ou-Mandel Interference with Independent Coherent States

4.1 Notes

The authors in a forthcoming publication are: Sascha Agne, Jeongwan Jin, Katanya B. Kuntz, Filippo Miatto, Jean-Philippe Bourgoin, and Thomas Jennewein.

4.2 Hong-Ou-Mandel Effect

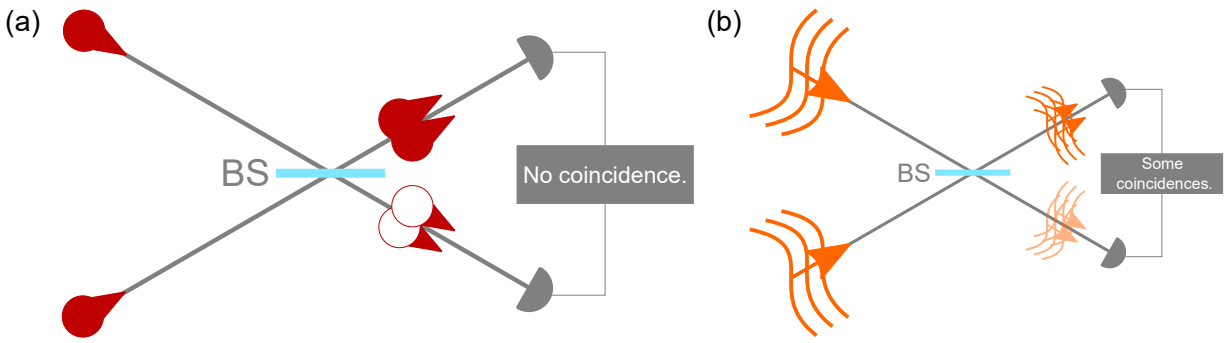

Figure 4.1: **Hong-Ou-Mandel Interference Using Quantum and Classical Light Sources. (a)** The Hong-Ou-Mandel effect with single, identical photons. **(b)** The analogue setup using classical light (continuous-wave lasers in our case). An anticorrelation dip is observed in both experiments and the only difference is that in the former, coincidences can completely vanish.

When two identical photons impinge on a symmetric beam splitter, as illustrated in Figure 4.1 (a), the output state is [103]

$$|\Psi_{34}\rangle = \frac{1}{\sqrt{2}}\Big(|2_3, 0_4\rangle - |0_3, 2_4\rangle\Big)\,, \tag{4.1}$$

and it is not difficult to see that the second-order cross-correlation function

$$G^{(2x)}(t_3, t_4) = \Big\langle \Psi_{34} \Big| \hat{E}_3^-(t_3)\hat{E}_4^-(t_4)\hat{E}_4^+(t_4)\hat{E}_3^+(t_3) \Big| \Psi_{34} \Big\rangle = 0\,, \tag{4.2}$$

which means that no coincidences are measured. Initially thought to be attributable to the bosonic nature of photons ("bunching"), this interpretation has to be taken with a grain of salt, for the same interference phenomena can be observed using photons without temporal overlap at the beam splitter [104], showing that it is really the two-photon amplitudes that interfere, and not the photons themselves. Moreover, HOM interference is not restricted to two Fock states and has been observed with various light sources. For example Rarity *et al.* [105] and Li *et al.* [106] interfered a single photon with a weak coherent pulse and a thermal state, respectively. The motivating question for Hong, Ou and Mandel concerned the simultaneity of photon-pair production in spontaneous parametric downconversion, which they upper-bounded to ∼100 fs. [59]. Despite its simplicity and the fact it was devised for a very concrete measurement, the HOM interferometer, as it became known, proved to be the most important and versatile of all the two-photon interferometers (other examples being Shih-Alley [60] and Franson [61] interferometers), which were devised towards the end of the 1980s. The ideal single-mode consideration in (4.1) and (4.2) cannot account for the shape of the coincidence dip that is observed in a HOM interference experiment, because the underlying assumption, that single photons populate a monochromatic wave, is not physical. Rather, photons are emitted as wavepackets $\zeta_k(t)$, and the second-order cross-correlation function becomes [103]

$$\begin{aligned} G^{(2x)}(t_3, t_4) &= |\zeta_1(t_3)|^2|\zeta_2(t_4)|^2 + |\zeta_2(t_3)|^2|\zeta_1(t_4)|^2 \\ &\quad - \zeta_1^*(t_3)\zeta_2^*(t_4)\zeta_1(t_4)\zeta_2(t_3) - \zeta_2^*(t_3)\zeta_1^*(t_4)\zeta_2(t_4)\zeta_1(t_3) \\ &= \Big|\zeta_1(t_4)\zeta_2(t_3) - \zeta_1(t_3)\zeta_2(t_4)\Big|^2 . \end{aligned} \tag{4.3}$$

For the longest time, $G^{(2)}(t_3, t_4)$ could not be directly measured, as the ∼ns detector time resolution T_R was much larger than the ∼ps width of $G^{(2)}(t_3, t_4)$ for single photons produced via spontaneous parametric downconversion. Instead, one measured the coincidence rate

$$R = \int_{T_R} dt_4 \int_{T_R} dt_3\, G^{(2x)}(t_3, t_4)\,. \tag{4.4}$$

This changed around 2004, when Legero *et al.* [107, 108] had access to a source that produced single photons "slow enough" so that wavepackets had $\sim \mu$s coherence length—much longer than typical single photon detector time resolutions. It was the first time that the HOM dip could be studied in a time-resolved manner and Legero *et al.* were immediately able to observe fringes *within* the HOM dip, which resulted from frequency beating of two photons. But let us not adorn quantum theory with laurels before its due [109]. Sixteen years earlier, Ou *et al.* used a HOM-like setup to extract both beat fringe [110] and HOM dip [111] in the interference of two classical beams. Nowadays, HOM interference of laser beams has entered metrology. For instance, Lebreton *et al.* measured the second-order cross-correlation function of nano-lasers and were able to conclusively tell whether the laser field is chaotic or coherent with amplitude fluctuations [112, 113]. Furthermore, broadband spectra fluctuations can be measured using this technique [114], and has become the basis for few-photon Fourier transform spectroscopy [115, 116]. Practical implementations of quantum communication protocols also found a work-around for Fock state HOM interference by simply replacing single photons with weak coherent pulses (WCP) [71, 117–120]. The use of pulses is trademark for most fourth-order interference experiments with coherent states, though recently continuous-wave (CW) lasers celebrated a revival [121–124], which is a flame we keep alive in this thesis. Before we proceed let me point out that the two light sources in HOM interference experiments need not be identical. In fact, their mutual independence affords a new degree of freedom and, for example, anticorrelations between laser and thermal light has been observed [125]. The first experimental demonstration of two-photon interference from "truly" independent photons came only in 2006 [126].

4.3 Interference of Independent Lasers

Working at optical frequencies, interference of statistically independent light sources rank among the more mysterious electromagnetic phenomena. In the early days of the laser, it was shown that two independently oscillating masers can show interference in time (frequency beating) [127] and space [128, 129]. For their latter experiments, Mandel and co-workers started to employ the "photon-billiard ball" picture, in which it seems strange that two photons (one from each laser) interfere despite the fact that "one photon is absorbed before the next one is emitted by one or the other source" [129]. As most quantum optics text books explain, interference is due to probability amplitudes associated with the photons, which are merely guided through the interference landscape [130]. Classical electromagnetism has in fact no difficulties to account for the effect [131, 132], as interference of independent radiation is, for people working in lower frequency ranges of the

electromagnetic spectrum, a common affair and most likely a nuisance when engineering communication systems. Admittedly, this argument only convinces a pragmatist, but the theoretical reasoning is not far away. For, as a direct consequence of the linearity of Maxwell's equations, interference comes about by superposing two or more fields. Crucially, the superposition principle remains valid at all intensities, even at the single photon level. For sure, there are pure quantum effects predicting *nonlinearities* in *vacuum*, for example light-by-light scattering, which happens when two close-by photons happen to simultaneously convert into an electron-positron pair (obeying the energy-time uncertainty relation, of course) [133]. However, the first experimental evidence for the occurrence of this process has been presented only earlier this year [134] and it seems unlikely that photon nonlinearities explain the interference effect observed by Mandel and co-workers. Hence, let us actually look at how classical optics accounts for the interference of independent lasers. I decided to study frequency beating instead of spatial fringes, as the literature is already skewed towards the latter and temporal interference is more relevant for our experiment.

Classically, if we superpose two monochromatic electric fields, the instantaneous intensity is periodic in the beat frequency $\Delta\omega \coloneqq \omega_2 - \omega_1$,

$$I(t) \propto E^-(t)E^+(t) = I_1 + I_2 + I_1 I_2 \cos\Big(\Delta\omega t + \Delta\Theta(t)\Big)\,. \tag{4.5}$$

However, fluctuations in the relative phase $\Delta\Theta$ may wash out interference when we have to integrate the instantaneous intensity over the resolving time of our detector. Thus, the question is under what conditions do we actually observe beating? First of all, our detection bandwidth needs to be bigger than $\Delta\omega$, which is easily achieved in most cases. More important is the detector time resolution Δt, which determines whether we can actually trace a particular sample of the random process, i.e. follow the instanteneous intensity, or whether we have to consider the ensemble average $\langle I\rangle = \langle I(t)\rangle_{\Delta\Theta}$, which is determined by fluctuations of the cosine term. For independent laser, $\langle\cos(\Delta\Theta)\rangle_{\Delta\Theta} = 0$, and no fringes are observed. The average we perform in an actual experiment is over time,

$$\overline{I}(t,\Delta t) = \frac{1}{\Delta t}\int_{t-\Delta t/2}^{t+\Delta t/2} dt\, I(t)\,, \tag{4.6}$$

and the limit $\lim_{\Delta t\to\infty}\overline{I} = \langle I\rangle$ for ergodic processes. However, if Δt is small enough,

$$\frac{1}{\Delta t}\int_{t-\Delta t/2}^{t+\Delta t/2} dt\, \cos\Big(\Delta\omega t + \Delta\Theta(t)\Big) \approx \cos\Big(\Delta\omega t + \Delta\Theta(t)\Big)\,, \tag{4.7}$$

and therefore, with a *fast* detector, the beat note is directly observable. Direct detection fails if the relative phase fluctuations are too rapid, but intensity correlation techniques

can be used to recover fringes, which is exactly what Magyar and Mandel [128] did for spatial fringes (see [135] for a recent demonstration).

Do we somehow need a quantum descriptions as soon as correlations are involved? In 2011, Chen *et al.* thought they found proof, both theoretical and experimental, that only two-photon interference can explain anticorrelations observed in a HOM interferometer with thermal input pulses [136]. Their starting point was the following decomposition of the second-order cross-correlation function,

$$G^{(2x)} = G^{(2)}_{AA} + G^{(2)}_{BB} + G^{(2)}_{AB}\,, \tag{4.8}$$

where the first two terms correspond to Hanbury-Brown-Twiss correlations between the two input modes A and B, respectively, and the last term is the interference term. A quantum-mechanical analysis results in a two-photon coincidence rate

$$R_{AB} \propto 1 - \exp\left(-\frac{\delta^2}{t_c^2}\right)\,, \tag{4.9}$$

where δ is the optical delay between the two inputs and t_c the width or coherence time of a pulse. The visibility is thus 50 % but can be made 100 % by subtracting the HBT terms, which are constant. They then proceeded to an analogous, classical analysis, but were not able to reproduce the rate (4.9), the dependence on the optical delay in particular. As pointed out earlier, however, there better be a classical field description, for otherwise, a classical state would be "quantized" by a simple, linear transformation (the beam splitter). This was pointed out in a reply to the paper of Chen *et al.* by Shapiro and Lantz [137]. They showed that the appropriate classical input fields are Gaussian pulses

$$E_\pm(t) = \frac{v_\pm}{\sqrt[4]{\pi\tau_p^2/2}} \exp\left(-\frac{[t \pm \delta t/2]^2}{\tau_p^2}\right) \exp(-i\omega_0 t) \tag{4.10}$$

with complex-valued Gaussian random variables $v_\pm$ (independent, identically distributed, zero-mean, isotropic) having constant intensities

$$\left\langle |v_+|^2 \right\rangle = \left\langle |v_-|^2 \right\rangle = N\,. \tag{4.11}$$

Obtaining a similar expression for the second-order cross-correlation function as we do later, they arrived at a rate structurally identical to (4.9). Anticorrelations are then a simple consequence of the complementarity of the two output ports of beam splitters, i.e. energy-conservation property of linear field transformations. Though challenging in general, so far we have always found a classical field description where one should exists. In the following section, we lay the groundwork for the theoretical description of our laser HOM interference experiment.

4.4 Continuous Mode Quantum Optics

4.4.1 The Electric Field for Continuous Mode Excitations

The goal of this section is to establish the relationship between electric field and *time-dependent* creation and annihilation operators. Given our detection method, we are mostly interested in the positive frequency part of the field. The canonical quantization with quantization volume V gives us for the electric field [138]

$$\hat{\mathbf{E}}^{+}(\mathbf{r},t) = i\sum_{\mathbf{k}}\sum_{s}\mathbf{e}_{\mathbf{k}s}\sqrt{\frac{\hbar\omega_k}{2\epsilon_0 V}}\hat{a}_{\mathbf{k}s}\exp\left(-i\omega_k t + i\mathbf{k}.\mathbf{r}\right) . \tag{4.12}$$

In our experiment, we only use Gaussian beams and our optical elements and detectors are insensitive to these *transversal modes*, which is why we can safely neglect them in our theoretical treatment[1]. Furthermore, all stray cavities, formed by back-reflection off optical elements, are completely negligible, as there is dominant, unidirectional flow of energy from source to detector. Consequently, quantization along the photon propagation axis has to be in a continuum of modes. This free-space quantization offers free choice of modes and it is convenient for us to pick so-called *spatio-temporal modes* instead of standard monochromatic plane waves. For now, let us define the appropriate field operator for spatially single-mode light and a continuum of modes in the z-direction [85],

$$\hat{\mathbf{E}}^{+}(z,t) = i\sum_{s}\mathbf{e}_s\int_0^\infty d\omega\,\sqrt{\frac{\hbar\omega}{4\pi\epsilon_0 cA}}\hat{a}_s(\omega)\exp\left(-i\omega\left[t-\frac{z}{c}\right]\right) . \tag{4.13}$$

For our experiment, we can set $z = 0$, corresponding, in the end, to a measurement directly after the HOM beam splitter. The continuous operators

$$\hat{a}_s^\dagger(\omega) \quad \text{and} \quad \hat{a}_s(\omega), \quad \text{with} \quad \left[\hat{a}_s(\omega), \hat{a}_{s'}^\dagger(\omega')\right] = \delta_{s,s'}\delta(\omega-\omega') , \tag{4.14}$$

create and annihilate photons at a certain frequency, and polarization s. In our experiment, the narrow-bandwidth approximation $\Delta\omega \ll \omega_0$ is valid [138], which justifies the approximation $\omega \approx \omega_0$ in the square-root factor in the integral and extension of the lower integration limit to $-\infty$. The field operator is therefore

$$\hat{\mathbf{E}}^{+}(t) = i\sqrt{\frac{\hbar\omega_0}{4\pi\epsilon_0 cA}}\sum_{s}\mathbf{e}_s\int_{-\infty}^{\infty}d\omega\,\hat{a}_s(\omega)\exp(-i\omega t) . \tag{4.15}$$

[1] A *spatial* multimode treatment may be useful later for spatial multi-mode field, which are encountered in multi-mode fibers and free-space communication channels.

This expression invites us to define new operators

$$\begin{aligned}\hat{a}_s(t) &= \frac{1}{\sqrt{2\pi}} \int_{-\infty}^{\infty} d\omega\, \hat{a}_s(\omega) \exp(-i\omega t) \\ \hat{a}_s^\dagger(t) &= \frac{1}{\sqrt{2\pi}} \int_{-\infty}^{\infty} d\omega\, \hat{a}_s^\dagger(\omega) \exp(i\omega t)\,,\end{aligned} \tag{4.16}$$

which, because the bosonic commutation relation is still preserved,

$$\left[\hat{a}_s(t), \hat{a}_{s'}^\dagger\,(t')\right] = \delta_{s,s'}\delta(t-t')\,, \tag{4.17}$$

annihilate and create, respectively, photons at time t in polarization mode s. The operators (4.16) are the quantum-mechanical analogue of *quasi*-monochromatic light amplitudes in the context of analytic signals of classical wave fields [139]. The operators (4.14) and (4.16) in the two domains tackle two distinct problems, namely "what frequency does the photon have" and "where in time is the photon"? Answers to these questions are mutually exclusive to a degree specified by Heisenberg's uncertainty relation. They also represent mathematical limits not achievable in any physical system. We usually have to deal with "lab" or "physical" photons, which describe excitations of wavepackets that have some localization in time and are of finite bandwidth. Since we perform correlation detection in time, corresponding correlation functions, and thus coincidence probabilities, are expressed in terms of time-dependent creation and annihilation operators, as we will see later. Using (4.16), the electric field operator (4.15) in the time-domain takes the final form

$$\begin{aligned}\hat{\mathbf{E}}^+(t) &= i\sqrt{\frac{\hbar\omega_0}{2\epsilon_0 cA}}\left(\mathbf{e}_H \hat{a}_H(t) + \mathbf{e}_V \hat{a}_V(t)\right) \\ &\equiv \mathbf{e}_H \hat{a}_H(t) + \mathbf{e}_V \hat{a}_V(t)\,,\end{aligned} \tag{4.18}$$

where we absorbed the constant into the units of measurement ("photon units") and called the two orthogonal polarization modes H (horizontal) and V (vertical). This is the field expression we are going to use, which implies that we are working in the Heisenberg picture.

4.4.2 Wavepacket Excitations

As said, photons described in the previous section are not physical, because the finite energy they carry would have to spread across $\mathbb{R}$ and thus a photon detection would not be possible at any time t. We are, however, free to pick any mode basis $\{\Phi_i(\omega)\}$ that is orthonormal and complete, i.e. which fulfills

$$\begin{aligned}\int_{-\infty}^{\infty} d\omega\, \Phi_i(\omega)\Phi_j^*(\omega) &= \delta_{i,j} \\ \sum_{i=0}^{\infty} \Phi_i^*(\omega)\Phi_i(\omega') &= \delta(\omega-\omega')\,.\end{aligned} \tag{4.19}$$

These modes can carry an excitation, as testified by the existence of annihilation and creation operators associated with these modes,

$$\begin{aligned}\hat{c}_s(\Phi_i) &= \int_{-\infty}^{\infty} d\omega\, \Phi_i^*(\omega)\hat{a}_s(\omega) \\ \hat{c}_s^\dagger(\Phi_i) &= \int_{-\infty}^{\infty} d\omega\, \Phi_i(\omega)\hat{a}_s^\dagger(\omega)\,.\end{aligned} \tag{4.20}$$

Again, these fulfill the canonical commutation relation,

$$\left[\hat{c}_s(\Phi_i), \hat{c}_{s'}^\dagger(\Phi_j)\right] = \delta_{s,s'}\delta_{i,j}\,, \tag{4.21}$$

and a Fock state photon in such a mode is simply

$$|1_s(\Phi_i)\rangle = \hat{c}_s^\dagger(\Phi_i)|0\rangle\,. \tag{4.22}$$

The transition to the time-domain is again facilitated by a Fourier transform

$$\Phi_i(t) = \frac{1}{\sqrt{2\pi}} \int_{-\infty}^{\infty} d\omega\, \Phi_i(\omega) \exp(-i\omega t)\,. \tag{4.23}$$

With time-dependent monochromatic operators defined in (4.16), we obtain *wavepacket annihilation and creation* operators

$$\begin{aligned}\hat{c}_s(\Phi_i) &= \int_{-\infty}^{\infty} dt\, \Phi_i^*(t)\hat{a}_s(t) \\ \hat{c}_s^\dagger(\Phi_i) &= \int_{-\infty}^{\infty} dt\, \Phi_i(t)\hat{a}_s^\dagger(t)\,.\end{aligned} \tag{4.24}$$

Since the Φ_i's are complete, we can easily obtain new, permissible, modes by linear superposition,

$$\zeta(t) = \sum_{i=1}^{\infty} c_i \Phi_i(t)\,, \tag{4.25}$$

with associated annihilation and creation operators

$$\begin{aligned}\hat{c}_s(\zeta) &= \sum_{i=1}^{\infty} c_i^* \hat{c}_s(\Phi_i) \\ \hat{c}_s^\dagger(\zeta) &= \sum_{i=1}^{\infty} c_i \hat{c}_s^\dagger(\Phi_i)\,.\end{aligned} \tag{4.26}$$

4.4.3 Spectrally Determined Wavepackets

Photon wavepackets (or pulses) in time are related to their spectra. As we will see later, classically, the source spectrum relates to statistical properties of emitted fields. Whenever

this is possible, we can rigorously define coherence properties of fields. For instance, the spectra considered here permit us to assign a *coherence length* τ_{coh} to the fields, which we can determine experimentally from measurements of the first-order correlation function via

$$\tau_{\text{coh}} = \int_{-\infty}^{\infty} d\tau \, \left| g^{(1)}(\tau) \right|^2 . \tag{4.27}$$

Three kinds of spectra are of particular interest in optical problems and they are all connected [138]. The ideal monochromatic spectrum (central frequency ω_0)

$$F_M(\omega) = \delta(\omega - \omega_0) \tag{4.28}$$

can be obtained from both the Lorentzian spectrum,

$$F_L(\omega) = \frac{1}{\pi} \frac{\gamma}{(\omega_0 - \omega)^2 + \gamma^2} , \tag{4.29}$$

and the Gaussian spectrum,

$$F_G(\omega) = \frac{1}{\sqrt{2\pi\Delta^2}} \exp\left(-\frac{[\omega_0 - \omega]^2}{2\Delta^2} \right) , \tag{4.30}$$

by taking the limits

$$F_M(\omega) = \lim_{\gamma \to 0} F_L(\omega) = \lim_{\Delta \to 0} F_G(\omega) . \tag{4.31}$$

The interpretation of γ depends on the physical model for the stochastic process leading to a Lorentzian spectrum, but we can regard it as a damping rate whose inverse is τ_{coh} (and likewise the linewidth Δ). Wavepackets associated with monochromatic spectra are, of course, plane waves $\exp(-i\omega_0 t)$. A Gaussian wavepacket has a Gaussian amplitude spectrum and linear spectral phase,

$$\zeta(\omega) = \sqrt[4]{\frac{\sigma^2}{2\pi}} \exp\left(-\frac{[\omega_0 - \omega]^2}{4/\sigma^2} \right) \exp(i\omega\delta\tau) , \tag{4.32}$$

where σ is the 1/e-width of the Gaussian and $\delta\tau$ a time-delay (a bit of change in notation here). In the time domain, this corresponds to a *time-shifted* Gaussian wavepacket,

$$\begin{aligned} \zeta(t) &= \frac{1}{\sqrt{2\pi}} \int_{-\infty}^{\infty} d\omega \, \zeta(\omega) \exp(-i\omega t) \\ &= \sqrt[4]{\frac{2}{\pi\sigma^2}} \exp\left(-\frac{[t - \delta\tau]^2}{\sigma^2} \right) \exp\left(i\omega_0 [t - \delta\tau] \right) . \end{aligned} \tag{4.33}$$

In complete analogy, the Lorentzian wavepacket is defined by

$$\zeta(\omega) = \sqrt{\frac{2\gamma^3}{\pi}} \frac{\exp(-i\omega\tau)}{(\omega_0 - \omega)^2 + \gamma^2} , \tag{4.34}$$

and the Fourier transform gives

$$\zeta(t) = \sqrt{\gamma}\exp\big(-\gamma|t-\tau| + i\omega_0[t-\tau]\big)\,. \tag{4.35}$$

Note that the constants are chosen to normalize the wavepackets,

$$\int_{-\infty}^{\infty} dt\,|\zeta(t)|^2 = \int_{-\infty}^{\infty} d\omega\,|\zeta(\omega)|^2 = 1\,. \tag{4.36}$$

4.5 Theoretical Exploration of Laser HOM Interference Landscapes

4.5.1 Second-Order Cross-Correlation Function

We commence with definition of the second-order cross-correlation function,

$$\begin{aligned} G^{(2x)}(t_3,t_4) &\coloneqq \Big\langle \hat{E}_3^-(t_3)\hat{E}_4^-(t_4)\hat{E}_4^+(t_4)\hat{E}_3^+(t_3)\Big\rangle \\ &= \frac{1}{4}\Big\langle \Big(\zeta_1^*(t_3)\hat{a}_1^\dagger(t_3) + \zeta_2^*(t_3)\hat{a}_2^\dagger(t_3)\Big)\Big(\zeta_1^*(t_4)\hat{a}_1^\dagger(t_4) - \zeta_2^*(t_4)\hat{a}_2^\dagger(t_4)\Big) \\ &\qquad \times \Big(\zeta_1(t_4)\hat{a}_1(t_4) - \zeta_2(t_4)\hat{a}_2(t_4)\Big)\Big(\zeta_1(t_3)\hat{a}_1(t_3) + \zeta_2(t_3)\hat{a}_2(t_3)\Big)\Big\rangle\,, \end{aligned} \tag{4.37}$$

where the two input modes to a beam splitter carry excitations described by mode envelope functions $\zeta_1(t)$ and $\zeta_2(t)$. We explicitly calculate

$$
\begin{aligned}
G^{(2x)}(t_3,t_4) = {} & \frac{|\zeta_1(t_3)\zeta_1(t_4)|^2}{4}\Big\langle \hat{a}_1^\dagger(t_3)\hat{a}_1^\dagger(t_4)\hat{a}_1(t_4)\hat{a}_1(t_3)\Big\rangle \\
& + \frac{\zeta_1^*(t_3)\zeta_1^*(t_4)\zeta_1(t_4)\zeta_2(t_3)}{4}\Big\langle \hat{a}_1^\dagger(t_3)\hat{a}_1^\dagger(t_4)\hat{a}_1(t_4)\hat{a}_2(t_3)\Big\rangle \\
& - \frac{\zeta_1^*(t_3)\zeta_1^*(t_4)\zeta_2(t_4)\zeta_1(t_3)}{4}\Big\langle \hat{a}_1^\dagger(t_3)\hat{a}_1^\dagger(t_4)\hat{a}_1(t_3)\hat{a}_2(t_4)\Big\rangle \\
& - \frac{\zeta_1^*(t_3)\zeta_1^*(t_4)\zeta_2(t_4)\zeta_2(t_3)}{4}\Big\langle \hat{a}_1^\dagger(t_3)\hat{a}_1^\dagger(t_4)\hat{a}_2(t_4)\hat{a}_2(t_3)\Big\rangle \\
& - \frac{\zeta_1^*(t_3)\zeta_2^*(t_4)\zeta_1(t_4)\zeta_1(t_3)}{4}\Big\langle \hat{a}_1^\dagger(t_3)\hat{a}_1(t_4)\hat{a}_1(t_3)\hat{a}_2^\dagger(t_4)\Big\rangle \\
& - \frac{\zeta_1^*(t_3)\zeta_2^*(t_4)\zeta_1(t_4)\zeta_2(t_3)}{4}\Big\langle \hat{a}_1^\dagger(t_3)\hat{a}_1(t_4)\hat{a}_2^\dagger(t_4)\hat{a}_2(t_3)\Big\rangle \\
& + \frac{\zeta_1^*(t_3)\zeta_2^*(t_4)\zeta_2(t_4)\zeta_1(t_3)}{4}\Big\langle \hat{a}_1^\dagger(t_3)\hat{a}_1(t_3)\hat{a}_2^\dagger(t_4)\hat{a}_2(t_4)\Big\rangle \\
& + \frac{\zeta_1^*(t_3)\zeta_2^*(t_4)\zeta_2(t_4)\zeta_2(t_3)}{4}\Big\langle \hat{a}_1^\dagger(t_3)\hat{a}_2^\dagger(t_4)\hat{a}_2(t_4)\hat{a}_2(t_3)\Big\rangle \\
& + \frac{\zeta_2^*(t_3)\zeta_1^*(t_4)\zeta_1(t_4)\zeta_1(t_3)}{4}\Big\langle \hat{a}_1^\dagger(t_4)\hat{a}_1(t_4)\hat{a}_1(t_3)\hat{a}_2^\dagger(t_3)\Big\rangle \\
& + \frac{\zeta_2^*(t_3)\zeta_1^*(t_4)\zeta_1(t_4)\zeta_2(t_3)}{4}\Big\langle \hat{a}_1^\dagger(t_4)\hat{a}_1(t_4)\hat{a}_2^\dagger(t_3)\hat{a}_2(t_3)\Big\rangle \\
& - \frac{\zeta_2^*(t_3)\zeta_1^*(t_4)\zeta_2(t_4)\zeta_1(t_3)}{4}\Big\langle \hat{a}_1^\dagger(t_4)\hat{a}_1(t_3)\hat{a}_2^\dagger(t_3)\hat{a}_2(t_4)\Big\rangle \\
& - \frac{\zeta_2^*(t_3)\zeta_1^*(t_4)\zeta_2(t_4)\zeta_2(t_3)}{4}\Big\langle \hat{a}_1^\dagger(t_4)\hat{a}_2^\dagger(t_3)\hat{a}_2(t_4)\hat{a}_2(t_3)\Big\rangle \\
& - \frac{\zeta_2^*(t_3)\zeta_2^*(t_4)\zeta_1(t_4)\zeta_1(t_3)}{4}\Big\langle \hat{a}_1(t_4)\hat{a}_1(t_3)\hat{a}_2^\dagger(t_3)\hat{a}_2^\dagger(t_4)\Big\rangle \\
& - \frac{\zeta_2^*(t_3)\zeta_2^*(t_4)\zeta_1(t_4)\zeta_2(t_3)}{4}\Big\langle \hat{a}_1(t_4)\hat{a}_2^\dagger(t_3)\hat{a}_2^\dagger(t_4)\hat{a}_2(t_3)\Big\rangle \\
& + \frac{\zeta_2^*(t_3)\zeta_2^*(t_4)\zeta_2(t_4)\zeta_1(t_3)}{4}\Big\langle \hat{a}_1(t_3)\hat{a}_2^\dagger(t_3)\hat{a}_2^\dagger(t_4)\hat{a}_2(t_4)\Big\rangle \\
& + \frac{|\zeta_2(t_3)\zeta_2(t_4)|^2}{4}\Big\langle \hat{a}_2^\dagger(t_3)\hat{a}_2^\dagger(t_4)\hat{a}_2(t_4)\hat{a}_2(t_3)\Big\rangle .
\end{aligned}
\tag{4.38}
$$

In general, all sixteen terms contribute, but for two independent light sources, only six terms can be non-zero [140]. This is true for both quantum and classical light such as single photon sources and star light, respectively, and is a direct consequence of randomizing the relative phase over $[0, 2\pi)$, which can be achieved in various ways. For instance, one can dither the optical path length in one input mode, so that $\hat{a}_k \to \hat{a}_k \exp(i\Phi_k)$, in which case the above expectation values are multiplied by expectation values of the form

$$
\Big\langle \exp\big(\pm im\Phi_k[t]\big)\Big\rangle = \frac{1}{2\pi}\int_0^{2\pi} d\Phi_k \, \exp(\pm i\Phi_k) , \tag{4.39}
$$

which is zero for unpaired annihilation (+) or creation (−) operators in the expectation value ($m = 1$ or $m = 2$). The only surviving terms are those with balanced creation and annihilation operators ($m = 0$ above), and we get

$$\begin{aligned} G^{(2x)}(t_3, t_4) = &\frac{1}{4}|\zeta_1(t_3)\zeta_1(t_4)|^2\left\langle \hat{a}_1^\dagger(t_3)\hat{a}_1^\dagger(t_4)\hat{a}_1(t_4)\hat{a}_1(t_3)\right\rangle \\ &+ \frac{1}{4}|\zeta_2(t_3)\zeta_2(t_4)|^2\left\langle \hat{a}_2^\dagger(t_3)\hat{a}_2^\dagger(t_4)\hat{a}_2(t_4)\hat{a}_2(t_3)\right\rangle \\ &+ \frac{1}{4}|\zeta_1(t_3)|^2|\zeta_2(t_4)|^2\left\langle \hat{a}_1^\dagger(t_3)\hat{a}_1(t_3)\hat{a}_2^\dagger(t_4)\hat{a}_2(t_4)\right\rangle \\ &+ \frac{1}{4}|\zeta_1(t_4)|^2|\zeta_2(t_3)|^2\left\langle \hat{a}_1^\dagger(t_4)\hat{a}_1(t_4)\hat{a}_2^\dagger(t_3)\hat{a}_2(t_3)\right\rangle \\ &- \frac{1}{2}\mathfrak{Re}\left\{\zeta_1^*(t_3)\zeta_1(t_4)\zeta_2(t_3)\zeta_2^*(t_4)\left\langle \hat{a}_1^\dagger(t_3)\hat{a}_1(t_4)\hat{a}_2^\dagger(t_4)\hat{a}_2(t_3)\right\rangle\right\}. \end{aligned} \tag{4.40}$$

In our case, the two impinging fields are statistically independent, resulting in a factorization of correlation functions,

$$\left\langle \hat{a}_1^\dagger(t)\hat{a}_1(t'')\hat{a}_2^\dagger(t'')\hat{a}_2(t''')\right\rangle = \left\langle \hat{a}_1^\dagger(t)\hat{a}_1(t')\right\rangle\left\langle \hat{a}_2^\dagger(t'')\hat{a}_2(t''')\right\rangle. \tag{4.41}$$

4.5.2 Optical Equivalence Theorem

The two fields we use are excited into mixtures of coherent states with complex amplitudes $\alpha_k = |\alpha_k|\exp(i\Theta_k)$, whose Glauber-Sudarshan P-Representation [141, 142] is given by

$$\hat{\rho} = \bigotimes_{k=1,2}\int_{\mathcal{C}_k} d\alpha_k\, P(\alpha_k)|\alpha_k\rangle\langle\alpha_k|\,, \tag{4.42}$$

where the integration is over an area in the complex plane. Evaluation of (4.40) using the state (4.42) is simplified dramatically by the optical equivalence theorem [142]. The theorem establishes a relation between quantum and classical expectation values and is thus particularly useful for the task at hand, namely the calculation of expectation values of functions

$$f_k\left(\hat{a}_k, \hat{a}_k^\dagger\right) = \sum_{n,m} c_{n,m}\hat{a}^{\dagger n}\hat{a}^m \tag{4.43}$$

of normally-ordered operators for states with a close classical correspondence. The theorem states

$$\begin{aligned}\left\langle f_k\left(\hat{a}_k,\hat{a}_k^\dagger\right)\right\rangle_{\mathrm{QM}} &= \int_{\mathcal{C}_k} d\alpha_k\, P(\alpha_k) \sum_{n,m} c_{n,m}\langle\alpha_k|\hat{a}_k^{\dagger n}\hat{a}_k^m|\alpha_k\rangle \\ &= \int_{\mathcal{C}_k} d\alpha_k\, P(\alpha_k) \sum_{n,m} c_{n,m}\alpha_k^{*n}\alpha_k^m \\ &= \int_{\mathcal{C}_k} d\alpha_k\, P(\alpha_k) f^{(N)}(\alpha_k,\alpha_k^*) \\ &= \left\langle f_k\left(\alpha_k,\alpha_k^*\right)\right\rangle_{\alpha_k}.\end{aligned} \tag{4.44}$$

This result implies that in all our calculations we do not have to evaluate a single quantum-mechanical expectation value but can replace all instances of annihilation and creation operators with the (classical) c-number functions α_k (laser amplitudes), and perform an ensemble average over all realizations of α_k with probability distribution $P(\alpha_k)$. The ensemble in our case is a phase-ensemble.

4.5.3 Statistical Assumptions

Applying the optical equivalence theorem to each mode separately we obtain

$$\begin{aligned}G^{(2x)}(t_3,t_4) = \frac{1}{4}\Bigg(&|\zeta_1(t_3)\zeta_1(t_4)|^2\left\langle|\alpha_1(t_3)|^2|\alpha_1(t_4)|^2\right\rangle_{\alpha_1} \\ &+ |\zeta_2(t_3)\zeta_2(t_4)|^2\left\langle|\alpha_2(t_3)|^2|\alpha_2(t_4)|^2\right\rangle_{\alpha_2} \\ &+ |\zeta_1(t_3)|^2|\zeta_2(t_4)|^2\left\langle|\alpha_1(t_3)|^2\right\rangle_{\alpha_1}\left\langle|\alpha_2(t_4)|^2\right\rangle_{\alpha_2} \\ &+ |\zeta_1(t_4)|^2|\zeta_2(t_3)|^2\left\langle|\alpha_1(t_4)|^2\right\rangle_{\alpha_1}\left\langle|\alpha_2(t_3)|^2\right\rangle_{\alpha_2} \\ &- 2\mathfrak{Re}\left\{\zeta_1^*(t_3)\zeta_1(t_4)\zeta_2(t_3)\zeta_2^*(t_4)G_1^{(1)}(\tau)G_2^{*(1)}(\tau)\right\}\Bigg).\end{aligned} \tag{4.45}$$

Here, the first-order autocorrelation functions

$$G_k^{(1)}(\tau) = \left\langle\alpha_k^*(t)\alpha_k(t+\tau)\right\rangle_{\alpha_k} \tag{4.46}$$

only depend on the detection-time difference $\tau \coloneqq t_4 - t_3$ because the fields are statistically stationary, which is fair assumption for continuous-wave lasers. The lasers also have statistically constant intensities,

$$\left\langle|\alpha_k(t)|^2\right\rangle_{\alpha_k} = G_k^{(1)}(0) = N_k\,, \tag{4.47}$$

and for sufficiently small τ, the intensity fluctuations are constant,

$$\left\langle |\alpha_k(t)|^2 |\alpha_k(t')|^2 \right\rangle_{\alpha_k} = N_k^2 \,. \tag{4.48}$$

Note that even though the laser phase is subject to a random process, leading to a non-trivial first-order autocorrelation function (in particular of the Lorentzian or Gaussian type), the laser is still coherent and not chaotic [112, 113, 143]. Thus, the intensity fluctuations are constant and *not* of, for example, Lorentzian or Gaussian type, as expected for chaotic light, which one would get using the Gaussian-moment factoring theorem [138]. Defining the degree of first-order coherence

$$g_k^{(1)}(\tau) \coloneqq \frac{G_k^{(1)}(\tau)}{G_k^{(1)}(0)} = \frac{G_k^{(1)}(\tau)}{N_k} \,, \tag{4.49}$$

we obtain

$$\begin{aligned} G^{(2x)}(t_0, t_0+\tau) = {} & \frac{N_1^2}{4} |\zeta_1(t_0)\zeta_1(t_0+\tau)|^2 + \frac{N_2^2}{4} |\zeta_2(t_0)\zeta_2(t_0+\tau)|^2 \\ & + \frac{N_1 N_2}{4} |\zeta_1(t_0)|^2 |\zeta_2(t_0+\tau)|^2 + \frac{N_1 N_2}{4} |\zeta_1(t_0+\tau)|^2 |\zeta_2(t_0)|^2 \\ & - \frac{N_1 N_2}{2} \mathfrak{Re}\left\{ \zeta_1^*(t_0)\zeta_1(t_0+\tau)\zeta_2(t_0)\zeta_2^*(t_0+\tau) g_1^{(1)}(\tau) g_2^{*(1)}(\tau) \right\} , \end{aligned} \tag{4.50}$$

where we changed notation to indicate that we are interested in an initial detection at t_0 and a subsequent one at $t_0 + \tau$.

4.5.4 Coincidence Detection Rate

In the lab we rarely measure correlation functions directly and only sometimes can reconstruct them from coincidence detection rates

$$R^{(2x)}(t_0, \tau, \Delta T) = \eta_1 \eta_2 \int_{t_0}^{t_0+\Delta T} dt_1 \int_{t_0+\tau}^{t_0+\tau+\Delta T} dt_2 \, G^{(2x)}(t_1, t_2) \,. \tag{4.51}$$

If the detector time resolution ΔT is much smaller than the width of $G^{(2x)}(t_1, t_2)$, then

$$R^{(2x)}(t_0, \tau, \Delta T) \approx \eta_1 \eta_2 (\Delta T)^2 G^{(2x)}(t_0, t_0+\tau) \,, \tag{4.52}$$

which means that we are working in the time-resolved regime. Moreover, if the absolute detection time t_0 is of no relevance, we integrate (sum over all events in the time tag files) over t_0 for the duration of measurement T_M,

$$R^{(2x)}(\tau, \Delta t) = \eta_1 \eta_2 \Delta T_2^2 \int_{-T_M/2}^{T_M/2} dt_0 \, G^{(2x)}(t_0, t_0+\tau) \,. \tag{4.53}$$

We will later see that this integration plays an important part in determining whether we resolve HOM interference landscapes. Since we are working in the time-resolved regime, we can safely continue working with $G^{(2x)}(t_0, t_0+\tau)$, as the coincidence rate only differs by a scaling factor (which we could factor out by data normalization if we wanted to). The analysis so far assumed a photon-number-resolving detector, which is not readily available and certainly not used in our experiments, namely silicon avalanche photodiodes (Si-APD). Rather, we have a so-called "bucket" detector, which is described by the projective measurement operators [144]

$$\begin{aligned} \hat{M}_{\text{click}} &= \sum_{n=1}^{\infty} Q(n)|n\rangle\langle n| \\ \hat{M}_{\text{no click}} &= \mathbb{1} - \hat{M}_{\text{click}}\,, \end{aligned} \tag{4.54}$$

with

$$Q(n) = 1 - (1-\eta)^n + \epsilon - \epsilon(1-(1-n)^n)\,, \tag{4.55}$$

where η and ϵ are the detector efficiency and dark count probability, respectively. In an accurate description of the detection process, these operators would replace normally-ordered operators inside the expectation value of the second-order cross-correlation function. Yet, given that the experiment *actually* works with Si-APDs, do the theoretical predictions change at all? The answer is "no" [145]. All we need to ensure is that we have only one photon in a time interval approximately equal to the detector dead time ($\sim \mu$s). But this is already implicitly assumed in the semi-classical model we employed in the derivation above [146] . Accordingly, the measured temporal correlation functions is ([145], Eq. 2.68)

$$\hat{\gamma}^{(2)}_{\text{click}}(\tau) = \frac{N_c(\tau;\Delta\tau)}{R_3 R_4 \Delta\tau T_{\text{int}}}\,, \tag{4.56}$$

where $N_c(\tau;\Delta\tau)$ are the number of coincidences in the histogram bin centered at detection time difference τ with bin size $\Delta\tau$, R_3 and R_4 are the single detection rates, and T_{int} is the integration time. This result is a solid bridge between the theoretical result (4.53) and the way we actually measure and analyze the data (time tag files, from which histograms are generated and HOM dips distilled).

4.5.5 Laser HOM Dips

The negative sign of the interference term in the second-order cross-correlation function (4.50) indicates that for certain wavepackets $\zeta_k(t)$ and degrees of first-order coherence $g^{(1)}_k(\tau)$ we can observe anticorrelations at the two output ports of a symmetric beam splitter. Note that both classical [137] and quantum [103] interpretations of this effect rely

on energy conservation at the beam splitter. Furthermore, anticorrelations are statistical in nature since our interference term contains a product of two first-order autocorrelation functions. For identical and phase-randomized, ideal coherent states, in which case $g_k^{(1)}(\tau) = \exp(-i\omega_k\tau)$, $N_1 = N_2 = N$, and $\omega_1 = \omega_2$, we get ($t_0 = 0$, as for stationary processes the origin in time doesn't matter)

$$G^{(2x)}(\tau) = \frac{N^2}{4}\left(|\zeta_1(0)\zeta_1(\tau)|^2 + |\zeta_2(0)\zeta_2(\tau)|^2 + \Big|\zeta_1(0)\zeta_2(\tau) - \zeta_1(\tau)\zeta_2(0)\Big|^2\right). \tag{4.57}$$

If the fields were excited in a single photon Fock state, i.e. $\hat{\rho} = |11\rangle\langle 11|$, then a similar calculation leads to an expression for the correlation function proportional to the third term in Eq. (4.57), which has the interesting property that no matter how different the mode functions $\zeta_1(t)$ and $\zeta_2(t)$ are, for $\tau = 0$ coincidences always vanish [107, 108], and 100 % visibility is obtained. In our case, the first two terms are non-zero and are responsible for the 50 % visibility bound for any classical field.

For a laser far above threshold, its amplitude is stable. Its phase, however, is subject to a diffusion process and leads to a laser's natural (Schawlow-Townes) linewidth [147]. The theory of random walks along the unit circle in the complex plane tells us that the degree of first-order coherence is (see for example [138])

$$g_k^{(1)}(\tau) = \Big\langle \exp\big(\Theta_k[t+\tau] - \Theta_k[t]\big)\Big\rangle_{\alpha_k} = \exp\left(-\frac{|\tau|}{\tau_k}\right)\exp(-i\omega_k\tau)\,, \tag{4.58}$$

where τ_k is source k's coherence length. When the laser is inhomogeneously broadened (e.g. Doppler broadening), the spectrum follows a Gaussian with a degree of first order coherence given by

$$g_k^{(1)}(\tau) = \exp\left(-\frac{\tau^2}{\tau_k^2}\right)\exp(-i\omega_k\tau)\,. \tag{4.59}$$

In the study of interference phenomena with broadband sources, for example thermal light and single photons from spontaneous parametric downconversion, the Gaussian model is often the more accurate one. In these cases, a filter is employed to narrow the spectrum to a "line", and more often than not, the frequency transmission function of the filter is a Gaussian. The second-order cross-correlation function then becomes

$$\begin{aligned} G^{(2x)}(t_0, t_0+\tau) = {} & \frac{N_1^2}{4}|\zeta_1(t_0)\zeta_1(t_0+\tau)|^2 + \frac{N_2^2}{4}|\zeta_2(t_0)\zeta_2(t_0+\tau)|^2 \\ & + \frac{N_1N_2}{4}\Big(|\zeta_1(t_0)|^2|\zeta_2(t_0+\tau)|^2 + |\zeta_1(t_0+\tau)|^2|\zeta_2(t_0)|^2\Big) \\ & - \frac{N_1N_2}{2}\mathfrak{Re}\Big\{\zeta_1^*(t_0)\zeta_1(t_0+\tau)\zeta_2(t_0)\zeta_2^*(t_0+\tau)\Big\}F(\tau)\cos\big(\Delta\omega\tau\big)\,, \end{aligned} \tag{4.60}$$

where

$$F(\tau) = \exp\left(-|\tau|\left[\frac{1}{\tau_1} + \frac{1}{\tau_2}\right]\right) \tag{4.61}$$

and

$$F(\tau) = \exp\left(-\tau^2\left[\frac{1}{\tau_1^2} + \frac{1}{\tau_2^2}\right]\right) \tag{4.62}$$

for Lorentzian and Gaussian spectra, respectively, and $\Delta\omega \coloneqq \omega_2 - \omega_1$. To evaluate this expression, we assume a CW laser (constant mode envelope),

$$\zeta_k(t) = 1\,, \tag{4.63}$$

emitting the same mean photon number, $N_1 = N_2 = N$, and furthermore that both sources undergo the same phase diffusion process with $\tau_1 = \tau_2 \equiv \tau_{\text{coh}}$. This way we obtain our first basic result,

$$G^{(2x)}(\tau) = N^2\left(1 - \frac{1}{2}\cos\left(\Delta\omega\tau\right)F(\tau)\right), \tag{4.64}$$

which is plotted in Figure 4.2. We find oscillations within the dip with a period corresponding to the beat frequency of the two lasers. In our experiment, however, two beams are derived from the same laser, and since we have no appreciable optical nonlinearity from source to detector, $\Delta\omega = 0$, which we assume for the remainder of this work. The visibility of laser HOM dips is determined by $F(\tau)$. For both Gaussian and Lorentzian type functions, minimum and maximum of 0 and 1 are achieved for $\tau \to \infty$ and $\tau = 0$, respectively. We thus calculate

$$\mathcal{V}_{\text{HOM}} \coloneqq \frac{G^{(2x)}(\tau)_{\max} - G^{(2x)}(\tau)_{\min}}{G^{(2x)}(\tau)_{\max}} = \frac{1 - 0.5}{1} = 0.5\,, \tag{4.65}$$

as expected. What if $N_1 \neq N_2$? Then we have

$$\mathcal{V}_{\text{HOM}} = \frac{\frac{1}{4}\left(N_1^2 + N_2^2 + 2N_1N_2\right) - \frac{1}{4}\left(N_1^2 + N_2^2\right)}{\frac{1}{4}\left(N_1^2 + N_2^2 + 2N_1N_2\right)} = \frac{2N_1N_2}{(N_1 + N_2)^2}\,. \tag{4.66}$$

Let us assume $N_1 = \alpha N_2$, for some $\alpha > 1$. The visibility is then given by

$$\mathcal{V}_{\text{HOM}} = \frac{2\alpha N_2^2}{(\alpha N_2 + N_2)^2} = \frac{2\alpha}{(1+\alpha)^2}\,, \tag{4.67}$$

which is plotted in Figure 4.3. We can then modify Equation (4.64) to become

$$G^{(2x)}(\tau) = N^2\left(1 - \mathcal{V}_{\text{HOM}}\cos\left(\Delta\omega\tau\right)F(\tau)\right). \tag{4.68}$$

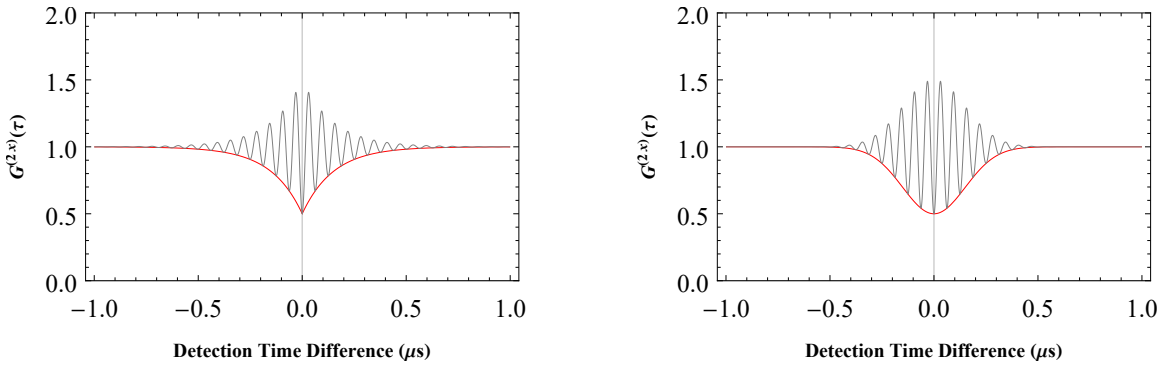

Figure 4.2: **Oscillations Within Laser HOM Dips.** The dip shape (red solid line) is determined by the laser spectrum: **(a)** Lorentzian and **(b)** Gaussian. Beating between two lasers (black solid lines) happens whenever there is a frequency difference and modulates the anticorrelation dip (see Equation 4.64).

4.5.6 Laser HOM Polarization Interference Landscapes

We now extend our study to more than two modes, namely two polarization modes at each input port of the HOM beam splitter. Polarization is not changing anything fundamentally, i.e. anticorrelations at a beam splitter, but provides us with a degree of freedom to engineer different dip shapes, which can be used to encode information via modulation techniques. Before we speak of those, we first need to find out how the second-order cross-correlation function is modified when the two input modes have arbitrary linear polarization.

Consider the following state for beam splitter input ports $k \in \{1, 2\}$ and polarization modes $s \in \{H, V\}$ (horizontal and vertical polarization, respectively),

$$\begin{aligned} \hat{\rho} &= \bigotimes_{\substack{k=1,2 \\ s=H,V}} \int_{\mathcal{C}_{k,s}} d\alpha_{k,s}\, P(\alpha_{k,s}) |\alpha_{k,s}\rangle\langle\alpha_{k,s}| \\ &= \hat{\rho}_{1H} \otimes \hat{\rho}_{1V} \otimes \hat{\rho}_{2H} \otimes \hat{\rho}_{2V}\,. \end{aligned} \tag{4.69}$$

Our single-photon detectors are not polarization-sensitive, in which case the second-order cross-correlation function decomposes as a sum over all possible polarization combinations

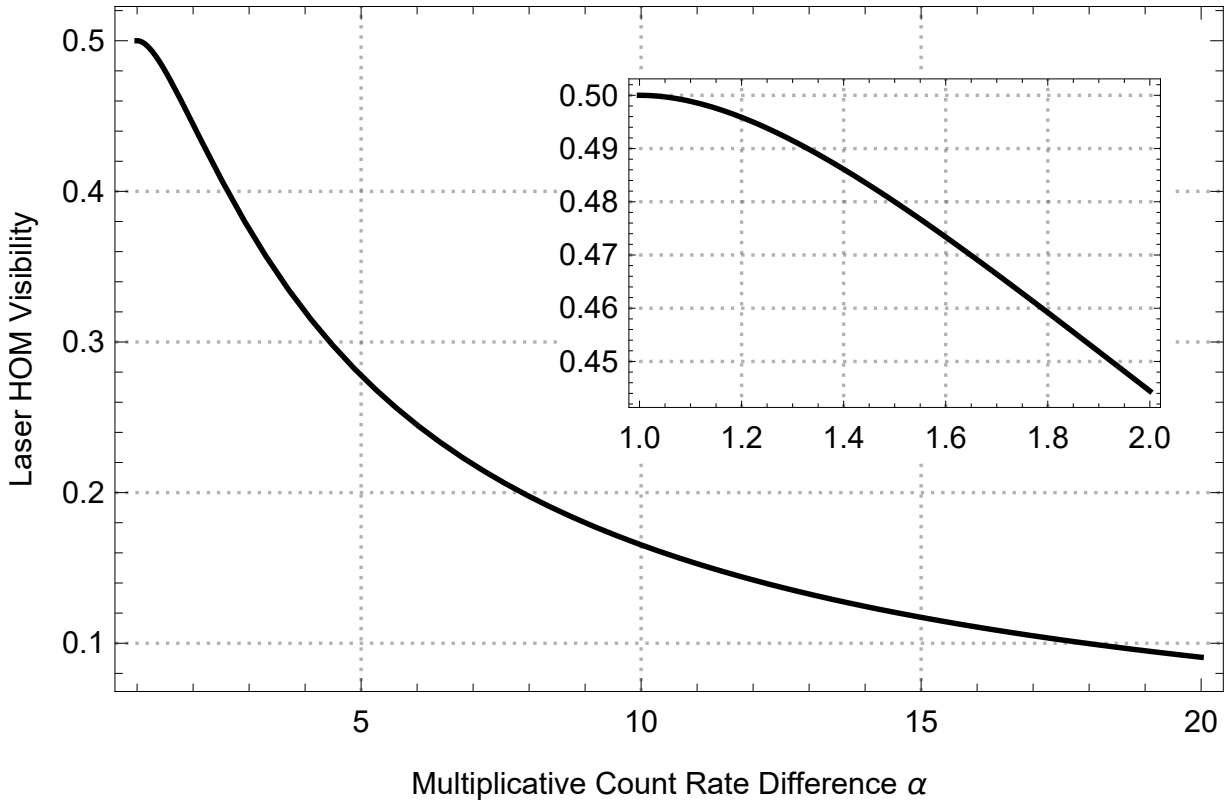

Figure 4.3: **Laser HOM Dip Visibility as Function of Count Rate Difference.** We see that the visibility, as predicted by Equation (4.67), drops only slowly, reaching $\mathcal{V}_{\text{HOM}} = 0.1$ for $\alpha = N_1/N_2 \approx 18$. The inset is a zoom into the plot region $\alpha \in [1, 2]$, which is the operating regime in practice. We see that, even if we have double the count rate in one detector, i.e. $\alpha = 2$, the visibility would still be 44.44 %.

[148],

$$\begin{aligned} G^{(2x)}(t_3, t_4) &= \sum_{s,s'} \text{Tr}\left\{\hat{\rho}\hat{a}^\dagger_{3s}(t_3)\hat{a}^\dagger_{4s'}(t_4)\hat{a}_{4s'}(t_4)\hat{a}_{3s}(t_3)\right\} \\ &= \text{Tr}\left\{\hat{\rho}\hat{a}^\dagger_{3H}(t_3)\hat{a}^\dagger_{4H}(t_4)\hat{a}_{4H}(t_4)\hat{a}_{3H}(t_3)\right\} + \text{Tr}\left\{\hat{\rho}\hat{a}^\dagger_{3V}(t_3)\hat{a}^\dagger_{4V}(t_4)\hat{a}_{4V}(t_4)\hat{a}_{3V}(t_3)\right\} \\ &+ \text{Tr}\left\{\hat{\rho}\hat{a}^\dagger_{3H}(t_3)\hat{a}^\dagger_{4V}(t_4)\hat{a}_{4V}(t_4)\hat{a}_{3H}(t_3)\right\} + \text{Tr}\left\{\hat{\rho}\hat{a}^\dagger_{3V}(t_3)\hat{a}^\dagger_{4H}(t_4)\hat{a}_{4H}(t_4)\hat{a}_{3V}(t_3)\right\} \\ &= G^{(2x)}_{HH}(t_3, t_4) + G^{(2x)}_{VV}(t_3, t_4) + G^{(2x)}_{HV}(t_3, t_4) + G^{(2x)}_{VH}(t_3, t_4)\,. \end{aligned} \tag{4.70}$$

The first two terms only depend on a single polarization, namely H and V, respectively, and should be quite similar to the second-order cross-correlation function we already obtained. The last two terms concern mixed polarizations and should not contribute to interference

terms. Inserting the expansion of $\hat{\rho}$, Equation (4.69), we get

$$\begin{aligned} G^{(2x)}(t_3,t_4) = &\operatorname{Tr}\left\{\hat{\rho}_{1H}\otimes\hat{\rho}_{2H}\left(\hat{a}^\dagger_{3H}(t_3)\hat{a}^\dagger_{4H}(t_4)\hat{a}_{4H}(t_4)\hat{a}_{3H}(t_3)\right)\right\} \\ &+\operatorname{Tr}\left\{\hat{\rho}_{1V}\otimes\hat{\rho}_{2V}\left(\hat{a}^\dagger_{3V}(t_3)\hat{a}^\dagger_{4V}(t_4)\hat{a}_{4V}(t_4)\hat{a}_{3V}(t_3)\right)\right\} \\ &+\operatorname{Tr}\left\{\hat{\rho}_{1H}\otimes\hat{\rho}_{1V}\otimes\hat{\rho}_{2H}\otimes\hat{\rho}_{2V}\left(\hat{a}^\dagger_{3H}(t_3)\hat{a}^\dagger_{4V}(t_4)\hat{a}_{4V}(t_4)\hat{a}_{3H}(t_3)\right)\right\} \\ &+\operatorname{Tr}\left\{\hat{\rho}_{1H}\otimes\hat{\rho}_{1V}\otimes\hat{\rho}_{2H}\otimes\hat{\rho}_{2V}\left(\hat{a}^\dagger_{3V}(t_3)\hat{a}^\dagger_{4H}(t_4)\hat{a}_{4H}(t_4)\hat{a}_{3V}(t_3)\right)\right\}. \end{aligned} \tag{4.71}$$

Henceforth, we assume $\alpha_{k,H}=\alpha_{k,V}$ (and thus $N_{kH}=N_{kV}\equiv N_k$), i.e. both coherent states are equally "strong". The analysis for $G^{(2x)}_{HH}(t_3,t_4)$ and $G^{(2x)}_{VV}(t_3,t_4)$ is conducted as before and the only difference is that now the mode envelope functions $\zeta_{k,H}$ and $\zeta_{k,V}$ are not constant but $\cos[\phi_k(t)]$ and $\sin[\phi_k(t)]$ for horizontal and vertical polarization, respectively. We calculate

$$\begin{aligned} G^{(2x)}_{HH}(t_3,t_4) = &\frac{N_1^2}{4}\cos^2\left[\phi_1(t_3)\right]\cos^2\left[\phi_1(t_4)\right]+\frac{N_2^2}{4}\cos^2\left[\phi_2(t_3)\right]\cos^2\left[\phi_2(t_4)\right] \\ &+\frac{N_1N_2}{4}\cos^2\left[\phi_1(t_3)\right]\cos^2\left[\phi_2(t_4)\right]+\frac{N_1N_2}{4}\cos^2\left[\phi_2(t_3)\right]\cos^2\left[\phi_1(t_4)\right] \\ &-\frac{N_1N_2}{2}\cos\left[\phi_1(t_3)\right]\cos\left[\phi_1(t_4)\right]\cos\left[\phi_2(t_3)\right]\cos\left[\phi_2(t_4)\right]\mathfrak{Re}\left\{g^{(1)}_1(\tau)g^{*(1)}_2(\tau)\right\}, \end{aligned} \tag{4.72}$$

and similarly,

$$\begin{aligned} G^{(2x)}_{VV}(t_3,t_4) = &\frac{N_1^2}{4}\sin^2\left[\phi_1(t_3)\right]\sin^2\left[\phi_1(t_4)\right]+\frac{N_2^2}{4}\sin^2\left[\phi_2(t_3)\right]\sin^2\left[\phi_2(t_4)\right] \\ &+\frac{N_1N_2}{4}\sin^2\left[\phi_1(t_3)\right]\sin^2\left[\phi_2(t_4)\right]+\frac{N_1N_2}{4}\sin^2\left[\phi_2(t_3)\right]\sin^2\left[\phi_1(t_4)\right] \\ &-\frac{N_1N_2}{2}\sin\left[\phi_1(t_3)\right]\sin\left[\phi_1(t_4)\right]\sin\left[\phi_2(t_3)\right]\sin\left[\phi_2(t_4)\right]\mathfrak{Re}\left\{g^{(1)}_1(\tau)g^{*(1)}_2(\tau)\right\}. \end{aligned} \tag{4.73}$$

Adding these two functions we obtain

$$\begin{aligned} G^{(2x)}_{HH}(t_3,t_4)+G^{(2x)}_{VV}(t_3,t_4) = &\frac{N_1^2}{4}P_\parallel[\phi_1(t_3),\phi_1(t_4)]+\frac{N_2^2}{4}P_\parallel[\phi_2(t_3),\phi_2(t_4)] \\ &+\frac{N_1N_2}{4}\left(P_\parallel[\phi_1(t_3),\phi_2(t_4)]+P_\parallel[\phi_2(t_3),\phi_1(t_4)]\right) \\ &-\frac{N_1N_2}{2}P_{\text{int}}(t_3,t_4)\mathfrak{Re}\left\{g^{(1)}_1(\tau)g^{*(1)}_2(\tau)\right\}, \end{aligned} \tag{4.74}$$

with

$$\begin{aligned} P_\parallel[\phi_k(t),\phi_l(t')] &:= \cos^2[\phi_k(t)]\cos^2[\phi_l(t')]+\sin^2[\phi_k(t)]\sin^2[\phi_l(t')] \\ P_{\text{int}}[\phi_1(t_3),\phi_1(t_4),\phi_2(t_3),\phi_2(t_4)] &:= \cos\left[\phi_1(t_3)\right]\cos\left[\phi_1(t_4)\right]\cos\left[\phi_2(t_3)\right]\cos\left[\phi_2(t_4)\right] \\ &\quad+\sin\left[\phi_1(t_3)\right]\sin\left[\phi_1(t_4)\right]\sin\left[\phi_2(t_3)\right]\sin\left[\phi_2(t_4)\right]. \end{aligned} \tag{4.75}$$

To make sure we derive correct contributions from the crossed-polarization terms, we better write them down explicitly. We do this for $G^{(2)}_{HV}(t_3, t_4)$, but the result is similar for $G^{(2)}_{VH}(t_3, t_4)$. We proceed along the lines of Equation (4.38), though we have to keep track of polarization mode indices.

$$
\begin{aligned}
G^{(2x)}_{HV}(t_3, t_4) &= \left\langle \hat{E}^-_{H3}(t_3)\hat{E}^-_{V4}(t_4)\hat{E}^+_{V4}(t_4)\hat{E}^+_{H3}(t_3)\right\rangle \\
&= \frac{1}{4}\left\langle \left(\zeta^*_1(t_3)\hat{a}^\dagger_{H1}(t_3) + \zeta^*_2(t_3)\hat{a}^\dagger_{H2}(t_3)\right)\left(\zeta^*_1(t_4)\hat{a}^\dagger_{V1}(t_4) - \zeta^*_2(t_4)\hat{a}^\dagger_{V2}(t_4)\right)\right. \\
&\quad \left.\times \left(\zeta_1(t_4)\hat{a}_{V1}(t_4) - \zeta_2(t_4)\hat{a}_{V2}(t_4)\right)\left(\zeta_1(t_3)\hat{a}_{H1}(t_3) + \zeta_2(t_3)\hat{a}_{H2}(t_3)\right)\right\rangle \\
&= \frac{1}{4}\zeta^*_1(t_3)\zeta^*_1(t_4)\zeta_1(t_4)\zeta_1(t_3)\left\langle \hat{a}^\dagger_{H1}(t_3)\hat{a}^\dagger_{V1}(t_4)\hat{a}_{V1}(t_4)\hat{a}_{H1}(t_3)\right\rangle \\
&+ \frac{1}{4}\zeta^*_1(t_3)\zeta^*_1(t_4)\zeta_1(t_4)\zeta_2(t_3)\left\langle \hat{a}^\dagger_{H1}(t_3)\hat{a}^\dagger_{V1}(t_4)\hat{a}_{V1}(t_4)\hat{a}_{H2}(t_3)\right\rangle \\
&- \frac{1}{4}\zeta^*_1(t_3)\zeta^*_1(t_4)\zeta_2(t_4)\zeta_1(t_3)\left\langle \hat{a}^\dagger_{H1}(t_3)\hat{a}^\dagger_{V1}(t_4)\hat{a}_{V2}(t_4)\hat{a}_{H1}(t_3)\right\rangle \\
&- \frac{1}{4}\zeta^*_1(t_3)\zeta^*_1(t_4)\zeta_2(t_4)\zeta_2(t_3)\left\langle \hat{a}^\dagger_{H1}(t_3)\hat{a}^\dagger_{V1}(t_4)\hat{a}_{V2}(t_4)\hat{a}_{H2}(t_3)\right\rangle \\
&- \frac{1}{4}\zeta^*_1(t_3)\zeta^*_2(t_4)\zeta_1(t_4)\zeta_1(t_3)\left\langle \hat{a}^\dagger_{H1}(t_3)\hat{a}^\dagger_{V2}(t_4)\hat{a}_{V1}(t_4)\hat{a}_{H1}(t_3)\right\rangle \\
&- \frac{1}{4}\zeta^*_1(t_3)\zeta^*_2(t_4)\zeta_1(t_4)\zeta_2(t_3)\left\langle \hat{a}^\dagger_{H1}(t_3)\hat{a}^\dagger_{V2}(t_4)\hat{a}_{V1}(t_4)\hat{a}_{H2}(t_3)\right\rangle \\
&+ \frac{1}{4}\zeta^*_1(t_3)\zeta^*_2(t_4)\zeta_2(t_4)\zeta_1(t_3)\left\langle \hat{a}^\dagger_{H1}(t_3)\hat{a}^\dagger_{V2}(t_4)\hat{a}_{V2}(t_4)\hat{a}_{H1}(t_3)\right\rangle \\
&+ \frac{1}{4}\zeta^*_1(t_3)\zeta^*_2(t_4)\zeta_2(t_4)\zeta_2(t_3)\left\langle \hat{a}^\dagger_{H1}(t_3)\hat{a}^\dagger_{V2}(t_4)\hat{a}_{V2}(t_4)\hat{a}_{H2}(t_3)\right\rangle \\
&+ \frac{1}{4}\zeta^*_2(t_3)\zeta^*_1(t_4)\zeta_1(t_4)\zeta_1(t_3)\left\langle \hat{a}^\dagger_{H2}(t_3)\hat{a}^\dagger_{V1}(t_4)\hat{a}_{V1}(t_4)\hat{a}_{H1}(t_3)\right\rangle \\
&+ \frac{1}{4}\zeta^*_2(t_3)\zeta^*_1(t_4)\zeta_1(t_4)\zeta_2(t_3)\left\langle \hat{a}^\dagger_{H2}(t_3)\hat{a}^\dagger_{V1}(t_4)\hat{a}_{V1}(t_4)\hat{a}_{H2}(t_3)\right\rangle \\
&- \frac{1}{4}\zeta^*_2(t_3)\zeta^*_1(t_4)\zeta_2(t_4)\zeta_1(t_3)\left\langle \hat{a}^\dagger_{H2}(t_3)\hat{a}^\dagger_{V1}(t_4)\hat{a}_{V2}(t_4)\hat{a}_{H1}(t_3)\right\rangle \\
&- \frac{1}{4}\zeta^*_2(t_3)\zeta^*_1(t_4)\zeta_2(t_4)\zeta_2(t_3)\left\langle \hat{a}^\dagger_{H2}(t_3)\hat{a}^\dagger_{V1}(t_4)\hat{a}_{V2}(t_4)\hat{a}_{H2}(t_3)\right\rangle \\
&- \frac{1}{4}\zeta^*_2(t_3)\zeta^*_2(t_4)\zeta_1(t_4)\zeta_1(t_3)\left\langle \hat{a}^\dagger_{H2}(t_3)\hat{a}^\dagger_{V2}(t_4)\hat{a}_{V1}(t_4)\hat{a}_{H1}(t_3)\right\rangle \\
&- \frac{1}{4}\zeta^*_2(t_3)\zeta^*_2(t_4)\zeta_1(t_4)\zeta_2(t_3)\left\langle \hat{a}^\dagger_{H2}(t_3)\hat{a}^\dagger_{V2}(t_4)\hat{a}_{V1}(t_4)\hat{a}_{H2}(t_3)\right\rangle \\
&+ \frac{1}{4}\zeta^*_2(t_3)\zeta^*_2(t_4)\zeta_2(t_4)\zeta_1(t_3)\left\langle \hat{a}^\dagger_{H2}(t_3)\hat{a}^\dagger_{V2}(t_4)\hat{a}_{V2}(t_4)\hat{a}_{H1}(t_3)\right\rangle \\
&+ \frac{1}{4}\zeta^*_2(t_3)\zeta^*_2(t_4)\zeta_2(t_4)\zeta_2(t_3)\left\langle \hat{a}^\dagger_{H2}(t_3)\hat{a}^\dagger_{V2}(t_4)\hat{a}_{V2}(t_4)\hat{a}_{H2}(t_3)\right\rangle .
\end{aligned}
\tag{4.76}
$$

We see immediately, on account of our earlier discussion, that only four terms can con-

tribute a non-zero value, namely

$$\begin{aligned}
\left\langle \hat{a}^\dagger_{H1}(t_3)\hat{a}_{H1}(t_3)\right\rangle\left\langle \hat{a}^\dagger_{V1}(t_4)\hat{a}_{V1}(t_4)\right\rangle &= N_1^2\\
\left\langle \hat{a}^\dagger_{H2}(t_3)\hat{a}_{H2}(t_3)\right\rangle\left\langle \hat{a}^\dagger_{V2}(t_4)\hat{a}_{V2}(t_4)\right\rangle &= N_2^2\\
\left\langle \hat{a}^\dagger_{H1}(t_3)\hat{a}_{H1}(t_3)\right\rangle\left\langle \hat{a}^\dagger_{V2}(t_4)\hat{a}_{V2}(t_4)\right\rangle &= N_1N_2\\
\left\langle \hat{a}^\dagger_{H2}(t_3)\hat{a}_{H2}(t_3)\right\rangle\left\langle \hat{a}^\dagger_{V1}(t_4)\hat{a}_{V1}(t_4)\right\rangle &= N_1N_2\,,
\end{aligned} \tag{4.77}$$

and we calculate

$$\begin{aligned}
G^{(2x)}_{HV}(t_3,t_4) = \frac{N_1^2}{4}\cos^2\left[\phi_1(t_3)\right]\sin^2\left[\phi_1(t_4)\right] + \frac{N_2^2}{4}\cos^2\left[\phi_2(t_3)\right]\sin^2\left[\phi_2(t_4)\right]\\
+ \frac{N_1N_2}{4}\Big(\cos^2\left[\phi_1(t_3)\right]\sin^2\left[\phi_2(t_4)\right] + \cos^2\left[\phi_2(t_3)\right]\sin^2\left[\phi_1(t_4)\right]\Big)\,,
\end{aligned} \tag{4.78}$$

$$\begin{aligned}
G^{(2x)}_{VH}(t_3,t_4) = \frac{N_1^2}{4}\sin^2\left[\phi_1(t_3)\right]\cos^2\left[\phi_1(t_4)\right] + \frac{N_2^2}{4}\sin^2\left[\phi_2(t_3)\right]\cos^2\left[\phi_2(t_4)\right]\\
+ \frac{N_1N_2}{4}\Big(\sin^2\left[\phi_1(t_3)\right]\cos^2\left[\phi_2(t_4)\right] + \sin^2\left[\phi_2(t_3)\right]\cos^2\left[\phi_1(t_4)\right]\Big)\,.
\end{aligned} \tag{4.79}$$

Adding these two functions we obtain

$$\begin{aligned}
G^{(2x)}_{HV}(t_3,t_4) + G^{(2x)}_{VH}(t_3,t_4) = \frac{N_1^2}{4}P_\perp[\phi_1(t_3),\phi_1(t_4)] + \frac{N_2^2}{4}P_\perp[\phi_2(t_3),\phi_2(t_4)]\\
+ \frac{N_1N_2}{4}\Big(P_\perp[\phi_1(t_3),\phi_2(t_4)] + P_\perp[\phi_2(t_3),\phi_1(t_4)]\Big)\,,
\end{aligned} \tag{4.80}$$

where

$$P_\perp[\phi_k(t),\phi_l(t')] \coloneqq \cos^2[\phi_k(t)]\sin^2[\phi_l(t')] + \sin^2[\phi_k(t)]\cos^2[\phi_l(t')]\,. \tag{4.81}$$

Now, using standard trigonometric identities,

$$\begin{aligned}
P_\parallel[\phi_k(t),\phi_k(t')] + P_\perp[\phi_k(t),\phi_k(t')] = 1\\
P_\parallel[\phi_1(t_3),\phi_2(t_4)] + P_\parallel[\phi_2(t_3),\phi_1(t_4)] + P_\perp[\phi_1(t_3),\phi_2(t_4)] + P_\perp[\phi_2(t_3),\phi_1(t_4)] = 1\,,
\end{aligned} \tag{4.82}$$

and adding Equations (4.74) and (4.80) gives thus

$$G^{(2x)}(t_3,t_4) = \frac{1}{4}\big(N_1+N_2\big)^2 - \frac{N_1N_2}{2}P_{\text{int}}(t_3,t_4)\mathfrak{Re}\Big\{g_1^{(1)}(\tau)g_2^{*(1)}(\tau)\Big\}\,. \tag{4.83}$$

For constant polarization angles $\phi_k(t) = \phi_k$,

$$P_{\text{int}}[\phi_1,\phi_2] = \cos^2(\phi_1)\cos^2(\phi_2) + \sin^2(\phi_1)\sin^2(\phi_2)\,, \tag{4.84}$$

which means the the anticorrelation dip visibility now depends on the relative polarization of the two lasers, though not its shape. For two CW lasers with Lorentzian or Gaussian spectrum we obtain the interference landscapes shown in Figure 4.4.

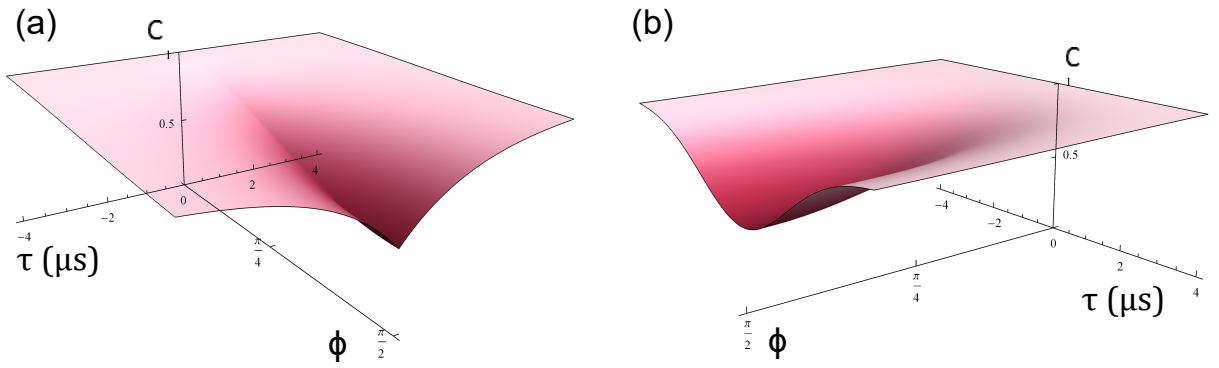

Figure 4.4: **Laser HOM Dip Polarization Interference Landscapes.** With polarization (via relative polarization angle ϕ) we have another degree of freedom in addition to the detection time difference τ for control over laser HOM interference. Plotted here is Equation (4.83) for **(a)** Lorentzian and **(b)** Gaussian spectrum with $\phi_2 = 0$. C = coincidences.

4.5.7 Laser HOM Square Wave Interference Landscapes

The typical HOM dip has an inverse Gaussian shape, but it is possible to obtain more "exotic" shapes. In type-II parametric downconversion, for example, one can get triangular shapes [149]. Non-stationary light sources such as pulsed lasers give rise to second-order cross-correlation functions that depend on the optical delay between the two modes, adding another degree of freedom. In fact any kind of intensity modulation technique gives rise to non-trivial wavepackets $\zeta_k(t)$, and since polarization modulation can be regarded a type of intensity modulation, we could work with non-trivial mode functions. However, we already laid the groundwork for our specific problem in the previous section and can directly make use of the result (4.83). In our experiment we switch between two linear and orthogonal polarizations, say H (horizontal) and V (vertical). An ideal switch between H and V polarization is described by the (Heaviside) step function

$$H(t) \coloneqq \begin{cases} 0 & \text{for} \quad |t| < 0 \\ \frac{1}{2} & \text{for} \quad t = 0 \\ 1 & \text{for} \quad |t| > 0 \end{cases}, \tag{4.85}$$

which we can press, whenever we like. For the current experiment we consider a simple, pre-determined sequence, namely a square wave $\Pi(x)$, which is defined as

$$\Pi(t) \coloneqq \begin{cases} 0 & \text{for} \quad |t| > \frac{1}{2} \\ \frac{1}{2} & \text{for} \quad t = \frac{1}{2} \\ 1 & \text{for} \quad |t| < \frac{1}{2} \end{cases}, \tag{4.86}$$

together with

$$\Pi(t+T) = \Pi(t)\,, \tag{4.87}$$

where T is the period. More generally, we can let the time argument

$$t \to \frac{t-\tau_{\text{opt}}}{T}\,, \tag{4.88}$$

where τ_{opt} and T are offset (which in our case results from an optical delay) and period, respectively. In a first step, let us make only one polarization angle time-dependent. Thus, let us set $\phi_2 = 0$ (second beam is always H-polarized), and ϕ_1 is modulated between 0 and $\pi/2$ so that

$$\phi_1(t) \coloneqq \begin{cases} 0 & \text{for} \quad |t| > \frac{1}{2} \\ \frac{\pi}{4} & \text{for} \quad t = \frac{1}{2} \\ \frac{\pi}{2} & \text{for} \quad |t| < \frac{1}{2} \end{cases}\,, \tag{4.89}$$

with $\phi_1(t+T) = \phi_1(t)$. More succinctly, we write

$$\phi_1(t) = \frac{\pi}{4}\left(1 + \text{SquareWave}\left[\frac{t-\tau_{\text{opt}}}{T}\right]\right)\,, \tag{4.90}$$

where SquareWave$(\cdot)$ represents the square wave in the Wolfram Language, and is plotted in Figure 4.5. The reason we adopt this definition is that the piece-wise definition (4.89) is not particularly useful theoretically, and analytical expressions such as [150]

$$\Pi(t) = \frac{A}{2}\sum_{n=-\infty}^{\infty} \text{Sinc}\left(\frac{n}{2}\right)\exp\left(2\pi i\frac{nt}{T}\right)\,, \tag{4.91}$$

though correct, more a burden than of help numerically. Thus, since we have to choose a representation of the square wave anyway, we may pick the most serviceable one right away. The polarization function then becomes ($t_0 \equiv t_3$ and $t_4 = t_0 + \tau$, and $\tau_{\text{opt}} = 0$ as the optical delay does not matter here)

$$P_{\text{int}}[\phi_1] = \frac{1}{4}\left(1 + \text{SquareWave}\left[\frac{t_0}{T}\right]\right)\left(1 + \text{SquareWave}\left[\frac{t_0+\tau}{T}\right]\right) \tag{4.92}$$

and the second-order cross-correlation function (4.83), with $N_1 = N_2 = 1$, takes the form

$$G^{(2x)}(t_0,\tau,\tau_{\text{opt}}) = 1 - \frac{F(\tau)}{8}\left(1 + \text{SquareWave}\left[\frac{t_0}{T}\right]\right)\left(1 + \text{SquareWave}\left[\frac{t_0+\tau}{T}\right]\right)\,. \tag{4.93}$$

For "true" coincidences $\tau = 0$, and thus $F(0) = 1$, as well as

$$P_{\text{int}}[\phi_1] = \frac{1}{2}\left(1 + \text{SquareWave}\left[\frac{t_0}{T}\right]\right)\,, \tag{4.94}$$

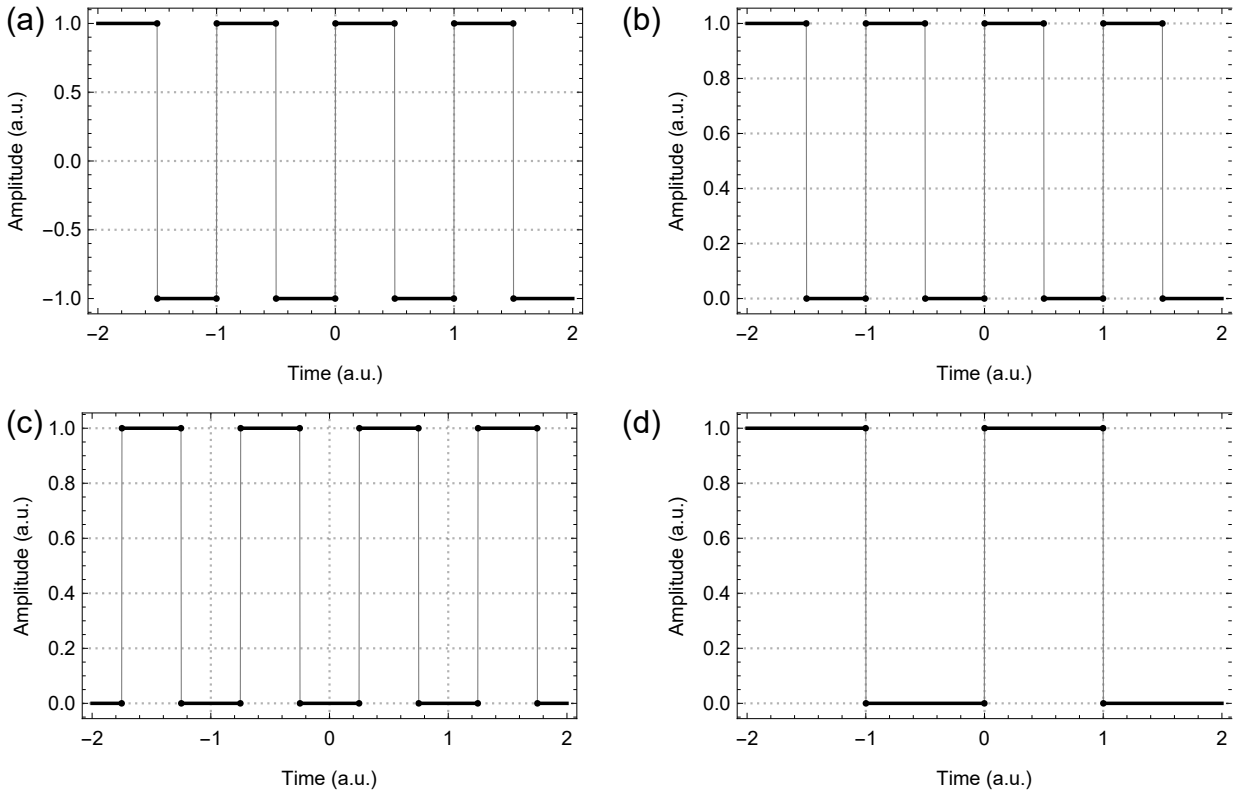

Figure 4.5: **Plot of Square Waves. (a)** Plot of SquareWave(t) as defined in the Wolfram Language. **(b)** Plot of the "normalized" version, identical to Eq. (4.92), which alternates between 0 and 1. A **(c)** shifted ($\tau_{\text{opt}} = 1/4$) version and **(d)** one with twice ($T = 2$) the period are also shown.

whereby

$$G^{(2x)}(t_0, \tau_{\text{opt}}) = 1 - \frac{1}{4}\left(1 + \text{SquareWave}\left[\frac{t_0 - \tau_{\text{opt}}}{T}\right]\right) . \tag{4.95}$$

Despite the fact that we are working with *continuous*-wave lasers, we do get a dependence of HOM interference on the optical delay. Intuitively, this makes sense because the modulation essentially gives us a pulse train (at least on the level on modes). At this point, the interested reader may want to revisit the dispute between Chen *et al.* [136] and Shapiro *et al.* [137], outlined in Section 4.3. Figure 4.6 shows the interference landscape described by Equation (4.93) but the question is whether we can actually resolve it? The problem is the t_0-dependence. The plots in Figure 4.6 assumed an arbitrarily fixed value. However, if we don't have this piece of information, a coincidence detection, and hence interference, can happen at any point t_0! As we accumulate statistics to actually reconstruct $G^{(2x)}(t_0, \tau, \tau_{\text{opt}})$ (remember, this *is* a statistical quantity), we do this for a certain measurement time T_M (essentially, we are replacing the ensemble with a time average), and thus integrate over

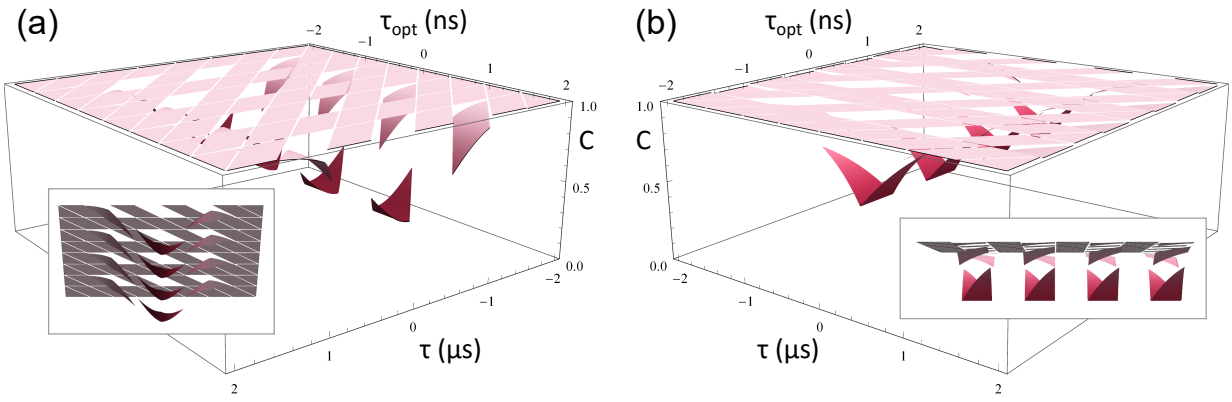

Figure 4.6: **Square Laser HOM Interference Landscapes.** The square wave polarization-modulation of one input field leads to an interference pattern in both detection time difference τ and optical delay τ_{opt}. **(a)** Gaussian and **(b)** Lorentzian spectrum. Parameters for Equation (4.93) are $t_0 = 0$ and $T = 1$. C = coincidences.

all possible t_0. For instance, in experiments without time resolution, instead of Equation 4.95, we would measure

$$\begin{aligned} G^{(2x)}(\tau_{\text{opt}}) &:= \int_{-T_M/2}^{T_M/2} dt_0\, G^{(2x)}(t_0, \tau_{\text{opt}}) \\ &= T_M - \frac{1}{4}\left(T_M + \int_{-T_M/2}^{T_M/2} dt_0\, \text{SquareWave}\left[\frac{t_0 - \tau_{\text{opt}}}{T}\right]\right) . \end{aligned} \tag{4.96}$$

For the evaluation of the integral we first perform a change of variables, namely

$$\begin{aligned} \tilde{t}_0 &:= \frac{t_0 - \tau_{\text{opt}}}{T} \\ d\tilde{t}_0 &= dt_0/T\,, \end{aligned} \tag{4.97}$$

so that the integration boundaries

$$\pm\frac{T_M}{2} \to \Lambda_\pm := \frac{\pm\frac{T_M}{2} - \tau_{\text{opt}}}{T} = \frac{\pm T_M - 2\tau_{\text{opt}}}{2T}\,. \tag{4.98}$$

The resulting integral,

$$\int_{\Lambda_-}^{\Lambda_+} d\tilde{t}_0\, \text{SquareWave}\left(\tilde{t}_0\right)\,, \tag{4.99}$$

is a matter of triviality when we consider that, usually, our measurement time T_M is much larger than either T or τ_{opt}. For example, $T \sim 10^{-6}$ (MHz modulation), $\tau_{\text{opt}} \sim 10^{-9}$, and $T_M \sim 1\,$seconds, which implies $\Lambda_\pm \approx \pm T$. This gives us integration limits with identical absolute values and so, to a very good approximation,

$$\int_{-T}^{T} d\tilde{t}_0\, \text{SquareWave}\left(\tilde{t}_0\right) \approx 0\,, \tag{4.100}$$

because SquareWave(t) is an antisymmetric function. With exception of the factor T_M, which can be absorbed into a coincidence rate or factored out via normalization, we thus obtain,

$$G^{(2x)}(\tau) = \frac{3}{4} T_M \,. \tag{4.101}$$

The coincidence reduction is only 25 % and thus, in general, we incur a drastic visibility cost from modulating without *phase information*, i.e. the inability to fix t_0. When a coincidence happens, polarizations are sometimes parallel (HH in this case), and sometimes perpendicular (HV). Because we modulate with a 50 % duty cycle (i.e. half the period H, the other half V), a coincidence reduction due to HOM interference can only happen half the time it usually does.

In summary, with polarization modulation we obtain a second-order cross-correlation function, Equation (4.93), that depends on both detection time difference τ and optical delay τ_{opt}. They are decoupled from each other, and yet it is not guaranteed that we can simply take a particular τ_{opt}-slice in the interference landscapes of Figure 4.6, i.e. do a "normal" HOM dip measurement, because without fixing t_0, the statistical average reduces the interference visibility. Lastly, note that Equation (4.101) is independent of τ_{opt}, which intuitively makes sense because the modulation is periodic and our average over time does not care about zero offsets.

4.5.8 Laser HOM Interference with Double Square Wave Modulation

We now consider the slightly more complicated situation where we modulate both polarization angles,

$$\begin{aligned} \phi_1(t) &= \frac{\pi}{4}\left(1 + \text{SquareWave}\left[\frac{t-\tau_{\text{opt}}}{T}\right]\right) \\ \phi_2(t) &= \frac{\pi}{4}\left(1 + \text{SquareWave}\left[\frac{t}{T}\right]\right) . \end{aligned} \tag{4.102}$$

Note that we do not explicitly introduce a separate optical delay for the second field, because the overlap polarization pattern at the beam splitter, and thus HOM interference, is only dependent on the relative optical delay. Restricting ourselves to true coincidences

($\tau = 0$, or, equivalently, $t_3 = t_4 \equiv t_0$), the polarization function becomes

$$\begin{aligned} P_{\text{int}}(t_0) &= \cos^2\left[\phi_1(t_0)\right]\cos^2\left[\phi_2(t_0)\right] + \sin^2\left[\phi_1(t_0)\right]\sin^2\left[\phi_2(t_0)\right] \\ &= \frac{1}{4}\left(1 + \text{SquareWave}\left[\frac{t_0}{T}\right]\right)\left(1 + \text{SquareWave}\left[\frac{t_0 - \tau_{\text{opt}}}{T}\right]\right) \\ &+ \frac{1}{4}\left(1 - \text{SquareWave}\left[\frac{t_0}{T}\right]\right)\left(1 - \text{SquareWave}\left[\frac{t_0 - \tau_{\text{opt}}}{T}\right]\right) \\ &= \frac{1}{2}\left(1 + \text{SquareWave}\left[\frac{t_0}{T}\right]\text{SquareWave}\left[\frac{t_0 - \tau_{\text{opt}}}{T}\right]\right), \end{aligned} \tag{4.103}$$

which gives us the following second-order cross-correlation function ($N_1 = N_2 = 1$)

$$G^{(2x)}(t_0, \tau_{\text{opt}}) = \frac{1}{4}\left(3 - \text{SquareWave}\left[\frac{t_0}{T}\right]\text{SquareWave}\left[\frac{t_0 - \tau_{\text{opt}}}{T}\right]\right). \tag{4.104}$$

This function spans the HOM interference landscape displayed in Figure 4.7. Clearly, double square wave modulation impresses itself, though the landscape's remarkable features only start to become apparent when we look at Figure 4.8. There we show the two modulator signals for ϕ_1 and ϕ_2, as well as $G^{(2x)}(t_0, \tau_{\text{opt}})$, as a function of initial detection time, or *modulator phase* t_0, for various optical delays τ_{opt}. First of all note that here the coincidences follow a square waveform, completely absent in traditional HOM *dips*. Moreover, the period and duty cycle of this waveform changes *not* as a function of modulation period (which stays constant, $T = 1$), but as a function of optical delay. In particular, for $\tau_{\text{opt}} = 0.25$ (we use arbitrary units here), the coincidence wave has half the original modulation period! This is not something we could get with a simple (single) modulation. We also see that the coincidence waveform follows the overlap pattern of the two modulator signals for ϕ_1 and ϕ_2 and if we look closely, we find a nice interpretation in the photon picture of HOM dips: whenever the two polarizations are identical, coincidences drop to 0.5, and whenever they are opposite, they rise to 1. In the extreme case when polarization modulation patterns are completely synchronized (corresponding here to $\tau_{\text{opt}} = 0$), then two photons at the beam splitter always have the same polarization (though whether it is H or V depends on time), and thus always show HOM interference with 50 % visibility. In the other extreme, when the optical delay is such that two photons always have opposite polarization at the beam splitter (corresponding here to $\tau_{\text{opt}} = 0.5$), they never interfere and therefore, coincidences are flat at 1.

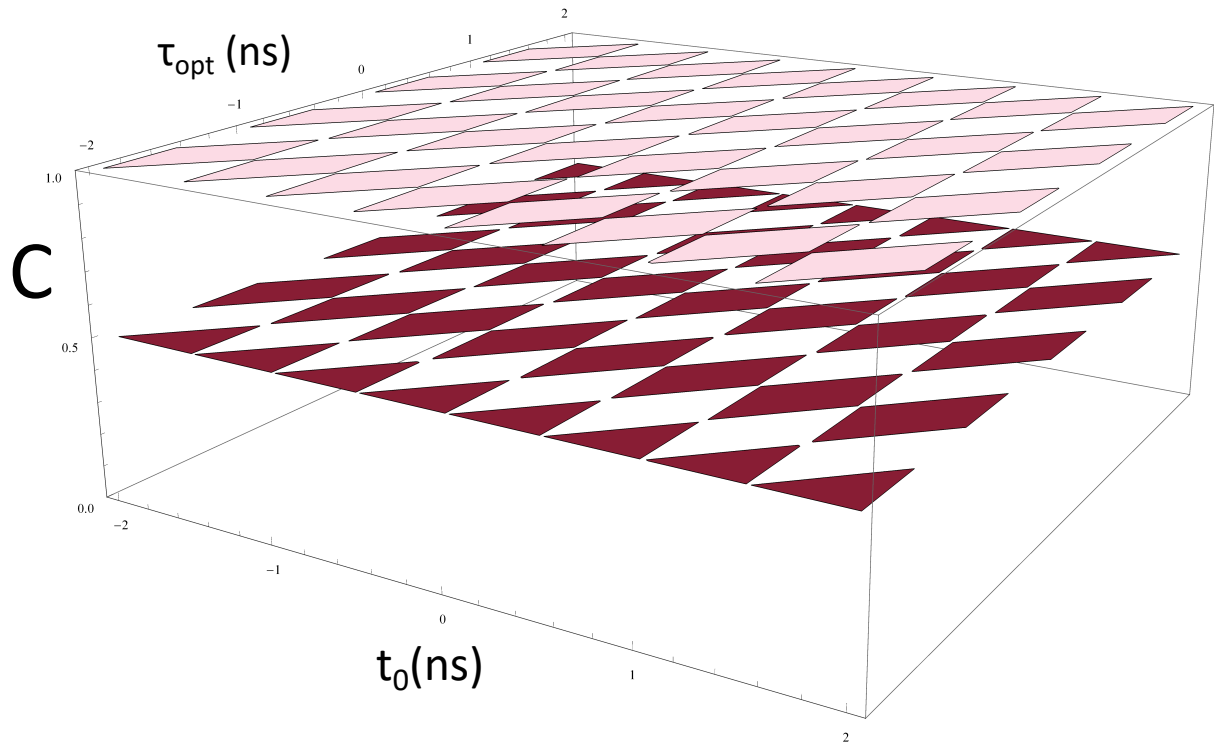

Figure 4.7: **Laser HOM Interference with Double Square Wave Modulation.** Plot of Equation (4.104) for $T = 1$. This two-photon coincidence landscape is distinguished by its rhomboid wells resulting from square-wave polarization modulation of *both* input fields to the HOM beam splitter. The well depths depend on "which" coincidences we consider: here we get the full 50 % well visibility as we restrict ourselves to "true" coincidences, namely those for which the detection time difference $\tau \approx 0$. Events $|\tau| \neq 0$ require us to take into account the visibility reduction governed by $F(\tau)$. C= coincidences.

4.5.9 Laser HOM Interference with Double Square Wave Modulation and Phase Averaging

We get another interesting phenomena when we neglect phase information t_0 but keep modulating both fields. Let us therefore integrate over t_0,

$$\begin{aligned} G^{(2x)}(\tau, \tau_{\text{opt}}) &= \int_{-T_M/2}^{T_M/2} dt_0 \, G^{(2x)}(t_0, \tau_{\text{opt}}) \\ &= T_M - \frac{1}{4}\left(T_M + p(\tau_{\text{opt}}, T_M)\right), \end{aligned} \tag{4.105}$$

where

$$p(\tau_{\text{opt}}, T_M) := \int_{-T_M/2}^{T_M/2} dt_0 \, \text{SquareWave}\left(\frac{t_0}{T}\right) \text{SquareWave}\left(\frac{t_0 - \tau_{\text{opt}}}{T}\right). \tag{4.106}$$

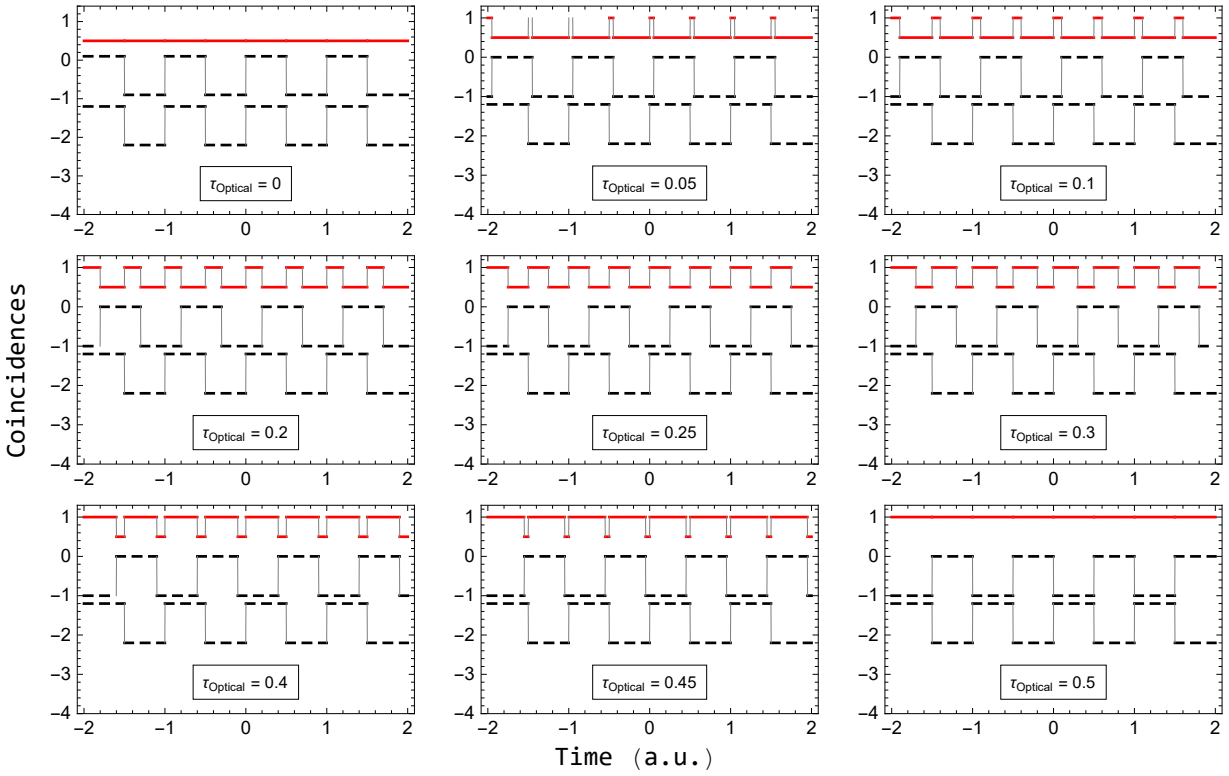

Figure 4.8: **Square HOM Waves.** Plots of Equation (4.104) (red solid line) for optical delays ranging from 0 to 0.5 (a.u.) and $T = 1$. For each τ_{opt} we also show traces of polarization modulator signals (black dashed lines), i.e. plots of Equations (4.102), which are rescaled and offset for sake of presentation. The bottom trace is the (reference) modulation signal for ϕ_2 (independent of τ_{opt}). The middle trace, i.e. modulation of ϕ_1, changes with τ_{opt}, as does the overlap pattern of the two modulator signals for ϕ_1 and ϕ_2 at the HOM beam splitter, which is reflected in the detected coincidences (detailed discussion in the main text).

Let us change the variables

$$\begin{aligned} \tilde{t}_0 &:= t_0/T \\ d\tilde{t}_0 &= dt_0/T\,, \end{aligned} \tag{4.107}$$

with new integration boundaries $\pm T_M/2T$, and define $\Delta := \tau_{\text{opt}}/T$. The result

$$p(\tau_{\text{opt}}, T_M) = T \int_{-T_M/2T}^{T_M/2T} d\tilde{t}_0\, \text{SquareWave}\left(\tilde{t}_0\right) \text{SquareWave}\left(\tilde{t}_0 - \Delta\right) \tag{4.108}$$

is reminiscent of the autocorrelation $\star$ of two functions, namely

$$(\text{SquareWave} \star \text{SquareWave})(\Delta) = \lim_{T_M \to \infty} p(\tau_{\text{opt}}, T_M), \tag{4.109}$$

which is related to their convolution $*$,

$$(\text{SquareWave} \star \text{SquareWave})(\Delta) = \text{SquareWave}\,(\Delta) * \text{SquareWave}\,(-\Delta)\ . \tag{4.110}$$

We know that convolving two square waves yields a triangle wave [151, 152], nudging us towards an educated guess that our autocorrelation function over a finite interval also has this form. Indeed, we can explicitly calculate (the factor T cancels with a scaling factor coming from the integration limits)

$$p(\tau_{\text{opt}}, T_M) = T_M \text{TriangleWave}\left(\Delta - \frac{3}{4}\right)\ , \tag{4.111}$$

where TriangleWave$(\cdot)$ represents the triangle wave in the Wolfram Language. As we substitute this result into (4.105), we finally get (replacing Δ with its definition)

$$G^{(2x)}(\tau_{\text{opt}}) = T_M\left(1 - \frac{1}{4}\left[1 + \text{TriangleWave}\left\{\frac{\tau_{\text{opt}}}{T} - \frac{3}{4}\right\}\right]\right). \tag{4.112}$$

This result is quite remarkable for the following reason. Apart from scaling factor T_M, which is unimportant, this equation looks remarkably similar to (4.95): the triangular wave takes the place of the square wave but without the t_0-dependence. In other words, despite the fact that we average over time, $G^{(2x)}$ does *not* lose its dependence on the optical delay! Compare that to the case we studied previously: if we modulate only one field, then integration over t_0 washes out interference patterns. Thus, whereas *individual* phase information is needed to resolve those features in the $G^{(2x)}$ interference landscape that are due to individually modulated fields, when both fields are modulated, traits depending on the *relative* phase (controlled via τ_{opt}) survive. This is one of those effects we demonstrate experimentally.

4.5.10 Remark

We took a semi-classical approach in that we commenced with the quantum mechanical correlation function, which subsequently is converted into a classical coherence function using the optical equivalence theorem. I believe this method is the most powerful and versatile for our task, in which we are asked to walk along the quantum-classical boundary. Adopting this *modus operandi*, we can always directly compare the results obtained with classical and quantum states of light. In particular, we move within the correct framework to prove the 50 % visibility bound for classical field states [103]. Nevertheless, other approaches for this particular problem exist. For example, in the study of weak coherent pulses one calculates the quantum-mechanical expectation value for truncated and fully

phase-randomized coherent states [105, 144, 153]. For CW lasers, a fully classical description in terms of intensity correlations can be used [121, 148]. In both cases, however, precisely because only one theoretical aspect of the phenomenon is studied, extra care needs to be taken.

4.6 Experimental Setup

We now proceed to experimentally demonstrate the results of our theoretical analysis. We first verify Equation (4.83), i.e. polarization sensitivity of the HOM dip. For this we use the setup sketched in Figure 4.9 (a). We then test the predictions of Equation (4.112), namely a HOM triangle wave. The critical addition to the previous setup is an optical delay line, as shown in Figure 4.9 (b). Finally, we are going to distill a HOM square wave, as suggested by Equation (4.104). The essential addition here is to use the trigger from the arbitrary waveform generator driving the polarization modulator, as shown in Figure 4.9 (c). Photos of the experimental setups in the lab are shown in Figures 4.10 and 4.11.

In the first setup, light from a continuous-wave grating-stabilized laser diode (single mode, 785 nm, > 2 mW, $\sim \mu$s coherence time, which can be varied) is attenuated to single photon levels using either ND filters in free space or a variable fiber attenuator (VFA). Photons are then split up in a 10:90 fiber beam splitter (FBS). The 10 % output is coupled into a variable free-space delay line (VFSD), though the delay is fixed for the first experiment. The 90 % output is coupled into a fixed fiber delay (FFD). Starting with 90 % we account roughly for the losses through the fiber (as compared to the free-space delay line losses). The fiber is ~ 2 km long and supports a single mode at around 1550 nm. Thus, for 785 nm the fiber is multimode. However, connecting a 785 nm single-mode fiber to the output of the telecom fiber acts like a spatial filter so that multimodicity only results in losses [154]. A far bigger concern are polarization drifts in the fiber. These only play a role, however, if the fiber, or the glass of which it is made of, is far from thermodynamic equilibrium. This happens if the fiber is bent or exposed to temperature and humidity changes. We take care of this by placing the fiber spool inside an insulating box and let it rest for a day before taking data. Photons from the two paths are then coupled into a free-space HOM interferometer, defined by a 50:50 non-polarizing beam splitter (BS). Before recombination at the BS, however, polarizers (POL) define linear polarization axis and a half-wave plate (HWP) is used to rotate the polarization of the beam, coming from the free-space delay line, into any desired linear polarization. After the BS, photons are coupled into single-mode fibers and sent into time-resolving single-photon detectors (TRSPD). The TRSPD consists of silicon avalanche photodiodes, which, whenever they detect a photon,

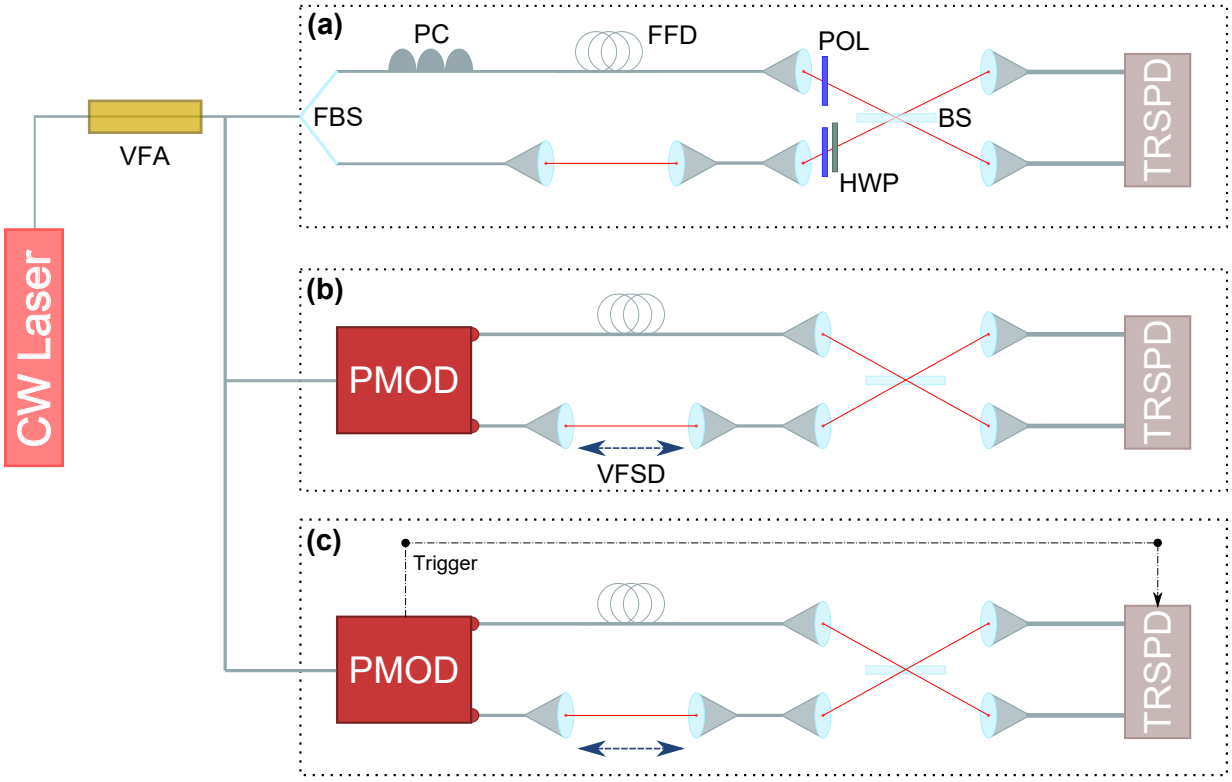

Figure 4.9: **Sketch of the Three Laser HOM Experiments.** Three CW Laser HOM Experiments to demonstrate **(a)** polarization dependence, **(b)** optical delay dependence and **(c)** modulator phase dependence. The first experiment is a "standard" Hong-Ou-Mandel experiment with laser light, where the distinguishability is controlled via polarization. (b) As we modulate polarization, and thereby change the relative overlap of the fields at the HOM beam splitter using a VFSD, the distinguishability becomes time-dependent. (c) However, only with additional timing information, delivered by the modulation trigger, can we actually resolve the HOM dip into the modulation pattern. VFA: variable fiber attenuator, FBS: 10:90 fiber beam splitter, PC: polarization controller, FFD: fixed 2 km fiber delay line, VFSD: variable free-space delay line, POL: polarizer, HWP: half-wave plate, BS: (HOM) 50:50 non-polarizing beam splitter, PMOD (see Figure 4.12 for details): polarization-modulator, TRSPD: time-resolving single-photon detectors.

sent a signal to time taggers, which assign time stamps to detection events with 78.125 ps time resolution.

The whole setup is basically a big Mach-Zehnder interferometer "pumped" with highly attenuated laser light. This permits interferometry in form of correlation measurements in the single-photon counting regime [110, 111, 155, 156]. The ubiquitous feature in our setup is, of course, the long (2 km) delay line in one of the two interferometer paths. However,

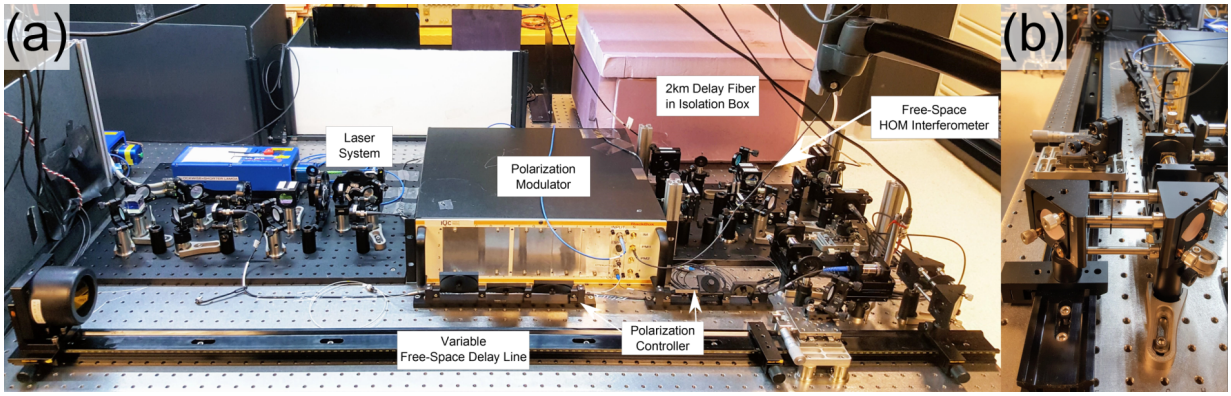

Figure 4.10: **Setup for Free-Space Laser HOM Experiment. (a)** The optical table with polarization-modulated, continuous-wave grating-stabilized laser diode, fixed fiber delay and variable free-space delay line, and Hong-Ou-Mandel interferometer. **(b)** View down the variable free-space delay line, with retroreflector positioned at maximum distance.

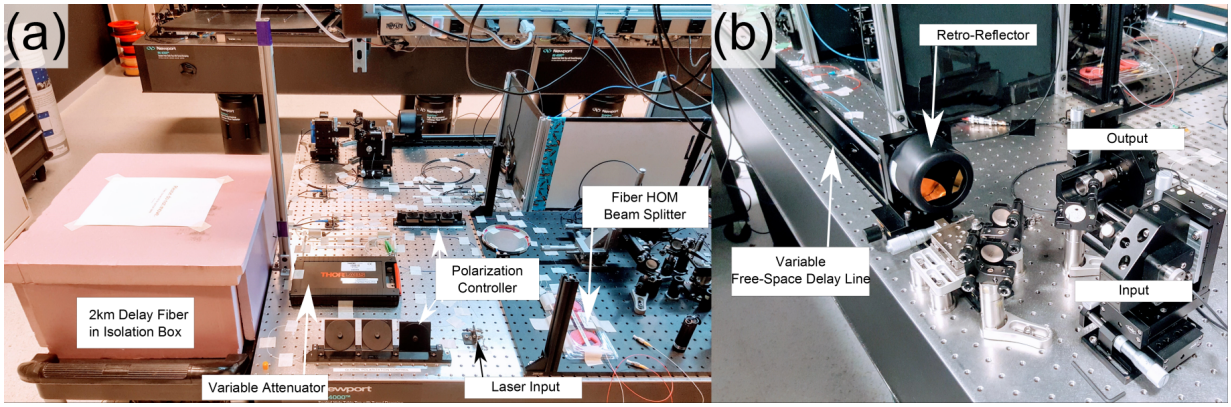

Figure 4.11: **Setup for Fiber-Based Laser HOM Experiment. (a)** The interferometer, with exception of the free-space delay line, is now fully fiber-based and a in-fiber variable attenuator is used instead of ND filters. The fiber beam splitter is a Thorlabs TN785R5F2 and has near-perfect 50:50 splitting ratio with negligible effect on polarization. **(b)** An updated version of the free-space delay line with improved fiber couplers and a longer delay line.

this path imbalance is only to suppress second-order interference at the output ports of the interferometer (the delay line is longer than the laser coherence length). Elimination of second-order interference allows us to isolate a pure fourth-order interference pattern, namely the (CW laser) HOM effect. There are other methods to phase-randomize two laser beams. Alternatively, one may consider fast modulation of the optical path length in one arm using a piezoelectric actuator [113], or the use of acousto-optic modulators [121].

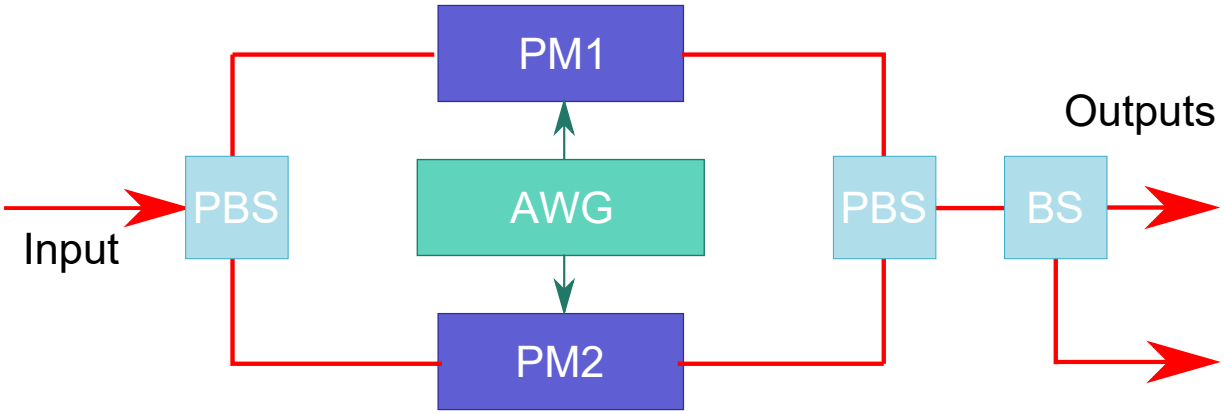

Figure 4.12: **Schematic of a Polarization Modulator (PMOD in Figure 4.9).** Light in a superposition of horizontal and vertical polarization is split at a polarizing beam splitter (PBS). The relative phase between horizontal and vertical polarization is controlled with two phase modulator driven by an arbitrary waveform generator (AWG). Light is then recombined on a second PBS, yielding output state (4.114). We split

In the second setup we send attenuated laser light directly into a polarization-modulator (PMOD), thus relaying the usable laser light to the modulator output: we essentially have a polarization-modulated laser. Though polarization modulation is entirely classical, we make use of Dirac's intuitive notation to briefly describe the working principle of our polarization modulator, which has been used for quantum key distribution (QKD) experiments in our labs (see for example [157, 158]), and which is illustrated in Figure 4.12. Treating the polarization modulator as a black box, the input state is

$$|\Psi\rangle_{\text{out}} = \alpha|H\rangle + \beta e^{i\phi}|V\rangle \tag{4.113}$$

and the output state

$$|\Psi\rangle_{\text{out}} = \alpha|H\rangle + \beta e^{i(\phi+\Theta)}|V\rangle\,, \tag{4.114}$$

where Θ is the relative phase impressed by the two phase modulators. In principle, we can employ both phase modulator (synchronized), in which case they impress phases Θ_1 and Θ_2 onto the fields. However, apart from technical reasons for doing this (share the workload between two modulators, i.e. reducing the voltage needed per modulator for a full π-shift), we accrue no benefit for such a detailed treatment here. Now, we can always set $\phi = 0$, for example by using a linear polarizer at the input. Then we can define the four time-*independent* output states shown in Table 4.1 using appropriate phase modulator driving voltages. The output states become time-dependent as soon as we start to modulate the phase modulator, i.e. sending a driving signal from an arbitrary waveform generator (AWG). Which of the four states we actually use for the experiment depends on

(unitary) polarization transformations along the experimental setup. As a simple example, we show in Table 4.1 the action of a QWP. In our experiment, we have fiber channels that apply random, time-dependent unitaries. Usually in that case, active polarization (pre-) compensation is required before any data can be taken. For example, implementations of the BB84 protocol encodes information using all four polarization states $|H\rangle$, $|V\rangle$, $|D\rangle$, and $|A\rangle$, but if we do not characterize our transmission channel, then the receiver won't be able to extract any meaningful message. Here, however, all we want are any two orthogonal polarization states, since the raw polarization HOM interference visibility only depends on the scalar product of two polarization states and not on the specific pair that gives us, for example, a scalar product of zero. Thus, in our experiment, we only use a manual polarization controller (PC, "bat ears") in one path to alter the relative polarization (see Figure 4.9). A simple two-state (H/V) polarization analyzer after any HOM beam splitter output port can be used to equalize the two channel unitaries using just this one PC. If the polarization modulation is to have any effect, we have to take out the POLs and HWP in front of the BS (which we use in the first experiment).

U_{PM} (V)	Θ	$\lvert\Psi\rangle_{\mathrm{out}}$	After QWP
1.65	$\frac{\pi}{2}$	$\alpha\lvert H\rangle + i\beta\lvert V\rangle$	$\lvert H\rangle$
4.95	$\frac{3\pi}{2}$	$\alpha\lvert H\rangle - i\beta\lvert V\rangle$	$\lvert V\rangle$
0	0	$\alpha\lvert H\rangle + \beta\lvert V\rangle$	$\lvert D\rangle$
2.3	π	$\alpha\lvert H\rangle - \beta\lvert V\rangle$	$\lvert A\rangle$

Table 4.1: **Polarization Modulator Settings.** Summarized are phase modulator voltages responsible for optical phase shifts Θ, and the polarization state $|\Psi\rangle_{\mathrm{out}}$ after the modulator. Also shown is the action of a quarter-wave plate (QWP) (see e.g. [159]): we can chose between two sets of orthogonal polarization states, namely (H, V) and (D, A). Note that the voltages depend on both temperature and modulation frequency and need to be adjusted accordingly.

Finally, for this experiment we need to make use of the free-space optical delay line. This part of the setup consists of an optical rail with 1/20-inches markers, which allows us to set the position with 1/40 inch accuracy, and a hollow retroreflector mounted on a carrier, which also has a marking engraved. Alignment of the optical delay line was performed prior to experiments and consisted of mounting the retroreflector centrally (ensure this using pin holes along propagation path) and coupling light out and into free space such

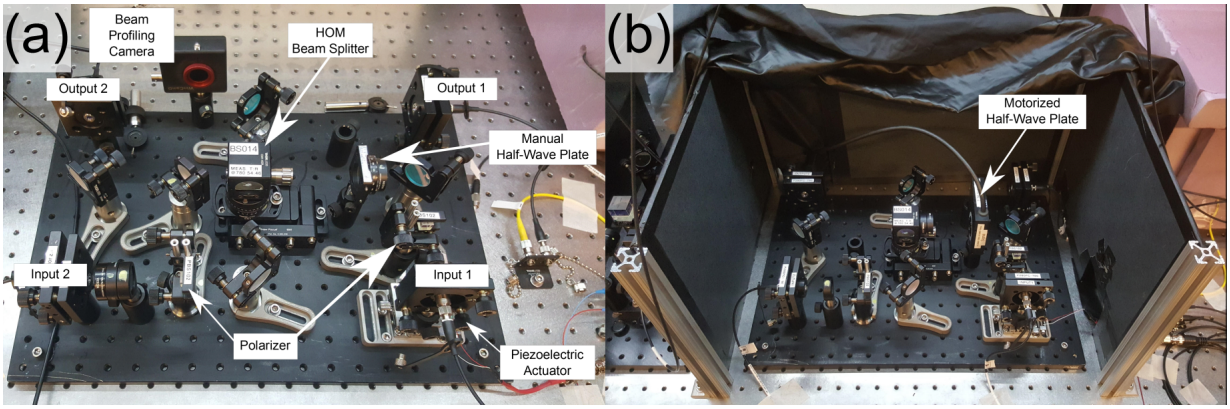

Figure 4.13: **Setup of the Free-Space HOM Interferometer. (a)** HOM interferometer alignment. To ensure photon indistinguishability, we need to overlap spatial modes at the HOM beam splitter (BS). This is achieved as follows. We split up laser light using a 50:50 BS and sent one beam into input 1 and the other into input 2 of the HOM interferometer. Since we use single-mode fibers, both beams are Gaussian. When the two beams overlap at the HOM BS, a spatial second-order interference pattern can be observed using a beam profiling camera: stripes tell us the relative inclination of the two beams, which can be steered using mirrors. A piezoelectric actuator can be used to scan the interferometer phase. As we scan the phase, a beating interference pattern is observed on the camera and as we align the beams using mirrors, stripes give way to a uniform intensity distribution that periodically varies between zero and maximum intensity. Achieving this beating at any two points along the beam in output port 2, where the camera is placed, we ensure perfect beam overlap at the beam splitter. **(b)** After the initial alignment, we put the half-wave plate in a motorized mount for better experimental precision. The polarizers ensure identical, horizontal polarization but need to be taken out, of course, for experiments with polarization modulation.

that at all positions of the retroreflector the coupling efficiency is roughly constant (use collimators with adjustable focus to control beam divergence).

The third setup is identical to the second one except for an additional signal that we record. The arbitrary waveform generator (AWG) that drives the PMOD (not drawn separately in Figure 4.9), can send a trigger signal whenever a new modulation period starts. We record a down-sampled version of this. Downsampling is necessary because the time tagger speed is only $\sim 10\,\mathrm{MHz}$ but our modulation speed is $\sim 350\,\mathrm{MHz}$. The downsampled signal we use is at $\sim 350\,\mathrm{kHz}$, and assuming good stability of the AWG, the missing trigger signals are equally spaced between the recorded trigger signals, allowing an exact interpolation during data analysis.

4.7 Experimental Results

4.7.1 Time Tag Analysis

Before showing any experimental results, I feel obliged to explain how to find the laser HOM dip. An excerpt of raw data produced in the experiment is shown in Table 4.2. We first sort the time stamps into two lists (retaining the order): one containing time stamps from detector 1 and the other containing time stamps from detector 2. The time stamps

Time Stamp	Detector	Shifted Time Stamp	Time Stamp (μs)
4004161838388906	2	0	0
4004161838389989	1	1080	0.169
4004161838392150	1	3250	0.508
4004161838403304	2	14400	2.250
4004161838428995	2	40090	6.264
4004161838429350	2	40450	6.320
4004161838431588	1	42680	6.669
4004161838439984	1	51080	7.981
4004161838452586	2	63680	9.950
4004161838457949	1	69040	10.788
4004161838460201	2	71300	11.141
4004161838464791	1	75890	11.858
4004161838475202	2	86300	13.484
4004161838481613	2	92710	14.486
4004161838515114	2	126210	19.720

Table 4.2: **Raw Data (Time Tag) Excerpt.** The first two columns are raw data: time stamp of the count event and channel or detector number where the count has occurred. A time tagger assigns time stamps in terms of in internal units, namely integer multiples of the time tagger resolution T_{Res}, which is 156.25 ps for this particular measurement. The time tagger does not start counting from zero. However, we can subtract the time stamp of the first event from all time stamps so that the first time stamp, which is now zero, indicates start of the experiment (column 3). We can multiply time stamps by T_{Res} to obtain the actual time an event has occurred (column 4).

are in units, i.e. multiples, of the time tagger resolution T_{Res}. Thus, the actual time can be found by simple multiplication (we worked with $T_{\text{Res}} = 78.125\,\text{ps}$ and $T_{\text{Res}} = 156.25\,\text{ps}$ time taggers). The conversion is only really needed for presentation of data, however, and not needed for finding coincidences. The analysis goal is to find all coincidences within a certain time window and note down the detection time difference τ. Then we plot the number of coincidences versus τ, which gives us a histogram. We first need to chose a *histogram width* T_{Hist}, which is time window that defines coincidences. Next we define the *histogram bin size* T_{bin}, which sets the (time) resolution of our histogram, i.e. the resolution with which we want to resolve coincidences. As discussed a bit later, $T_{\text{bin}} \gg T_{\text{Res}}$. The *number of bins*, i.e. the number of different delays we distinguish, can then be calculated as

$$N_{\text{bins}} = \left\lceil \frac{T_{\text{Hist}}}{T_{\text{bin}}} \right\rceil , \tag{4.115}$$

where the ceiling function $\lceil\rceil$ indicates that the fraction is rounded up to the nearest integer. Since $T_{\text{bin}} \gg T_{\text{Res}}$, we can also calculate the number of *time tagger bins* within a *histogram bin*,

$$N_{\text{TTbins}} = \left\lfloor \frac{T_{\text{Hist}}}{T_{\text{bin}} N_{\text{bins}}} \right\rfloor , \tag{4.116}$$

where the floor function $\lfloor\rfloor$ indicates that the fraction is rounded down to the nearest integer.

How do we actually find coincidences? The basic idea is to go through one of the two lists, say the one for detector 1, and for each detection event go through time stamp list for detector 2 and calculate time stamp differences. If this difference lies within T_{Hist}, then write it in a new list. We do this for all detection events. Following this algorithm we end up with a one-column list containing all the τ's we have found. We can now build a histogram, i.e. we put each of the τ's in one of the N_{bins} bins with resolution T_{bin}. There are of course rules how to deal with "border cases", i.e. cases where there is some ambiguity where exactly to put a particular τ. But these can be resolved. The actual algorithm we implemented in Matlab (see Appendix A) is a bit more involved. The complication arises from (i) making the search more efficient using break-conditions (we do not loop through the whole list of detector 2 for all events of detector 1) and (ii) to take into account multiple coincidences. However, the underlying idea remains and finding coincidences really boils down to comparison of detection events and decide whether the detection time difference falls within a coincidence window.

Figure 4.14 (a) shows a plot of raw coincidence we obtain using the method just described (I'll explain shortly how to obtain the fits). Admittedly, the plot is already polished for sake of presentation, however, it still exhibits a feature of unprocessed data: the default

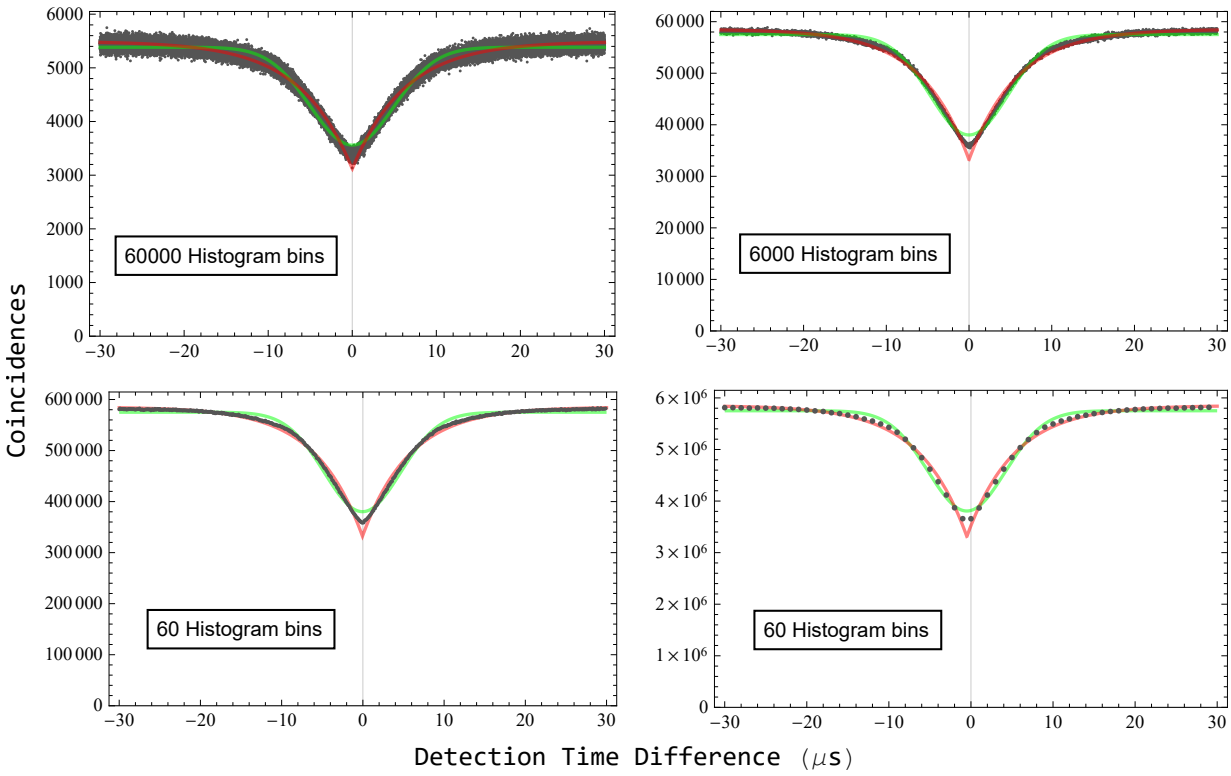

Figure 4.14: **Laser HOM Dip for Varying Histogram Bin Sizes.** As we vary the histogram bin size, holding the histogram size $T_{\text{Hist}} = 60\,\mu$s constant, the number of counts change but not the dip shape. The gray dots are measured coincidences and the green and red curves are Lorentzian (4.117) and Gaussian (4.118) fit models. We see that both fits are not quite right: the Gaussian fit underestimates the visibility, and the Lorentzian fit overestimates it.

choice of histogram parameters leads to huge fluctuations in the number of coincidences! What is going on? Working with coincidences and histograms, one has substantial degrees of freedom in the analysis stage. In Figure 4.14, we start with $T_{\text{Hist}} = 60\,\mu$s and $T_{\text{bin}} = 1\,$ns, giving us $N_{\text{bins}} = 60000$. The result are substantial fluctuations ($\sim \pm 200$) in the number of coincidence counts between neighboring bins. As we increase the bin size to 10 ns, 100 ns and 1 μs, corresponding to 6000, 600, and 60 bins, respectively, the fluctuations average out. A smooth coincidence curve appears, though the dip minimum starts to shift away from the origin. If we increase the bin size further still, the dip slowly washes out and disappears completely for $T_{\text{Hist}} = T_{\text{bin}}$. These artifacts, namely count fluctuations for small bin sizes, and dissolving structural features for large bin sizes are typical for histograms. Consequently, one needs to make a "reasonable" *choice* of histogram parameters so that quantities that are derived from histogram analysis only have a negligible dependence on

this choice. A good sign for us is already the dip shape's invariance under bin size scaling. What our eyes perceive, is backed up by the analysis results shown in Table 4.3. We see that both depth and width of the dip, corresponding to visibility $\mathcal{V}_{\mathrm{HOM}}$ and coherence length τ_{coh}, respectively, stay approximately constant. This is good news, for if we just pick say $N_{\mathrm{bins}} = 6000$, then the results we derive are not mere artifact of the coincidence analysis.

4.7.2 Laser HOM Dip Shape and Parameters

Let us now come to the fits to the second-order cross-correlation function (4.68), which we see already in Figure 4.14, and on which the numbers in Table 4.3 are based on. Since our laser linewidth (as low as 100 kHz) is much narrower than the resolution of

	N_{bins}	60000	6000	600	60
Lorentzian	$\mathcal{V}_{\mathrm{HOM}}(\%)$	43.3 ± 1.7	43.3 ± 3.0	43.3 ± 8.5	43.4 ± 26.4
	τ_{coh} (μs)	12.40	11.55	11.55	11.49
Gaussian	$\mathcal{V}_{\mathrm{HOM}}$ (%)	33.8 ± 1.0	33.9 ± 1.7	33.9 ± 5.7	33.8 ± 6.0
	τ_{coh} (μs)	9.93	9.38	9.38	9.41
Voigt	$\mathcal{V}_{\mathrm{HOM}}$ (%)	$39.7 \pm (0.04)$	$39.8 \pm (0.04)$	39.8 ± 0.1	40.0 ± 0.3
	τ_{coh} (μs)	10.76	10.16	10.16	10.18

Table 4.3: **Laser HOM Parameters Extracted from Fits.** Shown are estimated laser HOM dip visibilities and coherence lengths for the dips shown in Figures 4.14 and 4.16, and where the fit functions are given in Equations (4.117), (4.118), and (4.125), respectively. Errors are standard deviations (SD) of the respective fit parameters (see main text). SD's for coherence lengths are smaller than significant digits. For the same reason, visibility errors for $N_{\mathrm{bins}} = 60000$ and 6000 for the Voigt fit are shown in parenthesis. Large errors for $N_{\mathrm{bins}} = 600$ and 60 for both Lorentz and Gauss model are no fit artifacts. In fact, the dip shape is captured quite well, which is reflected by the small error for the dip width (coherence length). The fits fail at the dip minimum, however, which is also visible in the corresponding figures. The larger visibility error for decreasing bin size is then a consequence of diminishing spread in the data, i.e. less variability for the fit. The Voigt fit, on the other hand, captures all features of the dip, for any bin size choice, very well.

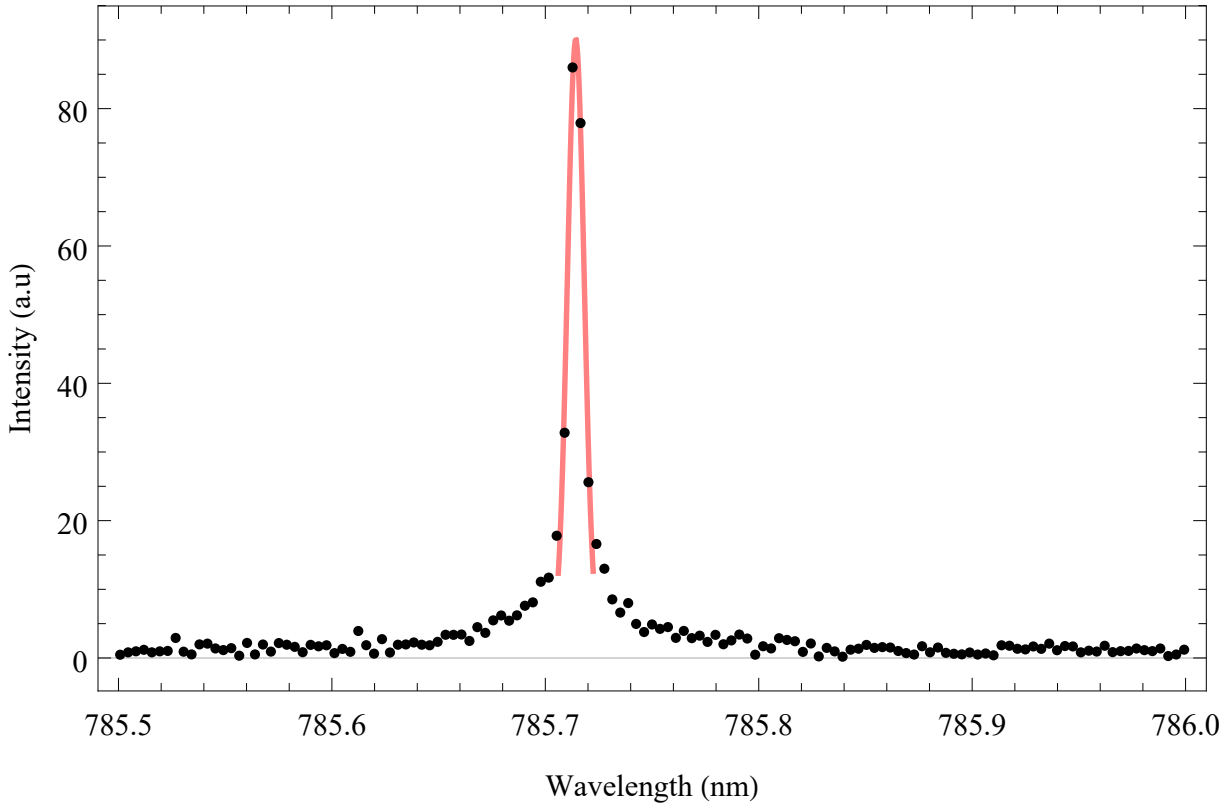

Figure 4.15: **Laser Spectrum.** We use a Bristol spectrum Analyzer 721 with 4 GHz resolution to look at the spectrum of our laser (Toptica DL Pro). We fit a Gaussian function to the central portion of the peak to extract the central wavelength, $\delta_0 = 785.714\,\text{nm}$. The width (FWHM) is 9.26 pm, corresponding to a coherence length of $l_{\text{coh}} = 21.2\,\text{m}$. However, this is only a lower-bound, for the actual laser linewidth is much smaller than the spectrum analyzer resolution.

our spectrometer (4 GHz—see also Figure 4.15), we do not know whether the first-order autocorrelation function is Lorentzian (4.58) or Gaussian (4.59). Thus, for nonlinear fit models we consider both Lorentzian type,

$$\widetilde{G}^{(2x)}_{\text{Lorentz}}(\tau) \coloneqq c\left(1 - b\exp\left[-\frac{2|\tau - d|}{a}\right]\right), \tag{4.117}$$

and Gaussian type,

$$\widetilde{G}^{(2x)}_{\text{Gauss}}(\tau) \coloneqq c\left(1 - b\exp\left[-\frac{2(\tau - d)^2}{a^2}\right]\right). \tag{4.118}$$

The fit parameter b estimates HOM visibilities and into c we absorb both the single count rates N_1 and N_2 and the proportionality constant in the relationship (4.52) between coincidence count rate and second-order cross-correlation function. The origin offset d takes

into account potential shifts of the dip due to histogram binning artifacts, as discussed above, but is usually negligible. Furthermore, we assume

$$\tau_1 = \tau_2 \equiv \tau_{\text{coh}} \mathrel{\widehat{=}} a\,, \tag{4.119}$$

which also explains the factor 2 in the exponents of (4.118) and (4.117). The equality of τ_1 and τ_2 is justified, because the two beams derive from the same laser, and no obvious random process influencing the field coherence lengths are identifiable in our setup shown in Figure 4.9.

Results of the fits can be seen in Figure 4.14. Though both functions roughly follow the dip shape, we would not say that the fits explain the shape in its entirety. In particular, on which fit should we base our visibility on? There are two simple possibilities. We either define an *experimental visibility*

$$\mathcal{V}_{\text{Exp}} \coloneqq \frac{C_{\max} - C_{\min}}{C_{\max}}\,, \tag{4.120}$$

where $C_{\max/\min}$ are the maximum and minimum number of measured coincidences, or we take some kind of average, for example

$$\mathcal{V}_{\text{Avg}} \coloneqq \frac{1}{2}\left(\mathcal{V}_{\text{HOM, Gauss}} + \mathcal{V}_{\text{HOM, Lorentz}}\right). \tag{4.121}$$

The former method is prone to outliers and entails a choice of representative maximum or minimum coincidences. The latter method demands some theoretical justification, i.e. why in particular the *arithmetic* mean? A third option is to reconsider source spectrum and with it the random process giving rise to the degree of first-order coherence in Equation (4.50). Now, this is a hard task for we would need to know much more about the inner workings of the laser. One educated guess we can make here is to assume that more than one random process contributes appreciably to the laser spectrum. In this case we have to deal with a composite spectrum. In our case, it seems reasonable to assume that the linewidth of the laser, which, again, we cannot resolve with our spectrum analyzer, is a composition of a Lorentzian and Gaussian, in which case [138]

$$F_V(\omega) = \int_{-\infty}^{\infty} d\nu\, F_G(\nu) F_L(\omega + \omega_0 - \nu) = \frac{1}{\sqrt{2\pi}\Delta}\mathfrak{Re}\left\{\text{Erf}\left(\frac{\omega_0 - \omega + i\gamma}{\sqrt{2}\Delta}\right)\right\}, \tag{4.122}$$

where ω_0 is the common center frequency. The latter equality is based on a certain integral representation of the (complex) error function $w(z)$, namely

$$\int_{-\infty}^{\infty} dt\, \frac{y e^{-t^2}}{(x-t)^2 + y^2} = \pi\mathfrak{Re}\left\{w(x+iy)\right\} \qquad \left(x \in \mathbb{R},\, y > 0\right), \tag{4.123}$$

which is integral (7.4.13) in Abramovitz and Stegun's Handbook of Mathematical Functions (10^{th} printing). The resulting lineshape is known as Voigt profile and is quite tedious to work with. At least in principle we can convert (4.122) into a probability density function in time and then calculate the first-order correlation function. However, we need to be careful here (apart from the mathematical difficulties), because we have to think about the physical reasons for the occurrence of both Gaussian and Lorentzian broadening mechanisms. Usually the two processes are linked, resulting in correlated processes. The difficulties are obvious but we can try to get away with the assumption of independence [160], in which case the probability distributions factorize and consequently

$$g^{(1)}(\tau)_{\text{Voigt}} = g^{(1)}(\tau)_{\text{Gaussian}} \cdot g^{(1)}(\tau)_{\text{Lorentzian}} \,. \tag{4.124}$$

Hence, we attempt the following nonlinear fit,

$$\widetilde{G}^{(2x)}_{\text{Voigt}}(\tau) \coloneqq c\left(1 - b\exp\left[-\frac{2|\tau - d_L|}{a_L} - \frac{2(\tau - d_G)^2}{a_G^2}\right]\right) , \tag{4.125}$$

where the six fit parameters retain their obvious meaning. The result is shown in Figure 4.16. A visible improvement is clearly discernible: when compared with the Gaussian and Lorentzian fits in Figure 4.14, the "Voigtian" fit is situated between them. Most importantly, whereas Gaussian and Lorentzian fits under- and overestimate the dip depth, respectively, the Voigt fit approximates the data minimum quite well. In all cases, the visibilities lie in-between those for Gaussian and Lorentzian type fits, as shown in Table 4.3.

Finally, let us find the coherence length associated with a Voigt profile. The lineshape is still single-peaked, and so we can sensibly assign a coherence length based on the inverse linewidth, however, determining the FWHM δ_{Voigt} is not trivial. We use the following approximation [161],

$$\delta_{\text{Voigt}} \approx 0.5346\,\delta_{\text{Lorentz}} + \sqrt{0.2166\,\delta^2_{\text{Lorentz}} + \delta^2_{\text{Gauss}}} \,. \tag{4.126}$$

Then, with $\delta_{\text{Lorentz}} = 1/\tau_L = 1/a_L$ and $\delta_{\text{Gauss}} = 1/\tau_G = 1/\sqrt{a_G}$, we can estimate

$$\tau_{\text{coh}} \approxeq \left(\frac{0.5346}{a_L} + \sqrt{\frac{0.2166}{a_L^2} + \frac{1}{a_G}}\right)^{-1} , \tag{4.127}$$

which are are also shown in Table 4.3. Without further (physical) motivation for better models, these visibilities represent the average we were looking for, and it is thus the Voigt random process, which best explains our anticorrelation data.

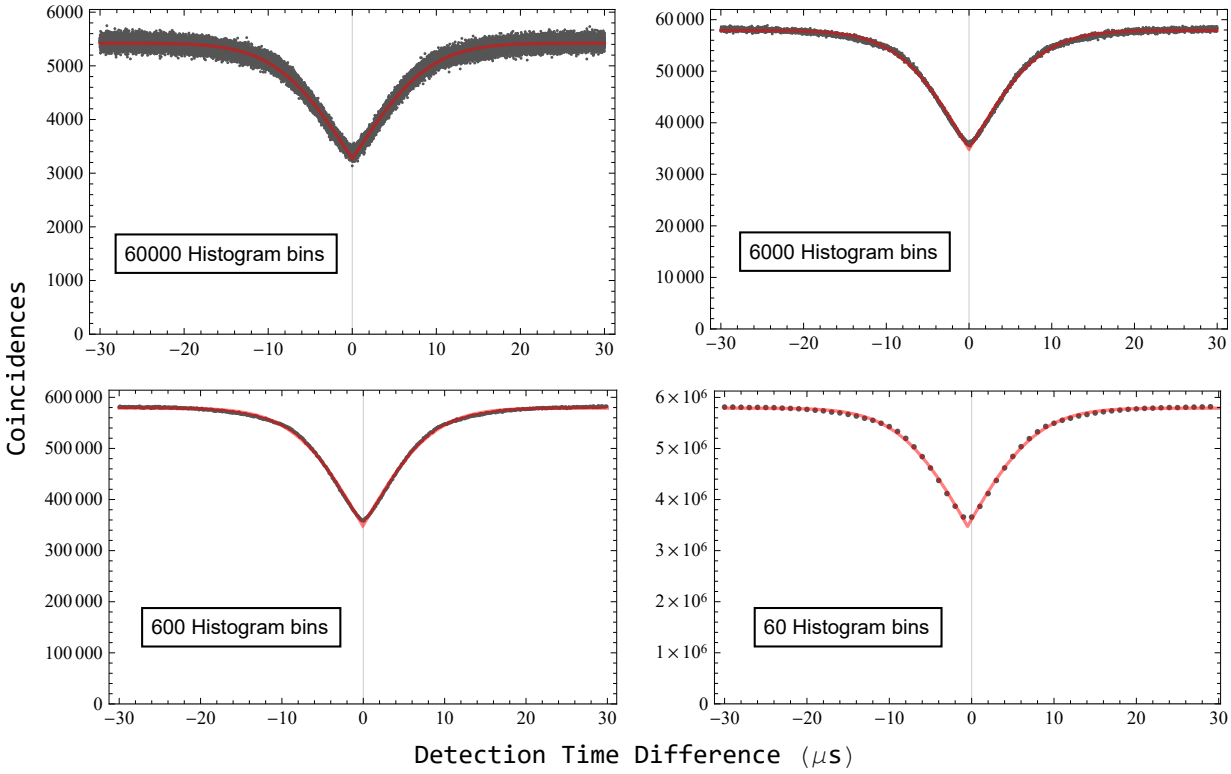

Figure 4.16: **Laser HOM Dip with Voigtian Fit.** Here we use Equation (4.125) to model the coincidence data and see see a clear improvement over both Lorentzian and Gaussian fits in Figure 4.14.

4.7.3 Laser HOM Dip Polarization Dependence

We move on to demonstrate the laser HOM dip's polarization dependence in a free-space HOM interferometer. We make sure that the two light fields have identical polarization just before the HOM beam splitter using polarizing beam splitters (PBS) oriented such that horizontal polarization is transmitted. Then, between PBS and HOM BS, we place a half-wave plate (HWP) in the path of one of the input fields, as shown in Figure 4.9. After finding the zero position, we rotate the HWP by an angle ϕ, which induces a polarization rotation of 2ϕ. Since we keep the polarization of the other input field constant, this varies the relative polarization and according to Equation (4.83). Indeed, Figure 4.17 shows laser HOM dips for various polarization angles, rotating the HWP in 10 degree steps. The maximum reduction of coincidences below the coincidences baseline, which is approximated by accidental coincidences

$$C_A = S_1 S_2 T_{\text{bin}} T_M \,, \tag{4.128}$$

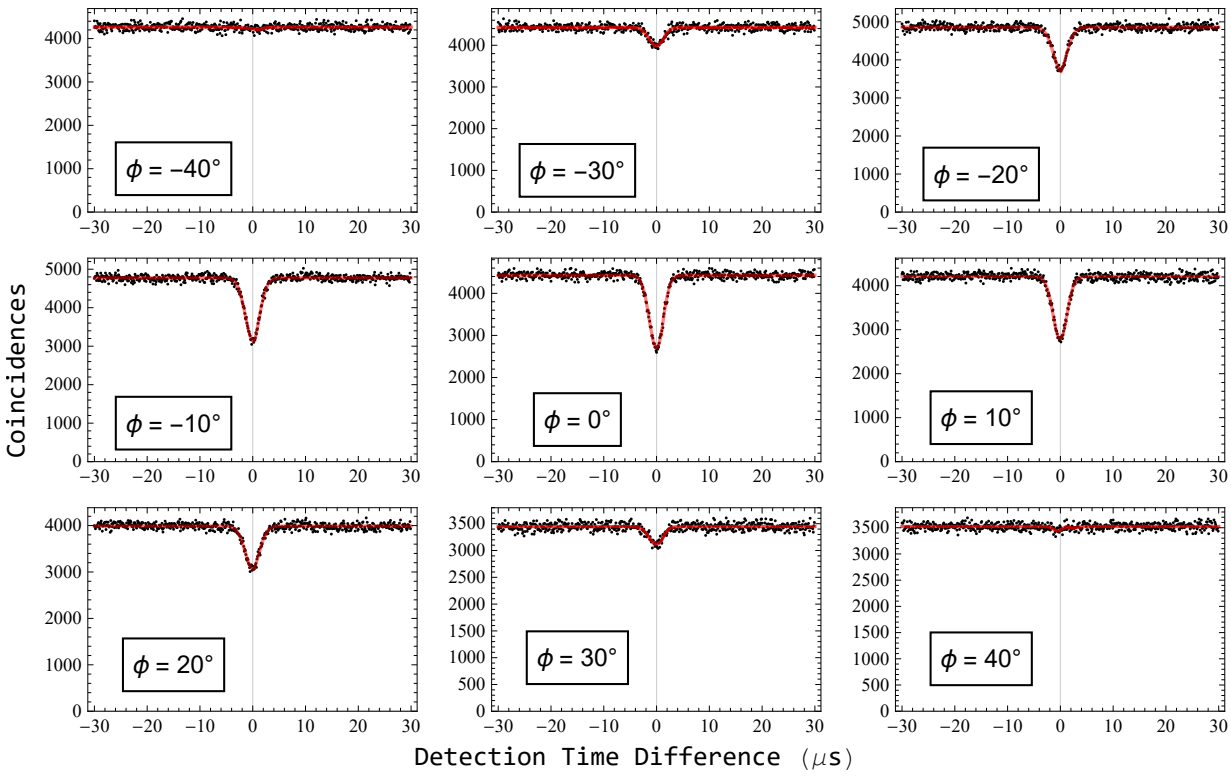

Figure 4.17: **Polarization Dependence of Laser HOM Dips.** As we vary the relative polarization between the two input fields (ϕ is HWP angle), the dip shape remains unaltered but its visibility varies between 0 (orthogonal polarization) and maximum (parallel polarization) visibility. Here, $N_{\text{bins}} = 600$ and the error bars are smaller than size of plot symbols. Red lines show fits using the Voigt model Equation (4.125).

is achieved for identical polarizations, i.e. $\phi = 0$. The corresponding visibility is

$$\mathcal{V}_{\text{HOM}}(\phi = 0) = (41.8 \pm 1.7)\,\%\,. \tag{4.129}$$

As we start to make the two input fields distinguishable by their polarization, Equation (4.83) predicts a cosine-squared variation of the visibility with relative polarization angle. This we verify by plotting visibilities as function of ϕ and fitting

$$\widetilde{\mathcal{V}}_{\text{HOM}}(\phi) \coloneqq a\cos^2\left(b\phi - c\right) - \Delta\mathcal{V}\,, \tag{4.130}$$

with fit parameters a, b, and c, as well visibility difference $\Delta\mathcal{V} = 0.5 - \mathcal{V}_{\text{HOM}}(\phi = 0)$ (here we only want to account for the cosine-squared dependence). The result is shown in Figure 4.18, which agrees well with the prediction. We briefly turn to the question, why the maximum visibility is below 50 %. In principle, there are various experimental imperfections that can explain this. Since we work with CW light, however, we do not have

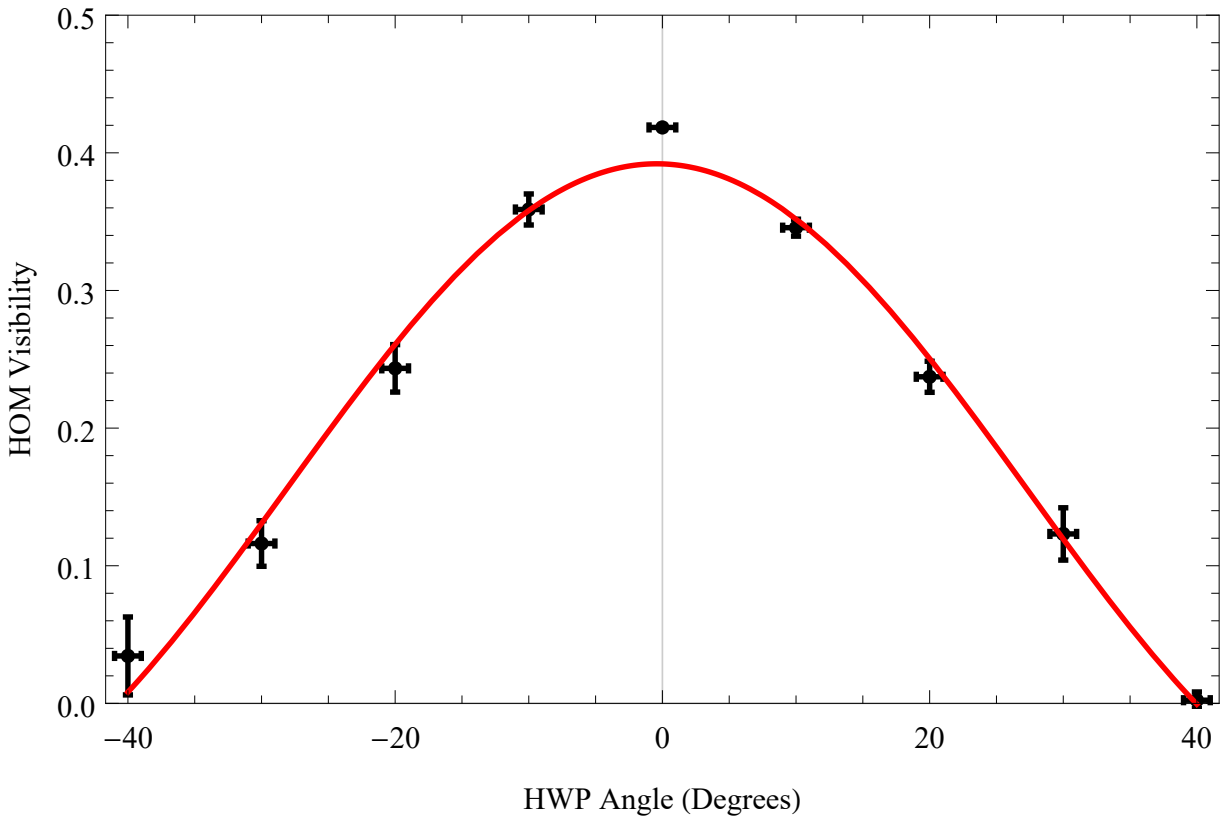

Figure 4.18: **Laser HOM Visibility vs. Relative Polarization.** Here we plot visibilities of the plots shown in Figure 4.17, together with a fit of the polarization function $P_{\parallel}(\phi) = \cos^2(\phi)$ (see main text). The error bars for ϕ are given by the HWP angular accuracy and the visibility error is composed of ϕ error and standard deviations from dip fits.

synchronization problems, i.e. overlap of pulses at the HOM beam splitter. Furthermore, the extinction ratio of our PBS' are $> 1000 : 1$, guaranteeing experimentally identical polarization. Both beams are coupled out and into single-mode fibers at 780 nm, which means that photons should also not be distinguishable in their spatial degree of freedom. Of course, the two beams can have slightly different divergence angles, or fail to completely overlap at the HOM beam splitter. However, the HOM interferometer alignment technique based on second-order interference showed very high visual fringe contrast so that we believe this cannot account for $\sim 8\,\%$ visibility reduction. It may be that the single count rate difference reduces the visibility. The single count rates in the measurements of Figure 4.17 are shown in Table 4.4. There we calculate $\alpha = 1.25$ for $\phi = 0$, in which case Equation (4.67) predicts a theoretical visibility $\mathcal{V}_{\mathrm{HOM}} \approx 49.4\,\%$. Thus, the single count rate difference contributes less than $1\,\%$ to the visibility loss. Lastly, it may also be that the the coherence

ϕ	-40	-30	-20	-10	0	10	20	30	40
T_M	220.8	220	225.5	223.5	222.2	222.9	221.3	220.7	218.3
N_1	112827	114260	119770	117658	111378	110483	109292	101772	102717
N_2	83437	85249	91692	90782	88551	85068	80746	74619	74863
α	1.35	1.34	1.31	1.30	1.26	1.30	1.35	1.36	1.37
C_A	4264	4428	4870	4779	4439	4216	3988	3441	3523

Table 4.4: **Typical Count Rate Data for Laser HOM Experiments.** Count data extracted from the time tag file for laser HOM dip results shown in Figure 4.17 (the relative polarization angle ϕ is measured in degrees): N_1 (detector 1) and N_2 (detector 2) are the total detected number of photons during measurement time T_M (milliseconds). The non-interfering, accidental, coincidences are calculated using Equation 4.128, and the multiplicative count rate difference α is calculated as N_1/N_2.

properties of the laser fields are not entirely described by our Gaussian-Lorentzian model. Rather than exploring the potential source for the missing visibility, we now proceed to design the laser HOM dip using its polarization dependence.

4.7.4 Triangle Laser HOM Interference

We now experimentally demonstrate triangle HOM interference predicted by Equation (4.112). We modulate the polarization of the laser between horizontal (H) and vertical (V) polarization with a 353 MHz square wave. The arbitrary waveform generator we use is a Tabor WX2184C. The experimental setup is as before, but now we move the retroreflector along an optical rail in two inch steps, thereby changing the optical delay τ_{opt}. We have to double this distance (i.e. four inches) to calculate $\Delta\tau_{\text{opt}} = 0.3389 \approx 0.34$ ns (using vacuum speed of light), because light travels this distance to and from reflection off the retroreflector. As mentioned in the description of the experimental setup, the accuracy with which we can set the retroreflector is 1/40 inches and so the error we make in setting the optical delay is $\sim 10^{-3}$ ns, which is negligible. Starting at $\tau_{\text{opt}} = 0$, we measure coincidences at 22 points along the optical rail (the last being thus $\tau_{\text{opt}} = 7.14$ ns). From each of these measurements, we extract HOM dips as before. Some of those are shown in Figure 4.20. For distillation of triangle laser HOM interference, we consider only coincidences for which $\tau \approx 0$. Moreover, since the (normalized) coincidences at $\tau = 0$ are directly proportional to the dip visibility, the latter, plotted as a function of optical delay, should also follow a

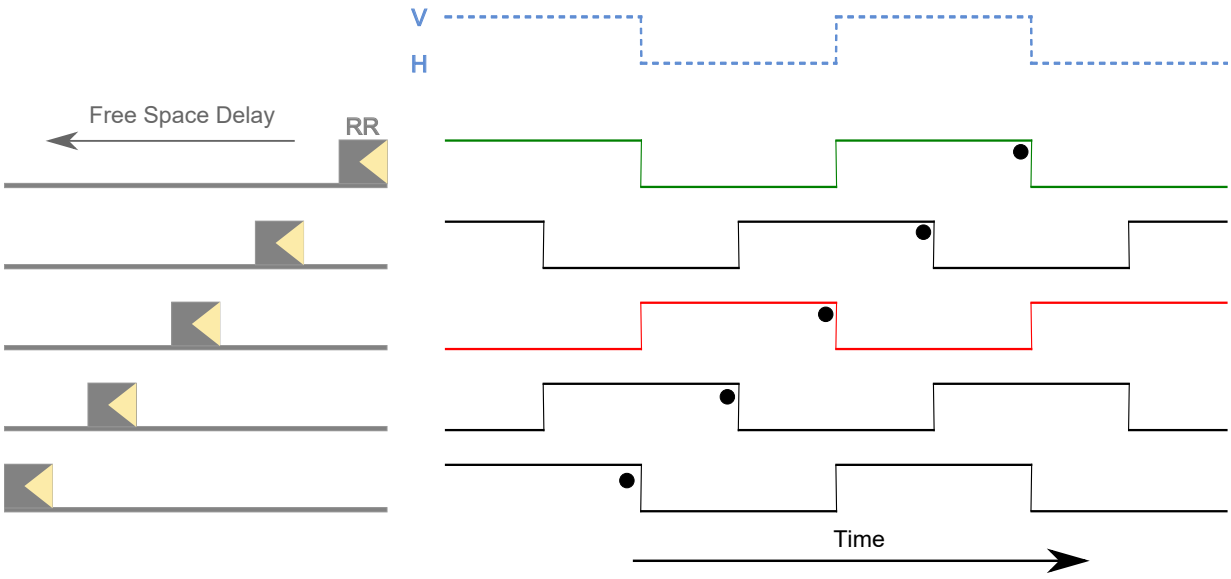

Figure 4.19: **Illustration of Polarization Modulation and Free-Space Delay.** Here we illustrate how the variable free-space delay line is used to control the polarization modulation pattern in time, as shown in Figure 4.8. The top trace (light blue dashed line) shows the polarization modulation pattern in time, namely a square wave alternating between horizontal (H) and vertical (V) polarization. The two beams used in the experiment are split at the output of the polarization modulator and thus, at the point of splitting their polarization pattern overlaps in time. One of the beams is traversing the free-space delay line. As the retroreflector (RR) is moved, the time it takes for the beam to travel through the delay line changes and thus the polarization pattern in time. Depending on the retroreflector position, polarization patterns either overlap completely (green trace) or not at all (red trace), or something in-between these two extreme cases. The overlap patterns determines the photon distinguishability in time, which in turn controls two-photon interference, as Figure 4.8 explains in more detail.

triangle wave. Taking into consideration data offsets and a proportionality constant with fit parameters a, d and b, respectively, we take

$$\widetilde{\mathcal{V}}_{\mathrm{HOMTW}}(\tau_{\mathrm{opt}}) \coloneqq a + \frac{b}{4}\left(3 - \mathrm{TriangleWave}\left[\frac{\tau_{\mathrm{opt}}}{c} - \frac{3}{4} + d\right]\right) , \tag{4.131}$$

as a data model for Equation (4.112). The essential fit parameter is c, which, according to Equation (4.112) estimates the polarization modulation period $T = 2.83\,\mathrm{ns}$. The results are shown in Figure 4.21. The triangular wave is clearly visible with an estimated period of $c = (2.80 \pm 0.04)\,\mathrm{ns}$, matching the polarization modulation period of quite well.

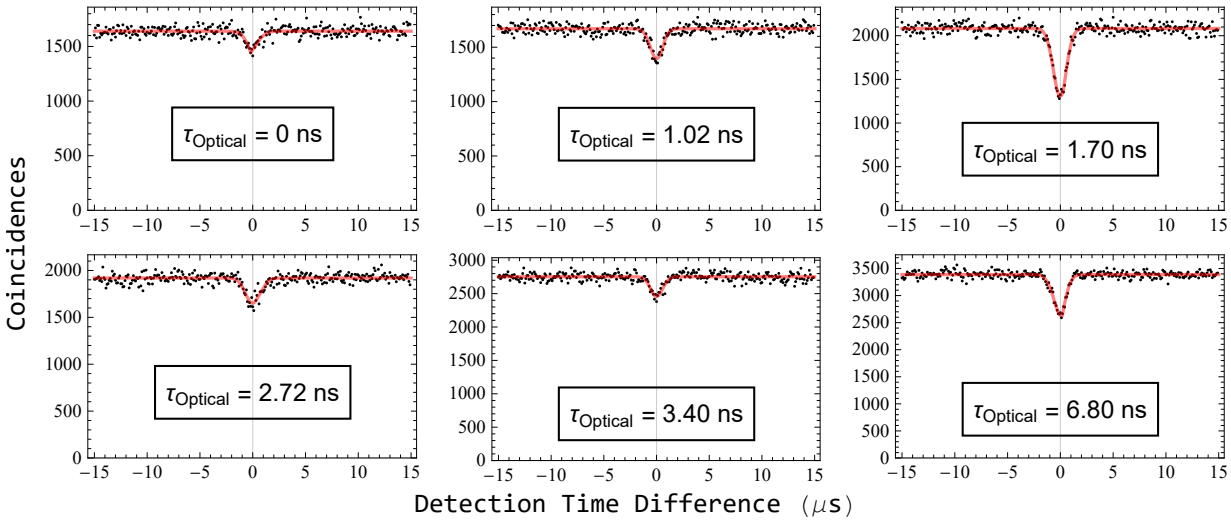

Figure 4.20: **Optical Delay Dependence of Laser HOM Dips.** As we scan the optical delay between two square-wave polarization modulated fields at 22 points, the HOM dip visibility changes periodically. The visibilities of the nine dips shown here are, respectively, (12.6±2.5) %, (18.6±1.8) %, (40.0±3.4) %, (12.7±2.7) %, (10.4±3.2) %, and (25.4±2.0) %. The visibilities of all 22 dips are plotted in Figure 4.21. Red lines show fits using the Voigt model Equation (4.125).

4.7.5 Square Laser HOM Interference

In the last experiment, we extract square HOM interference described by Equation (4.104). For the extraction to work we need one last piece of information, namely the modulation phase t_0. We call it this way because we need to analyze $\tau \approx 0$ coincidences with respect to the modulation phase. Remember that, given a certain polarization overlap pattern at the beam splitter (see Figures 4.8 and 4.19), a coincidence can happen anywhere within that pattern. Crucially, the coincidence probability depends on whether the polarizations are identical or orthogonal. Now, if, whenever we detect a coincidence, we have no information where within the overlap pattern it occurred, then we automatically lump all coincidences together: we have to integrate over t_0. Equation (4.104) asks us, however, to plot the coincidences *as a function of* t_0. This means we would like put coincidences in bins labeled by, let's say, $t_0 = 0\,\text{ns}$, $t_0 = 0.5\,\text{ns}$, $t_0 = 1\,\text{ns}$, and so on. Coincidences in each t_0-bin correspond to events that happened during exactly the same part (hence modulation phase) of the polarization overlap pattern. We obtain the required phase information directly from the arbitrary waveform generator (AWG). As before (triangle laser HOM interference), we use a Tabor WX2184C AWG to generate 353 MHz square waves. The AWG can send a trigger signal whenever a new modulation period starts, e.g. with the rising edges of square

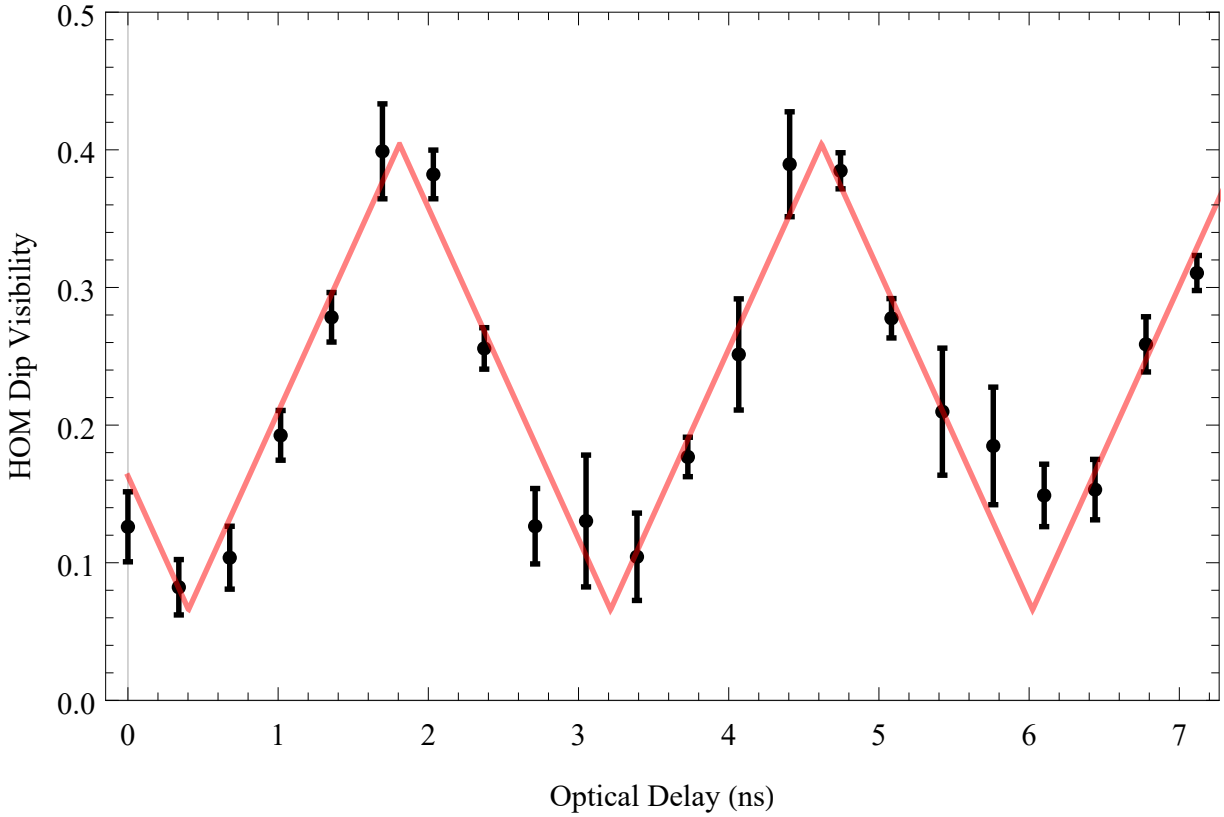

Figure 4.21: **Experimental Triangle Laser HOM Interference.** Plotting the visibility $\mathcal{V}_{\mathrm{HOM}}(\tau_{\mathrm{opt}})$ of laser HOM dips for 22 optical delays (step size 0.34 ns). The red curve is a fit described by Equation (4.131) with offsets of visibility $a = (-0.27 \pm 0.05)\,\%$ and origin $d = (0.85 \pm 0.02)\,\mathrm{ns}$. The period of the waveform is $c = (2.80 \pm 0.04)\,\mathrm{ns}$.

waves. We send this trigger signal to the very same time tagger that assigns time stamps to photon detection events in the two detectors after the HOM BS. Thus, the time tagger records *three* signals. A technical difficulty here is the fact that we modulate at 353 MHz, which is a rate the time tagger cannot cope with. We therefore program the AWG to send a downsampled version of the trigger, namely at 353 kHz. If the AWG trigger signal is stable enough (meaning the uncertainty in the time difference between consecutive triggers is $\ll 1\,\mathrm{ns}$), then we can interpolate the missing trigger signals later in the analysis stages and pretend they are real. We then have a constant reference signal with respect to which we can locate coincidences. Here I outline the analysis idea, and the full Matlab analysis code can be found in Appendix B.

The first task is to find two-photon coincidences. Since we restrict ourselves to coincidences $\tau \approx 0$, we pick a tiny coincidence window $T_{\mathrm{coin}} = k \cdot T_{\mathrm{Res}}$. The goal is to make k as small as possible. However, with a smaller coincidence window, we have fewer

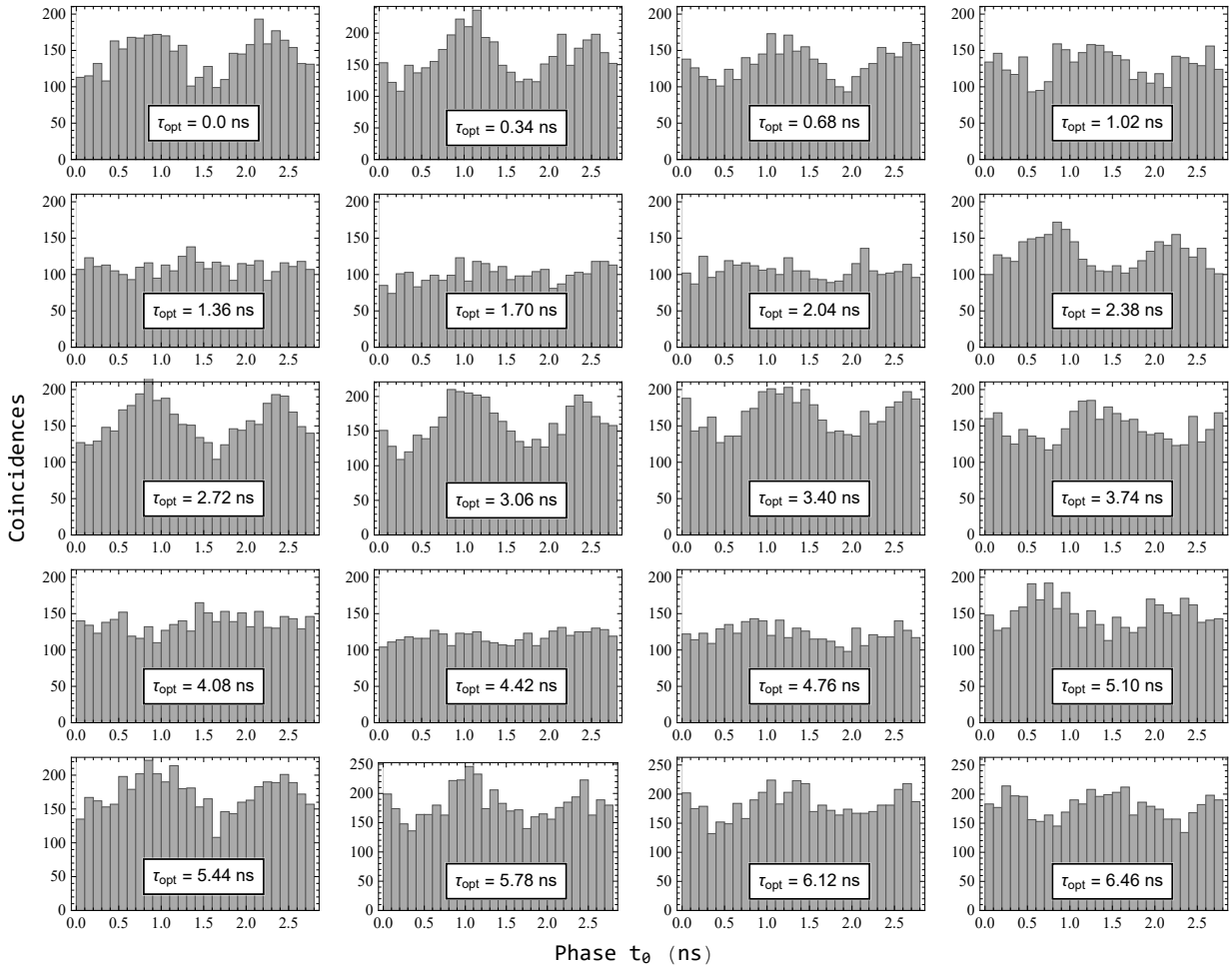

Figure 4.22: **Experimental Square Laser HOM Interference.** Two-photon detections within a $T_{\text{coin}} = 312.5\,\text{ps}$ coincidence window are plotted as a function of modulator phase t_0. The histogram bin size is 0.1 ns. As the optical delay τ_{opt} is varied in $\Delta\tau_{\text{opt}} = 0.34\,\text{ns}$ steps from 0 to 6.46 ns, the HOM square wave appears (0-1.02 ns) and disappears (1.36-2.04 ns). It then starts to appear again (2.38-3.74 ns). Note the similarity between the pairs (0, 2.72 ns), (0.34, 3.06 ns), 0.68, 3.40 ns), and 1.02, 3.74 ns), which are all separated by 2.72 ns, and so roughly the period of the polarization modulator (2.83 ns).

counts in that window. We found the best trade-off between "true coincidence" and good signal-to-noise ratio is $k = 2 - 4$. For the time tagger we used in the HOM square wave measurements, $T_{\text{Res}} = 78.125\,\text{ps}$, defining coincidence windows $T_{\text{coin}} = 156.25 - 312.5\,\text{ps}$.

Then we locate the coincidence *within* two *consecutive downsampled* trigger signals (remember we have their time stamps as well). After this rough localization, we interpolate the missing trigger signals within the two downsampled triggers and find the difference between two time stamps: the one corresponding to the coincidence, and the other corre-

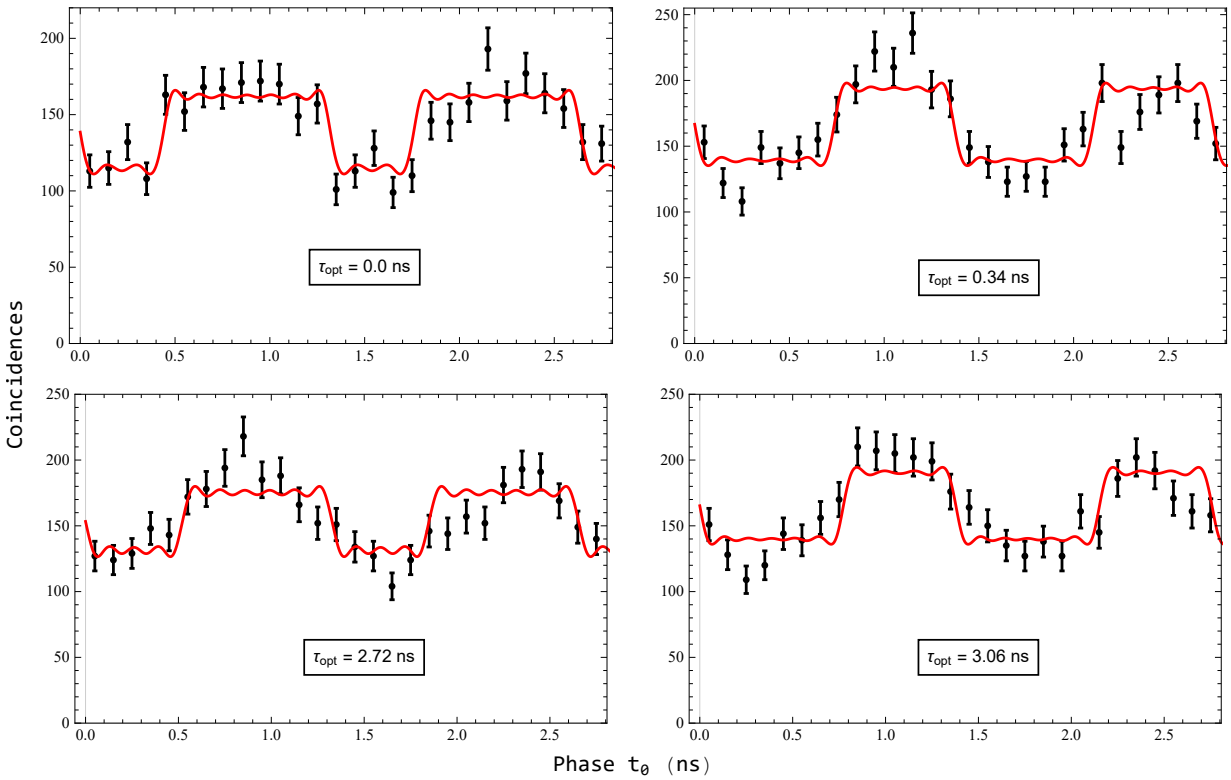

Figure 4.23: **Fits to Square HOM Interference Patterns.** Comparison of the HOM square waves for $\tau_{\text{opt}} = 0$, 0.34, 2.72 and 3.06 ns shown in Figure 4.22. The data points here have coordinates corresponding to bin height (y-axis) and t_0 of the center of the bin (x-axis). The error bars represent Poissonian counting errors.

sponding to the closest, interpolated trigger prior to the coincidence. This difference is the modulator phase t_0, which we save for each coincidence.

We locate all coincidences in this manner and end up with a distribution for t_0. Creating a histogram for t_0 is exactly what Equations (4.104) requires. A plot of histogram heights for optical delays ranging from $\tau_{\text{opt}} = 0 - 6.46$ ns is shown in Figure 4.22. The delay is again set by the retroreflector position on the optical rail. We clearly see both the emergence and fading away of a square waveform as the optical delay is changed. The data interference visibility is only about 25 %, which we attribute to problems with the phase modulators. Consequently, those square waves in Figure 4.8 that have very narrow features can hardly be distilled. Most importantly, however, we do see the HOM square waves with half the original (modulator) period. Consider for example the square waveform for $\tau_{\text{opt}} = 0$ ns: it's period is about 1.4 ns (note that the x-axis goes from 0 to 2.83 ns, i.e. one modulator period). We would like to fit Equation (4.104) to those plots, as they have

clearly discernible features. Our first attempt using

$$\widetilde{G}^{(2x)}(t_0) \coloneqq a + \frac{b}{4}\left(3 - \text{SquareWave}\left[\frac{t_0}{c}\right] \text{SquareWave}\left[\frac{t_0 - d}{c}\right]\right) \tag{4.132}$$

fails. This was expected because at speeds of several hundred MHz, the ideal square wave is hardly a good approximation to the modulation signal outputted by the AWG. In particular, the rise time of is of the order of a few 100 ps, which results in a noticeable slope for our square waves with less than 3 ns period. In the Fourier series expansion, the "real world" square wave deviates from the ideal square wave, which has only sine terms in it. So one could add cosine terms, but one needs a fairly good model to justify the assigned cosine amplitudes. A simpler approach is to pass the ideal square wave through a low-pass filter, which means to truncate the Fourier series at some (small) finite n. This is what we are going to do, i.e. we define

$$\text{RealSquareWave}_n(t) \coloneqq \sum_{k=1}^{n} c_k \sin(2\pi k t)\,, \tag{4.133}$$

where the Fourier coefficients are given by

$$c_k = 4\int_0^{1/2} dt\, \text{SquareWave}(t) \sin(2\pi k t)\,. \tag{4.134}$$

The chosen order n must enable us to synthesize a function closely resembling a square wave, but does not need to be excessively high unless there is good reasons for it ($c_k \sim 1/k$ and thus we must really look for specific features to take into account these small coefficients). With this in mind, we picked $n = 20$ and verified that higher orders do not improve the fit quality, giving us

$$\text{RealSquareWave}_{20}(t) = \frac{4}{\pi}\sin(2\pi t) + \frac{4}{3\pi}\sin(6\pi t) + \cdots + \frac{4}{19\pi}\sin(38\pi t)\,. \tag{4.135}$$

Our fit function is therefore

$$\widetilde{G}^{(2x)}(t_0) \coloneqq a + \frac{b}{4}\left(3 - \text{RealSquareWave}\left[\frac{t_0}{c}\right] \text{RealSquareWave}\left[\frac{t_0 - -d}{c}\right]\right), \tag{4.136}$$

which we use to compare the four HOM square waves from Figure 4.22, namely those for $\tau_{\text{opt}} = 0$, 0.34, 2.72 and 3.06 ns. The idea being that the square wave $\tau_{\text{opt}} = 0$ ns should closely resemble that from $\tau_{\text{opt}} = 2.72$ ns and likewise for the other pair. The results are shown in Figure 4.23. We see that the fits work quite well. In particular, the real world square wave model (4.136) captures the edges (slopes due finite rise and fall times). The

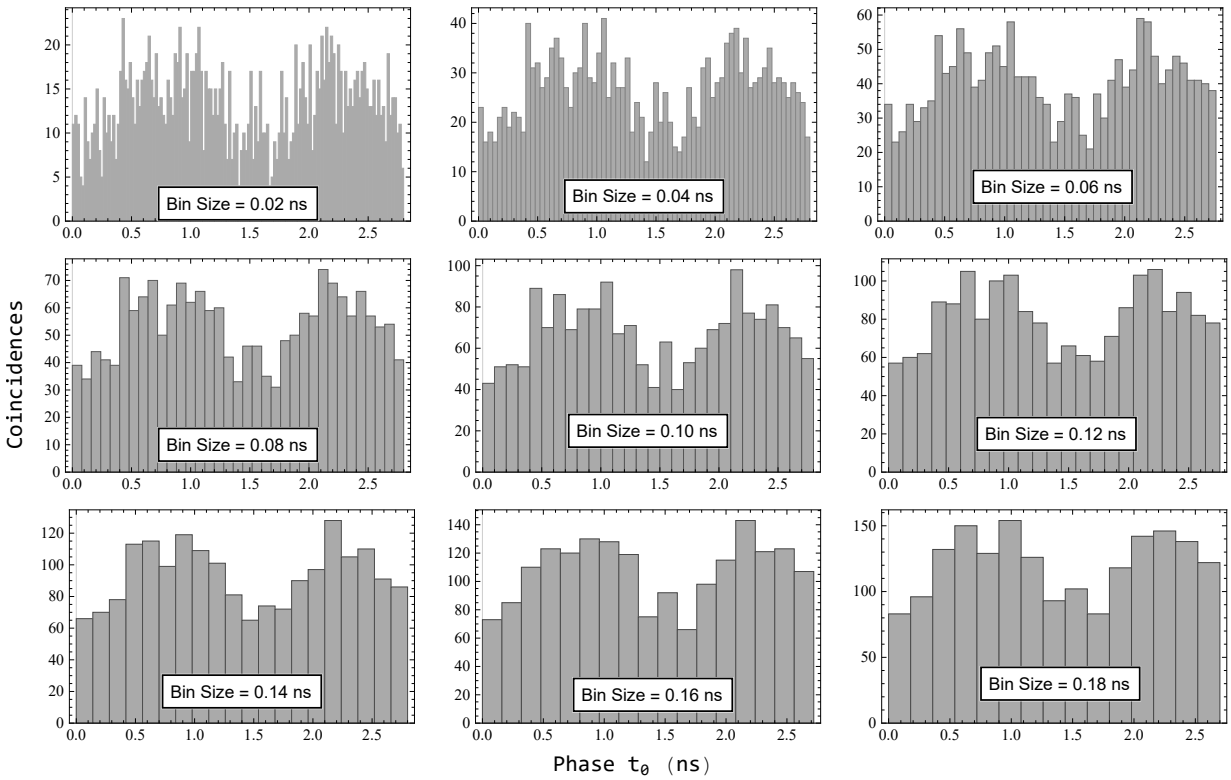

Figure 4.24: **Binning Choices for Square HOM Interference.** Illustration of how the HOM square wave changes with binning choice. At small bin sizes we have a corresponding low number of photon coincidence counts and the histogram appears noisy. At large bin sizes, the difference between lowest and highest bin starts to disappear. Though at both extremes, the square features start to get washed out, the structure never fully disappears and is discernible for all choices.

fits allow us to estimate the modulation period as

$$\begin{aligned} c_0 &= (2.64 \pm 0.02)\,\text{ns} \\ c_{0.34} &= (2.74 \pm 0.02)\,\text{ns} \\ c_{2.72} &= (2.65 \pm 0.02)\,\text{ns} \\ c_{3.06} &= (2.76 \pm 0.02)\,\text{ns}\,. \end{aligned} \tag{4.137}$$

These values are a bit off from the nominal $T = 2.83\,\text{ns}$ and the reason is that c is necessary to adjust the fit in a way to compensate for data features not captured by (4.136). However, these numbers are consistent within each comparison group, i.e. $c_0 \approx c_{2.72}$ and $c_{0.34} \approx c_{3.06}$.

Moreover, the fit parameters

$$\begin{aligned} d_0 &= (1.76 \pm 0.01)\,\text{ns} \\ d_{0.34} &= (2.10 \pm 0.02)\,\text{ns} \\ d_{2.72} &= (1.85 \pm 0.02)\,\text{ns} \\ d_{3.06} &= (2.15 \pm 0.02)\,\text{ns} \end{aligned} \tag{4.138}$$

permit estimates of the optical delay difference, namely $d_{0.34} - d_0 = (0.34 \pm 0.02)\,\text{ns}$ and $d_{3.06} - d_{2.72} = (0.35 \pm 0.03)\,\text{ns}$, which are exactly on the set point, $\Delta\tau_{\text{opt}} = 0.34\,\text{ns}$. Note also that d_0 and $d_{2.72}$ are very similar, as well as are $d_{0.34}$ and $d_{3.06}$. One would expect these to differ by 2.72 ns, i.e. roughly one period. And they do. The fit, however, sees a periodic function and therefore d gives us an estimate for $\Delta\tau_{\text{opt}}$ only modulo T.

Let me conclude this section by showing a series of histograms for $\Delta\tau_{\text{opt}} = 0$ in Figure 4.23. The coincidence window here is even smaller than for the results presented in Figures 4.22 and 4.23, namely $T_{\text{coin}} = 156.25\,\text{ps}$. Moreover, the HOM square wave persists as the histogram bin size, which is a second choice in the analysis (0.1 ns in the results presented above), is systematically varied. Taken together, this shows that the phenomenon is not artifact of a felicitous choice of analysis parameters.

4.8 Conclusion and Outlook

We studied, both theoretically and experimentally, ways to generate non-trivial continuous-wave laser Hong-Ou-Mandel (HOM) interference patterns. The core of the work centers around the second-order cross-correlation function, for which we derived various expressions depending on source characteristics (spectrum), control capabilities (polarization modulation) and detection modalities (taking into account trigger from arbitrary waveform generator). We are thus provided with three anchor points to design fourth-order interference patterns. Though experimental imperfections were lurking everywhere, we managed to distill both triangular and square wave HOM interference patterns. This is completely counterintuitive and it is true that with traditional Hong-Ou-Mandel analysis methods, one cannot find these new *interference landscapes*. While the polarization Hong-Ou-Mandel dip shows up in the detection time difference, the triangle and square wave appear when the data is analyzed in terms of optical delay and modulator phase, respectively. While it is true that ordinary HOM dip experiments with *pulses* also make use of the optical delay, here we use a *continuous*-wave laser, for which modulation is necessary to make photon interference dependent on the optical delay between two beam splitter input modes.

There are now three ways forward. The first one is to improve the current results, for which the setups needs optimization at various points, the polarization modulator in particular. The use of other lasers with varying spectrum (shape, central wavelength) and coherence length would also help to experimentally explore the opened up interference landscapes. The second avenue is to think about potential applications, the encoding of information in particular. For instance, the modulation between two HOM dip levels, corresponding to horizontal and vertical polarization, can be considered a bit. As the system is improved, we should be able to distinguish more than four HOM dip levels. Hence, we can think about encoding information in four polarization states for BB84-type MDI-QKD, and *decode* not with a polarization analyzer but with a *HOM dip analyzer*, where the four states correspond to four HOM dip levels. The third route combines the current free-space HOM interferometer with an atmospheric turbulence simulator. In such a setup, laser beams are subjected to controlled disturbances of the spatial mode, rendering the whole beam multimode (see also the multimode time-bin qubit analyzer presented in the next chapter). These beams can then be coupled into the HOM interferometer, allowing the dependence of HOM visibility on, say, turbulence strength, to be systematically studied. One may expect that the HOM visibility, due to phase-insensitivity of the interference pattern, is less sensitive to atmospheric turbulences and thus, in a way, more suitable for encoding information in turbulent free-space channels. But that remains to be seen.

Chapter 5

Multimode Time-Bin Qubit Interference Analyzers

5.1 Notes

The results presented in this chapter have been submitted for publication and are deposited on the arXiv preprint server as

> Jeongwan Jin, Sascha Agne, Jean-Philippe Bourgoin, Yanbao Zhang, Norbert Lütkenhaus, and Thomas Jennewein, "Efficient time-bin qubit analyzer compatible with multimode optical channels", *arXiv:1509.07490* (2015).

5.2 Introduction

In the short history of experimental quantum communication, polarization has been the preferred degree of freedom for free-space channels [162–166], and is used even for continuous-variable quantum key distribution [167]. Just recently, our group demonstrated successful key exchange between an airplane and a ground station with secure key lengths up to 200 kbit using polarization-encoded qubits [158]. However, we also believe that *time* is a viable alternative to polarization, and may prove to be superior in situations where the free-space channel includes media capable of polarization randomization. Thinking beyond practical concerns, all optical elements are ultimately polarization sensitive and as we devise experiments with precision beyond imagination [168], we never know when these minute effects start to become relevant. The aim of the experiment presented in

this chapter was and still is to make time-bin encoding accessible for free-space quantum communication. The adoption within the quantum communication community is hindered by the fact that, till now, no efficient time-bin qubit analyzer for multimode channels was available. Here, we investigate and experimentally realize two designs for such an analyzer and demonstrate its viability for quantum communication experiments.

In Chapter 2 we studied three-photon interference in an interferometer that can be regarded the successor to Franson's two-photon interferometer [61]. There, it may be remembered, the interference resource is *continuous* energy-time entanglement. In the conclusion of this experiment we alluded to the possibility to use a pulsed pump laser for generation of photon triplets that are entangled in energy and *discrete* time. Where is the discreteness coming from? If we send a laser pulse through an interferometer with short and long path, then we pump the first nonlinear crystal in two time slots, called *early* and *late*. As a result, photon pairs can be produced either in the early or late time slot. However, we can only get entanglement in time if there exists some form of coherence between the two time slots. The question of coherence must be our starting point before it makes sense to talk about advanced concepts such as quantum teleportation or applications in quantum communication. Brendel *et al.* in 1999 were the first to demonstrate a coherent superposition of time bins [84]. The generic time-bin setup, is sketched in Figure 5.2. The interferometric setup is in fact identical to the two-photon Franson interferometer but with an interesting twist. Assume we produce photon pairs with either early or late pump pulse. Send the photons into unbalanced interferometers that have path length differences identical to the one of the pump pulse interferometer (in practice, the allowed mismatch is bounded by the pump pulse coherence length). What do we expect to see? As with Franson's interferometer, there are four path combinations of interest, namely "short-short", "short-long", "long-short", and "long-long", depending on which path combination the two photons "realized". As Figure 5.2 shows, in a coincidence histogram, say with respect to detection of the red photon, we would see three peaks: one "early" time slot (the yellow photon took the short path), corresponding to the SL alternative, one "late" time slot (the yellow photon took the long path), corresponding to LS, and a "middle" time slot for the SS and LL alternatives. The latter two give us coincidences but, analogous to the situation in the Franson interferometer, since we do not know whether the pair was produced within the "early" or within the "late" pump pulse, we have no time reference with respect to which we could tell appart SS and LL. The situation is essentially the same as in the Franson interferometer but instead of having a continuuum of possible creation times, the pulses define two sharply peaked ones. Hence *discrete* energy-time entanglement. That events in the middle correspond to not merely a simple mixture of SS and LL, but a

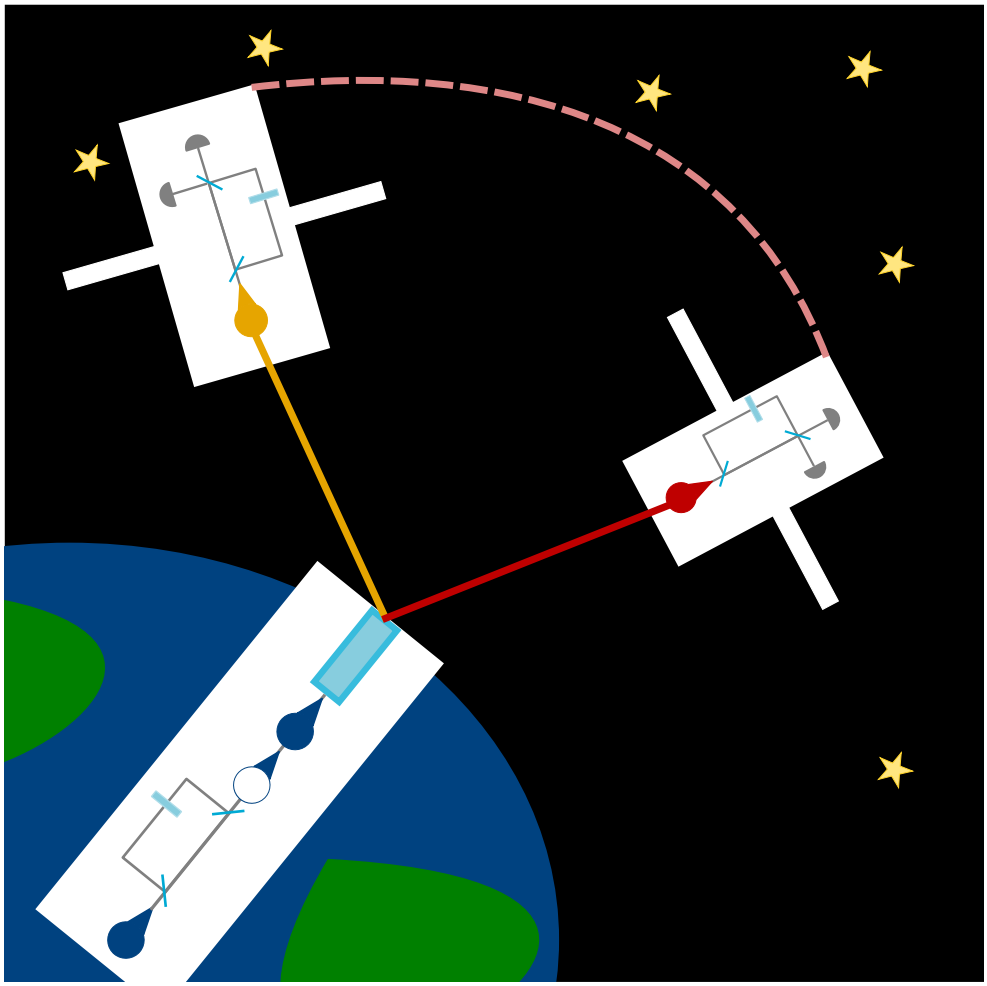

Figure 5.1: **Free-Space Quantum Communication with Time-Bins.** Sketch of how time-bin interferometers can be used to enable quantum communication between widely separated receivers. The present work is concerned with the development of a time-bin qubit analyzer, which is an interferometer whose main characteristic are unequal path lengths, suitable for multimode communication channels. These channels are encountered in many practical situations, for example on sea in the communication between ships. We are interested in quantum communication links between earth-based ground stations and airborne objects, say an airplane or satellite. The channel is naturally multimode because of refractive index fluctuations in the transmission medium, atmospheric turbulence in particular [169].

coherent superposition, is verified by varying interferometer phases. As we do this, counts in the middle bin should go up and down and this is exactly what Brendel *et al.* observed. Hence, time slots can be used to encode qubits (with remarkable simplicity). The encoding scheme is a natural extension to classical time-multiplexing, which was adopted to quantum

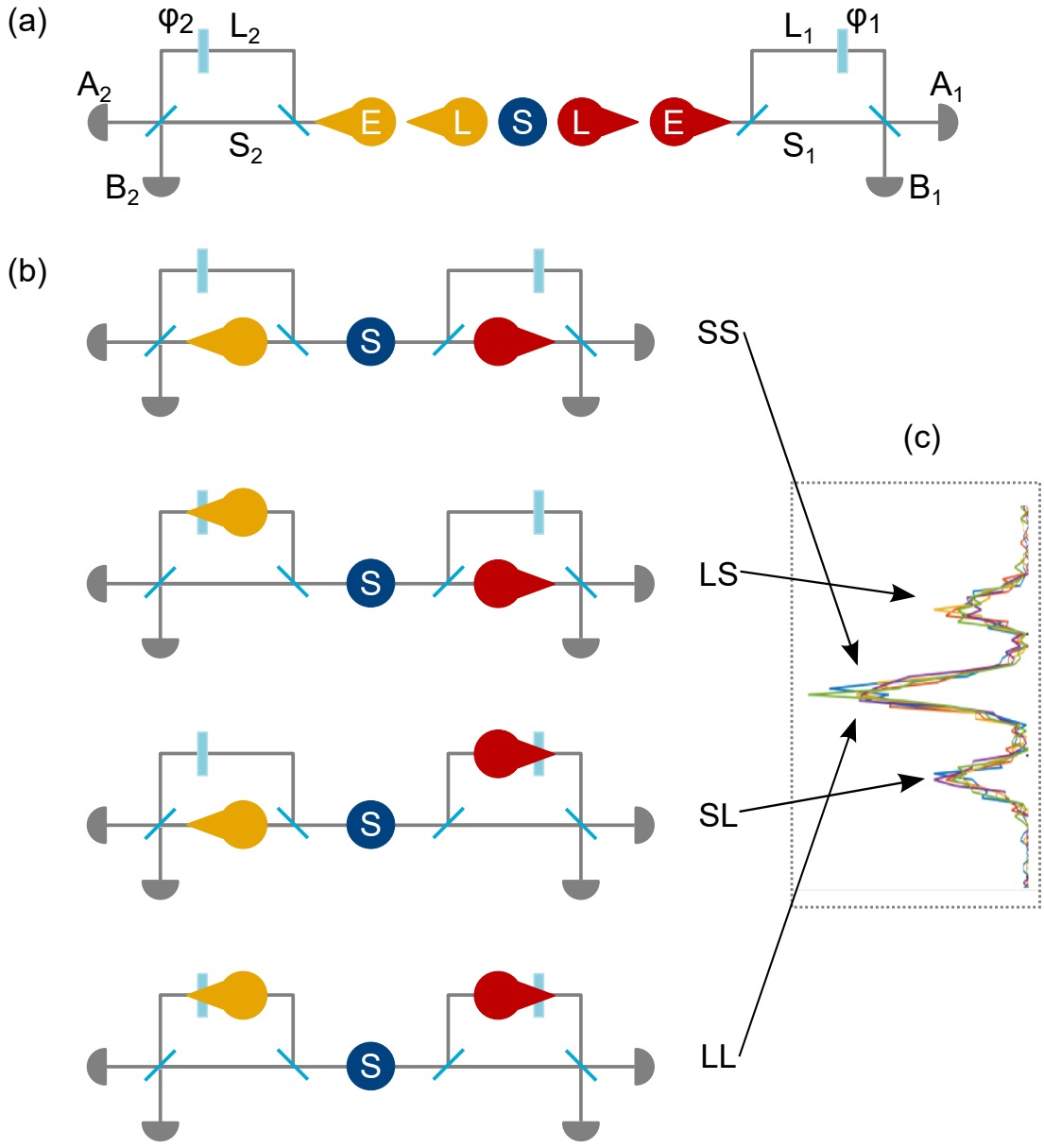

Figure 5.2: **Indistinguishable Alternatives in Time-Bin Interference.** **(a)** A generic time-bin interferometer setup where a source (S) emits photon pairs either in an early (E) or late (L) time slot. **(b)** Subsequently, photons can take either of four possible path combinations: short-short (SS), short-long (SL), long-short (LS), and long-long (LL). **(c)** The time-of-arrival (coincidence) histogram shows three peaks. As explained in the main text, the SS and LL alternatives are indistinguishable and thus, count rates in the middle peak are sensitive to variations in ϕ_1 and ϕ_2.

cryptography tasks a few years earlier [170, 171]. Subsequently, time-bin encoding proved to be the only viable degree of freedom for quantum communication through long optical

fibers [172–175] and has already been connected with quantum memories [176–178].

5.3 What are Time-Bin Qubits?

Coherence between two time slots allows us to encode a quantum bit onto the time slots, the *time-bin* qubit. A qubit is an abstract two-level system that is structurally identical to a two-dimensional Hilbert space $\mathcal{H}_T$ over the complex numbers. The canonical basis states are labeled by early and late time slots,

$$|E\rangle \equiv \begin{pmatrix} 1 \\ 0 \end{pmatrix}, \qquad |L\rangle \equiv \begin{pmatrix} 0 \\ 1 \end{pmatrix}. \tag{5.1}$$

Any linear superposition

$$|\Psi\rangle = c_1|E\rangle + c_2|L\rangle \tag{5.2}$$

of these two states can be realized experimentally, because parameters c_k (amplitudes) and γ_k (arguments) of the scalar products $\langle\Psi|E\rangle = |c_1|\exp(i\gamma_1)$ and $\langle\Psi|L\rangle = |c_2|\exp(i\gamma_2)$ can be controlled with beam splitters and phase shifters. In fact, any (unitary) transformation, i.e. elements in the group $U(N)$, can be constructed from these two optical elements [179]. For our purposes, the full generality is not needed and all we need to describe our interferometers are the symmetric beam splitter

$$B = \frac{1}{\sqrt{2}} \begin{pmatrix} 1 & 1 \\ 1 & -1 \end{pmatrix}, \tag{5.3}$$

and relative optical phase shifters

$$P = \begin{pmatrix} e^{i\phi} & 0 \\ 0 & 1 \end{pmatrix}. \tag{5.4}$$

The superposition states we consider here can be labeled by phase angles ϕ,

$$|\pm\phi\rangle = \frac{1}{\sqrt{2}}\Big(|E\rangle \pm e^{i\phi}|L\rangle\Big). \tag{5.5}$$

For instance,

$$\begin{aligned} |\pm\rangle \equiv |\pm\pi\rangle &= \frac{1}{\sqrt{2}}\Big(|E\rangle \pm |L\rangle\Big) \\ |\pm i\rangle \equiv |\pm\pi/2\rangle &= \frac{1}{\sqrt{2}}\Big(|E\rangle \pm i|L\rangle\Big). \end{aligned} \tag{5.6}$$

Observables of interest here are connected to Pauli operators

$$\begin{aligned}\hat{X} &= |E\rangle\langle L| + |L\rangle\langle E| \equiv \begin{pmatrix} 0 & 1 \\ 1 & 0 \end{pmatrix} \\ \hat{Y} &= i|L\rangle\langle E| - i|E\rangle\langle L| \equiv \begin{pmatrix} 0 & -i \\ i & 0 \end{pmatrix} \\ \hat{Z} &= |E\rangle\langle E| - |L\rangle\langle L| \equiv \begin{pmatrix} 1 & 0 \\ 0 & -1 \end{pmatrix}.\end{aligned} \tag{5.7}$$

Our measurements are described by simple projections operators. For measurements in X, Y, and Z basis, these are

$$\begin{aligned}\Pi_X &= \Big\{\Lambda_+ \equiv |+\rangle\langle +|, \qquad \Lambda_- \equiv |-\rangle\langle -|\Big\} \\ \Pi_Y &= \Big\{\Lambda_i \equiv |i\rangle\langle i|, \qquad \Lambda_{-i} \equiv |-i\rangle\langle -i|\Big\} \\ \Pi_Z &= \Big\{\Lambda_E \equiv |E\rangle\langle E|, \quad \Lambda_L \equiv |L\rangle\langle L|\Big\}.\end{aligned} \tag{5.8}$$

Detection probabilities are then calculated by forming expectation values, for instance a time-bin qubit in state $|\Psi\rangle$ has the following probabilities to be found in the early or late time slot,

$$\begin{aligned}P_E &= \langle\Psi|\Lambda_E|\Psi\rangle \\ P_L &= \langle\Psi|\Lambda_L|\Psi\rangle\,.\end{aligned} \tag{5.9}$$

5.4 Polarization-Time Hybrid Entanglement

In our experiment we actually work with two qubits. In addition to a time-bin qubit, we also have a polarization qubit, which lives in a Hilbert space

$$\mathcal{H}_P \cong \mathcal{H}_T\,. \tag{5.10}$$

The isomorphism implies that algebraic properties of both polarization and time-bin qubit are identical and all we need to do is change labels, i.e.

$$\begin{aligned}|E\rangle &\to |H\rangle \\ |L\rangle &\to |V\rangle\,.\end{aligned} \tag{5.11}$$

Of course, experimentally, polarization and time-bin qubits are distinguishable, but in the Hilbert space formalism they are identical. The composite system is then described by the

tensor product Hilbert space $\mathcal{H}_{TP} = \mathcal{H}_T \otimes \mathcal{H}_P$, which is spanned by products basis states (we use the short notation $|\Psi\psi\rangle \equiv |\Psi_T\rangle \otimes |\psi_P\rangle$)

$$|EH\rangle \equiv \begin{pmatrix} 1 \\ 0 \\ 0 \\ 0 \end{pmatrix}, \quad |EV\rangle \equiv \begin{pmatrix} 0 \\ 1 \\ 0 \\ 0 \end{pmatrix}, \quad |LH\rangle \equiv \begin{pmatrix} 0 \\ 0 \\ 1 \\ 0 \end{pmatrix}, \quad |LV\rangle \equiv \begin{pmatrix} 0 \\ 0 \\ 0 \\ 1 \end{pmatrix}. \tag{5.12}$$

In our experiment, we generate entangled photon pairs, which are best described in the *Bell basis*, comprising the four states

$$\begin{aligned}
\left|\Psi_+^{AB}\right\rangle &= \frac{1}{\sqrt{2}}\Big(|EV\rangle + |LH\rangle\Big) \equiv \begin{pmatrix} 0 \\ \frac{1}{\sqrt{2}} \\ \frac{1}{\sqrt{2}} \\ 0 \end{pmatrix} \\
\left|\Psi_-^{AB}\right\rangle &= \frac{1}{\sqrt{2}}\Big(|EV\rangle - |LH\rangle\Big) \equiv \begin{pmatrix} 0 \\ \frac{1}{\sqrt{2}} \\ -\frac{1}{\sqrt{2}} \\ 0 \end{pmatrix} \\
\left|\Phi_+^{AB}\right\rangle &= \frac{1}{\sqrt{2}}\Big(|EH\rangle + |LV\rangle\Big) \equiv \begin{pmatrix} \frac{1}{\sqrt{2}} \\ 0 \\ 0 \\ \frac{1}{\sqrt{2}} \end{pmatrix} \\
\left|\Phi_-^{AB}\right\rangle &= \frac{1}{\sqrt{2}}\Big(|EH\rangle - |LV\rangle\Big) \equiv \begin{pmatrix} \frac{1}{\sqrt{2}} \\ 0 \\ 0 \\ -\frac{1}{\sqrt{2}} \end{pmatrix}.
\end{aligned} \tag{5.13}$$

Despite the fact that we can segregate one photon from the other in physical space, two photons in any one of the Bell states are non-separable *as qubits*. In other words, the qubits *qua* carrier of quantum information are de-localized, though the physical carriers (time slots and photon polarization) are individually accessible. If the latter were not possible, then there would be no way physically to access the strong correlations inherent in biphotons (entangled photon-pairs). Experimental demonstration of a biphoton's logical inseparability requires some thought but since we are already standing on the shoulders of giants, we might as well make use of pre-existing knowledge [180]: the four observables we are looking for are (again, we use short notation here, $\hat{A}_k\hat{B}_l \equiv \hat{A}_k \otimes \hat{B}_l$)

$$\hat{A}_1\hat{B}_1, \quad \hat{A}_1\hat{B}_2, \quad \hat{A}_2\hat{B}_2, \quad \text{and} \quad \hat{A}_2\hat{B}_2\,, \tag{5.14}$$

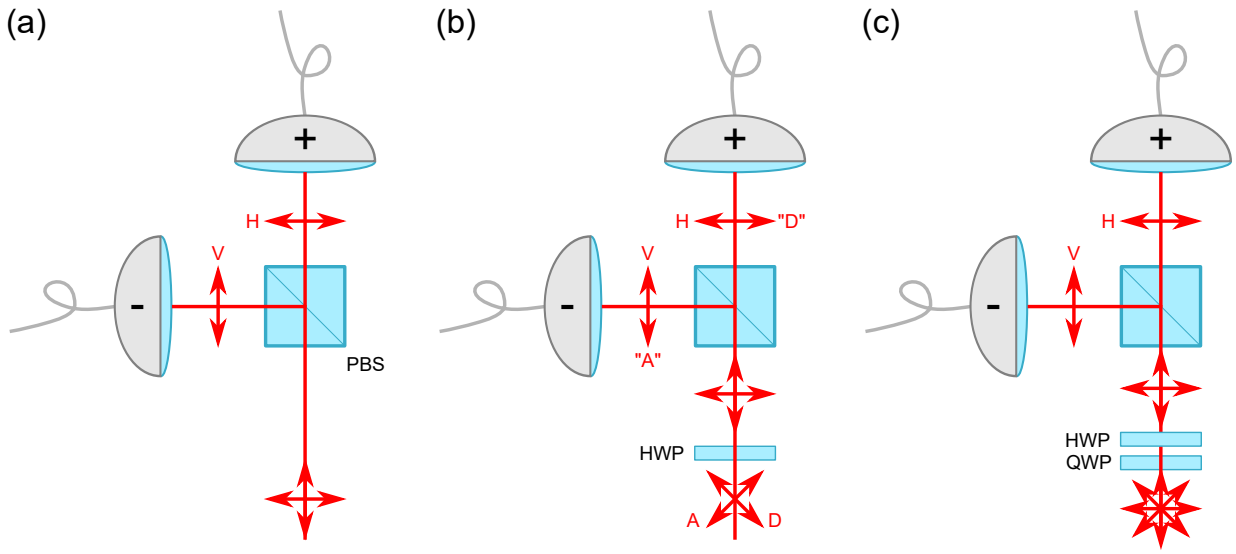

Figure 5.3: **Illustration of a Polarization Qubit Analyzer.** **(a)** A polarizing beam splitter (PBS) together with two single photon detectors allow us to measure the $\hat{Z}$ observable for a polarization qubit. **(b)** The addition of a half-wave plate (HWP) oriented at 22.5° permits measurements of the $\hat{X}$ observable. Though we are still detecting horizontal and vertical polarization, as in (a), the one-to-one map $H \leftrightarrow D$ and $V \leftrightarrow A$ via the HWP essentially lets us measure diagonal (D) and antidiagonal (A) polarization, respectively. Note: $|+\rangle$ represents D and $|-\rangle$ A polarization in the main text. In **(c)** we added a QWP to enable measurements in the $\hat{X} \pm \hat{Z}$-basis. With the same idea as in (b), the "eigenpolarizations" of this configuration are mapped to the H and V output ports of the PBS.

with single qubit observables

$$\begin{aligned} \hat{A}_1 &= \hat{Z} \\ \hat{A}_2 &= \hat{X} \end{aligned} \tag{5.15}$$

for the time-bin qubit and

$$\begin{aligned} \hat{B}_1 &= \frac{1}{\sqrt{2}}\left(\hat{X} + \hat{Z}\right) \equiv \frac{1}{\sqrt{2}} \begin{pmatrix} 1 & 1 \\ 1 & -1 \end{pmatrix} \\ \hat{B}_2 &= \frac{1}{\sqrt{2}}\left(\hat{X} - \hat{Z}\right) \equiv \frac{1}{\sqrt{2}} \begin{pmatrix} -1 & 1 \\ 1 & 1 \end{pmatrix} \end{aligned} \tag{5.16}$$

for the polarization qubit. We follow here the nomenclature and use letters A for the first qubit ("Alice") and letters B for the second qubit ("Bob"). What are these observables and how do we work with them experimentally? First of all, their eigenvalues are $\lambda = \pm 1$.

This is in fact true for any linear combination

$$\hat{W}(\alpha) = \sin(\alpha)\hat{X} + \cos(\alpha)\hat{Z}\,, \tag{5.17}$$

which can be quickly verified, for the matrix representation

$$W(\alpha) = \begin{pmatrix} \cos(\alpha) & \sin(\alpha) \\ \sin(\alpha) & -\cos(\alpha) \end{pmatrix} \tag{5.18}$$

has the characteristic polynomial $\lambda^2 = 1$. Not only does this tell us there are two measurement outcomes, but also that the analyzers feature two complementary detectors, i.e. detectors labeled by the sign of λ. For the polarization qubit, things are quite simple. For a measurement in the $\hat{Z}$ basis we only need a polarizing beam splitter (PBS) in front of two single photon detectors. As shown in Figure 5.3 (a), a PBS directs input photons in states $|H\rangle$ and $|V\rangle$ into "+" and "−" detectors, respectively. As already alluded to, the label $\pm$ indicates the measured eigenvalue $\lambda = \pm 1$ of $\hat{Z}$. For instance, when a photon is detected in the "+" detector, we say our measurement resulted in $\lambda = +1$ because $|H\rangle$ is eigenvector of $\hat{Z}$ with eigenvalue $+1$. Consequently, the *complementary* detector in the V output is the $\lambda = -1$ detector. Measurements in other bases require wave plates in front of the PBS. More specifically, we need a half-wave plate (HWP), represented by the unitary matrix

$$\mathrm{HWP}(\Theta) = \begin{pmatrix} \cos(2\Theta) & \sin(2\Theta) \\ \sin(2\Theta) & -\cos(2\Theta) \end{pmatrix}, \tag{5.19}$$

and a quarter-wave plate (QWP),

$$\mathrm{QWP}(\theta) = \frac{1}{\sqrt{2}} \begin{pmatrix} 1 + i\cos(2\theta) & i2\sin(\theta)\cos(\theta) \\ i2\sin(\theta)\cos(\theta) & 1 - i\cos(2\theta) \end{pmatrix}, \tag{5.20}$$

where Θ and θ are the physical rotation angles (which the "fast" axis makes with respect to the H-axis). For instance, an $\hat{X}$-basis measurement requires a HWP set to $\Theta = 22.5°$, as shown in Figure 5.3 (b). Why? Let us assume we have $|+\rangle$ as an input. Then

$$\mathrm{HWP}\,(22.5°)\,|+\rangle = \frac{1}{2}\begin{pmatrix} 1 & 1 \\ 1 & -1 \end{pmatrix}\begin{pmatrix} 1 \\ 1 \end{pmatrix} = \begin{pmatrix} 1 \\ 0 \end{pmatrix} \equiv |H\rangle\,, \tag{5.21}$$

which the following PBS directs into the "+" detector. Likewise, the input state $|-\rangle$ is transformed by the HWP into $|V\rangle$, which is then directed into the "−" detector. Therefore, this setup can *perfectly distinguish* between $|+\rangle$ and $|-\rangle$, and since these are the eigenstates of $\hat{X}$, a HWP set to $\Theta = 22.5°$, together with a PBS, acts as an $\hat{X}$-analyzer. The $\hat{Z}$-analyzer for a time-bin qubit is simpler in one sense and more involved in another. First, we only

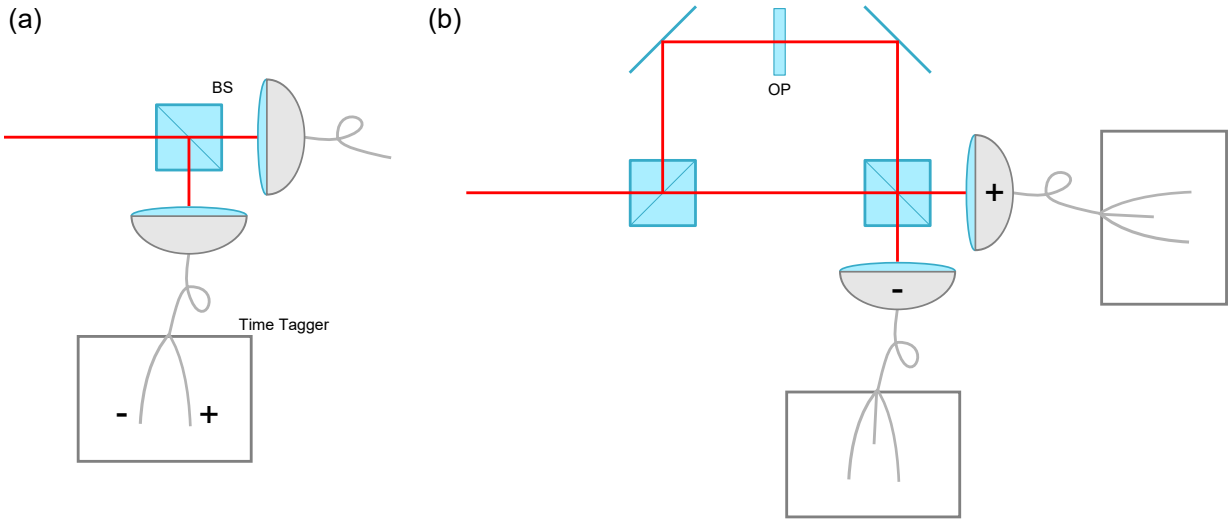

Figure 5.4: **Illustration of a Time-Bin Qubit Analyzer. (a)** Time-bin qubit measurement in $\hat{Z}$-basis. The beam splitter (BS) is not really necessary for this measurement and is only there for better illustration of (b). All we need is a single detector and a time tagger, which sorts photons into arrival time bins (with respect to a time reference, e.g. detection of a partner photon). The early and late time bins correspond to eigenvalue $+1$ and -1 measurement outcomes, respectively. **(b)** The addition of an unbalanced interferometer provides another path and with it a third arrival time possibility, which the time tagger recognizes as "middle bin". A second detector can now act as the complementary one, because, depending on the optical phase (OP), a middle bin detection happens either in the "+" or "-" detector due to interference. Probabilistic splitting at the BS' has the consequence that also here we detect time-bins in the $\hat{Z}$-basis.

need one physical detector and no optical elements in front of the detector. However, we need to perform photon detection in a time-resolved manner, i.e. we need to assign time stamps to detection signals with respect to some time reference (for instance a trigger signal). Figure 5.4 (a) shows such a setup where a beam splitter (BS) and second detector are included. Again, these are not essential for the $\hat{Z}$-analyzer but highlights that a $\hat{Z}$-analyzer is implicit also in a, say, $\hat{X}$-analyzer shown in (b). There we place an unbalanced interferometer in front of two detectors. Photons in the early and late time slots can now interfere provided the path length difference matches the separation in time. Depending on whether the interference is constructive or destructive, photons sort themselves into the "+" and "-" detectors.

In our experiment we generate photons in state $|\Phi_+^{AB}\rangle$, which means we take a vested interest in expectation values

$$\left\langle \hat{A}_k \hat{B}_l \right\rangle \equiv \left\langle \Phi_+^{AB} \middle| \hat{A}_k \hat{B}_l \middle| \Phi_+^{AB} \right\rangle . \tag{5.22}$$

We can explicitly calculate

$$\begin{aligned}
\left\langle \hat{A}_1 \hat{B}_1 \right\rangle = \frac{1}{2\sqrt{2}} \Big(& \left\langle E|\hat{Z}|E \right\rangle \left\langle H|\hat{X}|H \right\rangle + \left\langle E|\hat{Z}|L \right\rangle \left\langle H|\hat{X}|V \right\rangle \\
& + \left\langle L|\hat{Z}|E \right\rangle \left\langle V|\hat{X}|H \right\rangle + \left\langle L|\hat{Z}|L \right\rangle \left\langle V|\hat{X}|V \right\rangle \\
& + \left\langle E|\hat{Z}|E \right\rangle \left\langle H|\hat{Z}|H \right\rangle + \left\langle E|\hat{Z}|L \right\rangle \left\langle H|\hat{Z}|V \right\rangle \\
& + \left\langle E|\hat{Z}|E \right\rangle \left\langle H|\hat{Z}|H \right\rangle + \left\langle E|\hat{Z}|L \right\rangle \left\langle H|\hat{Z}|V \right\rangle \Big) \\
= \frac{1}{2\sqrt{2}} & \Big(1 \cdot 0 + 0 \cdot 1 + 0 \cdot 1 + (-1) \cdot 0 + 1 \cdot 1 + 0 \cdot 0 + 1 \cdot 1 + 0 \cdot 0 \Big) \\
= \frac{1}{\sqrt{2}} & ,
\end{aligned} \tag{5.23}$$

$$\begin{aligned}
\left\langle \hat{A}_1 \hat{B}_2 \right\rangle = \frac{1}{2\sqrt{2}} \Big(& \left\langle E|\hat{Z}|E \right\rangle \left\langle H|\hat{X}|H \right\rangle + \left\langle E|\hat{Z}|L \right\rangle \left\langle H|\hat{X}|V \right\rangle \\
& + \left\langle L|\hat{Z}|E \right\rangle \left\langle V|\hat{X}|H \right\rangle + \left\langle L|\hat{Z}|L \right\rangle \left\langle V|\hat{X}|V \right\rangle \\
& - \left\langle E|\hat{Z}|E \right\rangle \left\langle H|\hat{Z}|H \right\rangle - \left\langle E|\hat{Z}|L \right\rangle \left\langle H|\hat{Z}|V \right\rangle \\
& - \left\langle E|\hat{Z}|E \right\rangle \left\langle H|\hat{Z}|H \right\rangle - \left\langle E|\hat{Z}|L \right\rangle \left\langle H|\hat{Z}|V \right\rangle \Big) \\
= \frac{1}{2\sqrt{2}} & \Big(1 \cdot 0 + 0 \cdot 1 + 0 \cdot 1 + (-1) \cdot 0 - 1 \cdot 1 - 0 \cdot 0 - 1 \cdot 1 - 0 \cdot 0 \Big) \\
= -\frac{1}{\sqrt{2}} & ,
\end{aligned} \tag{5.24}$$

$$
\begin{aligned}
\left\langle \hat{A}_2\hat{B}_1 \right\rangle = \frac{1}{2\sqrt{2}}\Big(& \left\langle E|\hat{X}|E \right\rangle\left\langle H|\hat{X}|H \right\rangle + \left\langle E|\hat{X}|L \right\rangle\left\langle H|\hat{X}|V \right\rangle \\
& + \left\langle L|\hat{X}|E \right\rangle\left\langle V|\hat{X}|H \right\rangle + \left\langle L|\hat{X}|L \right\rangle\left\langle V|\hat{X}|V \right\rangle \\
& + \left\langle E|\hat{X}|E \right\rangle\left\langle H|\hat{Z}|H \right\rangle + \left\langle E|\hat{X}|L \right\rangle\left\langle H|\hat{Z}|V \right\rangle \\
& + \left\langle E|\hat{X}|E \right\rangle\left\langle H|\hat{Z}|H \right\rangle + \left\langle E|\hat{X}|L \right\rangle\left\langle H|\hat{Z}|V \right\rangle \Big) \\
= \frac{1}{2\sqrt{2}}\Big(& 0\cdot 0 + 1\cdot 1 + 1\cdot 1 + 0\cdot 0 + 0\cdot 1 + 1\cdot 0 + 0\cdot 1 + 1\cdot 0 \Big) \\
= \frac{1}{\sqrt{2}}\,, &
\end{aligned}
\tag{5.25}
$$

and

$$
\begin{aligned}
\left\langle \hat{A}_2\hat{B}_2 \right\rangle = \frac{1}{2\sqrt{2}}\Big(& \left\langle E|\hat{X}|E \right\rangle\left\langle H|\hat{X}|H \right\rangle + \left\langle E|\hat{X}|L \right\rangle\left\langle H|\hat{X}|V \right\rangle \\
& + \left\langle L|\hat{X}|E \right\rangle\left\langle V|\hat{X}|H \right\rangle + \left\langle L|\hat{X}|L \right\rangle\left\langle V|\hat{X}|V \right\rangle \\
& - \left\langle E|\hat{X}|E \right\rangle\left\langle H|\hat{Z}|H \right\rangle - \left\langle E|\hat{X}|L \right\rangle\left\langle H|\hat{Z}|V \right\rangle \\
& - \left\langle E|\hat{X}|E \right\rangle\left\langle H|\hat{Z}|H \right\rangle - \left\langle E|\hat{X}|L \right\rangle\left\langle H|\hat{Z}|V \right\rangle \Big) \\
= \frac{1}{2\sqrt{2}}\Big(& 0\cdot 0 + 1\cdot 1 + 1\cdot 1 + 0\cdot 0 - 0\cdot 1 - 1\cdot 0 - 0\cdot 1 - 1\cdot 0 \Big) \\
= -\frac{1}{\sqrt{2}}\,. &
\end{aligned}
\tag{5.26}
$$

When then calculate the CHSH-Bell parameter

$$
S = \left| \left\langle \hat{A}_1\hat{B}_1 \right\rangle - \left\langle \hat{A}_1\hat{B}_2 \right\rangle + \left\langle \hat{A}_2\hat{B}_1 \right\rangle + \left\langle \hat{A}_2\hat{B}_2 \right\rangle \right| = 2\sqrt{2} \approx 2.83\,, \tag{5.27}
$$

transgressing the classical bound $S_{\text{Classical}} = 2$. This violation is signature of the strong correlation inherent in biphotons such as the ones we produce. The expectation values are estimated experimentally in coincidence measurements, which we illustrate for the measurement of $\left\langle \hat{A}_1\hat{B}_1 \right\rangle$. In this setup, we count time-bin photons in the early and late bins, and polarization photons in the "+" and "-" detectors with the $\hat{X} \pm \hat{Z}$-analyzer ($\Theta = +11.25°$ and $\theta = 0°$) setup of Figure 5.3 (c). There are now four events possible, namely

$$
\begin{aligned}
N_{11}^{++} &:= \quad \text{Coincidences between } |E\rangle \quad \text{and} \quad |H\rangle \\
N_{11}^{+-} &:= \quad \text{Coincidences between } |E\rangle \quad \text{and} \quad |V\rangle \\
N_{11}^{-+} &:= \quad \text{Coincidences between } |L\rangle \quad \text{and} \quad |H\rangle \\
N_{11}^{--} &:= \quad \text{Coincidences between } |L\rangle \quad \text{and} \quad |V\rangle\,.
\end{aligned}
\tag{5.28}
$$

In a similar manner, we record coincidence counts for the other three measurement configurations, and can then calculate the (empirical) expectation value, defined as

$$E(\hat{A}_k\hat{B}_l) \coloneqq \frac{\sum_{p,q=\pm}\lambda_p\lambda_q N_{kl}^{pq}}{\sum_{p,q=\pm}N_{kl}^{pq}}\,, \tag{5.29}$$

where the products $\lambda_p\lambda_q = \pm 1$ are the possible measurement outcomes of joint-observables $\hat{A}_k\hat{B}_l$. The desired expectation values can now be estimated,

$$\begin{aligned}
\left\langle \hat{A}_1\hat{B}_1 \right\rangle &\hat{=} E(\hat{A}_1\hat{B}_1) = \frac{N_{11}^{++} + N_{11}^{--} - N_{11}^{+-} - N_{11}^{-+}}{N_{11}^{++} + N_{11}^{--} + N_{11}^{+-} + N_{11}^{-+}} \\
\left\langle \hat{A}_1\hat{B}_2 \right\rangle &\hat{=} E(\hat{A}_1\hat{B}_2) = \frac{N_{12}^{++} + N_{12}^{--} - N_{12}^{+-} - N_{12}^{-+}}{N_{12}^{++} + N_{12}^{--} + N_{12}^{+-} + N_{12}^{-+}} \\
\left\langle \hat{A}_2\hat{B}_1 \right\rangle &\hat{=} E(\hat{A}_2\hat{B}_1) = \frac{N_{21}^{++} + N_{21}^{--} - N_{21}^{+-} - N_{21}^{-+}}{N_{21}^{++} + N_{21}^{--} + N_{21}^{+-} + N_{21}^{-+}} \\
\left\langle \hat{A}_2\hat{B}_2 \right\rangle &\hat{=} E(\hat{A}_2\hat{B}_2) = \frac{N_{22}^{++} + N_{22}^{--} - N_{22}^{+-} - N_{22}^{-+}}{N_{22}^{++} + N_{22}^{--} + N_{22}^{+-} + N_{22}^{-+}}\,.
\end{aligned} \tag{5.30}$$

5.5 Multimode Time-Bin Qubit Analyzer

5.5.1 The Problem with Unbalanced Interferometers

Geometrical optics is very effective for exhibition of basic optical phenomena. One of the method it provides is *ray tracing*, which can be performed by hand or with the aid of computer programs for complicated problems. Consider the unbalanced Michelson interferometer in Figure 5.5. Let l_L and l_S denote the distance between center of beam splitter and mirror for long and short path, respectively. An incident ray can have an *angle of incidence* (AOI) α, which it makes with respect to the optical input axis. For normal incidence, $\alpha = 0$, a photon travels the distance $2l_L$ in the long path and $2l_S$ in the short path before exiting the interferometer. The path difference is $\Delta l_0 = 2(l_L - l_S)$. For a non-zero AOI, this quantity becomes α dependent, as we now show.

The distance between beam splitter diagonal and mirror front surface is ($i = S, L$)

$$\overline{\mathrm{BS} - \mathrm{M}_i} = \frac{l_i}{\cos(\alpha)}, \tag{5.31}$$

and then back again,

$$\overline{\mathrm{M}_i - \mathrm{BS}} = \frac{l_i\big(1 - \tan(\alpha)\big)}{\cos(\alpha) + \sin(\alpha)}\,. \tag{5.32}$$

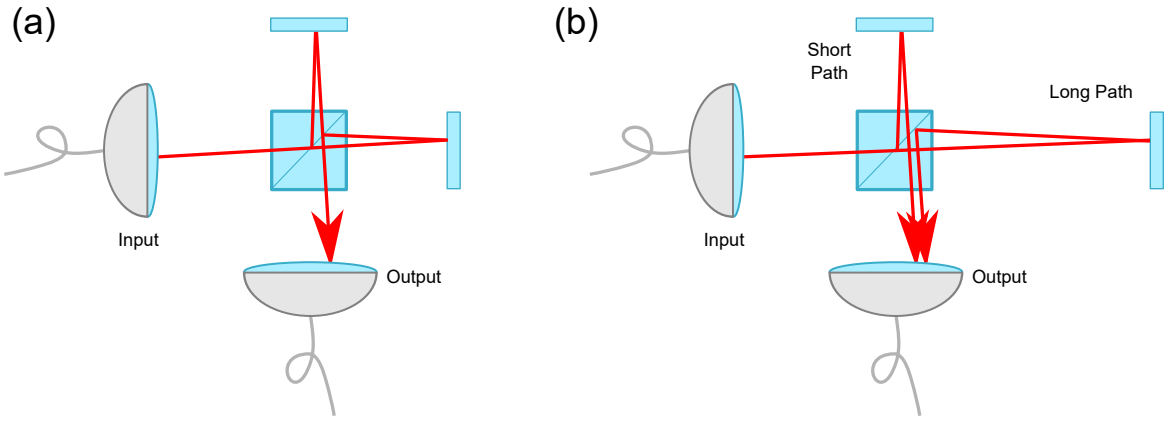

Figure 5.5: **Input Angle Problem for Unbalanced Interferometers.** Shown is a ray making an angle with respect to the system's optical axis. The angle translates into a distance-dependent lateral offset with respect to that axis. Hitting the beam splitter of the balanced interferometer shown in **(a)**, returning rays do not hit the center again. Crucially, however, since the paths are of same length, both rays hit the same spot. **(b)** This is no longer the case in an unbalanced interferometer. There, because a ray traveling along the short path accumulates less offset than a ray through the long arm, returning rays no longer intersect at the beam splitter. Substituting rays with beams, this leads to a reduced overlap and hence diminished interference visibility.

As Figure 5.5 (b) illustrates, paths do not overlap at the beam splitter for $\alpha \neq 0$ and there is an additional path difference after the beam splitter ("triangle difference"),

$$\overline{\text{Extra}} = \delta(\alpha) \tan\left(\alpha - \frac{\pi}{4}\right) , \tag{5.33}$$

where

$$\delta(\alpha) = \frac{\Delta l_0 \tan(\alpha)}{1 + \tan(\alpha)} \tag{5.34}$$

is the angle-dependent lateral offset between two exiting rays. Thus, the total, angle-dependent path difference rays accrue is given by

$$\Delta l(\alpha) = \frac{\Delta l_0}{2} \left(\frac{1}{\cos(\alpha)} + \frac{1 - \tan(\alpha)}{\cos(\alpha) + \sin(\alpha)} \right) + \delta(\alpha) \tan\left(\alpha - \frac{\pi}{4}\right) . \tag{5.35}$$

Leaving the ray picture, we consider a Gaussian input beam, which describes a light field exiting a single-mode fiber. Neglecting beam expansion during propagation, the intensity interference pattern of two Gaussian beams exiting the interferometer is governed by beam overlap at the beam splitter [181]. With lateral offset $\delta(\alpha)$, the Gaussian beam intensity at the interferometer output is

$$I\big(\delta(\alpha), \phi\big) = I_0 \left(1 + \exp\left[- \left\{ \frac{\delta(\alpha)}{2\sigma} \right\}^2 \right] \cos(\phi) \right) , \tag{5.36}$$

with input beam intensity I_0, beam width σ, and interferometer phase ϕ. We calculate the interference visibility for the unbalanced Michelson interferometer (UMI) as

$$\mathcal{V}_{\text{UMI}} \coloneqq \frac{I\big(\delta(\alpha), \phi\big)_{\max} - I\big(\delta(\alpha), \phi\big)_{\min}}{I\big(\delta(\alpha), \phi\big)_{\max} + I\big(\delta(\alpha), \phi\big)_{\min}} . \tag{5.37}$$

The minimum and maximum of (5.36) with respect to ϕ are easily found. To the result we multiply the system visibility $\mathcal{V}_0$, which is the best visibility we achieve with the interferometer (at $\alpha = 0$). It is usually less than 1 due to other experimental imperfections that render two beams distinguishable. Absorbing all those visibility degradations into $\mathcal{V}_0$, we get the visibility as a function of α,

$$\mathcal{V}(\alpha) = \mathcal{V}_0 \exp\left(- \left[\frac{\Delta l_0 \tan(\alpha)}{\sqrt{2}\sigma\{1 + \tan(\alpha)\}} \right]^2 \right) . \tag{5.38}$$

The visibility drops rapidly with α (as we demonstrate experimentally). For example, starting with a system efficiency $\mathcal{V}_0 = 91\,\%$, a beam of width $\sigma = 1.49\,\text{mm}$ through our interferometer with $\Delta l_0 = 60\,\text{cm}$, we get $\mathcal{V}(0.1^\circ) = 70\,\%$. There are two scenarios where we actually encounter beams with a non-zero α. First, if we couple into the interferometer a free-space beam, then we typically do so with some AOI. In the free-space

quantum communication experiment between the islands La Palma and Tenerife [162], for instance, atmospheric turbulence lead to beam wander within an angular range of $\sim 0.004°$ ($75\,\mu$rads). Moving systems suffer from additional pointing errors, which can be quite substantial. The QKD experiments to a moving truck in our group, for example, showed an angular spread of ~ 0.06 [169]. The second source for a α variation (a distribution, really) is provided by multimode beams. These posses non-trivial spatial intensity distributions with a correspondingly broad transversal Fourier spectrum. If we consider a multimode beam in a plane $z = 0$ (z is the propagation direction, and $z = 0$ can be, for example, the exit facet of a multimode fiber), then the angular spectrum representation of wave fields [139] tells us that each spatial frequency component in the $z = 0$ plane is associated with exactly one plane-wave mode, which all travel in different directions (hence angular spectrum). In free-space quantum communication we almost always have to deal with turbulent channels (within cities, or to airborne objects) that render a single-mode beam multimode. The receiver, for any kind of qubit encoding technique, has to deal with those highly structured beams. Of course, one could make use of spatial filters such pin holes —or simply couple light into a single-mode fiber. These methods, however, are by their very nature highly inefficient [182]. Depending on the application, any losses in addition to channel loss may be unacceptable, in particular when dealing with (entangled) single photons. So the question is, how can we solve this angle problem with minimal photon loss?

5.5.2 Compensation Optics for Unbalanced Interferometers

We investigate here two solutions for the AOI problem outlined in the previous section. The first is based on imaging optics, and the second makes use of refractive index differences. Though we arrived at the resulting interferometer design independently, the general idea has been discovered before us [183–185]. In fact, much earlier designs exist [186], namely Mertz "dielectric method" and Connes "telescope method". The root of the problem is the unbalanced interferometer's intrinsic asymmetry. We want this with respect to *time* but not with respect to *spatial mode*. Thus, grandly speaking, our aim is to symmetrize the interferometer with respect to space while leaving time untouched. In the beginning we thought about intricate "mirror mazes" embedded into the interferometer to compensate for the offset. In hindsight this was foolish, for a particular mirror arrangement can account for only one offset. What is needed here is an optical system that also maps angles to lateral offset, namely an imaging system. More precisely, we need a $4f$-system, i.e. two identical lenses with focal length f separated by a distance $2f$, which maps an object at distance f from the first lens to an image at distance f from the second lens. The magnification

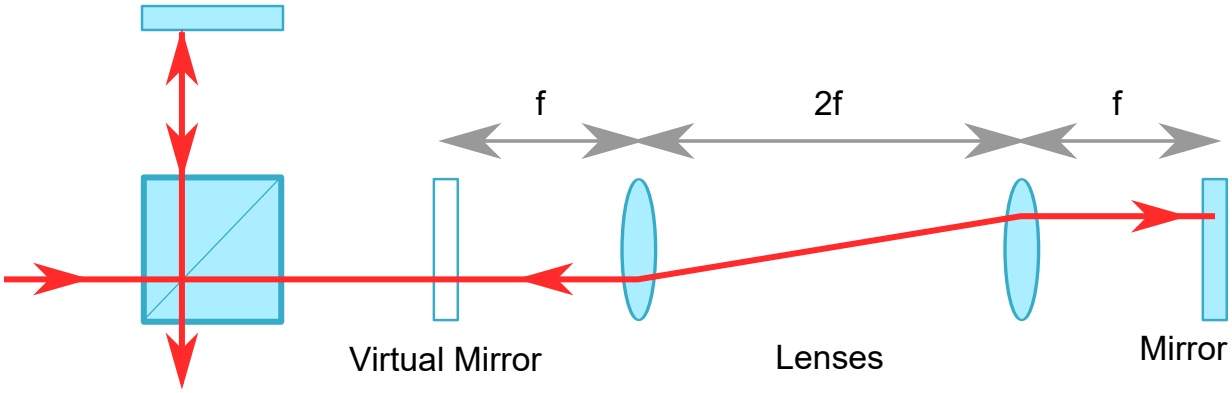

Figure 5.6: **Relay Lens System in an Unbalanced Interferometer.** Illustrating with a single ray how a $4f$-lens system in the long arm of an unbalanced Michelson interferometer maps everything it "sees" in the virtual mirror plane back to it after propagation (object plane is identical with the image plane). As explained in more detail in the main text, with respect to the spatial mode, the interferometer appears balanced.

is -1 so that we get an inverted image identical in size to the object. Propagating again through such a system, we get a magnification of 1, as matrix optics verifies,

$$\left[\begin{pmatrix} 1 & f \\ 0 & 1 \end{pmatrix}\begin{pmatrix} 1 & 0 \\ -1/f & 1 \end{pmatrix}\begin{pmatrix} 1 & 2f \\ 0 & 1 \end{pmatrix}\begin{pmatrix} 1 & 0 \\ -1/f & 1 \end{pmatrix}\begin{pmatrix} 1 & f \\ 0 & 1 \end{pmatrix}\right]^2 = \mathbb{1}\,, \tag{5.39}$$

and which is illustrated in Figure 5.6 with a single ray (see also setup Figure 5.7 (c)). This means, despite the fact that a beam traversed a distance $8f$, the output wavefront (the image) looks identical to the input wavefront (the object). This is why the $4f$-system is also known as relay lens system because it simply relays an object. This is exactly what we need. If we place a relay system in the long path of the unbalanced interferometer such that at distance f from the first lens we would have the mirror *if* the interferometer was balanced (virtual mirror), and if the actual mirror is a distance f behind the second lens, then we have the following situation: a beam still travels the whole distance through the long arm, thus accruing a time difference with respect to the beam traveling along the short path, but the wavefront is the same for both paths. This is because the relay system in the long arm "picks up" the wavefront from position of the virtual mirror, preserves it during propagation and "puts it back" to the position of the virtual mirror with the result that the effective mirror position, which determines the offset at the beam splitter due to α, is identical for both arms. Thus, with respect to the spatial mode, the interferometer is balanced; with respect to time it remains unbalanced.

Over the course of the experiment, we investigated a second approach to solve the problem. As later shown in Figure 5.7 (f), a piece of glass in the long arm also produces

an angle-dependent lateral offset [183], which can be used, by careful choice of refractive index and length of the glass, to compensate lateral offsets coming from non-zero input angles. Again, the idea is to produce a virtual mirror for the spatial mode at the location where a real mirror would make the interferometer balanced. As before, consider an input beam with angle α with respect to the optical axis. The optical path difference of the interferometer is then given by

$$\Delta l = 2\Big(n_L l_L \cos(\alpha_L) - n_S l_S \cos(\alpha_S)\Big)\,, \tag{5.40}$$

where n_i and α_i $(i = S, L)$ are refractive indices and reflection angles (off mirrors), respectively. For small angles α_i, we can use Taylor's approximation for Snell's law and get

$$\Delta l \approx 2\Big(n_L l_L - n_S l_S\Big) - \sin^2\left(\alpha\left[\frac{l_L}{n_L} - \frac{l_S}{n_S}\right]\right)\,. \tag{5.41}$$

We see that, with a proper choice of parameters, the two terms cancel and the effective path difference is, to first order, zero. These, then, are the two schemes on which our multimode time-bin qubit analyzers (MM-TQA) are based on.

5.5.3 Experimental Demonstration of a Multimode Time-Bin Qubit Analyzer

We now proceed to an experimental demonstration of multimode time-bin qubit analyzers. Schematics for the two realized compensation schemes are shown in Figure 5.7 (c) and (f). For the relay system we employ $f = 7.5\,\text{mm}$ achromatic lenses, which sets the path difference to $\Delta l_0 = 8f = 60\,\text{cm}$, or 2.0 ns. For the refractive-index material we had available a 118 mm long glass cube with refractive index n_G=1.4825 (the refractive index in the short path is that of air $n_{\text{air}} \approx 1$), which determines the path difference as $\Delta l_0 = 17\,\text{cm}$ or 0.57 ns. The best total throughput we achieve from input to output is 0.74. First of all, we assess the severity of visibility reduction with multimode beams. For that we use a continuous-wave grating-stabilized laser at 776 nm, and couple light through a single mode (SM) fiber into an unbalanced interferometer without correcting optics. As shown in Figure 5.7 (d), the visibility decreases rapidly from its initial value of $\mathcal{V}_0^{\text{SM}} = (91 \pm 1)\,\%$ and matches nicely with the predictions of Equation (5.38). The same is true for the (shorter) interferometer we use with the glass cube: here, if we take out the glass cube, the visibility also drops from $\mathcal{V}_0^{\text{SM}} = (94 \pm 1)\,\%$, but much more slowly. The reason is, of course, that the path difference is only 17 cm. With either of the two correction optics in place, however, the visibility stays constant. But does it also work for a multimode beam? To test this, we couple the same laser light into a 1 m-long step-index multimode fiber (Thorlabs M43L01) and repeat the

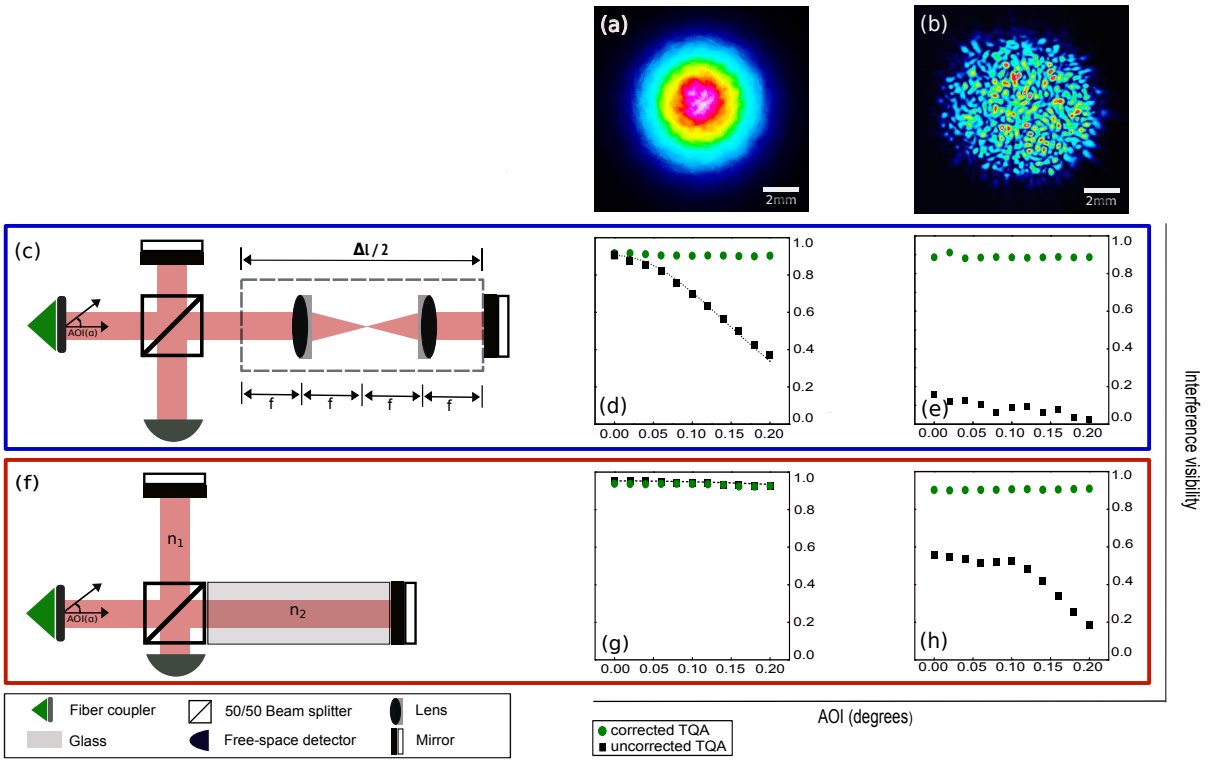

Figure 5.7: **Demonstration of Two Compensation Schemes for Unbalanced Interferometers.** (from Jin *et al.* [187]) We compare the interference visibilities for **(a)** single and **(b)** multimode beams (images taken with a WinCamD-UCD12 beam profiling camera). The relay lens method is sketched in **(c)**, and refractive-index method in **(f)**. The results are summarized in **(d)** (single mode, design (c)), **(e)** (multimode, design (c)), **(g)** (single mode, design (f)) and **(h)** (multimode, design (d)). There we plot the visibilities measured with the respective interferometer and also compare them with those measured when the compensation system is taken out (uncorrected interferometer). Solid lines are fits of Equation (5.38) and error bars are smaller than plot symbol size.

measurements. We immediately see a huge drop in the best achievable visibility, namely $\mathcal{V}_0^{\mathrm{MM}} = (16 \pm 1)\,\%$, which continues diminishing as α is increased. With imaging and glass cube in place, however, we achieve constant visibilities of $\mathcal{V}_0^{\mathrm{MM}} = (89 \pm 1)\,\%$ and $\mathcal{V}_0^{\mathrm{MM}} = (90 \pm 1)\,\%$, respectively.

5.6 Experimental Hybrid Entanglement of Polarization and Multimode Time-bin Qubits

5.6.1 Experimental Setup

We now integrate the newly developed multimode time-bin qubit analyzers in an experiment using entangled photons. The setup is shown in Figure 5.8. We first produce polarization-entangled photons using a nonlinear crystal embedded in a Sagnac interferometer (setup EPS in Figure 5.8). The Sagnac entangled photon source has been used extensively in our labs and in fact, my first task as a PhD student was to align the Sagnac source we used for our time-bin experiments. The crystal is a 30 mm long periodically poled potassium titanyl phosphate (PPKTP) slab, which we pump with a continuous-wave grating stabilized laser (404 nm, 6 mW). When the pump polarization is set to a superposition of H and V, then two processes can happen (neglecting normalization), namely

$$\begin{aligned} |V\rangle_P + |H\rangle_P \xrightarrow{\text{PBS}} &\left\{ \begin{array}{c} |H\rangle_P \xrightarrow{\text{SPDC}} |H\rangle_s|V\rangle_i \xrightarrow{\text{HWP}} |V\rangle_s|H\rangle_i \\ |V\rangle_P \xrightarrow{\text{HWP}} |H\rangle_P \xrightarrow{SPDC} |H\rangle_s|V\rangle_i \end{array} \right\} \\ &\xrightarrow{\text{PBS}} |H\rangle_s|V\rangle_i + |V\rangle_s|H\rangle_i\,, \end{aligned} \tag{5.42}$$

where the crystal is phase-matched for type-II spontaneous parametric downconversion (SPDC). Signal (s) and idler (i) photons have wavelengths 842 nm and 776 nm, respectively. We get an entangled state only when the two processes are indistinguishable, which is the most critical part (alignment of the Sagnac interferometer). Once aligned, however, the two paths of our ring-interferometer are absolutely identical and therefore we do not have to worry about phase-difference fluctuations between the two processes over time. The downconverted photons are sent through bandpass filters to remove residual 404 nm photons. For both photons we have set up polarization qubit analyzers (PQA) to measure the source entanglement visibility. However, 776 nm photons can also be directed into a time-bin qubit converter, which maps

$$|V\rangle \to |E\rangle \quad \text{and} \quad |H\rangle \to |L\rangle. \tag{5.43}$$

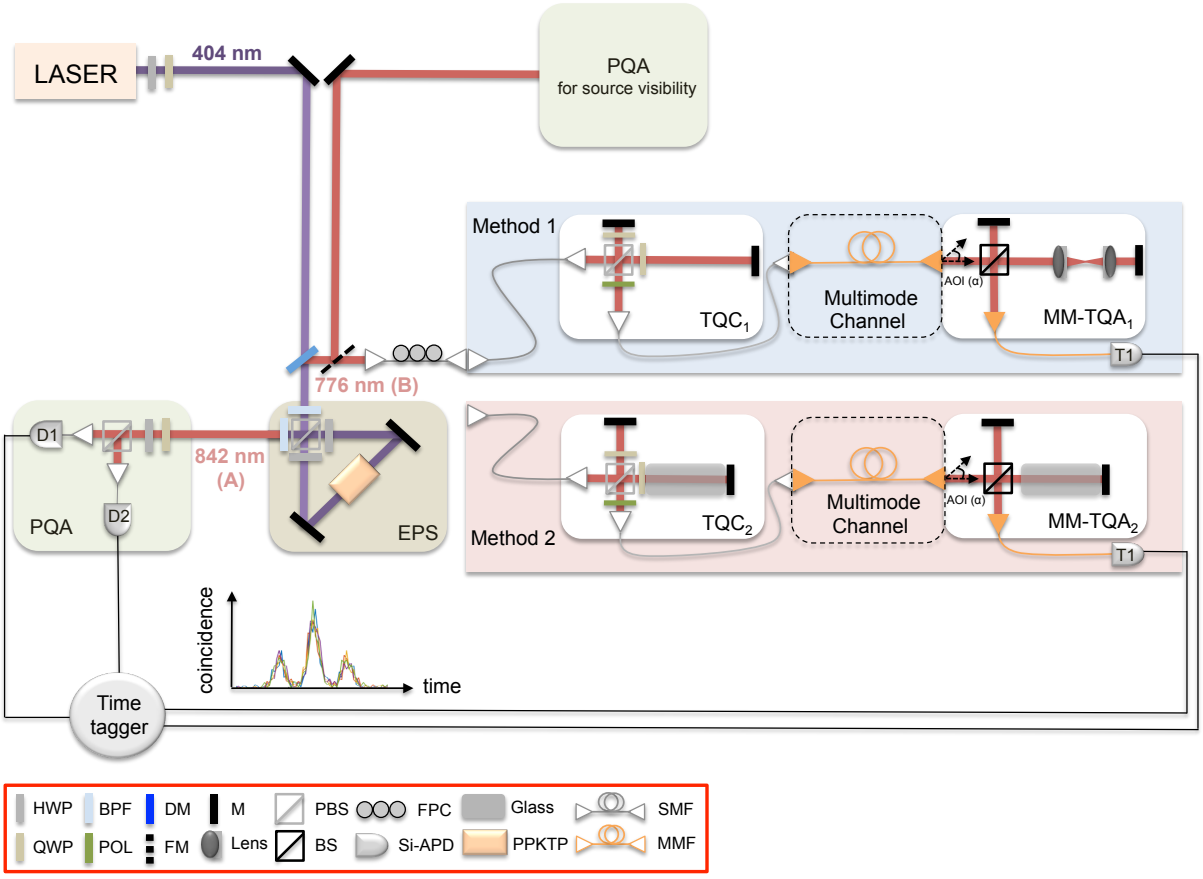

Figure 5.8: **Experimental Setup for Polarization-Time-Bin Entanglement with Multimode Channels.** (from Jin *et al.* [187]) The experiment consists of three parts: generation of polarization-entangled photons, conversion of one polarization qubit into a time-bin qubit, and the analysis stage. The setup is detailed in the main text. EPS: entangled photon source, TQC: time-bin qubit converter, MM-TQA: multimode time-bin qubit analyzer, PQA: polarization qubit analyzer, HWP: half-wave plate, QWP: quarter-wave plate, BPF: bandpass filter, POL: polarizer, DM: dichroic mirror, FM: flip mirror, M: mirror, PBS: polarizing beam splitter, BS: beam splitter, FPC: fiber polarization controller, Si-APD: silicon-avalanche photodiodes, PPKTP: periodically poled potassium titanyl phosphate crystal, SMF: single mode fiber, MM: multimode fiber.

The way this is achieved is as follows. First a PBS directs H and V polarized photons into the long and short path of an unbalanced interferometer, respectively. Since this is also the preparation interferometer of our time-bin qubit, the interferometer is ideally identical to the time-bin qubit analyzer. We use QPWs set to $\theta = 22.5°$ in double-pass configuration (imitating a HWP set to $\Theta = 45°$) to change the polarization of photons in long and short path to V and H, respectively, so that both are sent into the same output port of the PBS. A polarizer (POL) set to 45° ensures that polarization information is deleted and thus no physical label for early and late time-bin exists (other than the partner photon itself). We have now produced the desired state Bell state $|\Phi_+^{AB}\rangle$ from Equation (5.13). Time-bin qubits are now sent through a multimode fiber (as before the 776 nm laser in the visibility experiments) into either of the two presented MM-TQA's. We use standard silicon avalanche photodiodes to detect photons and assign time stamps to all detection events with time taggers. The MM-TQA's we built for the experiments have no active phase control, which prevents deterministic setting of time-bin qubit superposition bases for observables like $\hat{X}$. Hence, in the experiment we have no control over $\hat{W}(\alpha)$, Equation (5.17). This is a problem for a true Bell test, however, later we show how to obtain an estimate for S.

5.6.2 Experimental Results

We first take images of single time-bin qubit photons after the multimode fiber using an electron multiplier CCD camera. Figure 5.9 (a) testifies to the multimodocity of our photons' spatial mode. Before attempting a Bell test, for which the observables are given in Equation (5.14), we determine entanglement visibilities and their robustness against angular input fluctuations. To start with, we measure both qubits in the $\hat{Z}$-basis, i.e. the observable is $\hat{Z}\hat{Z}$. Experimentally this means to measure coincidences N^{pq}, $p, q = \pm$, analogous to the one outlined for the observable $\hat{A}_1\hat{B}_1$ in Equation (5.28). The results are shown in Figure 5.9 (b). Dashed boxes in the histogram surround those time slots that correspond to counts in the $\hat{Z}$-basis. We see that around 12 ns a peak corresponding to $|LV\rangle$ coincidences appear (orange trace), and around 9 ns a peak corresponding to $|EH\rangle$ coincidences appears (green trace). These are the only states contributing to $|\Phi_+^{AB}\rangle$. Consequently, no contributions from $|LH\rangle$ and $|EV\rangle$ are expected. The histogram clearly shows that coincidences corresponding to these two states are barely above the noise level.

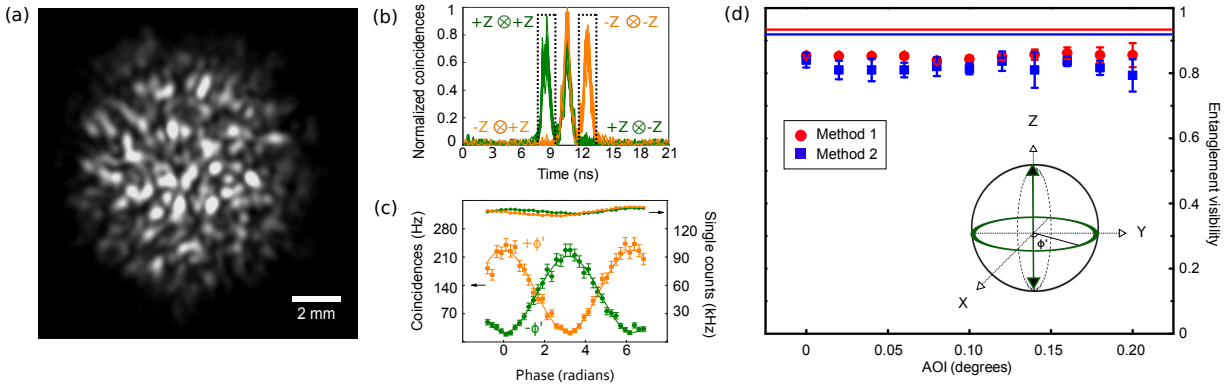

Figure 5.9: **Measured Entanglement Visibilities with Multimode Time-bin Qubits.** (from Jin *et al.* [187]) **(a)** We use a Hamamatsu electron multiplier CCD camera (C9100-13) to take images of photons that encode the time-bin qubit. The multimodicity is clearly visible and similar to Figure 5.7 (b). Two-photon coincidences for the observables **(b)** $\hat{Z}\hat{Z}$ and **(c)** $\hat{\phi}\hat{\phi}'$ demonstrate high-visibility entanglement (discussion in main text) despite the multimodicity of time-bin photons. In (c) we also show the single counts, which are essentially flat, showing that we observe two-photon interference. **(d)** The measured visibilities remain constant, as the AOI α is scanned from 0° to 0.2°.

We can make this qualitative difference precise by calculating visibilities

$$\begin{aligned} \mathcal{V}_+ &:= \frac{N_{++} - N_{-+}}{N_{++} + N_{-+}} \\ \mathcal{V}_- &:= \frac{N_{--} - N_{+-}}{N_{--} + N_{+-}}, \end{aligned} \tag{5.44}$$

from which we obtain average visibilities

$$\begin{aligned} \mathcal{V}^{(1)}_{\hat{Z}\hat{Z}} &:= \frac{\mathcal{V}^{(1)}_+ + \mathcal{V}^{(1)}_-}{2} = (95 \pm 1)\,\% \\ \mathcal{V}^{(2)}_{\hat{Z}\hat{Z}} &:= \frac{\mathcal{V}^{(1)}_+ + \mathcal{V}^{(2)}_-}{2} = (92 \pm 1)\,\%, \end{aligned} \tag{5.45}$$

where the superscript indicates which compensation method [relay lenses (1), or glass cube (2)] has been used. Now that we have verified that our MM-TQA's can handle photons with multimode wavefronts, we continue with a continuous phase-scan along the $\widehat{XY}$-plane of the Bloch sphere: the polarization qubit is transformed into a superposition of the form (5.5), where ϕ' is continuously varied using motorized waveplates: the QWP is set to $\theta = 45°$ and the HWP continuously rotated from $\Theta = 0°$ to 90°. For the time-bin qubit we could not set the superposition basis deterministically, as mentioned above, but if we scan fast, the interferometer phase should be stable enough to give us a high-visibility fringe.

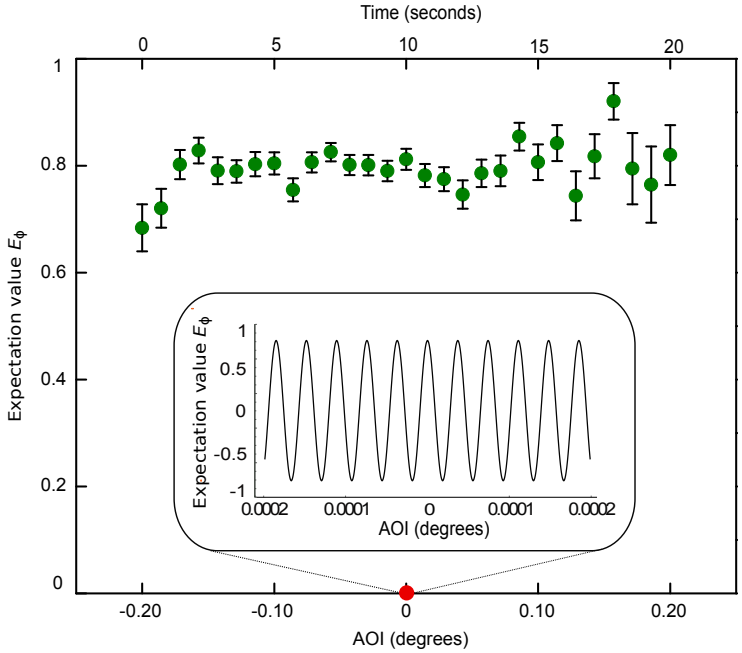

Figure 5.10: **Phase Stability of the Time-Bin Qubit Analyzer.** (from Jin *et al.* [187]) Using the time-bin qubit analyzer with relay optics, we continuously scan the AOI from -0.2° to +0.2° over 20 seconds. The expectation value E_ϕ stays essentially constant around $E_\phi = (80 \pm 1)\,\%$.

The results are shown in Figure 5.9 (c), which are counts in the central time slot in (b). We see two complementary sine curves, for which we can calculate visibilities

$$\begin{aligned} \mathcal{V}^{(1)}_{\hat{\phi}\hat{\phi}'} &:= \frac{\mathcal{V}^{(1)}_{+} + \mathcal{V}^{(1)}_{-}}{2} = (80 \pm 1)\,\% \\ \mathcal{V}^{(2)}_{\hat{\phi}\hat{\phi}'} &:= \frac{\mathcal{V}^{(2)}_{+} + \mathcal{V}^{(2)}_{-}}{2} = (77 \pm 1)\,\%\,. \end{aligned} \tag{5.46}$$

The average visibilities in these experiments are therefore

$$\begin{aligned} \mathcal{V}^{(1)} &:= \frac{\mathcal{V}^{(1)}_{\hat{Z}\hat{Z}} + 2\mathcal{V}^{(1)}_{\hat{\phi}\hat{\phi}'}}{2} = (85 \pm 1)\,\% \\ \mathcal{V}^{(2)} &:= \frac{\mathcal{V}^{(2)}_{\hat{Z}\hat{Z}} + 2\mathcal{V}^{(2)}_{\hat{\phi}\hat{\phi}'}}{2} = (82 \pm 1)\,\%\,. \end{aligned} \tag{5.47}$$

Despite the lack of active phase control for MM-TQA's and multimodicity of time-bin photons, we achieve entanglement visibilities remarkably close to the measured (average) EPS visibilities of $\mathcal{V}^{\text{source}} = (93 \pm 1)$ and $(91 \pm 1)\,\%$ for the times when experiments with method (1) and (2) were carried out, respectively [see Figure 5.9 (d)]. The last step is now to verify that these visibilities remain constant as the AOI is varied. For this we carry out

the measurement from (c) for $\alpha \in [0°, 0.2°]$ and extract visibilities, which are plotted in Figure 5.9 (d). With both compensation methods, the visibilities stay relatively constant and, more importantly, do not drop. As a last measurement, we consider the question whether our multimode time-bin analyzer is also robust against phase fluctuations, which are normally present in uncorrected interferometers for varying AOI α [188]. The origin of these phase fluctuations is the following. As α changes, so does geometrical path length, as we know from (5.35). This also means that the optical path length changes and with it the optical phase. Since interference is only concerned with the optical phase, and not its origin, the interferometer has effectively changed its path length and therefore its phase setting. In our case, from Equation (5.35) we expect a $5\,\pi$-shift with an AOI of only 1×10^{-4} degrees, leading to rapid oscillations in expectation values (see inset to Figure 5.10). Thus, in order to assess the phase stability of our analyzer with relay optics experimentally, we pick any phase from Figure 5.9 (c) and vary the angle. If the interferometer's phase is insensitive to α variations, then the phase should stay constant and hence the expectation value

$$E_\phi \coloneqq \frac{N_{\phi(+\phi')} - N_{\phi(-\phi')}}{N_{\phi(+\phi')} + N_{\phi(-\phi')}}\,, \tag{5.48}$$

with the signs being understood from Figure 5.9 (c). Ideally we do this measurement for a large E_ϕ, i.e. at maximum fringe separation in Figure 5.9 (c). As we sweep $\alpha \in [-0.2°, 0.2°]$ over 20 seconds, Figure 5.10 shows that E_ϕ only fluctuates with a small amplitude but never varies strongly and sinusoidally. This demonstrates the phase stability of our relay lens based MM-TQA. Note that in all measurements, the AOI scan range is already larger than angle fluctuations expected in free-space quantum communication experiments to moving receivers (e.g. [169], see above). Hence, the results are representative for potential outdoor time-bin qubit quantum communication experiments.

The interested reader is referred to our paper [187] for a more rigorous assessment of the entanglement quality using the negative partial transpose criterion. Here I would like to conclude with an estimation for the CHSH-Bell parameter (5.27). The polarization qubit observables $\hat{B}_1$ and $\hat{B}_2$ are measured by setting the QWP to $\theta = 0°$ and the HWP to $\Theta = \pm 11.25°$. As mentioned above (description of experimental setup), we had no active phase control for our MM-TQA and could only induce phase drifts over time. We do this by directing a heat gun at the analyzers, which results in turbulence inside the interferometer. We then monitor coincidences over time, as shown in Figure 5.11. Coincidences for $\hat{A}_1\hat{B}_1$, $\hat{A}_2\hat{B}_1$ are shown in (a) and those for $\hat{A}_1\hat{B}_2$, $\hat{A}_2\hat{B}_2$ in (c). Due to lack of phase control we were not able to set $\hat{A}_2 = \hat{X}$. The coincidences in the middle temporal bin thus correspond to an arbitrary phase basis $\hat{A}_2 = \hat{\phi}$. However, as the interferometer drifts over time, there are moments where expectation values are maximized (or minimized in the

complementary detector). In the analysis stage we can therefore search for expectation values that maximize the CHSH-Bell parameter S, as shown in (b) and (d). We thus extract $\tilde{S} = (2.42 \pm 0.05) > S_{\text{classical}}$.

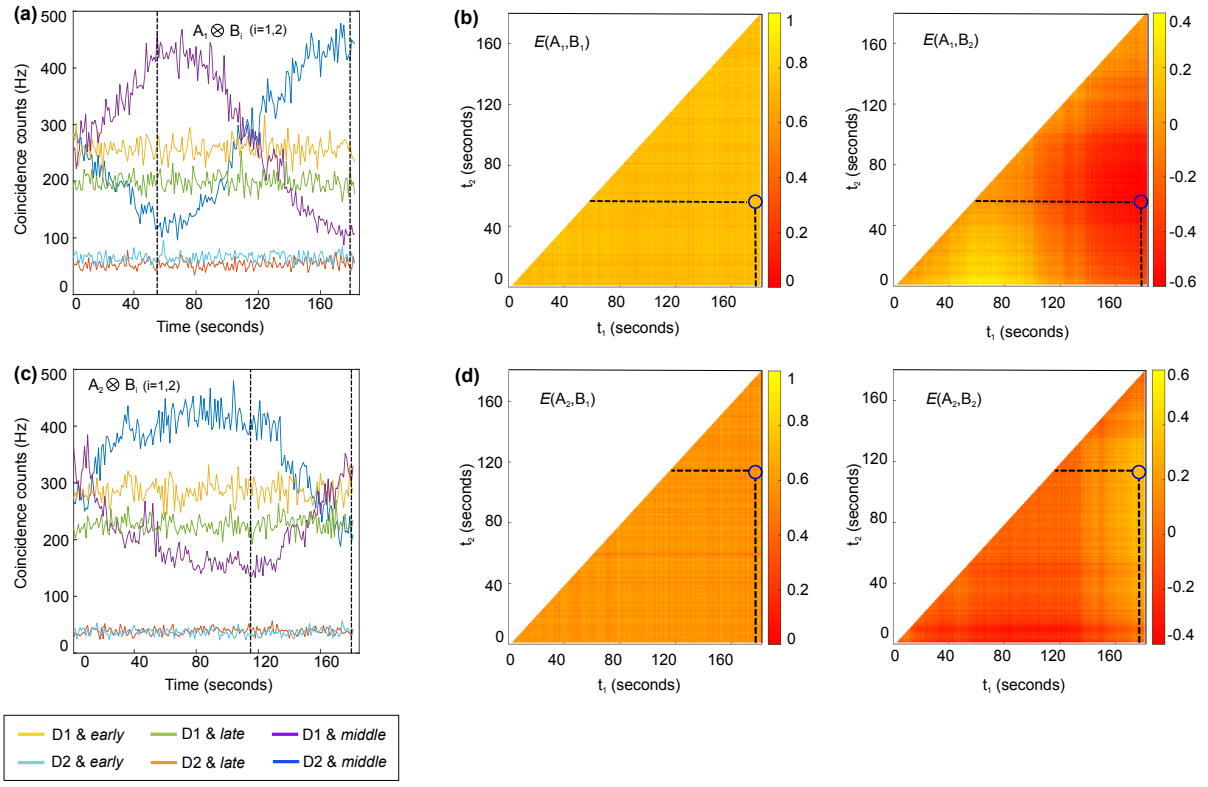

Figure 5.11: **Estimation of CHSH-Bell Parameter.** (from Jin *et al.* [187]) Using the time-bin qubit analyzer with relay optics, we perform coincidence measurements of the observables required to calculate the CHSH-Bell parameter S. **(a)** The yellow and light blue lines show coincidences for $\hat{B}_1$ (+/-) and $\hat{A}_1$ (early temporal bin), the green and orange lines show coincidences for $\hat{B}_1$ (+/-) and $\hat{A}_1$ (late temporal bin), and the purple and blue lines show coincidences for $\hat{B}_1$ (+/-) and $\hat{A}_2 = \hat{\phi}$ (middle temporal bin). **(c)** The yellow and light blue lines show coincidences for $\hat{B}_2$ (+/-) and $\hat{A}_1$ (early temporal bin), the green and orange lines show coincidences for $\hat{B}_2$ (+/-) and $\hat{A}_1$ (late temporal bin), and the purple and blue lines show coincidences for $\hat{B}_2$ (+/-) and $\hat{A}_2 = \hat{\phi}$ (middle temporal bin). **(b)** and **(d)** show surface plots of calculated expectation values for the projection measurements in (a) and (c), respectively. Black dashed lines indicate times for which maximal expectation values are found.

5.7 Conclusion and Outlook

We realized two multimode time-bin qubit analyzers (MM-TQA) that are suitable for measurements with spatially distorted photons. In multimode channels, as they propagate, photons progressively populate more (transversal) spatial modes. This can be intentional but most often it is a consequence of uncontrolled turbulences in the transmission medium. In the kind of experiments we are interested in, namely quantum communication between sender and receiver with a free-space channel linking them, we cannot avoid turbulences and ignore their effect on efficiency, quantum bit error rate and so on. The results of our demonstration are very promising indeed. First we showed that time-bin interferometers equipped with correction optics can *passively* compensate the intrinsic path asymmetry of unbalanced interferometers. In our case, the uncorrected time-bin interferometer supports only $(16 \pm 1)\,\%$ interference visibility for a multimode beam. With correction optics in place, however, we measured up to $(90 \pm 1)\,\%$. Moreover, while the former drops with increasing angle of incidence of the input beam, the latter stays constant. Hence, only with correction optics in place can we hope to use time-bin qubits over turbulent free-space channels. In the second part of this work we employed the MM-TQAs in an actual entanglement experiment. We generated polarization-time-bin Bell states and demonstrate average entanglement visibilities of up to $(85 \pm 1)\,\%$. This clearly shows that we are able to access the strong correlations of entangled photon pairs despite the fact that one of them was transmitted through a multimode channel. Though an entanglement visibility of $(85 \pm 1)\,\%$ may not seem high, with respect to the source visibility (which is in indeed a bit low), we only lose $8 - 9\,\%$ through the multimode channel. The next step, then, is to improve the interferometers (for example switch from Michelson to Mach-Zehnder configuration to allow detection in a second, complementary, output port) and take them outside for real field tests, i.e. quantum communication experiments through actual free-space links.

Chapter 6

Conclusion and Outlook

In this thesis we explored a broad spectrum of higher-order quantum optical interference phenomena. We used one (Chapter 3), two (Chapters 4 and 5), and three (Chapter 2) photons to tackle fundamental open questions and provide new methods, in particular for quantum communication applications.

The main result is surely the experimental proof that strong correlations of three entangled photons are transferable into an interferometric setting. The distillation of more than 90 % genuine three-photon interference shows how far we have come in less than seven years after development of the first photon triplet source. Yet we also have to concede that progress is rather slow, for where are photon quadruplet, quintet, ... sources? At this point in time we can only guess at the fabulous interference landscapes that must exist in these higher orders. One day it may be possible to say "I need ten-photon interference with 80 % visibility, a little bit of nine-photon interference, say 2 %, nothing between four- and eight-photon interference, and one- to three-photon interference, each with 6 %". Is it even possible? How so? What problems require such precise specification? Quantum optics would surely benefit from answers to these questions and results will surely rub off on quantum information processing implementations. A good way to start is to think about the possible ways to combine one-, two-, three-,... photon interference phenomena *in addition* to genuinely new phenomena that arise in those higher orders. However, we can only hope to tackle these questions experimentally if we progress in designing sources for multiphoton states with tailored (quantum) correlations.

In the meantime, we can advance our understanding of lower-order interference phenomena and with "understanding" I mean a full classification. The mathematical structures best equipped for such a task appear to be group and representation theory, which I used here to identify interference terms in N-path (or N-slit) experiments. My confidence rests

upon a certain refinement that the concept "alternatives" experiences in quantum theory via the notion of distinguishability. If N alternatives are indistinguishable, then every attempt to label them must fail—*ergo* we have symmetry in the system. The algebraic properties are thus (partially) captured by group theory, and after "exposure" we can let representation theory develop the picture for us. This already works remarkably well in other disciplines. For example, symmetries of atomic arrangements are described by groups. The *effect* of this symmetry on physical *observables* is then determined via representation theory, namely vibrational spectra of molecules in this case. The three-slit experiment, to which group theory was applied, is only a single photon system, but considering the exchange symmetry of photons in linear optical networks alone (boson sampling), we can get a feel for how powerful these methods become.

The classification will also require us to clearly identify classical and quantum trademarks in a given interference phenomenon. Of course, in order to obtain the HOM *dips, triangle and square waves* shown in Chapter 4, we need to work in the single photon counting regime. However, the theoretical derivation also shows how many classical features factor in. The dip shape, for example, is entirely determined by the source's spectral properties, which in turn is described by a classical random process. Though light is ultimately quantized, we would do good not to throw all phenomena into the "quantum bin", for mathematical models represent, above all in the physical sciences, laws of thought, and if we fail to recognize tiny features because of our inability to handle various mathematical structures simultaneously, then how can we ever be audacious enough to seduce nature for another act of interaction without interaction (which is what interference is, as far as the superposition principle is concerned)?

Bibliography

[1] Norbert Lütkenhaus strenuously emphasized this point on various occasions.

[2] Giora Hon and Bernard R. Goldstein. *From Summetria to Symmetry: The Making of a Revolutionary Scientific Concept (Archimedes)*. Springer, 2008.

[3] Klaus Jänich. *Lineare Algebra*. Springer, 1993.

[4] Sascha Agne, Thomas Kauten, Jeongwan Jin, Evan Meyer-Scott, Jeff Z. Salvail, Deny R. Hamel, Kevin J. Resch, Gregor Weihs, and Thomas Jennewein. Observation of genuine three-photon interference. *Phys. Rev. Lett.*, 118:153602, 2017.

[5] Albert Einstein, Boris Podolsky, and Nathan Rosen. Can quantum-mechanical description of physical reality be considered complete? *Phys. Rev.*, 47:777–780, 1935.

[6] Daniel M. Greenberger, Michael A. Horne, and Anton Zeilinger. *Going Beyond Bell's Theorem*. Springer Netherlands, 1989.

[7] N. David Mermin. What's wrong with these elements of reality? *Physics Today*, (June), 1990.

[8] N. David Mermin. Quantum mysteries revisited. *American Journal of Physics*, 58:731, 1990.

[9] Hannes Hübel, Deny R. Hamel, Alessandro Fedrizzi, Sven Ramelow, Kevin J. Resch, and Thomas Jennewein. Direct generation of photon triplets using cascaded photon-pair sources. *Nature*, 466:601, 2010.

[10] Jian-Wei Pan, Zeng Bing Chen, Chao Yang Lu, Harald Weinfurter, Anton Zeilinger, and Marek Zukowski. Multiphoton entanglement and interferometry. *Rev. Mod. Phys.*, 84:777, 2012.

[11] Adrian J. Menssen, Alex E. Jones, Benjamin J. Metcalf, Malte C. Tichy, Stefanie Barz, W. Steven Kolthammer, and Ian A. Walmsley. Distinguishability and many-particle interference. *Phys. Rev. Lett.*, 118:153603, 2017.

[12] Daniel M. Greenberger, Michael A. Horne, Abner Shimony, and Anton Zeilinger. Bell's theorem without inequalities. *Am. J. Phys.*, 58:1131, 1990.

[13] Anton Zeilinger, Michael A. Horne, and Daniel M. Greenberger. Higher-Order Quantum Entanglement. In *Proceedings of the International Workshop on Squeezed States and Uncertainty Relations*, 1992.

[14] Hyung Sup Choi. Generalized Parametric Down Conversion, Many Particle Interferometry, and Bell's Theorem. In *Workshop on Squeezed States and Uncertainty Relations*, pages 101–102. NASA, 1992.

[15] Michael A. Horne, Herbert J. Bernstein, Daniel M. Greenberger, and Anton Zeilinger. Use of entanglement in quantum optics. In *Proceedings of the International Workshop on Squeezed States and Uncertainty Relations*, 1992.

[16] Daniel M. Greenberger, Michael A. Horne, and Anton Zeilinger. Multiparticle interferometry and the superposition principle. *Physics Today*, 46:22, 1993.

[17] Anton Zeilinger, Marek Zukowski, Michael A. Horne, Herbert J. Bernstein, and Daniel M. Greenberger. Einstein-Podolsky-Rosen correlations in higher dimensions. In *Proceedings of the Adriatico Workshop on Quantum Interferometry, World Scientific*, pages 159—-169, 1993.

[18] Dien A. Rice, Charles F. Osborne, and Peter Lloyd. Multiparticle interference. *Phys. Lett. A*, 186:21, 1994.

[19] Anton Zeilinger, Michael A. Horne, Harald Weinfurter, and Marek Żukowski. Three-particle entanglements from two entangled pairs. *Phys. Rev. Lett.*, 78:3031, 1997.

[20] Marek Zukowski. Quest for GHZ states. *Acta Physica Polonica A*, 93(1):187–195, 1998.

[21] Michael A. Horne. Fringe Visibility for a Three-Particle Beam-Entanglement. *Fortschritte der Physik*, 46:683–688, 1998.

[22] Stephen M. Barnett, Nobuyuki Imoto, and Bruno Huttner. Photonic de Broglie wave interferometers. *J. Mod. Opt.*, 45:2217, 1998.

[23] T. E. Keller, M. H. Rubin, and Y. H. Shih. Three-Photon Entangled State. *Fortschritte der Physik*, 46:673–682, 1998.

[24] Benjamin J. Metcalf, Nicholas Thomas-Peter, Justin B. Spring, Dmytro Kundys, Matthew A. Broome, Peter C. Humphreys, Xian-Min Jin, Marco Barbieri, W. Steven Kolthammer, James C. Gates, Brian J. Smith, Nathan K. Langford, Peter G. R. Smith, and Ian A. Walmsley. *Nature Communications*, 4:1356, 2013.

[25] Nicolò Spagnolo, Chiara Vitelli, Lorenzo Aparo, Paolo Mataloni, Fabio Sciarrino, Andrea Crespi, Roberta Ramponi, and Roberto Osellame. Three-photon bosonic coalescence in an integrated tritter. *Nature Communications*, 4:1606, 2013.

[26] Scott Aaronson and Alex Arkhipov. The Computational Complexity of Linear Optics. *Theory of Computing*, 9:143–252, 2013.

[27] Malte C. Tichy. *Entanglement and Interference of Identical Particles*. PhD thesis, University of Freiburg, 2011.

[28] Stephen Wolfram. *A New Kind of Science*. Wolfram Media, Inc., 2016.

[29] Alfred J. Menezes, Paul C. van Oorschot, and Scott A. Vanstone. *Handbook of Applied Cryptography (Discrete Mathematics and Its Applications)*. CRC Press, 1996.

[30] Sheldon Ross. *Introduction to probability models*. Academic Press, 2010.

[31] David N. Klyshko. The Bell and GHZ theorems: a possible three-photon interference experiment and the question of nonlocality. *Phys. Lett. A*, 172:399, 1993.

[32] Alexander V. Belinsky and David N. Klyshko. A modified N-particle Bell theorem, the corresponding optical experiment and its classical model. *Phys. Lett. A*, 176:415, 1993.

[33] Marek Zukowski and Dagomir Kaszlikowski. Critical visibility for N-particle Greenberger-Horne-Zeilinger correlations to violate local realism. *Physical Review A*, 56:R1682–R1685, 1997.

[34] B. Hensen, H. Bernien, A. E. Dréau, A. Reiserer, N. Kalb, M. S. Blok, J. Ruitenberg, R. F. L. Vermeulen, R. N. Schouten, C. Abellán, W. Amaya, V. Pruneri, M. W. Mitchell, M. Markham, D. J. Twitchen, D. Elkouss, S. Wehner, T. H. Taminiau, and R. Hanson. Loophole-free Bell inequality violation using electron spins separated by 1.3 kilometres. *Nature*, 526:682–686, 2015.

[35] Marissa Giustina, Marijn A. M. Versteegh, Sören Wengerowsky, Johannes Handsteiner, Armin Hochrainer, Kevin Phelan, Fabian Steinlechner, Johannes Kofler, Jan Åke Larsson, Carlos Abellán, Waldimar Amaya, Valerio Pruneri, Morgan W. Mitchell, Jörn Beyer, Thomas Gerrits, Adriana E. Lita, Lynden K. Shalm, Sae Woo Nam, Thomas Scheidl, Rupert Ursin, Bernhard Wittmann, and Anton Zeilinger. Significant-Loophole-Free Test of Bell's Theorem with Entangled Photons. *Physical Review Letters*, 115:1–7, 2015.

[36] Lynden K. Shalm, Evan Meyer-Scott, Bradley G. Christensen, Peter Bierhorst, Michael A. Wayne, Martin J. Stevens, Thomas Gerrits, Scott Glancy, Deny R. Hamel, Michael S. Allman, Kevin J. Coakley, Shellee D. Dyer, Carson Hodge, Adriana E. Lita, Varun B. Verma, Camilla Lambrocco, Edward Tortorici, Alan L. Migdall, Yanbao Zhang, Daniel R. Kumor, William H. Farr, Francesco Marsili, Matthew D. Shaw, Jeffrey A. Stern, Carlos Abellán, Waldimar Amaya, Valerio Pruneri, Thomas Jennewein, Morgan W. Mitchell, Paul G. Kwiat, Joshua C. Bienfang, Richard P. Mirin, Emanuel Knill, and Sae Woo Nam. Strong Loophole-Free Test of Local Realism. *Physical Review Letters*, 115:1–10, 2015.

[37] Jian-Wei Pan and Anton Zeilinger. Greenberger-Horne-Zeilinger-state analyzer. *Physical Review A*, 57(3):2208–2211, 1998.

[38] Jian-Wei Pan, Dik Bouwmeester, Matthew Daniell, Harald Weinfurter, and Anton Zeilinger. Experimental test of quantum nonlocality in three-photon greenberger-horne-zeilinger entanglement. *Nature*, 403:515, 2000.

[39] Dik Bouwmeester, Jian-Wei Pan, Matthew Daniell, Harald Weinfurter, and Anton Zeilinger. Observation of three-photon greenberger-horne-zeilinger entanglement. *Phys. Rev. Lett.*, 82:1345, 1999.

[40] Wei-Bo Gao, Chao-Yang Lu, Xing-Can Yao, Ping Xu, Otfried Gühne, Alexander Goebel, Yu-Ao Chen, Cheng-Zhi Peng, Zeng-Bing Chen, and Jian-Wei Pan. Experimental demonstration of a hyper-entangled ten-qubit Schrödinger cat state. *Nature Physics*, 6:11, 2010.

[41] Robert J. C. Spreeuw. Classical wave-optics analogy of quantum-information processing. *Phys. Rev. A*, 63:062302, 2001.

[42] Philip Walther, Kevin J. Resch, Časlav Brukner, and Anton Zeilinger. Experimental entangled entanglement. *Physical Review Letters*, 97:1–4, 2006.

[43] Michae A.l Horne. Complementarity of Fringe Visibilities in Three-Particle Quantum Mechanics. In *Epistemological and Experimental Perspectives on Quantum Physics*, pages 211–220. Springer Netherlands, 1999.

[44] Anton Zeilinger, Gregor Weihs, Thomas Jennewein, and Markus Aspelmeyer. Happy centenary, photon. *Nature*, 433(7023):230–238, 2005.

[45] David Bohm. *Quantum Theory*. Prentice-Hill, 2012.

[46] John S. Bell. On the Einstein Podolsky Rosen paradox. *Physics*, 1:195–200, 1964.

[47] Stuart J. Freedman and John F. Clauser. Experimental Test of Local Hidden-Variable Theories. *Physical Review Letters*, 28(14):938–941, 1972.

[48] Alain Aspect, Philippe Grangier, and Gérard Roger. Experimental Tests of Realistic Local Theories via Bell's Theorem. *Physical Review Letters*, 47:460–463, 1981.

[49] Michael A. Horne and Anton Zeilinger. A Bell-type EPR experiment using linear momenta. In P. Lahti and P. Mittelstaedt, editors, *Symposium on the Foundations of Modern Physics*, pages 435–439. World Scientific Publishing Co., 1985.

[50] Michael A. Horne and Anton Zeilinger. A possible spin-less experimental test of Bell's inequality. In *Microphysical Reality and Quantum Formalism*, page 401, 1988.

[51] John C. Howell, Ryan S. Bennink, Sean J. Bentley, and Robert W. Boyd. Realization of the einstein-podolsky-rosen paradox using momentumand position-entangled photons from spontaneous parametric down conversion. *Physical Review Letters*, 92:1–4, 2004.

[52] Michael A. Horne, Abner Shimony, and Anton Zeilinger. Two-particle interferometry. *Phys. Rev. Lett.*, 62:2209, 1989.

[53] P. G. Kwiat, A. M. Steinberg, and R. Y. Chiao. High-visibility interference in a Bell-inequality experiment for energy and time. *Phys. Rev. A*, 47:2472, 1993.

[54] R. Ghosh and Leonard Mandel. Observation of nonclassical effects in the interference of two photons. *Physical Review Letters*, 59:1903–1905, 1987.

[55] John G. Rarity and Paul R. Tapster. Experimental violation of Bells inequality based on phase and momentum. *Physical Review Letters*, 64:2495–2498, 1990.

[56] Yanhua Shih. *An introduction to quantum optics : photon and biphoton physics*. CRC Press, 2011.

[57] Jan Klaers, Julian Schmitt, Frank Vewinger, and Martin Weitz. Bose-einstein condensation of photons in an optical microcavity. *Nature*, 468:545–548, 2010.

[58] Joseph Jacobson, Gunnar Björk, Isaac Chuang, and Yoshihisa Yamamoto. Photonic de Broglie Waves. *Physical Review Letters*, 74:4835–4838, 1995.

[59] Chung K. Hong, Zhe Y. Ou, and Leonard Mandel. Measurement of subpicosecond time intervals between two photons by interference. *Physical Review Letters*, 59:2044–2046, 1987.

[60] Yanhua. H. Shih and Carroll O. Alley. New type of einstein-podolsky-rosen-bohm experiment using pairs of light quanta produced by optical parametric down conversion. *Physical Review Letters*, 61:2921–2924, 1988.

[61] J. D. Franson. Bell inequality for position and time. *Phys. Rev. Lett.*, 62:2205, 1989.

[62] Philip Walther, Jian-Wei Pan, Markus Aspelmeyer, Rupert Ursin, Sara Gasparoni, and Anton Zeilinger. De Broglie wavelength of a non-local four-photon state. *Nature*, 429:158, 2004.

[63] Morgan W. Mitchell, Jeff S. Lundeen, and Aephraim M. Steinberg. Super-resolving phase measurements with a multiphoton entangled state. *Nature*, 429:161, 2004.

[64] Tomohisa Nagata, Ryo Okamoto, Jeremy L. O'Brien, Keiji Sasaki, and Shigeki Takeuchi. Beating the Standard Quantum Limit with Four-Entangled Photons. *Science*, 316:726–729, 2007.

[65] Kevin J. Resch, Kenneth L. Pregnell, Robert Prevedel, Alexei Gilchrist, Geoff J. Pryde, Jeremy L. O'Brien, and Andrew. G. White. Time-reversal and super-resolving phase measurements. *Physical Review Letters*, 98:2–5, 2007.

[66] Bernard Yurke and David Stoler. Einstein-Podolsky-Rosen effects from independent particle sources. *Physical Review Letters*, 68:1251–1254, 1992.

[67] Bernard Yurke and David Stoler. Bells-inequality experiments using independent-particle sources. *Physical Review A*, 46:2229–2234, 1992.

[68] Marek Zukowski, Anton Zeilinger, Michael A. Horne, and Arthur K. Ekert. "Event-ready-detectors" Bell experiment via entanglement swapping. *Physical Review Letters*, 71:4287–4290, 1993.

[69] Caslav Brukner and Anton Zeilinger. Young's experiment and the finiteness of information. *Philosophical Transactions of the Royal Society A: Mathematical, Physical and Engineering Sciences*, 360:1061–1069, 2002.

[70] Gregor Weihs and Anton Zeilinger. Photon statistics at beam splitters: an essential tool in quantum information and teleportation. *Coherence and Statistics of Photons and Atoms*, pages 1–28, 2001.

[71] Hoi-Kwong Lo, Marcos Curty, and Bing Qi. Measurement-Device-Independent Quantum Key Distribution. *Physical Review Letters*, 108:130503, 2012.

[72] Koji Azuma, Kiyoshi Tamaki, and Hoi-Kwong Lo. All-photonic quantum repeaters. *Nature Communications*, 6:6787, 2015.

[73] Marek Zukowski, Anton Zeilinger, and Harald Weinfurter. Entangling Photons Radiated by Independent Pulsed Sources. *Annals of the New York Academy of Sciences*, 755:91–102, 1995.

[74] Anton Zeilinger, Michael A. Horne, and Harald Weinfurter. Independent Photons and Entanglement . A Short Overview. *International Journal of Theoretical Physics*, 38:501–517, 1999.

[75] Xiao-Feng Fan, Tao Yang, Jian Li, Chuan-Feng Li, and Guang-Can Guo. Generating three-particle entanglement states. *Physics Letters A*, 284(2-3):59–62, 2001.

[76] John G. Rarity and Paul R. Tapster. Three-particle entanglement from entangled photon pairs and a weak coherent state. *Physical Review A*, 59:R35–R38, 1999.

[77] T. Guerreiro, A. Martin, B. Sanguinetti, J. S. Pelc, C. Langrock, M. M. Fejer, N. Gisin, H. Zbinden, N. Sangouard, and R. T. Thew. Nonlinear interaction between single photons. *Physical Review Letters*, 113:1–5, 2014.

[78] María Corona, Karina Garay-Palmett, and Alfred B. U'Ren. Experimental proposal for the generation of entangled photon triplets by third-order spontaneous parametric downconversion in optical fibers. *Optics Letters*, 36:190, 2014.

[79] Michael G. Moebius, Felipe Herrera, Sarah Griesse-Nascimento, Orad Reshef, Christopher C. Evans, Gian Giacomo Guerreschi, Alán Aspuru-Guzik, and Eric Mazur. Efficient photon triplet generation in integrated nanophotonic waveguides. *Optics Express*, 24:9932, 2016.

[80] L. Krister. Shalm, Deny. R. Hamel, Zhizhong Yan, Christopher Simon, Kevin J. Resch, and Thomas Jennewein. Three-photon energy-time entanglement. *Nat. Phys.*, 9:19, 2012.

[81] Deny R. Hamel, Lynden K. Shalm, Hannes Hübel, Aaron J. Miller, Francesco Marsili, Varun B. Verma, Richard P. Mirin, Sae Woo Nam, Kevin J. Resch, and Thomas Jennewein. Direct generation of three-photon polarization entanglement. *Nat. Phot.*, 8:801, 2014.

[82] Z. Y. Ou, X. Y. Zou, L. J. Wang, and L. Mandel. Observation of nonlocal interference in separated photon channels. *Physical Review Letters*, 65:321–324, 1990.

[83] J. Brendel, E. Mohler, and W. Martiennsen. Experimental test of Bell inequality for energy and time. *Europhysics Letters*, 20:575, 1992.

[84] J. Brendel, N. Gisin, W. Tittel, and H. Zbinden. Pulsed energy-time entangled twin-photon source for quantum communication. *Phys. Rev. Lett.*, 82:2594, 1999.

[85] K. J. Blow, Rodney Loudon, Simon J. D. Phoenix, and T. J. Shepherd. Continuum fields in quantum optics. *Phys. Rev. A*, 42:4102–4114, 1990.

[86] Mark Hillery, Vladimír Bužek, and André Berthiaume. Quantum secret sharing. *Phys. Rev. A*, 59:1829, 1999.

[87] Giuseppe Vallone, Paolo Mataloni, and Adán Cabello. Multiparty multilevel energy-time entanglement. *Phys. Rev. A*, 81:032105, 2010.

[88] N. David Mermin. Extreme quantum entanglement in a superposition of macroscopically distinct states. *Phys. Rev. Lett.*, 65:1838, 1990.

[89] George Svetlichny. Distinguishing three-body from two-body nonseparability by a Bell-type inequality. *Phys. Rev. D*, 35:3066, 1987.

[90] Julio T. Barreiro, Nathan K. Langford, Nicholas A. Peters, and Paul G. Kwiat. Generation of hyperentangled photon pairs. *Phys. Rev. Lett.*, 95:260501, 2005.

[91] Daniel M. Greenberger, Herbert J. Bernstein, Michael A. Horne, Abner Shimony, and Anton Zeilinger. Proposed GHZ experiments using cascades of down-conversion. In H. Ezawa and Y. Murayama, editors, *Quantum Control and Measurement, Proceedings of the ISQM Satellite Workshop*, pages 23–28. Elsevier Science Publishers, 1993.

[92] Urbasi Sinha, Christophe Couteau, Thomas Jennewein, Raymond Laflamme, and Gregor Weihs. Ruling out multi-order interference in quantum mechanics. *Science*, 329:418–421, 2010.

[93] Francisco J. Duarte. *Quantum optics for engineers*. Taylor & Francis, 2013.

[94] Rahul Sawant, Joseph Samuel, Aninda Sinha, Supurna Sinha, and Urbasi Sinha. Nonclassical paths in quantum interference experiments. *Phys. Rev. Lett.*, 113:120406, 2014.

[95] Aninda Sinha, Aravind H. Vijay, and Urbasi Sinha. On the superposition principle in interference experiments. *Sci. Rep.*, 5:10304, 2015.

[96] Thomas Kauten, Robert Keil, Thomas Kaufmann, Benedikt Pressl, Caslav Brukner, and Gregor Weihs. Obtaining tight bounds on higher-order interferences with a 5-path interferometer. *New Journal of Physics*, 19:033017, 2017.

[97] Rafael D. Sorkin. Quantum mechanics as quantum measure theory. *Mod. Phys. Lett. A*, 9:3119, 1994.

[98] Inspired by a similar figure in http://https://en.wikipedia.org/wiki/Inclusion%E2%80%93exclusion_principle (Accessed: 2017-06-19).

[99] H. F. Jones. *Groups, representations, and physics*. CRC Press, 1998.

[100] F. Yates. Complex experiments. *Supplement to the Journal of the Royal Statistical Society*, 2(2):181–247, 1935.

[101] Harold Hotelling. Some improvements in weighing and other experimental techniques. *The Annals of Mathematical Statistics*, 15(3):297–306, 1944.

[102] Daniel N. Rockmore. Some applications of generalized FFT's. In L. Finkelstein and W. M. Kantor, editors, *Proceedings of DIMACS Workshop in Groups and Computation*, pages 329–370. AMS, 1995.

[103] Zhe Y. Ou. *Multi-Photon Quantum Interference*. Springer, 2007.

[104] Todd Pittman, Dmitry Strekalov, Alan Migdall, Morton Rubin, Alexander Sergienko, and Yanhua Shih. Can Two-Photon Interference be Considered the Interference of Two Photons? *Physical Review Letters*, 77:1917–1920, 1996.

[105] John G. Rarity, Paul R. Tapster, and Rodney Loudon. Non-classical interference between independent sources. *J. Opt. B: Quantum Semiclass. Opt.*, 7:6, 2005.

[106] X. Li, L. Yang, L. Cui, Z. Y. Ou, and D. Yu. Observation of quantum interference between a single-photon state and a thermal state generated in optical fibers. *Optics Express*, 16:12505–12510, 2008.

[107] Thomas Legero, Tatjana Wilk, Axel Kuhn, and Gerhard Rempe. Time-resolved two-photon quantum interference. *Applied Physics B: Lasers and Optics*, 77:797–802, 2003.

[108] Thomas Legero, Tatjana Wilk, Markus Hennrich, Gerhard Rempe, and Axel Kuhn. Quantum beat of two single photons. *Phys. Rev. Lett.*, 93:1–4, 2004.

[109] R. Kaltenbaek, J. Lavoie, and K. J. Resch. Classical analogues of two-photon quantum interference. *Phys. Rev. Lett.*, 102:243601, 2009.

[110] Z. Y. Ou, E. C. Gage, B. E. Magill, and L. Mandel. Observation of beating between blue and green light. *Optics Communications*, 69:1–5, 1988.

[111] Z. Y. Ou, E. C. Gage, B. E. Magill, and L. Mandel. Fourth-order interference technique for determing the coherence time of a light beam. *J. Opt. Soc. Am. B*, 6:100–103, 1989.

[112] A. Lebreton, I. Abram, R. Braive, I. Sagnes, I. Robert-Philip, and A. Beveratos. Theory of interferometric photon-correlation measurements: Differentiating coherent from chaotic light. *Phys. Rev. A*, 88:1–7, 2013.

[113] A. Lebreton, I. Abram, R. Braive, I. Sagnes, I. Robert-Philip, and A. Beveratos. Unequivocal differentiation of coherent and chaotic light through interferometric photon correlation measurements. *Phys. Rev. Let.*, 110:1–5, 2013.

[114] Xavier Brokmann, Moungi Bawendi, Laurent Coolen, and Jean-Pierre Hermier. Photon-correlation Fourier spectroscopy. *Optics Express*, 14:6333–6341, 2006.

[115] Thiago Ferreira da Silva, Gustavo C. do Amaral, Douglas Vitoreti, Guilherme P Temporão, and Jean Pierre von der Weid. Spectral characterization of weak coherent state sources based on two-photon interference. *Journal of the Optical Society of America B*, 32:545, 2015.

[116] G. C. Amaral, T. Ferreira da Silva, G. P. Temporão, and J. P. von der Weid. Few-photon heterodyne spectroscopy. *Optics Letters*, 41:1502, 2016.

[117] Hoi-Kwong Lo and John Preskill. Security of quantum key distribution using weak coherent states with nonrandom phases. *Quantum Information and Computation*, 7:431–458, 2006.

[118] Yong Su Kim, Oliver Slattery, Paulina S. Kuo, and Xiao Tang. Conditions for two-photon interference with coherent pulses. *Physical Review A*, 87:1–4, 2013.

[119] Z. L. Yuan, M. Lucamarini, J. F. Dynes, B. Fröhlich, M. B. Ward, and A. J. Shields. Interference of short optical pulses from independent gain-switched laser diodes for quantum secure communications. *Physical Review Applied*, 2:1–6, 2014.

[120] Yujun Choi, Osung Kwon, Minki Woo, Kyunghwan Oh, Sang-Wook Han, Yong-Su Kim, and Sung Moon. Plug-and-play measurement-device-independent quantum key distribution. *Physical Review A*, 93:032319, 2016.

[121] Yong-Su Kim, Oliver Slattery, Paulina S. Kuo, and Xiao Tang. Two-photon interference with continuous-wave multi-mode coherent light. *Optics Express*, 22:3611–20, 2014.

[122] Yuchen He, Jianbin Liu, Songlin Zhang, Wentao Wang, Bin Bai, Mingnan Le, and Zhuo Xu. Studying the optical second-order interference pattern formation process with classical light in the photon counting regime. *Journal of the Optical Society of America A*, 32:2431, 2015.

[123] Jianbin Liu, Mingnan Le, Bin Bai, Wentao Wang, Hui Chen, Yu Zhou, Fu Li Li, and Zhuo Xu. The second-order interference of two independent single-mode He-Ne lasers. *Optics Communications*, 350:196–201, 2015.

[124] Jianbin Liu, Dong Wei, Hui Chen, Yu Zhou, Huaibin Zheng, Hong Gao, Fu-li Li, and Zhuo Xu. Second-order interference of two independent and tunable single-mode continuous-wave lasers. *Chinese Physics B*, 25:034203, 2016.

[125] Jianbin Liu, Yu Zhou, Fu-li Li, and Zhuo Xu. The second-order interference between laser and thermal light. *Europhysics Letters*, 105:64007, 2014.

[126] Rainer Kaltenbaek, Bibiane Blauensteiner, Marek Zukowski, Markus Aspelmeyer, and Anton Zeilinger. Experimental interference of independent photons. *Physical Review Letters*, 96:1–4, 2006.

[127] A. Javan, E. A. Ballik, and W. L. Bond. Frequency Characteristics of a Continuous-Wave He-Ne Optical Maser. *J. Opt. Soc. Am.*, 52:96–98, 1962.

[128] G. Magyar and L. Mandel. Interference Fringes Produced by Superposition of Two Independent Maser Light Beams. *Nature*, 198:255–256, 1963.

[129] R. L. Pfleegor and L. Mandel. Interference of Independent Photon Beams. *Physical Review*, 159:1084–1088, 1967.

[130] Louis De Broglie and J. Andrade E Silva. Interpretation of a Recent Experiment on Interference of Photon Beams. *Physical Review*, 172:1284–1285, 1968.

[131] Leonard Mandel. Photon interference and correlation effects produced by independent quantum sources. *Physical Review A*, 28:929–943, 1983.

[132] H. Paul. Interference between independent photons. *Reviews of Modern Physics*, 58:209–231, 1986.

[133] J. M. Jauch. *The Theory of Photons and Electrons : the Relativistic Quantum Field Theory of Charged Particles with Spin One-half*. Springer Berlin Heidelberg, 1976.

[134] ATLAS Collaboration. Evidence for light-by-light scattering in heavy-ion collisions with the ATLAS detector at the LHC. *arXiv:1702.01625*, 24, 2017.

[135] Jianbin Liu and Guoquan Zhang. Observation on the incompatibility between the first-order and second-order interferences with laser beams. *Optics Communications*, 284:2658–2661, 2011.

[136] Hui Chen, Tao Peng, Sanjit Karmakar, Zhenda Xie, and Yanhua Shih. Observation of anticorrelation in incoherent thermal light fields. *Phys. Rev. A*, 84:033835, 2011.

[137] Jeffrey H. Shapiro and Eric Lantz. Comment on "observation of anticorrelation in incoherent thermal light fields". *Physical Review A*, 85:3–5, 2012.

[138] Rodney Loudon. *The Quantum Theory of Light (Oxford Science Publications)*. Oxford University Press, 2000.

[139] Leonard Mandel and Emil Wolf. *Optical Coherence and Quantum Optics*. Cambridge University Press, 1995.

[140] Marlan Scully. *Quantum optics*. Cambridge University Press, 1997.

[141] Roy J. Glauber. Photon correlations. *Phys. Rev. Lett.*, 10:84–86, 1963.

[142] E. C. G. Sudarshan. Equivalence of semiclassical and quantum mechanical descriptions of statistical light beams. *Phys. Rev. Lett.*, 10:277–279, Apr 1963.

[143] Martin J. Stevens, Burm Baek, Eric A. Dauler, Andrew J. Kerman, Richard J. Molnar, Scott A. Hamilton, Karl K. Berggren, Richard P. Mirin, and Sae Woo Nam. High-order temporal coherences of chaotic and laser light. *Optics Express*, 18:1430–1437, 2010.

[144] Pieter Kok and Brendon W. Lovett. *Introduction to optical quantum information processing*. Cambridge University Press, 2010.

[145] Alan Migdall. *Single-Photon Generation and Detection : Physics and Applications*. Elsevier Science, 2013.

[146] Jeffrey H. Shapiro and Ke-Xun Sun. Semiclassical versus quantum behavior in fourth-order interference. *Journal of the Optical Society of America B*, 11:1130, 1994.

[147] A. L. Schawlow and C. H. Townes. Infrared and optical masers. *Physical Review*, 112:1940–1949, 1958.

[148] Thomas Legero. *Zeitaufgelöste Zwei-Photonen-Interferenz*. PhD thesis, 2005.

[149] W. Grice and I. Walmsley. Spectral information and distinguishability in type-II down-conversion with a broadband pump. *Phys. Rev. A*, 56:1627–1634, 1997.

[150] Jack Gaskill. *Linear systems, Fourier transforms, and optics*. Wiley, 1978.

[151] Eric Hansen. *Fourier transforms : principles and applications*. Wiley, 2014.

[152] William Hartmann. *Signals, sound, and sensation*. American Institute of Physics, 1997.

[153] Hua Chen, Xue-Bi An, Juan Wu, Zhen-Qiang Yin, Shuang Wang, Wei Chen, and Zhen-Fu Han. HongOuMandel interference with two independent weak coherent states. *Chinese Physics B*, 25:020305, 2016.

[154] E. Meyer-Scott, H. Hübel, A. Fedrizzi, C. Erven, G. Weihs, and T. Jennewein. Quantum entanglement distribution with 810 nm photons through telecom fibers. *Applied Physics Letters*, 97:1–4, 2010.

[155] Y. Miyamoto, T. Kuga, M. Baba, and M. Matsuoka. Measurement of ultrafast optical pulses with two-photon interference. 18:900–902, 1993.

[156] R. B. Patel, A. J. Bennett, K. Cooper, P. Atkinson, C. A. Nicoll, D. A. Ritchie, and A. J. Shields. Postselective two-photon interference from a continuous nonclassical stream of photons emitted by a quantum dot. *Physical Review Letters*, 100:1–4, 2008.

[157] Z. Yan, E. Meyer-Scott, J. P. Bourgoin, B. L. Higgins, N. Gigov, A. MacDonald, H. Hubel, and T. Jennewein. Novel high-speed polarization source for decoy-state bb84 quantum key distribution over free space and satellite links. *Journal of Lightwave Technology*, 31:1399–1408, 2013.

[158] Christopher J. Pugh, Sarah Kaiser, Jean-Philippe Bourgoin, Jeongwan Jin, Nigar Sultana, Sascha Agne, Elena Anisimova, Vadim Makarov, Eric Choi, Brendon L. Higgins, and Thomas Jennewein. Airborne demonstration of a quantum key distribution receiver payload. *Quantum Science and Technology*, 2:024009, 2017.

[159] B. E. A. Saleh and M. C. Teich. *Fundamentals of photonics*. Wiley-Interscience, 2007.

[160] Jeanna Buldyreva. *Collisional line broadening and shifting of atmospheric gases : a practical guide for line shape modeling by current semi-classical approaches*. World Scientific, 2011.

[161] J. J. Olivero and R. L. Longbothum. Empirical fits to the Voigt line width: A brief review. *Journal of Quantitative Spectroscopy and Radiative Transfer*, 17:233–236, 1977.

[162] R. Ursin, F. Tiefenbacher, T. Schmitt-Manderbach, H. Weier, T. Scheidl, M. Lindenthal, B. Blauensteiner, T. Jennewein, J. Perdigues, P. Trojek, B. Ömer, M. Fürst, M. Meyenburg, J. Rarity, Z. Sodnik, C. Barbieri, H. Weinfurter, and A. Zeilinger. Entanglement-based quantum communication over 144 km. *Nature Physics*, 3:481–486, 2007.

[163] Xiao-Song Ma, Thomas Herbst, Thomas Scheidl, Daqing Wang, Sebastian Kropatschek, William Naylor, Bernhard Wittmann, Alexandra Mech, Johannes Kofler, Elena Anisimova, Vadim Makarov, Thomas Jennewein, Rupert Ursin, and Anton Zeilinger. Quantum teleportation over 143 kilometres using active feed-forward. *Nature*, 489:269–73, 2012.

[164] Juan Yin, Ji-Gang Ren, He Lu, Yuan Cao, Hai-Lin Yong, Yu-Ping Wu, Chang Liu, Sheng-Kai Liao, Fei Zhou, Yan Jiang, Xin-Dong Cai, Ping Xu, Ge-Sheng Pan, Jian-Jun Jia, Yong-Mei Huang, Hao Yin, Jian-Yu Wang, Yu-Ao Chen, Cheng-Zhi Peng, and Jian-Wei Pan. Quantum teleportation and entanglement distribution over 100-kilometre free-space channels. *Nature*, 488:185–188, 2012.

[165] Sebastian Nauerth, Florian Moll, Markus Rau, Christian Fuchs, Joachim Horwath, Stefan Frick, and Harald Weinfurter. Air-to-ground quantum communication. *Nature Photonics*, 7:382–386, 2013.

[166] Thomas Herbst, Thomas Scheidl, Matthias Fink, Johannes Handsteiner, Bernhard Wittmann, Rupert Ursin, and Anton Zeilinger. Teleportation of entanglement over 143 km. *Proceedings of the National Academy of Sciences*, 112(46):14202–14205, 2015.

[167] B. Heim, C. Peuntinger, N. Killoran, I. Khan, C. Wittmann, Ch Marquardt, and G. Leuchs. Atmospheric continuous-variable quantum communication. *New Journal of Physics*, 16, 2014.

[168] LIGO Scientific Collaboration and Virgo Collaboration. Observation of gravitational waves from a binary black hole merger. *Phys. Rev. Lett.*, 116:061102, 2016.

[169] Jean-Philippe Bourgoin, Brendon L. Higgins, Nikolay Gigov, Catherine Holloway, Christopher J. Pugh, Sarah Kaiser, Miles Cranmer, and Thomas Jennewein. Free-space quantum key distribution to a moving receiver. *Optics Express*, 23:33437, 2015.

[170] P. D. Townsend. Secure key distribution system based on quantum cryptography. *Electronics Letters*, 30:809–811, 1994.

[171] A. Muller, T. Herzog, B. Huttner, W. Tittel, H. Zbinden, and N. Gisin. Plug and play systems for quantum cryptography. *Applied Physics Letters*, 70:793, 1997.

[172] D. Stucki, N. Gisin, O. Guinnard, G. Ribordy, and H. Zbinden. Quantum key distribution over 67 km with a plug&play system. *New Journal of Physics*, 4:341, 2002.

[173] Kyo Inoue, Edo Waks, and Yoshihisa Yamamoto. Differential phase shift quantum key distribution. *Physical Review Letters*, 89:037902, 2002.

[174] I. Marcikic, H. de Riedmatten, W. Tittel, H. Zbinden, and N. Gisin. Long-distance teleportation of qubits at telecommunication wavelengths. *Nature*, 421:509–513, 2003.

[175] Damien Stucki, Claudio Barreiro, Sylvain Fasel, Jean-Daniel Gautier, Olivier Gay, Nicolas Gisin, Rob Thew, Yann Thoma, Patrick Trinkler, Fabien Vannel, and Hugo Zbinden. Continuous high speed coherent one-way quantum key distribution. *Optics Express*, 17:13326–13334, 2009.

[176] Erhan Saglamyurek, Neil Sinclair, Jeongwan Jin, Joshua A. Slater, Daniel Oblak, Félix Bussières, Mathew George, Raimund Ricken, Wolfgang Sohler, and Wolfgang Tittel. Broadband waveguide quantum memory for entangled photons. *Nature*, 469:512–515, 2011.

[177] Jeongwan Jin, Joshua A. Slater, Erhan Saglamyurek, Neil Sinclair, Mathew George, Raimund Ricken, Daniel Oblak, Wolfgang Sohler, and Wolfgang Tittel. Two-photon interference of weak coherent laser pulses recalled from separate solid-state quantum memories. *Nature Communications*, 4:2386, 2013.

[178] Erhan Saglamyurek, Jeongwan Jin, Varun B. Verma, Matthew D. Shaw, Francesco Marsili, Sae Woo Nam, Daniel Oblak, and Wolfgang Tittel. Quantum storage of entangled telecom-wavelength photons in an erbium-doped optical fibre. *Nature Photonics*, 9:83–87, 2014.

[179] Michael Reck, Anton Zeilinger, Herbert J. Bernstein, and Philip Bertani. Experimental realization of any discrete unitary operator. *Physical Review Letters*, 73:58–61, 1994.

[180] Benjamin Schumacher and Michael Westmoreland. *Quantum processes, systems, and information*. Cambridge University Press, 2010.

[181] Hiromichi Mishina and Toshimitsu Asakura. Two gaussian beam interference. *Nouvelle Revue d'Optique*, 5:101–107, 1974.

[182] Hideki Takenaka, Morio Toyoshima, and Yoshihisa Takayama. Experimental verification of fiber-coupling efficiency for satellite-to-ground atmospheric laser downlinks. *Opt. Express*, 20:15301–15308, 2012.

[183] R. L. Hilliard and G. G. Shepherd. Wide-Angle Michelson Interferometer for Measuring Doppler Line Widths. *Journal of the Optical Society of America*, 56:362, 1966.

[184] David J Erskine. White Light Velocity Interferometer. *US Patent*, (5,642,194), 1997.

[185] David J Erskine. Single and Double Superimposing Interferometer Systems. *US Patent*, (6,115,121), 2000.

[186] George Vanasse (edt.). *Spectrometric Techniques: v. 1.* Academic Press, 1977.

[187] Jeongwan Jin, Sascha Agne, Jean-Philippe Bourgoin, Norbert Lütkenhaus, and Thomas Jennewein. Efficient time-bin qubit analyzer compatible with multimode optical channels. *arXiv:1509.07490v2*, 2015.

[188] P. Ben Dixon, David J. Starling, Andrew N. Jordan, and John C. Howell. Ultrasensitive beam deflection measurement via interferometric weak value amplification. *Phys. Rev. Lett.*, 102:173601, 2009.

Appendix A

Matlab Code for Finding Two-Photon Coincidences

Presented here is a Matlab code to search time tag files for coincidences. It has been used for the laser Hong-Ou-Mandel experiments. The first two columns of Table 4.2 show a typical .dat file produced by our time taggers. The main text surrounding this Table explains the meaning of the important variables in this code. The result of running this code is the array "detc". It contains the detection time differences of coincidences that fall within the histogram window THist. I wrote this code with suggestions from Jean-Philippe Bourgoin (optimizing loops).

```
clear; tic;
%% Set parameters and read in rawdata.
% Time Tagger resolution.
TTres=78.125*10^-12;%156.25*10^-12;
% Histogram size (coincidence window).
THist=30e-6;
% Time tagger channel number of detectors 1 and 2.
det1_ch=1; det2_ch=2;
rawdata=double(dlmread('filename.dat','\t'));
%% Generate two time tag lists for time tags from detector 1 and 2.
det1=[]; det2=[]; k=1; l=1;
for i=1:length(rawdata)
    if rawdata(i,2)==det1_ch
        det1(k)=rawdata(i,1);
        k=k+1;
    end
    if rawdata(i,2)==det2_ch
```

```
        det2(l)=rawdata(i,1);
        l=l+1;
    end
end
clear rawdata;
%% Find D1-D2 coincidences
a=1; b=1; detc=[];
Nbins=ceil(THist/1e-7);
Tbin=floor(THist/TTres/Nbins);
Δ=Nbins*Tbin/2;
for i=1:numel(det1)
    coinc=0;
    for j=a:numel(det2)
        c=det2(j)-det1(i);
        if c>-Δ
            if coinc<0.5
                if c<Δ
                detc(b)=c; % First coincidence.
                a=j;
                b=b+1;
                coinc=1;
                end
            elseif c<Δ
                detc(b)=c; % Another coincidence.
                b=b+1;
            elseif coinc>0.5
                break; % Exit loop; no more coincidences for this det1.
            end
        else
            a=a+1;
        end
    end
end
toc
```

Appendix B

Matlab Code for Finding Two-Photon and Trigger Coincidences

Presented here is a Matlab code to search time tag files for coincidences *with respect to the modulator phase* in the laser Hong-Ou-Mandel experiments. Again, raw data files look like the first two columns of Table 4.2. However, here we have an additional detector channel (channel 3 in this case) for the modulator trigger. The goal is to first find a coincidence within a very narrow window and then find the time difference (the "phase" variable) between this coincidence and the nearest (interpolated) trigger time stamp. Do this for all coincidences and then save the phase variable. Do this for all optical delays (retroreflector positions). Further data processing (histograms and data fitting) is done with a Mathematica program. I wrote this code but benefited from discussions with Jean-Philippe Bourgoin and Brendon L. Higgins (making efficient use of Matlab's mod function to calculate the phase).

```
clear; tic;
%% Set parameters.
% Time Tagger resolution.
TTres=78.125*10^-12;%156.25*10^-12;
% Coincidence window.
coinwin=4*TTres;
% The trigger rate, downsampled trigger rate and downsample factor.
trigrate=353*10^6; dstrigrate=353*10^3; dsfactor=trigrate/dstrigrate;
% Time tagger channel number of detectors 1, 2 and trigger.
det1_ch=1; det2_ch=2; trig_ch=3;
% Retroreflector scan step size.
step=2; fileindex=15:step:57; histindex=1;
```

```
%% Loop through all files.
for files=1:length(fileindex)
rawdata=double(dlmread(sprintf('HOM_square_353MHz_353kHz_%g.dat', ...
    fileindex(files)),'\t'));
%% Generate three time tag lists for time tags from detector 1 and 2, ...
    as well as laser trigger tags.
det1=[]; det2=[]; trig=[];
k=1; l=1; m=1;
shift=0;%1.4*10^-9/TTres;
for i=1:length(rawdata)
        if rawdata(i,2)==det1_ch
            det1(k)=rawdata(i,1);
            k=k+1;
        end
        if rawdata(i,2)==det2_ch
            det2(l)=rawdata(i,1);
            l=l+1;
        end
        if rawdata(i,2)==trig_ch
            trig(m)=rawdata(i,1)+shift;
            m=m+1;
        end
end
clear rawdata;
%% Find D1-D2 coincidences
a=1; b=1; detc=[];
for i=1:numel(det1)
    for j=a:numel(det2)
        if abs(det1(i)-det2(j))<coinwin/TTres
            detc(b)=det1(i); % Coincidence.
            b=b+1; a=a+1;
            break;
        end
        if (det2(j)-det1(i))>coinwin/TTres
            break; % Exit loop; no more coincidences for this det1.
        end
        a=a+1;
    end
end
%% Find two downsampled laser triggers containing the coincidences.
c=1;d=1;phase=[];trigpair=[];
for i=1:numel(detc)
    for j=c:numel(trig)-1
        if (detc(i)-trig(j)>0) && (detc(i)-trig(j+1)<0)
```

```
55              phase(d)=TTres*mod(detc(i)-trig(j),(trig(j+1)-trig(j))/dsfactor);
56              d=d+1;
57              c=j; % Don't need to look at previous trigger tags anymore.
58              trigpair(d)=j; % Index of trigger pair containing ...
                    coincidence.
59              break;
60          end
61      end
62  end
63  %% Save phases.
64  filename=strcat(sprintf('%g',fileindex(files)),'.xlsx');
65  xlswrite(filename,phase')
66  end
67  toc
```